Role of the Interaction of BRCA2 and DDX5 in the DNA Damage Response

Gaetana Sessa

▶ **To cite this version:**

Gaetana Sessa. Role of the Interaction of BRCA2 and DDX5 in the DNA Damage Response. Cancer. Université Paris-Saclay, 2020. English. NNT : 2020UPASS116 . tel-03184571v1

HAL Id: tel-03184571

https://theses.hal.science/tel-03184571v1

Submitted on 29 Mar 2021 (v1), last revised 9 Apr 2021 (v2)

HAL is a multi-disciplinary open access archive for the deposit and dissemination of scientific research documents, whether they are published or not. The documents may come from teaching and research institutions in France or abroad, or from public or private research centers.

L'archive ouverte pluridisciplinaire **HAL**, est destinée au dépôt et à la diffusion de documents scientifiques de niveau recherche, publiés ou non, émanant des établissements d'enseignement et de recherche français ou étrangers, des laboratoires publics ou privés.

université PARIS-SACLAY

Role of the interaction of BRCA2 and DDX5 in the DNA damage response

Thèse de doctorat de l'université Paris-Saclay

École doctorale n° 582 : cancérologie : biologie - médecine - santé (CBMS)
Sciences de la vie et de la santé
Université Paris-Saclay, CNRS, Stress génotoxique et cancer, 75248, Paris 05, France.
Faculté de médecine

Thèse présentée et soutenue à Orsay, le 9 Juillet 2020, par

Gaetana SESSA

Composition du Jury

Simon SAULE Directeur de Recherche, Institut Curie	Président
Angelos CONSTANTINOU Directeur de Recherche, Institut de Génétique Humaine CNRS	Rapporteur & Examinateur
Gaëlle LEGUBE Directeur de Recherche, Centre de biologie intégrative CBI, LBCMCP	Rapportrice & Examinatrice
Stéphan VAGNER Directeur de Recherche, Institut Curie	Examinateur
Aura CARREIRA Directeur de Recherche, Institut Curie	Directrice de thèse

Thèse de doctorat

NNT : 2020UPASS116

To my aunt Alfonsina,
to her story, my strongest motivation

(A mia zia Alfonsina,
alla sua storia, la mia più grande motivazione)

ACKNOWLEDGEMENTS

Here we are, at the end of this wonderful path that gave me so much during these four years! Of course, I am curious about the next part, the "everything" outside that is waiting for me, but I am sure that the person I will be will be "shaped" by the experience of these amazing years. Therefore, I wish to thank all the people that have contributed to make so beautiful my "PhD" journey.

First, this project would have been not possible without the financial support provided by MESRI-University of PSL for the first three years and "Fondation ARC pour la Recherche sur le cancer" that financed my 4th year of PhD.

I would like to thank all members of my Jury for having accepted to evaluate my thesis work: Simon Saule, Stephan Vagner, Gaëlle Legube and Angelos Constantinou. In particular, my special thanks go to Gaëlle Legube and Angelos Constantinou who read and evaluate my manuscript.

Thanks to Stephan Vagner, who was also member of my "Comité de these" for the half-time evaluation and who gave me special advice and contributions during my whole PhD project. Thanks, in particular, to Sylavin Martineau, from Vagner's Lab who helped me with "laser microirradiation" experiments.

I would like to thank Andres Aguilera and members of his lab, in particular Belen Gómez-González: their help and experience in this field was a precious contribution to this project.

But, of course, this work would have been not possible without my thesis director and supervisor, Aura Carreira, who accepted me in her lab, first for my Erasmus Internship and then for my PhD and who was my guide for these last four years. Thank you for your enthusiasm and your motivation, for showing always devotion for your job. Thank you for teaching me how to work in science, to suggest me how to proceed and face so many "everyday" problems. In particular, thank you for believing in me and increased confidence in myself.

I could never forget, of course, all present and past lab members that contributed to make happier this journey: Asa, for being always kind and helpful, for her always welcomed advices; Juan, who, with patience, guided me through my first years in the lab; Charlotte, for her joy, for being always caring and available for work (or not)-related chats. And still, Isaac, for the laughs and the amazing time, for being always helpful; Romane for being kind, caring and supporting, for her great help on analysis of IFs; Anna, for her support, for having brought a little of my Italy in the lab. And still, Davide, Domi and all the other members that joined us during these years.

Thanks to all members of UMR3348 unit, for the support, the advices and the great time spent together, especially during lunch breaks.

I would also like to thank Marie-Noelle Soler and especially Laetitia Besse from Imaging Facility for the great help with image acquisition and analysis, Patricia Duchambon from the recombinant protein platform at I. Curie for the help with protein purification and members of Mass Spectrometry Facility in Curie Paris.

But I would have never been able to get to the end of this experience without the unfailing support of my Family. Thank you Mum and Dad, for being always with me, no matter what, for your help during these years, for being always so proud of me. Thanks to my sisters, for supporting me during this path, for the advices, the laughs, for being my eyes on Mum and Dad during this time. A special thanks to my sweet Irene, the latest arrival in our family, for making this last period happier and easier to face. Thanks to my sweetheart Davide, I could have never done this without you, your unconditional support, your courage in facing these years with me, so far away from each other. I can't wait to start the next part of my life with you!

Thank you to all my family, my friends, near and far, especially to my little "Italian" family here in Paris: it would have been not the same without you! Thank you for dinners, laughs and your help in the most difficult moments.

And last but absolutely not least, I'd like to thank a person that is not with us anymore but who inspired me during these years; my aunt Alfonsina, to which I have dedicated this work. Her story represented my strongest motivation to continue this work and knowing that, even if to a small extent, our work contributes every day to helping people like her, makes me proud and honoured of the path that led me here today.

INDEX

CHAPTER 1 - INTRODUCTION

The genetic information of every living organism is contained within the DNA and its integrity needs to be preserved for the inheritance of traits to their offspring. Therefore, cells have developed a complex DNA repair system to protect genetic information from endogenous and exogenous sources of DNA damage. In this Introduction, I will describe the main DNA damaging insults and their origin. Next, I will introduce general aspects of the DNA damage response (DDR), describing main features of DNA damage sensing, DDR signalling and DNA repair pathways. This thesis project relates to the interplay between DNA repair factors involved in homologous recombination repair pathway (HR), in particular the Breast Cancer susceptibility gene 2 (BRCA2), with RNA binding proteins/ RNA helicases, in this context. Therefore, I will give an extensive and detailed overview on these topics presenting the mechanistic and functional aspects of HR and describing BRCA2 structure, functions and its involvement in tumorigenesis. I will emphasize the link between DNA-RNA structures or R-loops, genomic instability and DDR discussing the interplay of RNA helicases and nucleases and DNA repair proteins in resolving R-loops. Finally, I will focus on RNA helicases involved in RNA metabolism specifically at DNA breaks that is the general context in which I am going to describe and discuss the results of my project regarding BRCA2 and the RNA helicase DDX5.

The role of DNA-RNA hybrids at DSBs has attracted a lot of interest in the last few years and although is being actively studied, there are many aspects of their function that are controversial. Moreover, a growing number of factors have been implicated in DNA-RNA hybrid regulation at DSBs yet fundamental mechanistic aspects of this process remain to be elucidated. This thesis project should contribute to advance our understanding on this recent field.

1. Importance of the DNA damage response and DNA-RNA hybrids metabolism in maintaining genome integrity

1.1. The DNA damage response

The maintenance of genomic integrity is important for the survival of all organisms. The DNA molecule is highly vulnerable to chemical modification, which can cause numerous lesions. In fact, our genome is constantly exposed to diverse sources of damage (Fig. 1); it is estimated that the DNA can experience up to 10^5 spontaneous lesions of different origin per day[1]. These insults can arise from endogenous and exogenous sources: examples of endogenous sources are spontaneous reactions like hydrolysis, leading to the formation of abasic sites and causing deamination or alkylation[2]. Another example is represented by the reactive oxygen species (ROS) generated by mitochondria, peroxisomes etc., that induce extensive damage to the genome including base oxidation and DNA single-strand breaks (SSBs)[3]. Common exogenous agents causing lesions in the DNA include ultraviolet (UV) or ionizing radiations (IR): the main consequence of UV rays on the DNA structure is the formation of covalent links between adjacent pyrimidine bases (photodimers), whereas IR induce base modifications, SSBs and DNA double-strand breaks (DSBs) by direct ionization or indirect ROS production. Other exogenous sources of DNA damage are chemical agents used in cancer chemotherapy (alkylating agents, crosslinking agents such as mitomycin C (MMC) and cisplatin) or man-produced chemicals (ex. hidrocarbons or aldehydes in cigarette smoke)[4].

To preserve genomic integrity, cells have developed an arsenal of DNA healing strategies-collectively known as the DNA damage response (DDR) that detect different types of damage and initiate the appropriate repair pathway or, if irreparable, induce cell cycle arrest and/or apoptosis. In the case of errors in DNA repair or in DNA replication itself, these lesions can be converted into permanent mutations and therefore passed-on to the next generations of cells. One important consequence of mutations is the loss of tumor-suppressor genes and the improper activation of oncogenes, which can trigger uncontrolled cellular proliferation and the development of malignant cells. Indeed, genome instability is a hallmark of all forms of cancer[1,6].

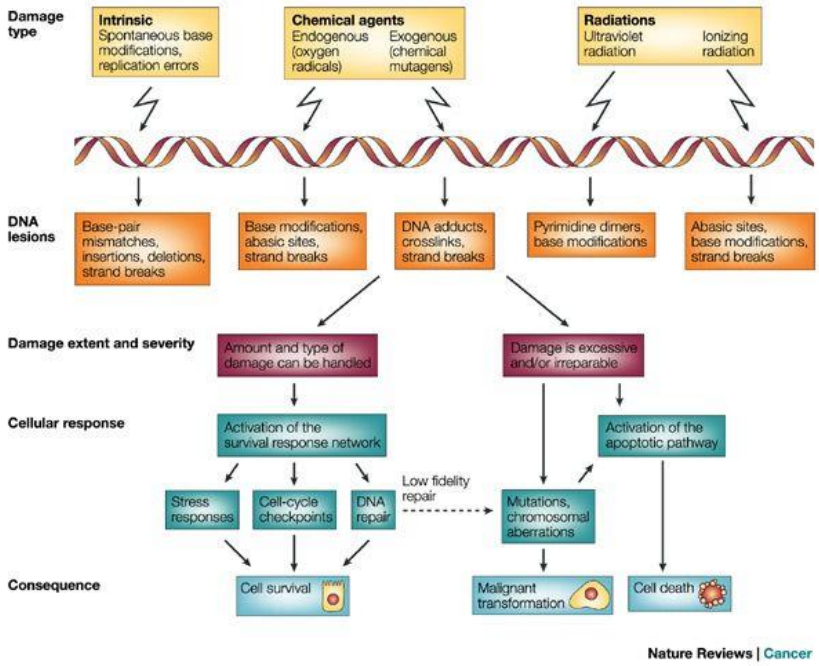

Figure 1. Damage types, DNA lesions and cell fate. Top: most common endogenous and exogenous sources of DNA damage and resulting DNA lesions. Bottom: according to the amount of DNA damage, cells can activate DNA damage-specific repair processes or induce apoptosis, leading to cell survival or death, respectively. However, in both scenarios mutations can occur engendering malignant transformation (Shiloh, *2003*[5]).

1.1.1. DNA damage sensing and signalling

The DDR is a signal transduction pathway consisting of sensors, transducers and effectors that detects DNA damage and induces a specific response to this in order to protect the cell and ensure genome integrity[7]. In the last 30 years, a conserved set of DNA damage signalling kinases have been identified and widely characterized; they are traditionally categorized in apical and downstream (or effector) kinases (Fig. 2). The apical kinases are ataxia telangiectasia-mutated (ATM), ATM and Rad3-related (ATR), that belong to the PIKK kinase family, and the DNA-dependent protein kinase, catalytic subunit, (DNA-PKcs) [8]. Generally, ATR is activated by a wide range of genotoxic stresses, such as replication stress. ATR is recruited via its partner protein ATRIP to extended tracts of ssDNA coated with the ssDNA binding protein replication protein A (RPA) [11]. ATRIP-bound ATR interacts directly with ssDNA-coated RPA and promotes ATR localization to sites of replication stress and DNA damage[9]. Full activation of ATR requires also the presence of activator proteins such as TopBP1, and ssDNA/dsDNA junctions[11].

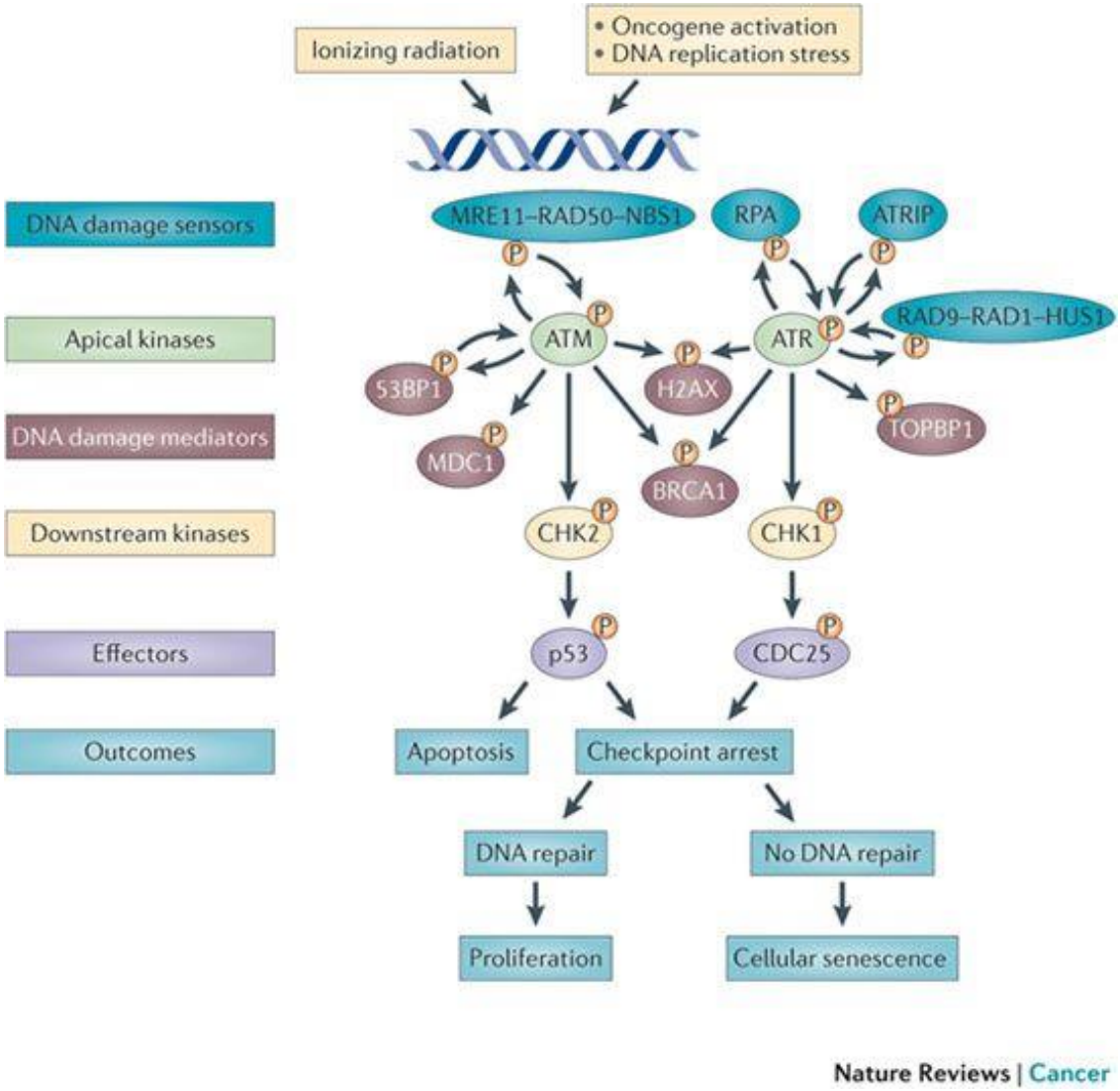

Figure 2. DNA damage response activation. DNA damage sensor proteins (MRN complex, RPA and ATRIP) are essential for apical kinases activation (ATM, ATR and DNA-PKcs). Once activated, apical kinases phosphorylate and activate downstream kinases, essential for responses to DNA damage, such as cell-cycle arrest, in order to allow DNA damage repair. (*Sulli et al. 2011*[13])

In contrast to ATR, ATM and DNA-PKcs associate with the ends of DSBs[8]. In particular, the heterodimer Ku (Ku70/Ku80) binds to the ends of DSBs first and recruit DNA-PKcs in order to start a cascade of phosphorylation events on downstream targets that are involved in DSBs DNA blunt ends processing[10]. By contrast, ATM is recruited to chromatin in response to DSBs in a process that requires ATM binding to the C-terminus of NBS1, a component of the MRE11-RAD50-NBS1 (MRN) complex, which contributes also to ATM activation[11].

Activated apical kinases transfer stimulatory phosphorylation to the downstream effector

checkpoint kinases, CHK1 and CHK2, that in turn catalyze phosphorylation events that would coordinate the cellular responses to DNA damage as part of the canonical DNA damage checkpoint. ATM and ATR utilize checkpoint adaptors to mediate the transfer of phosphorylation to effector kinases: ATR relies on Claspin to mediate activation of CHK1, whereas two adaptors, MDC1 and 53BP1, have been linked to the signalling axis ATM-CHK2. MDC1 and 53BP1 possess BRCT domains that directly bind to phosphorylated variant histone H2AX (γH2AX), whose phosphorylation is mediated by ATM or ATR in response to replication stress[8]. Once activated, DNA damage signalling kinases CHK1 and CHK2 mediate a number of cellular responses such as cell cycle arrest[8]: CHK1 and CHK2 can promote, in turn, the proteasomal degradation of CDC25, a phosphatase that removes inhibitory modifications from mitotic cyclin-dependent kinases (CDKs) in order to slow down or arrest cell-cycle progression. This prevents the cells from entering mitosis prematurely, providing the time required to repair the DNA or, if the damage is too extensive, for the activation of senescence or apoptotic pathways[11]. Another critical mediator of cell cycle arrest in humans is the p53 transcription factor, whose classical function is to trigger the apoptotic program. p53-mediated expression of the CDK inhibitor protein p21 represents the primary mechanism by which p53 blocks progression through the cell cycle [8,12]. Other cellular processes affected by the activation of DNA damage signalling kinases are replication fork stability, transcriptional response, inhibition of replication origin firing and dNTP regulation[8].

Although the DNA damage checkpoints were originally considered as non-essential regulatory factors, it is now clear that they are one important and integrated part of the DDR. One typical example that illustrates the physiological importance of these checkpoint proteins is the disorder Ataxia Telangiectasia. Individuals carrying two mutated ATM alleles may show loss of motor control owing to Purkinje cell loss, immune deficiencies and increased predisposition to cancer[7].

1.1.2. DNA repair pathways

Because of the plethora of possible DNA lesions, cells have evolved a sophisticated and highly regulated set of DNA repair systems specific for almost all types of damage (Fig. 3). In some cases, more than one pathway is required for the repair of one type of DNA damage. In the next section, I will give an overview of the canonical DNA repair pathways focusing my attention on DSBs repair, the HR pathway and on its important mediator BRCA2.

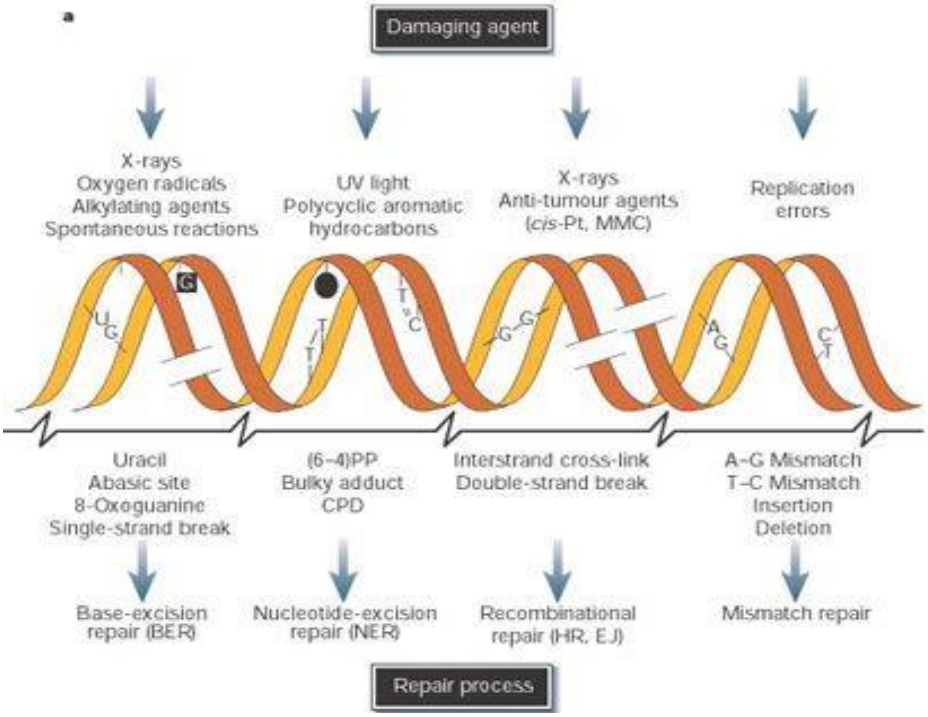

Figure 3. DNA damage repair pathways. Top**:** common DNA damage agents leading to the formation of different kind of DNA lesions. Bottom: DNA repair pathways induced in response to specific DNA lesions (Adapted from *Hoeijmakers, 2001*[14])

1.1.2.1. Direct repair, BER, NER, mismatch and DNA damage-associated replication stress repair

Alkylating agents are a source of DNA damage. They represent a class of reactive chemicals highly abundant in the environment and in living cells. Externally, alkylating agents can be components of air, water, food and pollutants whereas within the cells they can result from oxidative stress. Moreover, due to their cytotoxic properties, many alkylating agents are currently used as chemotherapeutic drugs[15]. As reactive chemicals, they are able to transfer alkyl-carbon groups onto the DNA generating a variety of covalent adducts. The pattern of DNA lesions generated by an alkylating agent depends on the number of reactive sites within the alkylating agent (monofunctional versus bifunctional), its particular chemical reactivity, the type of alkyl-group addition (methyl or chloroethyl) and the DNA substrate (double-stranded (ds) or single-stranded (ss)) [15]. Among the most common alkylating agents-induced lesions there are N7-methylguanine (7meG),

N3-methyladenine (3meA) and O^6-methylguanine (O^6meG). Although 7meG is a relatively harmless lesion, 3meA and O^6meG generate more serious effects and compromise genomic integrity inducing mutagenesis or blocking essential cellular processes like DNA replication or transcription[15]. Therefore, the repair of these lesions is essential for the survival of the cell. The main repair mechanisms for alkylation damage include direct DNA repair, base excision repair (BER), nucleotide excision repair (NER) and mismatch repair (MMR).

- Direct DNA repair is mediated by a variety of DNA methyl and alkyltransferase such as O^6meG DNA methyltransferase (MGMT) and O6-alkylguanine DNA alkyltransferase (AGT). In general, their mechanism of action consists in a reaction that transfers the methyl or alkyl group from the O^6 position of a guanine to a highly conserved cysteine residue inside AGT or MGMT[15, 16], thereby removing the DNA lesion. Another important enzyme involved in DNA direct repair is AlkB homologue (ALKBH) family of α-ketoglutarate-dependent dioxygenases that catalyse the hydroxylation of aberrant methyl groups[15] (Fig.4a).

- Base excision repair (BER) is a highly conserved pathway from bacteria to humans and is responsible for repairing the vast majority of endogenous DNA damage including alkylations, oxidations, deaminations and depurinations, as well as SSBs. The initial step in BER is the search for the lesions in DNA by DNA glycosylases[17]. In humans, there are currently 11 known DNA glycosylases, alkyladenine-DNA glycosylase (AAG) is one example (see fig. 4b) [15]. The glycosylases that recognize uracil, thymine, and alkylated bases remove the damaged base by cleaving the N-glycosyl bond between the base and the sugar. The resulting abasic site is recognized by an apurinic (AP) endonuclease, APE1, that cleaves the abasic site leaving a sugar attached to the 5′ side of the nick. The resulting 3′ hydroxyl is a substrate for the repair polymerase, DNA polymerase β (Pol β). The gap is finally filled in and sealed by a DNA ligase[17]. Importantly, each step of BER generates intermediates that are highly toxic; therefore, it is essential to prevent the accumulation of these intermediates. The X-Ray Cross Complementing 1 (XRCC1), a key BER protein, coordinates the DNA-processing events of BER to ensure its proper completion[15].

- Nucleotide excision repair (NER) is a versatile mechanism that removes helix-distorting DNA lesions and structures from the genome. NER removes lesions from the entire genome[15]; however, it partitions in two branches: (i) transcription-coupled repair (TCR) which involves the repair of DNA damage that specifically blocks the progression of RNA polymerase II (RNAP) along the DNA strand during transcription. (ii) Global genomic

repair (GGR); a slower and transcription-independent random process that inspects the entire genome for DNA damage[18].

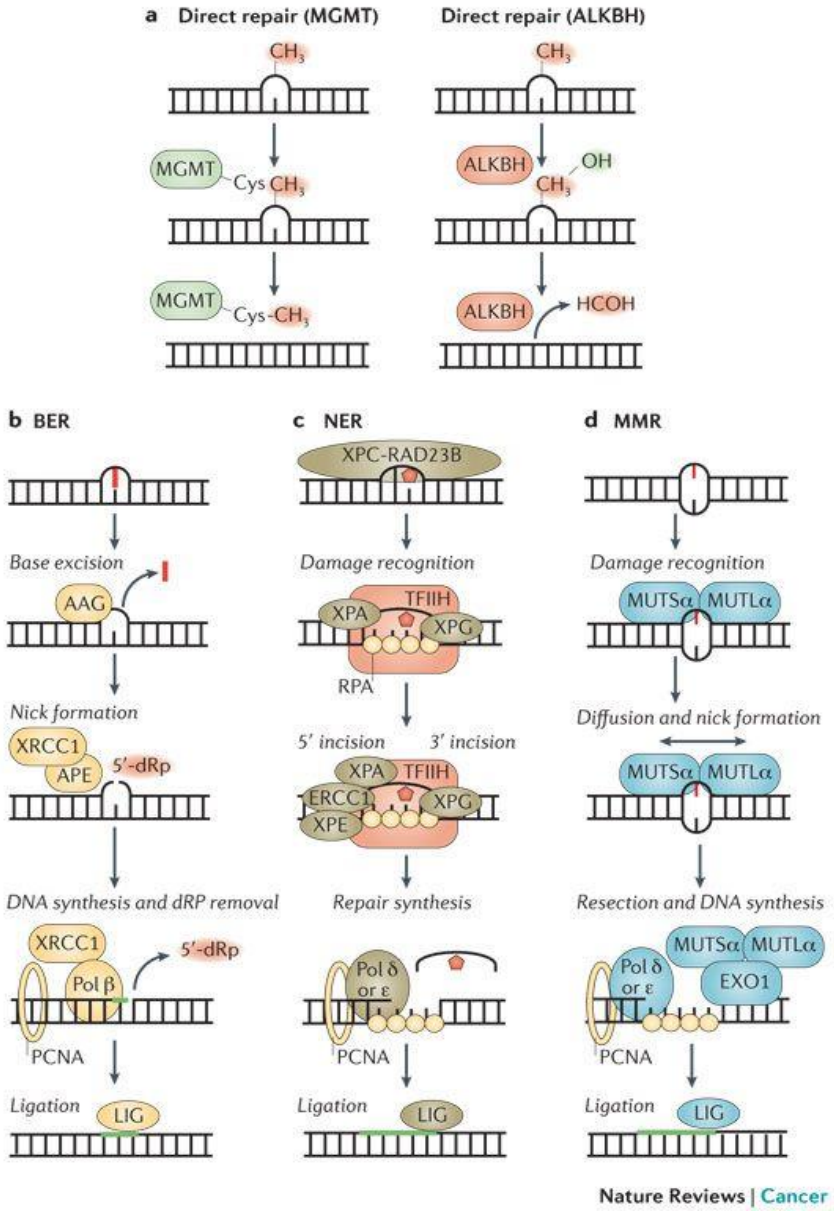

Figure 4. DNA damage repair pathways for alkylated bases. (a) Direct repair consists on the reversal of an alkylated base to a normal base without the need of excision and generation of DNA breaks. (b) BER removes simple alkyl and oxidative base lesions. (c) NER is especially implicated in eliminating helix-distorting lesions. (d) MMR mediates the removal of mismatched bases and miss-pairs. See text for details on the mechanisms. (From *Fu et al. 2012*[15])

The NER process begins with the recognition of a DNA lesion. Then, dual incisions flanking the lesion are generated. The lesion-bearing oligonucleotide is removed, a patch is

synthesized using the undamaged complementary strand as a template, and the patch is ligated to the contiguous strand (Fig. 4c). Although, most of the steps of NER process are common between GGR and TCR, the recognition of the DNA lesion differs: in GGR repair, a helix distorting lesion or structure is directly recognized by XPC, complexed with hRAD23B and Centrin 2 (CETN2). Then, the complex melts the DNA around the lesion and recruits the multiprotein complex TFIIH. By contrast, in TCR-recognized DNA lesions such as bulky adducts, RNAP arrest constitutes the first step for damage recognition. The arrested elongation complex recruits CSB (ERCC6), a transcription elongation factor that translocates along the template DNA together with RNAP. CSB strongly binds the polymerase when it is blocked at a lesion and changes the DNA conformation by wrapping the DNA around itself, altering the interface between RNAP and DNA. CSB recruits the CSA complex and other NER factors whose role is to remove or backtrack RNAP to allow access to TFIIH[18]. At this step, in both GGR and TCR, XPB and XPD, two components of TFIIH complex, unwind the DNA to create a 20–30-nucleotide bubble[18] and then XPA, RPA and XPG are recruited. XPA facilitates the release of the CDK-activating kinase (CAK) sub-complex from TFIIH, possibly promotes lesion verification by TFIIH and binds to the DNA lesion in a single-stranded configuration. RPA binds the ssDNA coding strand and likely has a role in DNA damage signalling by activating the DNA damage response kinase ATR. Together, TFIIH, XPA and RPA promote the recruitment and positioning of the endonucleases ERCC1–XPF and XPG, which incise the DNA 5′ and 3′ sides of the lesion, respectively. Following excision of the damaged DNA, the gap is filled by DNA synthesis and ligation, mediated by proliferating cell nuclear antigen (PCNA), DNA polymerase δ, ε or κ and DNA ligase 1 or XRCC1–DNA ligase 3[19].

Defects in NER lead to diverse clinical consequences such an extreme predisposition to cancer as it occurs in patients suffering from Xeroderma Pigmentosum (XP), a pathological disorder leading to hypersensitivity to UV radiation, sun-induced cutaneous features such as hypopigmentation and hyperpigmentation, and high risk of skin-cancer among others. Other serious effects derived from NER pathways defects include neurodevelopmental diseases like Cockayne syndrome and the even more severe cerebro-oculo-facio skeletal syndrome (COFS), characterized by microcephaly, mental retardation, retinal degeneration, photosensitivity, among other defects, and a highly reduced life-expectancy[20].

- Mismatch repair (MMR) is implicated in correcting error-containing sections of the newly synthesized DNA strand generated after replication. These errors arise especially

within repeated-sequence motifs, such as microsatellites, when primer and template strands dissociate and re-anneal incorrectly generating heteroduplex DNA molecules. As a result, the number of repeated units in the template and in the newly synthesized strand is different. These heterogeneities are known as insertion/deletion loops (IDLs) and together with base–base mismatches due to DNA polymerases errors that escape their proofreading function, represent the main target of MMR repair proteins[21]. In MMR, mismatches are identified and firstly bound by MutSα heterodimer (MSH2–MSH6) forming a sliding clamp. Upon an ATP-dependent conformational change, MutSα recruits and binds MutLα heterodimer (PMS2–MLH1). Diffusion of MUTSα–MUTLα complex leads to nicking of the DNA either upstream or downstream of the mismatch mediated by the endonuclease activity of the PMS2 subunit [15, 22]. The nicking serves as an entry point for exonuclease 1 (EXO1) that removes a segment of DNA which is then filled in and repaired by a combination of Pol δ, Pol ε and sealed by DNA ligase[22] (Fig. 4d). Loss of MMR activity, due to the lack of function of any of its key players, is associated with tumor development, microsatellite instability (MSI tumors) and triplet repeat expansions, the latter being at the origin of neurological diseases such as Huntington disease and myotonic dystrophy[23, 24].

- DNA damage-associated replication stress repair generally arises when replication fork progression during genome duplication is impeded by obstacles of intracellular or extracellular origin leading to the condition of "replication stress"[25, 26]. The most common causes of replication stress include limited nucleotide pool, nicks or gaps in ssDNA, unrepaired DNA lesions, ribonucleotide incorporation, repetitive DNA motifs, DNA secondary structures in the DNA (ex. DNA hairpins, G-quadruplexes) or DNA-RNA hybrids generating transcription-replication conflicts[26].

The first signal of replication stress is represented by stalling or slowed progression of the replication fork and/or DNA synthesis. All the obstacles mentioned above can lead to the generation of ssDNA caused by the uncoupling of the polymerase and the DNA helicase that continues to unwind the DNA helix regardless the stalling of the polymerase. Persistence of ssDNA adjacent to the stalled replication fork leads to the coating of ssDNA by RPA, which in turn stimulates the activation of the DNA damage–checkpoint kinases ATR and CHK1[25, 26] (Fig. 5). ATR-mediated signalling orchestrates different pathways at stalled replication forks allowing cell-cycle arrest and the regulation of intracellular dNTP levels, thus ensuring proper fork repair and restart. In addition, ATR phosphorylates and regulates the activity of several replisome components and fork-remodelling enzymes: for example, ATR promotes the association of the Fanconi anemia (FA) protein FANCD2

with the MCM replicative helicase and this interaction slows DNA synthesis and prevents the formation of long ssDNA stretches under conditions of reduced nucleotide pools. Moreover, ATR activation can either prevent new origin firing by inhibiting replication initiation, or promote firing of dormant origins within pre-existing replication factories, thus allowing completion of DNA synthesis in the vicinity of perturbed replication forks[25].

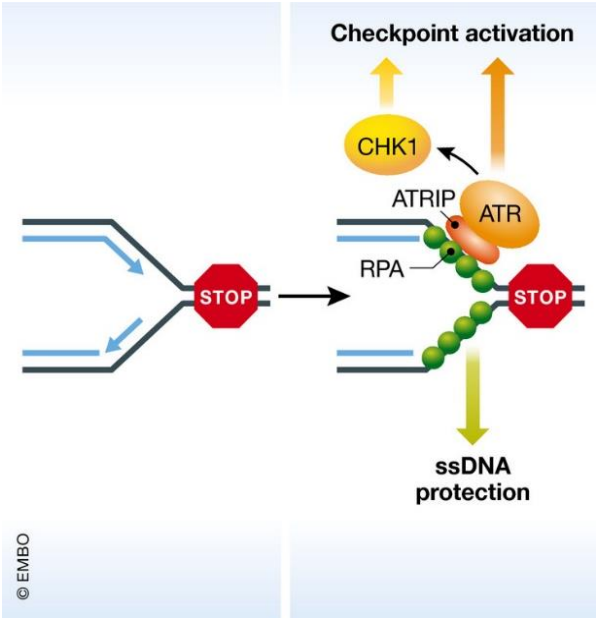

Figure 5. The ATR-mediated replication stress response. After replication fork stalling, the ssDNA generated by polymerase–helicase uncoupling is coated by RPA to prevent secondary structure formation. RPA-coated ssDNA is recognized by ATR. ATR kinase targets CHK1 phosphorylation which prevents progression through the cell cycle until replication is completed (Adapted from *Liao et al, 2018*[43])

Stalled replication forks and gaps can be restarted by different mechanisms including translesion synthesis (TLS), template switching (TS), fork regression or HR[27]. TLS is catalyzed by specialized low-fidelity DNA polymerases (Pol η, Pol ι, Pol κ, and Rev1) to bypass DNA lesions. Due to a large active site and the lack of proofreading activity, these polymerases allow the incorporation of a nucleotide opposite to a damaged DNA template. On the contrary, TS is proposed to use a recombination-like mechanism by which the nascent DNA of the sister chromatid is utilized as a temporary template for replication (Fig. 6 a, b). TLS and TS are generally considered as mechanisms evolved to deal with damage encountered during replication, a condition commonly known as DNA damage tolerance (DDT). This pathway allows the replication to continue in the presence of a DNA lesion by promoting damage bypass. The choice between these two pathways of DDT

(TLS and TS) is important because it can determine an error-prone or error-free outcome and a key player driving this choice is proliferating cell nuclear antigen (PCNA). PCNA regulating role in DDT is mediated by its ubiquitination and SUMOylation[28].

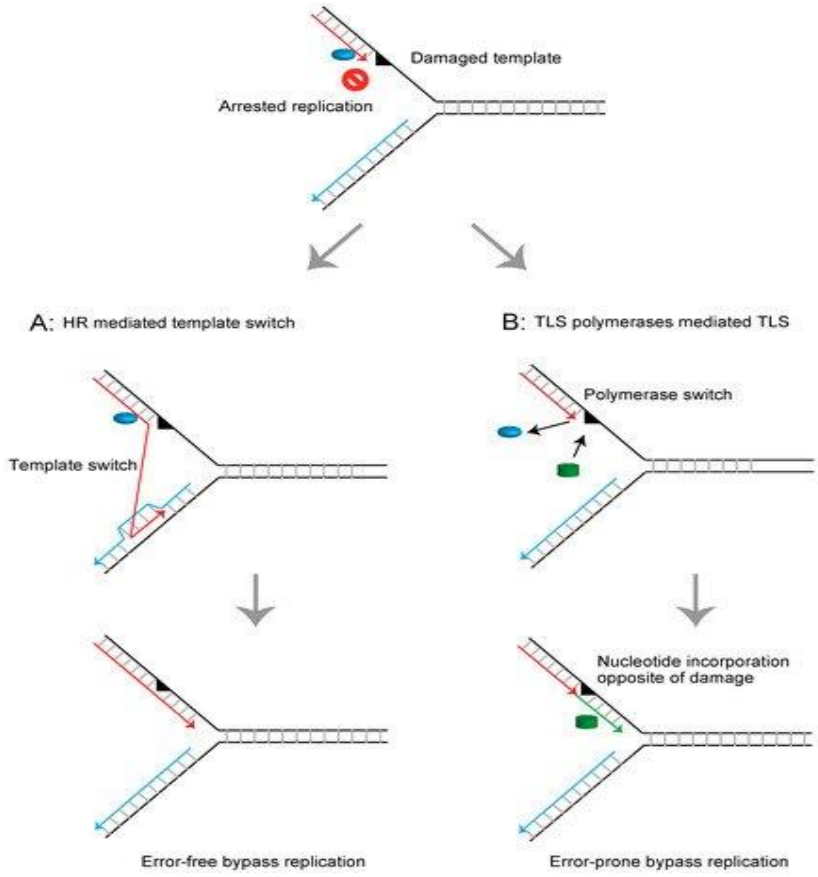

Figure 6. Schematic representation of the mechanisms restoring the arrested replication fork at the damaged DNA template. (a) Homologous recombination (HR)-mediated template switch restores the arrested replication fork using intact newly synthesized DNA as the template strand and promotes error-free bypass replication. (b) Translesion DNA synthesis (TLS) polymerases mediate direct bypass replication across the damaged template in an error-prone manner. (From *Abe et al., 2018*[33]).

HR plays a pivotal role in the repair of ssDNA gaps and DSBs and contributes to the general robustness of DNA replication[29, 30]. With the help of recombination mediator proteins such as BRCA2, RAD51 recombinase nucleates onto ssDNA to form a nucleoprotein filament. Subsequently, this filament performs the homology search on the

intact strand and promotes strand invasion within the homologous DNA duplex. This results in the formation of a D-loop structure within which the 3′end of the invading strand primes DNA synthesis[30]. For a more extensive explanation of HR pathways see section 1.2 (page 29).

Another important contribution of HR proteins at the replication fork is the protection of the fork from aberrant nuclease activity[31, 32]. Upon the inhibition of fork elongation, the BRCA2, RAD51 and many other factors such as breast cancer type 1 susceptibility protein BRCA1 or the Fanconi anemia (FA) protein FANCD2[297] protect newly replicated DNA from unscheduled degradation by nucleases such as MRE11[31, 32, 164-166]. First evidence of BRCA2 in protection of stalled replication forks came from a study showing that BRCA2 deficiency de-stabilizes the structure of DNA intermediates formed at stalled replication forks induced by exposure to hydroxyurea (a common replication stress inducing agent), subsequently triggering their collapse into DSBs, leading to the proposal that BRCA2 stabilizes the structure of arrested forks to allow their error-free resolution[133]. Years later, a study using a mutant at the C-terminal RAD51 binding site of BRCA2 showed that this region is dispensable for HR but required to protects nascent DNA strands at stalled forks from degradation by the MRE11 nuclease[31]. Following this discovery, much efforts have been devoted to uncovering the nucleases and regulatory factors leading to extensive fork degradation, as well as the structure of the replication fork required for protection and HR proteins recruitment. Indeed, recent studies have identified that in a BRCA-deficient background the structure targeted by nucleases is a reversed replication fork[167-170]. Fork reversal is a key mechanism that allows replication forks to reverse their course in order to cope with DNA lesions[171]. These studies have demonstrated that BRCA2, as well as BRCA1, is required to stabilize the RAD51 filament on the regressed arms of the reversed replication fork, thereby protecting the nascent DNA from nucleolytic degradation (Fig. 7). In addition, BRCA2 has been proposed to prevent ssDNA gap accumulation both at replication fork junctions and behind forks by stabilizing RAD51 binding[167]. In the absence of BRCA2, forks with persistent ssDNA gaps would be converted into reversed forks, leading to extensive degradation. In the context of BRCA-deficient tumors, MRE11 was the first nuclease associated with fork degradation[31, 32, 164-166]. However, later studies have also identified EXO1 and DNA2 as nucleases contributing to fork degradation in BRCA-deficient tumors[168]. In addition, CtIP protein is likely required to initiate MRE11-dependent fork degradation[168], although a more recent study seems to contradict this conclusion proposing a role for CtIP in protecting stalled replication forks from

degradation[172].

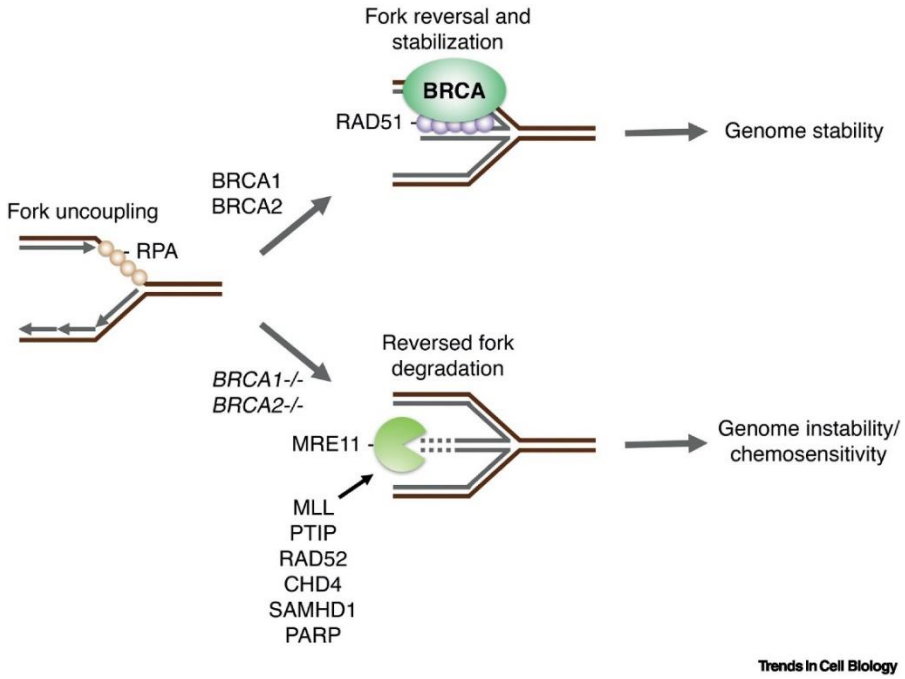

Figure 7. Role of HR factors BRCA1/2 and RAD51 in protection of stalled replication forks: Schematic representation of recent findings on the role of BRCA proteins and RAD51 at stalled replication forks. In BRCA proficient cells, in case of replication stress causing the stall of the fork, the fork is reversed and BRCA1/2 are recruited here to stabilize RAD51 nucleoprotein filament preventing ssDNA degradation. This excessive degradation might be occurring in BRCA-deficient tumors. (From *Byrum, Vindigni, and Mosammaparast 2019*[70]).

However, it is important to distinguish this excessive degradation of stalled replication intermediates that underlies the pathological effects of resection from the limited resection of nascent DNA strands which is required for efficient fork restart. For example, controlled DNA2-dependent resection of reversed replication forks is a functionally relevant mechanism mediating reversed-fork restart and providing resistance to prolonged genotoxic treatments[25].

DNA replication stress is the major source of spontaneous DSBs in dividing cells. Prolonged fork stalling or failure to resume DNA synthesis by the mechanisms described above lead to fork collapse and formation of one-ended DSBs[25]. Fork collapse or under-replication of the DNA can contribute to ultrafine bridges, MiDAS (mitotic DNA synthesis) and sister chromatid bridges as a consequence of the excess of ssDNA generated at arrested forks, that can subsequently result in chromosomal instability and diseases[298]. For example, mutations in the cognate binding partner of ATR, ATRIP lead to Seckel

syndrome, characterized by developmental delay, microcephaly and mental retardation. Loss of proteins that recognize or repair DNA lesions also leads to a number of human diseases. For example, loss of the specialized DDT polymerase Pol η, involved in TLS, results in a variant form of the cancer-susceptibility condition of Xeroderma Pigmentosum[26].

1.1.2.2. Inter-strand crosslink repair

Inter-strand crosslinks (ICLs) are lesions that covalently link two bases on the complementary strands of DNA. These lesions are generated by chemicals with two reactive electrophilic groups. The formation of ICLs is highly dependent on the sequence because two nucleophilic groups on opposite strands must be aligned geometrically to allow the cross-link to occur[34]. The presence of an ICL affects the unwinding of the DNA, an essential step in DNA replication and transcription; thus, ICLs are detrimental for cells, especially those in rapid division. Not surprisingly, several crosslinking agents such as mitomycin C (MMC) and cisplatin are used in the clinic as anti-cancer drugs. ICLs such as aldehydes also form naturally as by-products of cellular metabolism[34].

Since ICLs compromise both DNA replication and transcription, it is clear that their repair is of high importance. Several DNA repair pathways are involved in the repair of ICLs including NER, HR and TLS. The pathway involved in repairing them will depend on how the DNA lesion is recognised[35, 36, 37]. Although in most cases ICLs repair is coupled to replication and triggered when a DNA replication fork collides with the ICL[35], in the context of non-replicating DNA, the distortion of the DNA helical structure caused by the lesion attracts proteins involved in the global damage surveillance of DNA. This process has been shown to involve proteins of the NER pathway, as XPC implicated in the initial recognition[36].

In replicating cells, the stalled fork at the site of the lesion attracts protein of the Fanconi anemia (FA) pathway (Fig. 8). The FA pathway comprises 22 gene products (FANCA to FANCW). Autosomal biallelic germline inactivation of any of the 22 FA genes (with the exception of FANCB, which is X-chromosomal) causes Fanconi anemia[174], a genetic disease that results in sensitivity to ICLs and predisposes patients to bone marrow

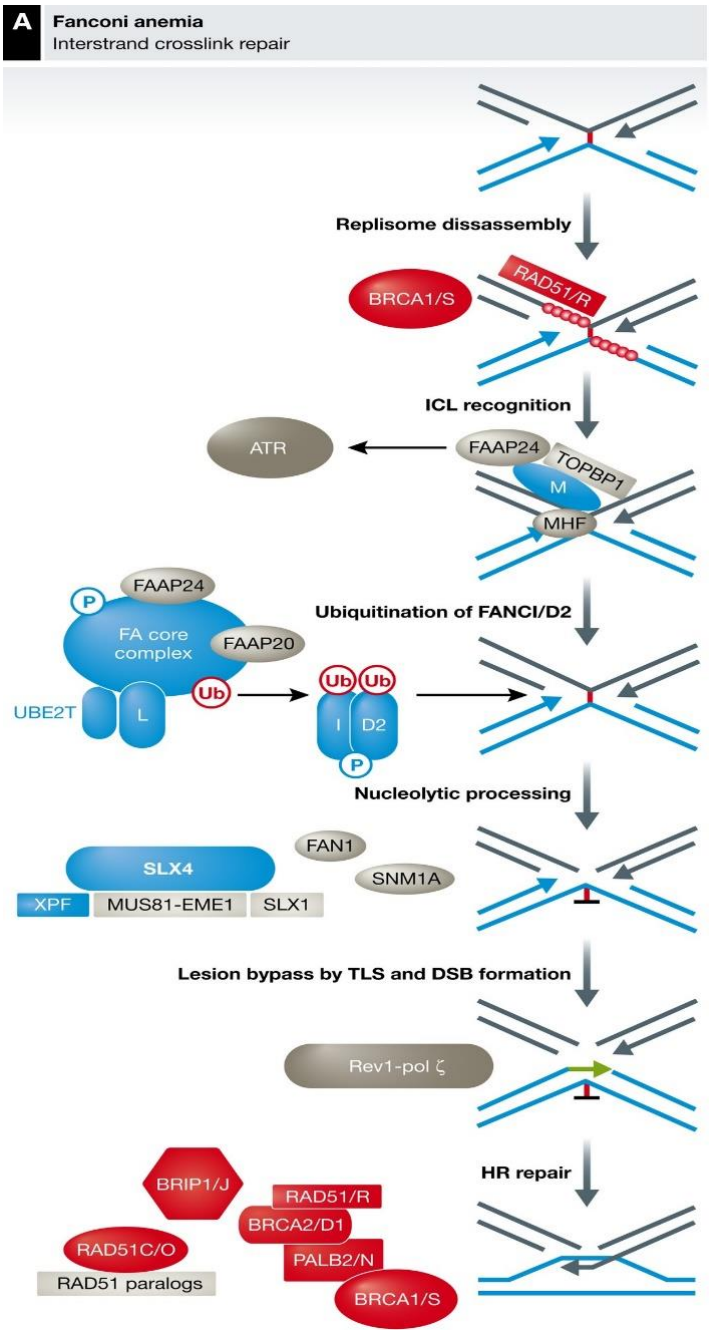

Figure 8. FA pathway for ICLs repair: Upon fork stalling at ICL sites, FANCM–FAAP24–MHF1/2 complex binding activates ATR signalling and promotes recruitment of the FA core complex. The core complex in turn ubiquitinates the FANCI–FANCD2 heterodimer, which acts to promote the next steps of nucleolytic incision to unhook the ICL, translesion synthesis and, finally, HR pathway to repair the nucleolytic-induced DSB (Adapted from *Michl, Zimmer and Tarsounas 2016*[38])

failure and development of cancer[37, 174]. The inability to repair DNA ICLs is a key cellular feature of FA and cellular markers for its diagnosis are usually represented by chromosome breakages[174]. Interestingly, biallelic mutations in breast and ovarian cancers susceptibility genes such as BRCA1/2 and PALB2 are found also in FA patients[175]. In particular, BRCA2 was found to be identical to FANCD1 as BRCA2 transient transfection could

restore ICL repair in FANCD1 deficient cells, establishing a role for BRCA2 in this pathway[176, 177].

The FA pathway operates mainly during the S phase of the cell cycle and requires converging replication forks. ICL repair is elicited when the replisome is partially dismantled by eviction of MCM replicative helicase subunits from the chromatin, thereby enabling ICL recognition by FANCM and its interacting partners FAAP24 and MHF1/2. FANCM binding adjacent to ICLs leads to recruitment of the FA core complex formed by FANCI–FANCD2 and ATR-dependent checkpoint activation, which stalls the replisome. The binding of the FA core complex to the lesion triggers monoubiquitination of the FANCI–FANCD2 complex, as the central event in the FA pathway. Monoubiquitinated FANCI–FANCD2 is recruited to the damaged chromatin and promote downstream reactions including endonucleolytic incision of the ICL, probably mediated by ERCC4 (NER), translesion synthesis and nucleolytic cleavage-induced DSB repair[37, 38]. This last step is preferentially mediated by HR, since many of the first identified FA pathway factors were involved in HR[175]. As in DSB repair, the HR step in ICL repair requires the loading of RAD51 (FANCR) onto the resected DNA followed by strand invasion to resolve the DSB. Therefore, HR proteins such as PALB2 (FANCN), BRCA1 (FANCS), BRCA2 (FANCD1), among others, are essential in this step. Furthermore, RAD51 is also necessary to protect stalled forks at a ICL lession[299] and a recent study reported a similar function for BRCA2[300].

1.1.2.3. DNA single-strand break (SSB) repair

DNA single-strand breaks (SSBs) are discontinuities in one strand of the DNA double helix and are usually accompanied by loss of a single nucleotide and by damaged 5'- and/or 3'-termini at the site of the break. SSBs can arise from oxidized nucleotides/bases during oxidative stress, intermediate products of DNA repair pathways (e.g., BER), and aborted activity of cellular enzymes[39, 40]. It has been estimated that more than 10,000 SSBs are generated per mammalian cell each day representing the most common type of DNA lesion[40].

It is generally accepted that SSBs are repaired by various DNA repair mechanisms that, globally involve SSB detection, DNA end processing, DNA gap filling, and DNA ligation steps[40]. SSB detection is primarily mediated by poly (ADP-ribose) polymerase-1 (PARP1)[39, 40]. PARP1 rapidly binds to and is activated by DNA strand breaks and subsequently

modifies itself and other target proteins through the addition of chains of poly-ADPribose (PAR) using NAD^+ as substrate[40, 41]. PARP1 promotes the recruitment of XRCC1, a critical scaffold protein that interacts with several enzymatic components of SSB repair and accelerates the process[40]. The following step of DNA end processing is mediated by protein binding partners necessary for conversion of different types of damaged termini to conventional 3′-hydroxyl and 5′-phosphate termini, including Polβ (to remove 5′-deoxyribose phosphate termini during BER), PNKP (to remove 3′-phosphate and 5′-hydroxyl termini), APTX (to remove 5′-AMP during abortive DNA ligation events), and TDP1 (to remove Top1 peptide from 5′-termini) [42]. Once damaged 3'-termini at SSB have been restored to their conventional hydroxyl configuration, gap filling can occur; which often involves insertion of the single nucleotide that is missing at most SSBs (short-patch repair). Other SSBs involve larger DNA gaps (long-patch repair) which require FEN-1 flap-endonuclease to remove the displaced 5'-nucleotides. The gap filling is carried out by Pol β, although other DNA polymerases, such as Pol δ and Pol ε can also perform this role[40]. Finally, the DNA ligation step is carried out by Lig1 and Lig3α[40, 42].

Unrepaired SSBs are implicated in human diseases such as neurodegenerative disorders, cancer, and heart failure. SSB repair has been associated with hereditary genetic diseases including ataxia-oculomotor apraxia 1 (AOA1) and spinocerebellar ataxia with axonal neuropathy 1 (SCAN1). Importantly, all SSB repair proteins currently associated with neurological disease are associated with DNA processing step. Both germline and tumor-associated variants of genes encoding SSB repair proteins (e.g., XRCC1, APE1, and Pol β) have been identified in humans, suggesting SSB repair also as a tumor suppressor mechanism[39, 42].

1.1.2.4. DNA double-strand break (DSB) repair

DSBs are generated when the two complementary strands of the DNA double helix are physically dissociated into two separate chains. They are considered as the most cytotoxic DNA lesions and it has been calculated that even one single DSB can trigger the arrest of the cell cycle[46]. DSBs pose an immediate threat to the stability of the genome because when repaired inappropriately they can lead to chromosome rearrangements, amplification or loss of chromosome material or translocations, thereby disrupting gene structure and function. Indeed, germline mutations in DSB repair genes cause genomic instability in numerous hereditary human diseases such as many forms of cancer, developmental disorders and premature ageing[44,45].

As many kind of DNA damage lesions, DSBs can form as a result of exposure to either exogenous or endogenous agents. Some well-known exogenous DSBs inducing agents are anticancer chemotherapeutic drugs (cisplatin, MMC, radiomimetic compounds and topoisomerase inhibitors) and ionizing radiation (IR). IR leads to extensive base damage[47]: generally, the more common outcome of IR exposure are SSBs by producing radiolysis radicals that attack the sugar-phosphate backbone, which can be later converted into DSBs. Frequently, at high doses of irradiation, two such nicks are present in both complementary DNA strands within one helical turn leading to DSBs[47, 48]. Endogenous sources of DSBs include ROS that trigger both SSBs and DSBs upon DNA base oxidation[49]or defective telomere metabolism that may originate DSBs at chromosome termini[50].

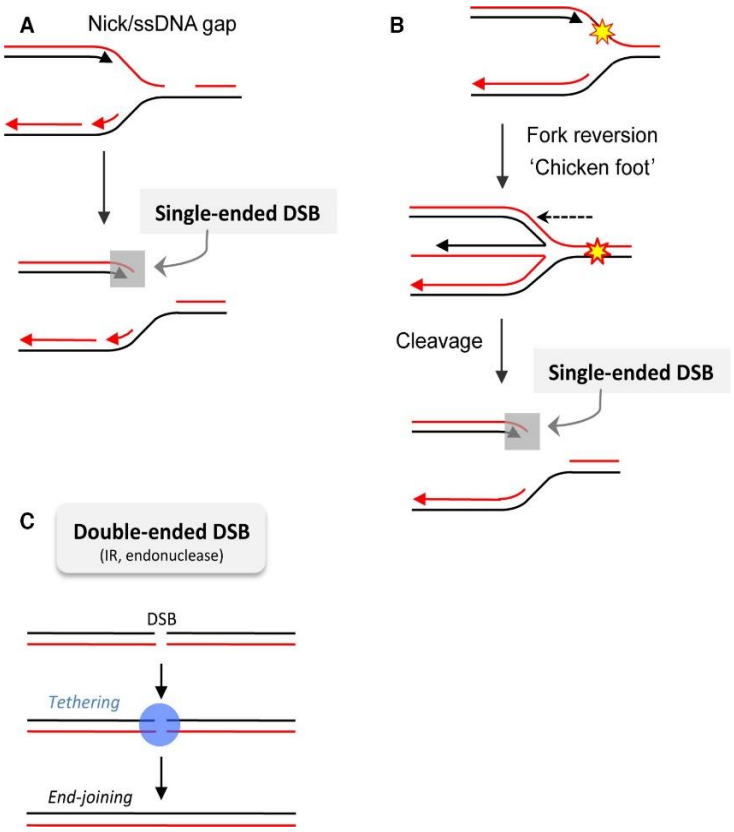

Figure 9. Induction of single- and double-ended DSBs (A) In the presence of a SSB, the replication fork is converted into a single-ended DSB. (B) When replication fork progression is impeded by a blocking DNA lesion, the complementary nascent strands create a so called "chicken foot" structure by reversion of the stalled fork and re-annealing of the parental strands; cleavage of this structure induces a single-ended DSB. (C) Double-ended DSB, generally induced by IR exposure or endonuclease cleavage. (From *So et al. 2017*[51])

However, most of the endogenously-generated DSBs are associated with DNA replication. SSBs are transformed into DSBs when reached by a replication fork (Fig. 9A). In addition,

when a replication fork is blocked, fork regression through annealing of the nascent strands (which are complementary) generates a four-branched structure called chicken foot. Specialized endonucleases can resolve this structure generating a DSB (Fig. 9B). In both of these cases, replication fork stalling leads to the formation of single-ended DSBs, whereas double ended DSBs are generally associated to IR or endonuclease induced DNA damage (Fig. 9C)[51]. Despite their high toxicity, DSBs may be deliberately generated by the cell for a specific biological purpose, for instance, to initiate recombination between homologous chromosomes during meiosis. Also, DSBs naturally occur as intermediates during developmentally regulated rearrangements, such as V(D)J recombination and immunoglobulin class-switch recombination in B-cells. Recent evidence suggest the coevolution of processes that couple introduction of programmed DSBs to their accurate repair in order to constitute an effective safeguard against genomic instability[52].

Repair of DSBs involves four possible pathways (Fig. 10): two of them, classical non homologous end joining (C-NHEJ) and HR have been extensively studied and are considered the two main DSBs repair mechanisms. More recently, two other pathways, alternative end joining (alt-EJ) and single-strand annealing (SSA), have been shown to operate in many different conditions and to contribute to genomic rearrangements and oncogenic transformation[45, 53]. Among the four, HR and C-NHEJ have evolved as high-fidelity processes.

C-NHEJ can take place along the entire cell cycle and it does not require a homologous sequence. The starting step in c-NHEJ consists on the rapid binding of KU proteins, Ku70–Ku80, to both ends of the broken DNA molecule to prevent promiscuous end resection. Once bound, Ku70–Ku80 recruits and activates DNA-PKcs which, in turn, triggers an extensive signalling cascade that orchestrates downstream repair[54]. Briefly, binding of KU to blunt DNA ends requires minimal DNA processing mediated by the nuclease Artemis, activated upon interaction with DNAPKcs, and specialized DNA polymerases λ and μ, and repair is directly assisted by two scaffold proteins, XRCC4 and the non-homologous end-joining factor 1 (XLF) that bind to DNA ligase 4 (LIG4) responsible for sealing the break [45,54]. A number of accessory factors support or regulate c-NHEJ, including the MRN complex, found involved in the stabilization of distant breaks and in the processing of DNA ends [55] and PARP proteins implicated in the correct ligation of DNA ends[56]. Several additional positive and negative regulators of Ku70/Ku80 have been identified such as proteins containing a KU binding motif like the Aprataxin-and-polynucleotide kinase/phosphatase-like Factor (APLF) and the exonuclease/helicase mutated in Werner

syndrome (WRN) [57].

Despite the mutagenicity of c-NHEJ that may arise in repetitive sequences, the fast kinetics of c-NHEJ has a clear role in protecting genome integrity notably by suppressing chromosomal translocations, at least for the majority of repair events[53]. Mutations in c-NHEJ pathway components are associated with a variety of human pathological disorders such as diverse immunodeficiency-associated syndromes, observed in carriers of mutated Artemis, XRCC4 and DNA-PKcs[54].

HR takes place mainly during the S phase of the cell cycle, where a sister chromatid can be used as a homologous template to copy and restore the DNA sequence missing on the damaged chromatid. The search for sequence homology as a template for HR requires the presence of ssDNA at the DSB end. This intermediate can be generated by the resection step which consists in the nucleolytic degradation of the 5'strand of a DSB. Some

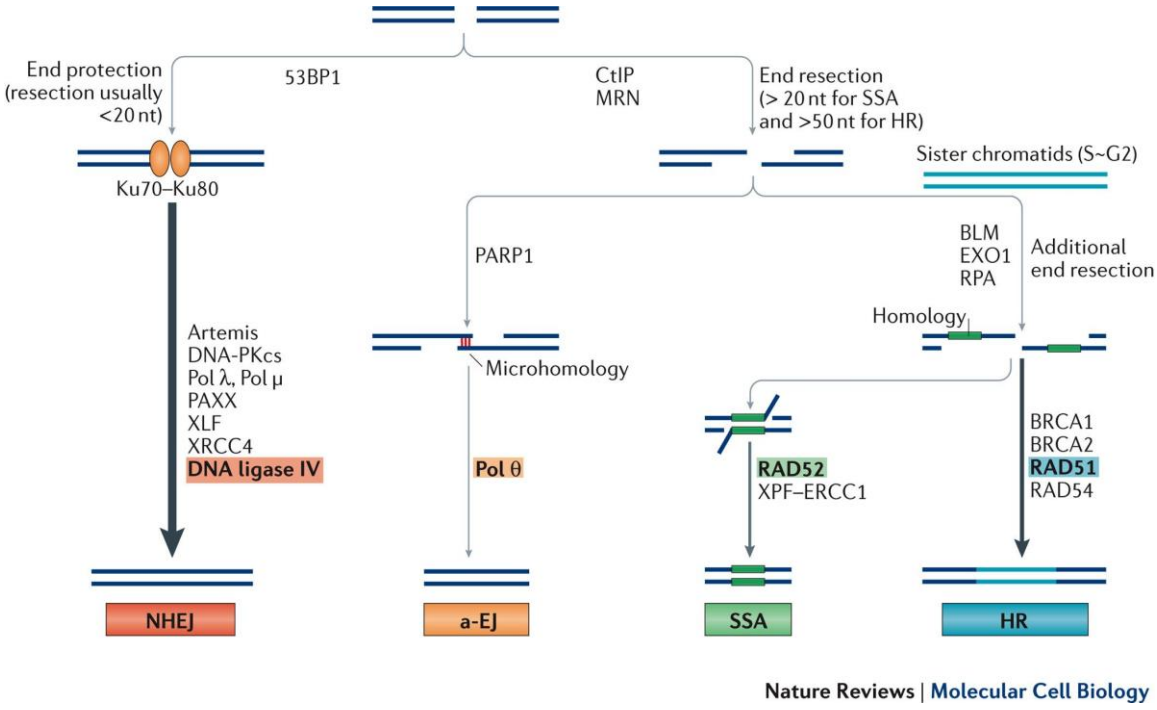

Figure 10. Four pathways to repair DSBs. The repair of DSBs relies primarily on whether DNA end resection occurs. When resection is blocked, repair through c-NHEJ is favored (left). However, when DNA resection occurs, three pathways (alt-EJ, SSA and HR) can compete for the repair of DSBs (from left to right). Details of each pathway are described in the text. (From *Chang et al. 2017*[54])

of the most important players of HR pathway are the proteins BRCA2 and RAD51. As HR-mediated DSBs repair is particularly relevant for this thesis project, I will include an extensive description of it in section 1.2 (page 29).

Alt-EJ is an alternative pathway that mainly operates during the S and G2 phases of the cell cycle on 3' ssDNA ends generated by DNA resection when c-NHEJ is compromised[53, 54]. PARP1 plays the initial role in alt-EJ recognizing and tethering either ssDNA nicks or blunt dsDNA ends. In addition, PARP1 recruits MRN and CtIP to the DSB end. CtIP enhances the MRN endonuclease activity resulting in an internal single-strand break within the 5′ strand. The short single-strand fragment at the DSB end is then degraded by the MRN exonuclease activity. The loading of the EXO1 or DNA2 generates longer stretches of RPA-coated ssDNA. Following resection, short regions of sequence complementarity ranging from 2 to 20 nucleotides are exposed within the RPA-coated ssDNA regions. Here, PARP1 plays another role in DNA end bridging and alignment, at which point non-complementary 3' tails are removed. Error-prone gap filling is performed most likely by the polymerase Polθ, and sealing of the nick is carried out by LIG1 or LIGIIIα[58, 59]. Repair of DSBs by alt-EJ is inherently mutagenic potentially giving rise to chromosomal translocations as well as intra- and inter-chromosomal deletions and insertions[45, 53, 58, 59].

SSA is a non-conservative homology-directed repair (HDR) pathway (which, generally, involve loss of nucleotides), that does not entail the presence of a sister chromatid[54, 60]. Similarly to alt-EJ and HR, SSA is initiated by end resection mediated by CtIP, thus occurs preferentially during the late S and G2 phases of the cell cycle. However, in contrast to alt-EJ, SSA requires >20bp of homology. SSA joins direct repeat sequences (e.g., tandem repeats) at 3'ssDNA end through annealing at the cost of deletion of the intervening sequence between the repeats. RAD52 is responsible for the annealing of the flanking repeats resulting from the end resection[61]. The nuclease activity of ERCC1 in complex with ERCC4 then removes the non-homologous 3'ssDNA tails, which is enhanced by RAD52. Polymerases and ligases are in charge of the final steps - gap filling and ligation - although the exact players remain poorly understood[60]. In order to reveal complementary homologous sequences, SSA requires extensive DNA end resection and RPA displacement; moreover, sequence information can be lost or rearranged if the overlapping ends pairs are unsuitably joined. Therefore, SSA is considered to be an obligatorily error-prone pathway[60]. Given the various possibilities available for DSBs repair, these four pathways could potentially compete for access to the free DNA ends of a DSB.

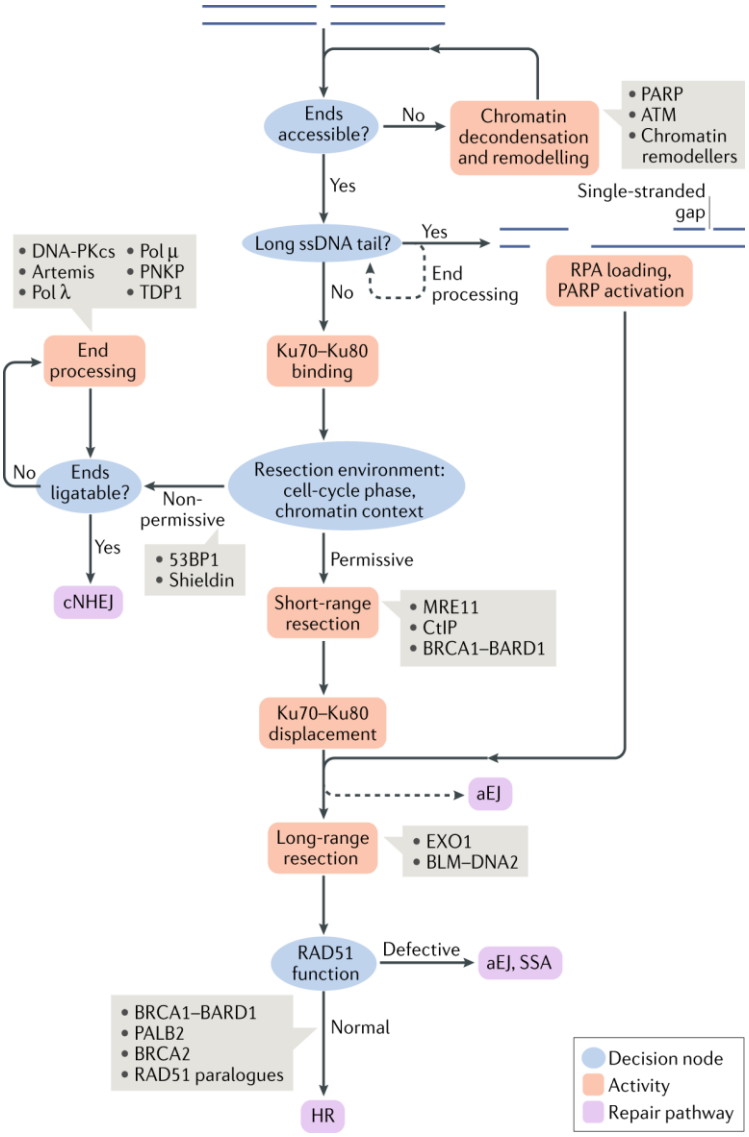

Figure 11. A decision tree for DNA double-strand break repair. Schematic representation of DSB repair pathway choice. In blue, the critical aspects influencing the choice of the repair pathway (in violet). In red, the activity triggered after pathway choice. In grey, most important mediators of each DSB repair pathway. (From *Scully et al. 2019*[45])

Thus, as illustrated in Figure 11, the regulation of pathway choice could be depicted as a "decisional tree" where the branch points represent points of commitment to c-NHEJ or HR, points where physiological sub-pathways are selected and steps at which repair intermediates are vulnerable to hijacking by error-prone repair pathways[45]. One crucial factor that determines pathway choice in this context is DNA end resection: the presence of a ssDNA tail, for instance, can affect Ku70-Ku80 binding and c-NHEJ pathway. Extensive end resection is stimulated in the S/G2 phase of the cell cycle in a manner that depends on CDK activity, which mediates phosphorylation of multiple substrates such as CtIP[45, 53].

Thus, the phase of the cell cycle is also a key influencing DSB repair pathway choice. Accessory factors also contribute via the modulation of end resection; for instance, the balance between BRCA1 and 53BP1 regulates pathway choice by either promoting or preventing end resection[53]. In addition, it is becoming increasingly clear that the native chromatin state of the damaged DNA and its position within the nucleus influences DNA repair kinetics and pathway choice[60]. Finally, once resection takes place, the formation of a RAD51 nucleoprotein filament becomes the critical step to trigger a conservative repair by sister chromatid recombination instead of other error-prone pathways that also require resection. For instance, RAD51 is negatively controlled at different levels by key factors of other resection-dependent DSB repair pathways such as Polθ, implicated in Alt-EJ[53].

1.2. Homologous recombination-mediated DSB repair

HR is an essential process that uses the redundant genetic information existing on the sister chromatids (or homologous chromosomes) when both strands of the DNA double helix are compromised by DNA damage[64]. HR plays essential roles as DNA replication support, the repair of DSBs in somatic cells and in meiosis, where it is important to generate genetic diversity[48, 52]. In contrast to SSA that can be mutagenic, HR is a conservative homology-directed pathway.

Upon DSB induction, the MRN complex rapidly localizes to the damaged DNA. MRE11 binds to CtIP for the initiation of DNA-end resection through endonucleolytic cleavage of the 5′-terminated strand upstream from the DSB end. Starting from the nick, the exonuclease activity of MRE11 degrades DNA in a 3′ to 5′ direction towards the DSB end. The resulting single-stranded DNA (ssDNA) overhang is immediately coated by RPA to protect the ssDNA from degradation or self-annealing. The 5′-recessed end now represents a preferred substrate for the 5′ to 3′ exonuclease EXO1 to carry out extended resection. Alternatively, extended resection is catalyzed by the combined endonuclease and helicase activities of DNA2-BLM in human cells[63, 64] (Fig. 12).

Other DNA end resection regulators, both positive and negative, have been described. For example, BRCA1, in complex with BRCA1-associated RING domain protein 1 (BARD1), interacts with CtIP and MRN and is implicated in DNA end resection especially counteracting the NHEJ factor 53BP1 in S/G2 phase of cell cycle[66]. Another important function of BRCA1 is in a later step of HR; indeed, it allows the recruitment of BRCA2 to

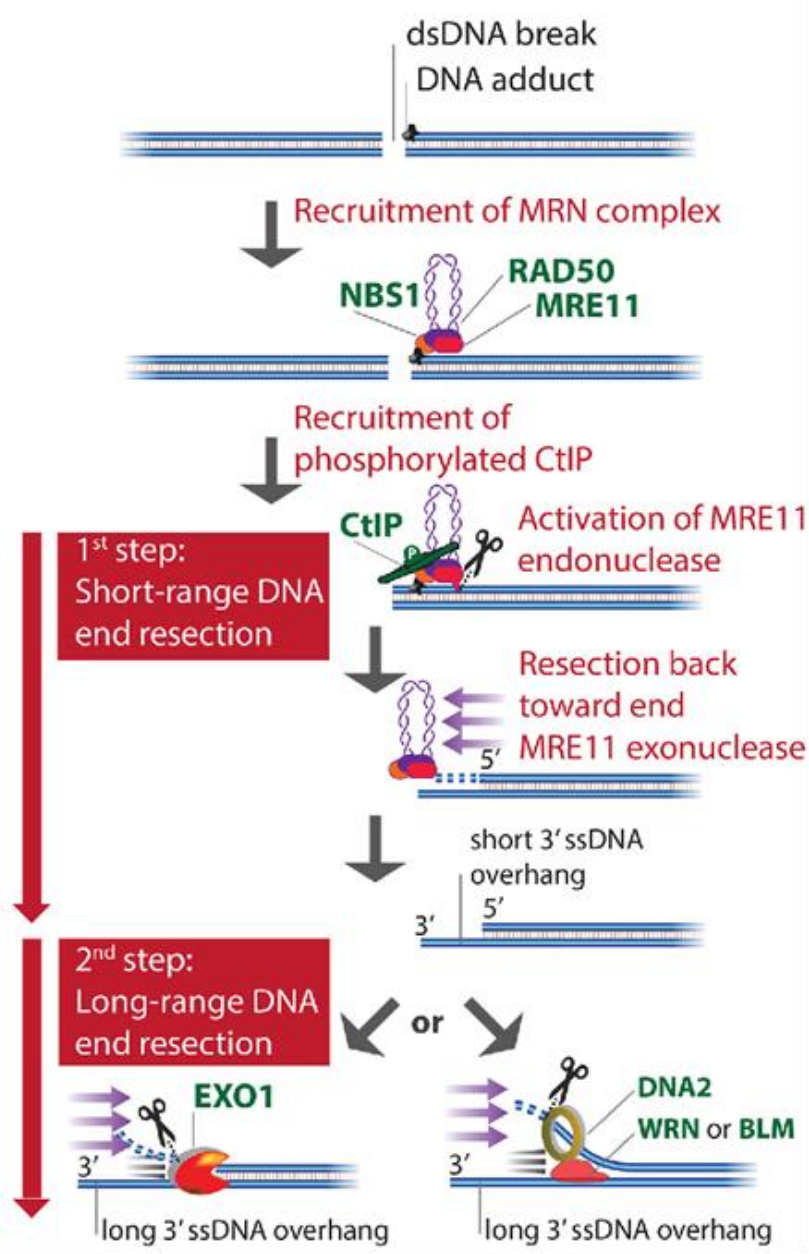

Figure 12. DNA end resection upon DSB induction. Representation of the main DNA-end resection events in human cells. First step is the recruitment of MRN complex; hence, MRE11-CtIP action is essential for an endonucleolytic cleavage and initial short-range DNA end resection. Subsequent step of extensive DNA resection (long-range DNA end resection) is mediated by EXO1 or DNA2/BLM. (From *Ranjha, Howard & Cejka 2017*[304])

DSBs through the bridging protein PALB2. BRCA2 is required to assist RAD51 loading onto ssDNA and displace RPA and thus, to promote RAD51 nucleoprotein filament formation[67, 68, 69]. In particular, my PhD supervisor and her collaborators showed, using both single molecule visualization of individual RAD51 nucleoprotein filaments and ensemble experiments, that through the BRC motifs, BRCA2 stimulates the ssDNA

binding activity of RAD51 by modulating its ATPase activity while preventing the assembly of RAD51 onto dsDNA[107, 108].

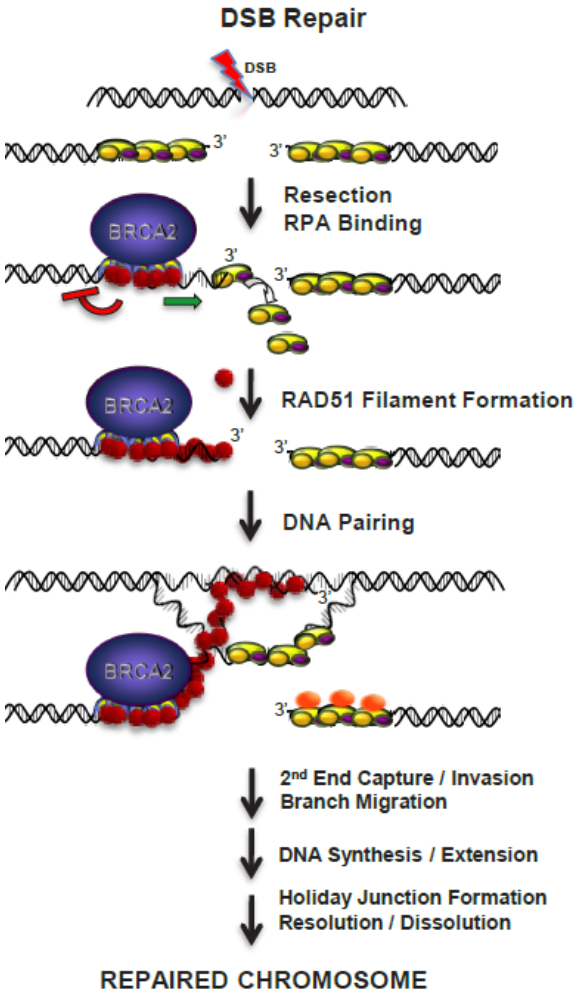

Figure 13. Model depicting the function of BRCA2 in HR-mediated DSBs repair. A DSB is resected to reveal a 3' ssDNA tail that is immediately coated by RPA. BRCA2 binds to the ssDNA /dsDNA junction and loads RAD51 onto the RPA-coated ssDNA while preventing its unproductive assembly on dsDNA. This allows the formation of a stable pRAD51 nucleoprotein filament, essential for the search of homology on a donor DNA duplex and to promote DNA strand invasion for the repair of the damaged chromosome. (From Jensen, *Carreira and Kowalczykowski 2010*[67])

The modulation of RAD51 DNA binding preference then promotes the subsequent steps of recombination. The successful purification of full-length BRCA2 allowed them to confirm these findings with the entire BRCA2[67, 68] (Fig. 13).

The RAD51-ssDNA nucleoprotein filament searches the entire genome for homology regions in association with other factors, such as RAD54. Five RAD51 paralogs are involved in assisting RAD51-ssDNA nucleoprotein filament stability, optimizing its

efficiency and, at the same time, restricting RAD51 function to appropriate DNA substrates. Mutations in any of the RAD51 paralogs lead to defects in RAD51 foci formation and DNA damage sensitivity, thus suggesting that all of them are essential and could have specific function[72]. During synapsis (physical connection between two DNA regions with homology), the RAD51-ssDNA complex facilitates the base-pairing between the invading DNA substrate and the homologous duplex DNA template resulting on a displaced strand or D-loop. Upon pairing of the 3' extremity of the broken molecule with the donor sequence, DNA synthesis by a polymerase (usually Polδ or TLS polymerases) restores the sequence information disrupted by the DSB[65, 72]. Depending on how the D-loop structure is disrupted, it is possible to distinguish different HR sub-pathways (Fig. 14). The double Holliday junction (dHJ) formation and the synthesis dependent strand annealing (SDSA) are the two main HR sub-pathways. **dHJ** is predominant in meiotic recombination and occurs when the D-loop captures also the second end of the break not involved in strand invasion. Subsequently, the 3'ssDNA overhang forms a dHJ with the homologous chromatid which can be processed by a resolvase complex (composed of MUS81 and EME1 and structure-specific endonucleases)[73]. The outcome of this process is

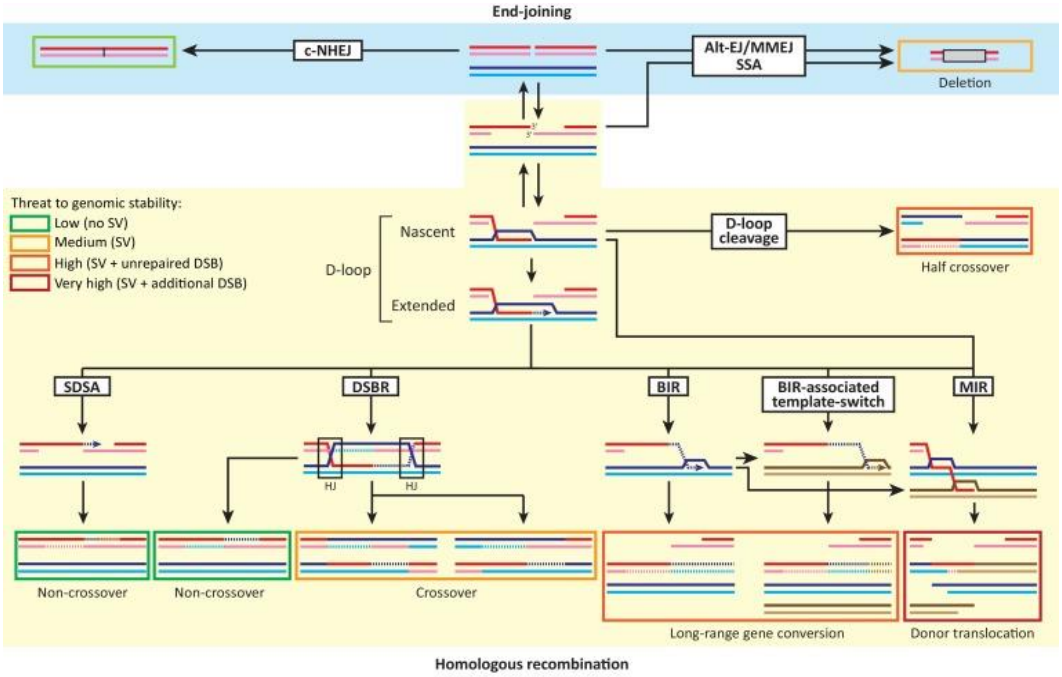

Figure 14. HR sub-pathways. Top: first step HR mediated DSBs repair pathway leading to search for homology, DNA invasion and formation of D-loop heteroduplex. Resolution of D-loop structure can occur in different ways, generating HR sub-pathways: from the left to the right SDSA, formation of dHJ and BIR. (From *Piazza and Heyer 2019*[65])

mainly crossover products, although, because of the possible gene conversion events, non-crossover products can also be generated[65, 71, 73]. **SDSA** is the major HR sub-pathway in somatic cells; in it, the strand invasion leads to the copying of the template but, in this case, the new strand is displaced from the donor and is captured by the second end of the DSB. The resulting single Holliday junction then slides down the DNA duplex in the same direction in a process called branch migration, displacing the extended strand from the template strand. This displaced strand pops up to form a 3'overhang in the original double-stranded break duplex, which can then anneal to the opposite end of the original break through complementary base pairing. Therefore, SDSA produces only non-crossover products because the flanking markers of the heteroduplex DNA are not exchanged[65, 71, 73].
Break-induced replication (**BIR**) occurs when a single end of the DSB acts independently; this may take place when one side of the break fails to engage with a homologous sequence or when the two ends find different homologous templates. In addition, BIR arises in case of single-ended DSBs, which, as described above, can occur due to replication through a DNA lesion that results in fork stalling or collapse, or through telomere erosion that exposes a single-ended DSB. The most relevant difference between BIR and other HR sub-pathways is the DNA synthesis mode; in BIR, after DNA strand invasion and D-loop formation, the invading strand is extended by DNA synthesis (mostly mediated by Polα) concomitant to D-loop migration, driven by a helicase, potentially Pif1 or MCM. In the process, the newly synthesized DNA accumulates unrepaired DNA lesions[74]. Therefore, although HR is generally considered an error-free pathway, if not perfectly regulated, it can also lead to the accumulation of lesions and chromosome rearrangements[65].

1.3. BRCA2: structure and roles as a custodian of genome integrity

1.3.1. The tumor suppressor BRCA2

BRCA2 was discovered in 1995 as a gene implicated in the predisposition to breast and ovarian cancer[75, 301]. In addition, inherited mutations affecting a single copy of *BRCA2* also significantly elevate the risk of cancers in the pancreas, male breast, prostate, and other tissues[70, 76, 77]. Furthermore, biallelic mutations in BRCA2 are also found in Fanconi anemia patients leading to predisposition to various types of cancer at early age[175].
The earliest clues about the importance of BRCA2 in maintaining genome integrity came from observations in mice showing that *Brca2*-mutated mice exhibited early embryonic

lethality and DNA repair defects similar to *Rad51*-defective mice[78, 79]. At the same time, BRCA2 was found to physically interact with RAD51 *in vitro*[80]. In addition, *Brca2*-defective mouse cells where shown to exhibit chromosome rearrangements such as translocations and chromosome breakages[81] making the hypothesis of a direct role of BRCA2 in DNA repair even stronger. Later on, the role of BRCA2 in HR was directly measured using a recombination reporter assay in CAPAN-1 cells (pancreatic BRCA2 deficient cancer cells)[82] which could be rescued by transient transfection of BRCA2[130]. Afterwards, based on the established interactions between the BRC motifs of BRCA2 and RAD51, together with the preferential binding of BRCA2 to ss DNA[112], it was proposed that BRCA2 could facilitate recruitment of RAD51 to sites of processed DSBs requiring repair and enhance RAD51-promoted strand invasion[111]. In support of this hypothesis, Brh2 (BRCA2 ortholog in *U. maydis*), was shown to stimulate the ATPase activity of Rad51 on RPA-coated DNA containing a single-stranded gap and to promote Rad51-filament formation on RPA-coated gapped DNA, while decreasing the amount of bound RPA, suggesting its role as a Rad51 mediator[88].

Therefore, it is not surprising that BRCA2 (as well as other factors involved in DNA repair, such as BRCA1 and PALB2) function as tumor suppressors and that inherited mutations in these genes confer significant lifetime risks of breast, ovarian, and other cancers. Indeed, BRCA-deficient cells usually accumulate aberrations in both chromosome structure (translocations, large deletions or chromosome fusions[129]) and number, reflecting inaccurate chromosome segregation[81, 129]and genome instability which are hallmarks of tumorigenesis[70]. The structural aberrations typically include breaks affecting a single sister chromatid, as well as tri-radial and quatri-radial chromosomes (Fig. 15). These abnormalities denote defects in HR and can be explained by error-prone

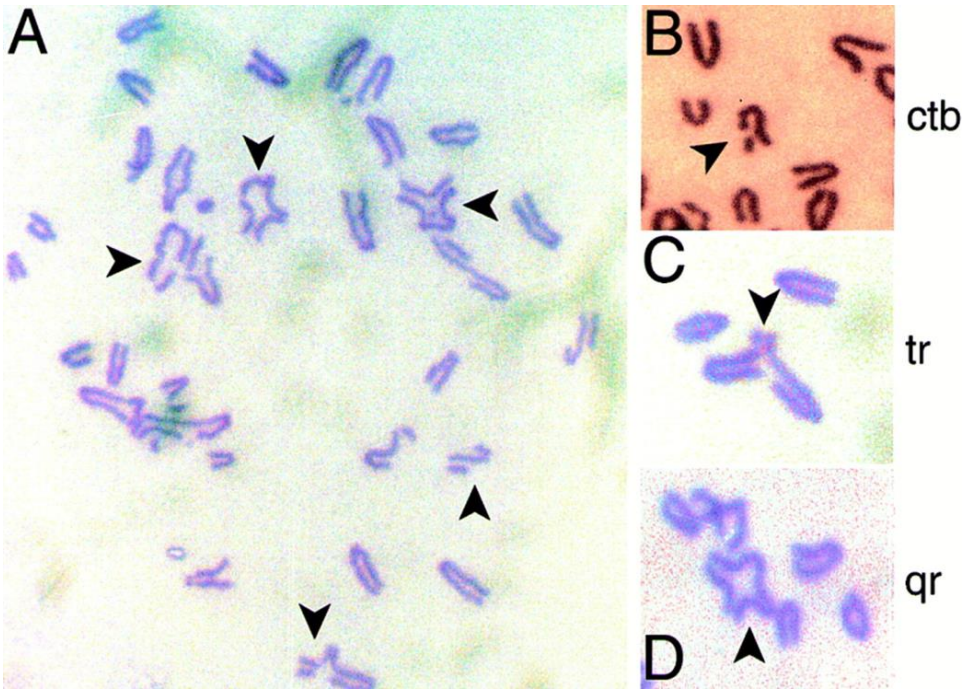

Figure 15. Structural chromosomal aberrations in metaphase spreads from murine embryonic fibroblasts homozygous for a targeted truncation in Brca2. (A) Typical metaphase spread, with arrows marking abnormal chromosomes. Chromatid-type aberrations enlarged in (B-D) show breaks affecting a single sister chromatid, tri-radial and quatri-radial chromosomes, respectively. (From *Patel et al. 1998*[81])

mechanisms like NHEJ or SSA[82, 130, 131] that take over the DNA lesions in the absence of BRCA2. These pathways promiscuously re-ligate broken DNA ends, particularly across short microhomologies. Consistent with this notion, human cancers harbouring homozygous mutations in BRCA2 display not only extensive structural rearrangements in chromosomes but also many short deletions (≤50 bp) with overlapping microhomology at breakpoint junctions[132].

The abnormal chromosome number may be explained by other functions of BRCA2 in mitosis such its role in cytokinesis[83, 98, 104] and in the alignment of chromosomes that we have recently reported[84].

As mention above, BRCA2 mutation carriers typically inherit a single mutated copy in their germline. Following the Knudson 2-hits theory for tumor suppressors[320], the wild-type copy is lost in a process called loss-of-heterozygosity (LOH)[134, 135, 136]. However, recent genomic studies have shown that a fraction of these tumor retain BRCA2 wild-type allele, suggesting that heterozygous mutations affecting BRCA2 might suffice for carcinogenesis[137]. If so, haploinsufficiency may be the driver condition for tumorigenesis. Along these lines, a recent study proposes that exposure to naturally occurring

concentrations of formaldehyde or acetaldehyde may contribute to the carcinogenesis in individuals with heterozygous BRCA2 mutations[138].

1.3.2. Structure and functional domains of BRCA2

Human BRCA2 is 3,418 amino acids in size (~390 kDa) comprised in 26 exons of different sizes[85] (Fig.16). Since it was discovered, an ever increasing number of interacting partners of BRCA2 have been described, especially in those BRCA2 regions containing well defined functional domains. Arguably, the search for new potential interactors of BRCA2 may be a good strategy to characterize the disordered regions still poorly understood. Indeed, the lack of significant sequence similarity with other human proteins as well as the little conservation in mammalian evolution have made BRCA2 a protein particularly difficult to characterize. As an example, mouse Brca2 shows only 59% amino acid identity with the human BRCA2[86]. Nevertheless, BRCA2 homologs have been found in several eukaryotes, including fungi, worms, plants and flies. For instance, the counterpart in the fungus *Ustilago maydis*, Brh2, was the first to be shown to load RAD51 onto ssDNA at the junction with dsDNA[87, 88]. As mentioned before, BRCA2 binds primarily to RAD51 through the BRC repeats, an array of 8 consecutive interspersed motifs of about 35 aa in length contained in the central region of BRCA2. This interaction is essential for the formation of RAD51 foci at DNA breaks *in vivo*[106]. Accordingly, single point mutations within an individual BRC motif, some of which are associated with familial early-onset cancer, are sufficient to disrupt the interaction with RAD51[157]. In humans, the BRC repeats cover around 1200 aa, and at least 6 of them directly interact with RAD51, with BRC4 having the highest affinity for RAD51[107].

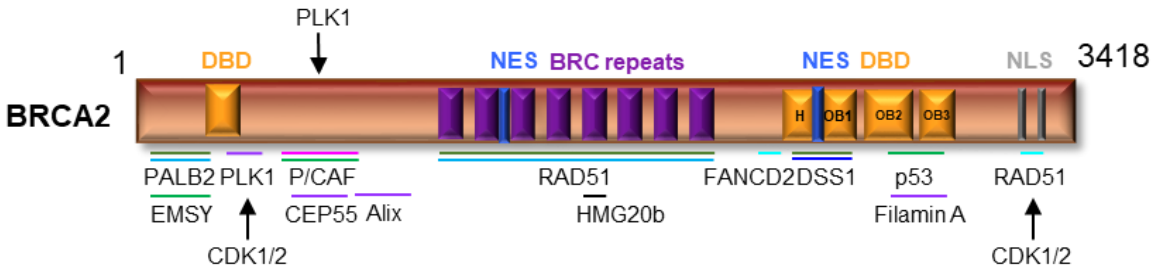

Figure 16. BRCA2 structure. Schematic representation of BRCA2 structure displaying its functional domains (in color) and its interaction partners (below) as well as phosphorylation sites by CDKs (P). Details are described in the text. (Adapted from *Martinez, Baldeyron and Carreira 2015*[86])

Via this interaction, the BRC repeats alter the conformation of RAD51 and modulate the DNA binding preference of RAD51. First, BRC repeats promote assembly and stability of RAD51 on ssDNA by locally reducing its ATPase activity; in addition, they block the assembly of RAD51 on dsDNA[107, 108] thus favouring the formation of an active RAD51 nucleoprotein filament on ssDNA. The BRC repeats 1-4 allow RAD51 nucleation onto ssDNA and stabilize the nascent nucleoprotein filament by limiting its ATPase activity (locked conformation). Once nucleation has been completed, BRC repeats 5–8 bind the nascent RAD51 nucleoprotein filament and further promote filament extension (Fig. 17). In addition, a study from our lab showed that the BRC repeats can also bind to the meiosis-specific recombinase, DMC1 promoting the formation of DNA strand invasion products (D-loops) between homologous molecules in a fashion similar to RAD51[118]. They demonstrated that BRC6-8 bind with higher affinity to DMC1 rather than RAD51, and all BRC repeats (with the exception of BRC4) stimulate joint molecule formation by DMC1, identifying BRCA2 as a mediator of HR in meiotic cells[118].

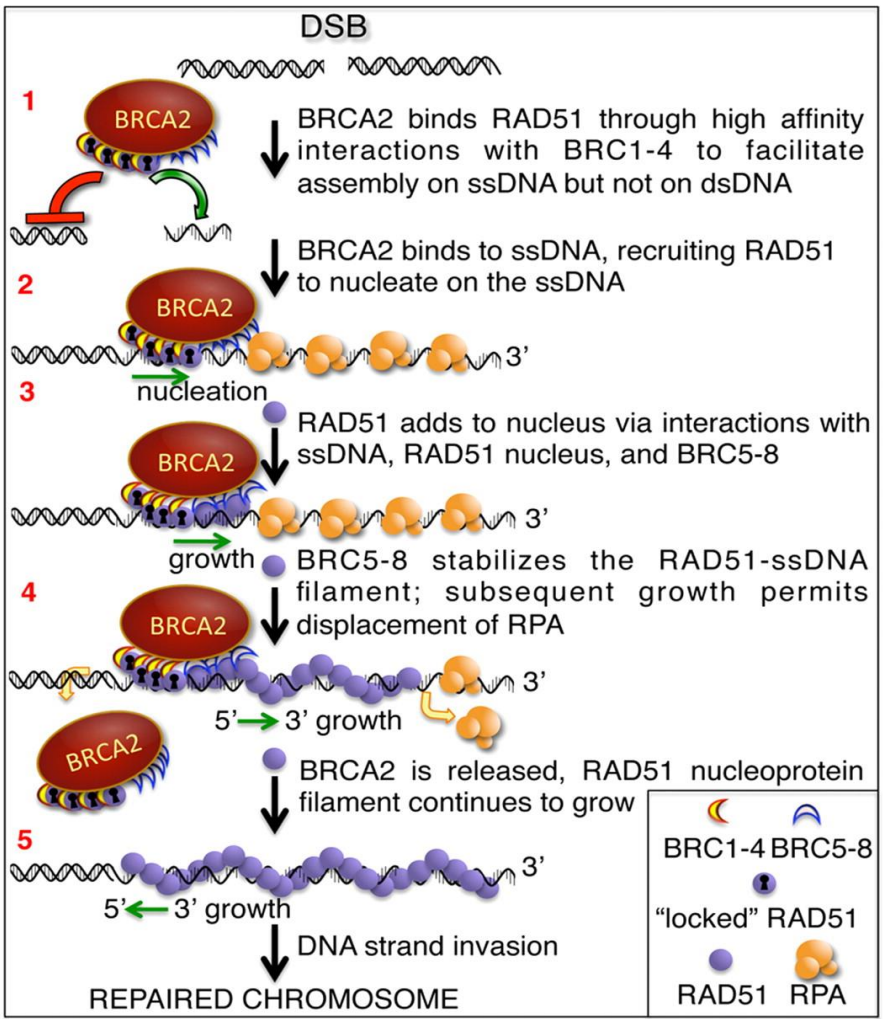

Figure 17. Role of BRCA2 in promoting RAD51 nucleoprotein filament assembly in HR-mediated DSBs repair: Proposed model for BRCA2 function during HR pathway to allow the assembly of RAD51 nucleoprotein filament essential for DNA strand invasion and search for homology during HR. Five crucial steps can be identified in this process. (details in the figure and in the text). (From *Carreira and Kowalczykowski 2011*[108])

The BRC repeat region is followed by the C-terminal region composed of approximately 1000 residues which is the best conserved portion of BRCA2 (Fig. 16). This aspect has facilitated the description of the functional domains included in this region. This is also the only region so far where pathogenic missense mutations have been described; our lab has also contributed to their characterization[302] . This region comprises the canonical DBD which is composed of five domains: 3 oligonucleotide/oligosaccharide binding folds (OB folds), a helical domain, and a tower domain[111]. The CTD together with one BRC repeat BRCA2 are sufficient to promote the assembly of RAD51 onto ssDNA and ssDNA/dsDNA junctions[67, 112]. The CTD binds to DSS1 (deleted in split hand/split foot)

[111], a small acidic protein that has been shown to promote RAD51-loading activity of BRCA2[115] and its stability[113]. Moreover, the interaction of DSS1 masks a nuclear export signal in BRCA2 and thereby controls both BRCA2 and RAD51 nuclear localization[114]. More recently, DSS1 has been proposed to promote BRCA2-dependent HR by reducing the affinity of RPA for ssDNA, thereby facilitating a handoff of ssDNA from RPA to RAD51[116].

Unlike the C-terminal region, The N-terminal region of BRCA2 (hereafter $BRCA2_{NT}$) is particularly weakly conserved and highly disordered[89, 90]. Disordered regions usually exist as highly dynamic ensembles with thousands of conformations and undergo disorder-to-structure transitions upon binding to their partners. A relevant contribution to $BRCA2_{NT}$ characterization came from a recent work from our lab that revealed of a novel DNA binding domain (DBD) in this region. In particular, in this work the lab found that, *in vitro*, this second N-terminal DNA binding domain (NTD) comprised in the region from 250-500 aa, can bind different DNA structures including dsDNA and can promote the DNA strand exchange activity of RAD51 in isolation. In addition, a missense breast cancer variant located in the NTD affects NTD dsDNA-binding and impairs HR stimulation on dsDNA/ssDNA junction containing substrates[105]. These results suggest that both NTD and CTD are required for RAD51 assembly onto ssDNA in the context of full length BRCA2. Recently, three-dimensional electron microscopy reconstructions of full-length human BRCA2 have reported that it dimerises to form an elliptical kidney-bean shape in which two sets of BRC repeats with bound RAD51 line up in the middle part. The dimeric BRCA2 is shown to bind to ~ 70nt ssDNA and promotes RAD51 nucleation, but not filament growth[163]. This finding could be in agreement with a model depicting a role of both NTD and CTD in RAD51 loading during HR[105]. Additional studies are necessary to explore the interplay between these two DBDs, especially in order to know how they are coordinated *in vivo* and if they exhibit specificity for different DNA substrates or DNA damage.

In addition, $BRCA2_{NT}$ binds to the Partner and Localizer of BRCA2 (PALB2). PALB2 chromatin association is important to localize BRCA2 at the sites of DNA damage[91, 92]. In addition, PALB2 binds BRCA1 serving as the molecular scaffold in the formation of the BRCA1-PALB2-BRCA2 complex[93]. Moreover, PALB2 binds DNA, preferentially D-loop structures, and directly interacts with RAD51 to stimulate strand invasion[94]. Depletion of PALB2 leads to a decrease in HR efficiency, MMC hypersensitivity and reduction of the retention of BRCA2 in the nucleus[91]. Therefore, as BRCA1 and BRCA2, PALB2 is also

considered a breast cancer predisposing gene. PALB2 BRCA2-binding site is shared with another factor called EMSY. EMSY-BRCA2 interaction leads to deactivation and transcriptional repression of BRCA2; indeed, sporadic breast and ovarian cancer cells show strong amplification of EMSY and this is associated with poor prognosis[95].

The N-terminal region also contains several binding sites for the cell cycle master regulator Polo-like kinase 1 (PLK1) [96]. CDK1 phosphorylation of T77 residue triggers this interaction, which in turn favors further BRCA2 phosphorylation at S193. These events promote BRCA2 localization to the midbody where it interacts with Myosin IIC (NMCII), a molecular motor protein that binds to cytoskeletal actin and regulates cytokinesis[99]. . In addition, BRCA2 interacts with other components of midbody, such as CEP55 and Alix in order to promote abscission[104]. Moreover, CDK-dependent BRCA2-PLK1-binding is important to facilitate PLK1-mediated RAD51 phosphorylation, which, in turn, mediates the association of RAD51 with stressed replication forks in order to protect the genomic integrity of proliferating human cells[100].

Importantly, in a recent work from the lab, we showed a new role for PLK1-mediated BRCA2 phosphorylation in the control of mitosis. We identified a conserved PLK1-phosphorylated site at T207 of BRCA2 that is phosphorylated during mitosis. We found that this step promotes the formation of a tetrameric complex between BRCA2, PLK1 the phosphatase PP2A and phosphorylated-BUBR1, which is required for the formation of stable kinetochore-microtubule attachments[101]. Impairing BRCA2 phosphorylation by PLK1, as observed in BRCA2 breast cancer variants S206C and T207A, alters the tetrameric complex resulting in unstable kinetochore-microtubule interactions, misaligned chromosomes, faulty chromosome segregation and aneuploidy[84]. Interestingly, this function appears to be distinct from the HR activity of BRCA2.

BRCA2 residues 290-453 specifically interact with histone acetyl-transferase P/CAF[97], which acetylates BUBR1 in mitosis. BRCA2 has been shown to act as a scaffold protein bringing together P/CAF and BUBR1 for proper spindle assembly checkpoint (SAC) activation[102]. Moreover, the interaction with P/CAF suggests a role of BRCA2 in transcriptional activation exploiting the histone modifying activity of P/CAF. BRCA2 cooperates with both BRCA1 and P/CAF to enhance AR (Androgen Receptor) and GRIP1 (coactivator of AR)-mediated transactivation, promoting the anti-proliferative effect of AR[103].

The regions interspaced between the BRC repeats also harbor a PLK1 phosphosite although its function remains unknown (ref 98). This region also harbours a nuclear export

signal (NES) required for cytoplasmatic localization of BRCA2[109] and an interaction site for the kinesin-like coiled-coil high mobility group protein HMG20b (known also as BRAF35), essential for BRCA2 functions in cytokinesis; specifically, disruption of this interaction leads to delayed cell division and accumulation of binucleated cells[110]. In addition, the C-terminal region of BRCA2 binds to the actin binding protein Filamin A, relevant for BRCA2 localization to the midbody during cytokinesis[104].

The C-terminal region of BRCA2 also includes a binding site for the tumor suppressor p53. Indeed, p53 transactivation deficiency leads to HR suppression and overexpression of BRCA2 inhibits the apoptotic and transcriptional activity of p53 reducing the expression levels of its targets genes, such as p21[119]. At the extreme C-terminus, BRCA2 contains two nuclear localization signals (NLS). Thus, truncated mutants not containing this region are non-functional because they cannot translocate into the nucleus[121].

Finally, a second RAD51 binding site lays in the C-terminal region although, unlike the BRC repeats, this region seems to bind only RAD51 oligomeric form. Phosphorylation of S3291 by CDKs takes place in G2/M transition of the cell cycle and prevents this interaction, which, in turn, promotes disassembly of RAD51 filaments once HR repair is complete[120]. Interestingly, disrupting this interaction by a S3291A or S3291E mutation impairs the protective function of BRCA2 at stalled replication forks while sparing DSB repair establishing a new role for the interaction between BRCA2 and RAD51[31].

1.3.3. BRCA2 variants of unknown clinical significance (VUS)

As mentioned above, germline mutations affecting a single copy of BRCA2 significantly increase the risk of breast and ovarian cancer[75, 122, 123]. Indeed, recent studies report that inherited mutations in BRCA2 gene are associated to a 69% of risk to develop breast cancer by the age of 80 and 17% of risk to develop ovarian cancer; BRCA2 mutations also increase the risk of prostate, pancreas and male breast cancer[76].

Since BRCA2 discovery, thousands of variants that occur in the human BRCA2 gene have been identified, but only a fraction of them are reliably known to cause cancer susceptibility[124, 125]. Founder mutations inducing cancer susceptibility have been identified amongst the Ashkenazi Jewish population, as well as in Iceland for instance. The great majority of pathogenic or likely pathogenic mutations (80%) generate a premature termination codon, truncating the encoded protein and potentially decreasing its expression through nonsense-mediated mRNA decay[126] and are, usually, distributed throughout the

protein. By contrast, a 10% of pathogenic mutations are missense variants that generate a stable mutant protein; they have been found to cluster in specific and limited regions of the protein, such as OB folds region and helical domain in BRCA2[76]. However, a large number of missense alleles are classified as being variants of unknown significance (VUS), posing a challenge for accurate risk assessment and clinical management in mutation carriers. Many efforts have been done to assess a classification of these variants considering the frequency of the variant in cases versus controls, co-occurrence with a known deleterious mutation, co-segregation with the disease in families, occurrence of disease in relatives, and biochemical evidence, such as residue position, conservation and functional assays[139]. Given the growing number of BRCA2 (and BRCA1) VUS, their organized collection appeared mandatory. For this reason, in 2009 the Evidence-based Network for the Interpretation of Germline Mutant Alleles (ENIGMA) international consortium was established (https://enigmaconsortium.org/)[140]. ENIGMA is a wide research-based consortium with the aim of providing methods to facilitate specifically the classification of variants of *BRCA1* and *BRCA2* and of other breast cancer susceptibility genes of which our lab has been part of. the consortium provides the criteria for assessing variant significance based on multifactorial likelihood models that include population, clinical evaluation, bioinformatics prediction, functional characterization and promotes data sharing of large-scale projects with variant annotations[141, 142]. Over time, the ENIGMA variant classification data have been collected in the global BRCA Exchange database, together with data from other clinical and population databases (e.g., ClinVar, LOVD, GnomAD), to provide updated and revised reports of variant interpretations[143].

VUS are difficult to classify for three main reasons: i) lack of sufficient population-based statistical evidence, especially if found in many different pathological conditions and population subgroups ii) scarcity of functional evidence, since they are often missense or synonymous substitutions located in domains of not known functional relevance, and iii) different evaluations by clinicians and researchers[144]. Through great efforts, several experimental approaches have been developed in the last few years to determine variant functions in pathological processes[145]. In this context, it is important to choose the appropriate model system to recapitulate the biochemical alterations and their biological consequences. The evaluation of missense substitutions is more challenging than truncating mutations since, in the former, the effects on protein structure and/or function is not straight forward[144]. The importance of the functional evaluation of VUS has become even more evident in recent years with the increase in the number of VUS detected thanks

to the advance in sequencing technologies and to the advent of personalized therapies such as PARP inhibitors (PARPi)[145-148] : indeed, the assignment of specific treatments depending on the mutational profile of the tumor can have a big impact on the management and prognosis of patients. The number of functional assays is expanding ranging from HDR (HR) assays[149] to studies with conditional knock-out cells allowing the evaluation of the capacity of the gene variant to rescue lethality, DNA repair, and resistance to PARPi[150, 151]. Other assays focus on micronucleus formation and centrosome amplification in mutated cell lines or on the restoration of resistance to damaging agents by BRCA2 variant complementation, or on increased chromosome breakage after γ-irradiation[152-154].

In time, these functional assays will provide data that could be used to establish a model for VUS evaluation as demonstrated in this study to which our group has contributed to[302]. This model will become an indispensable tool for the assessment of the clinical relevance of variants of uncertain significance.

1.4. R-loops and genome instability

In the past decade, the advances in next-generation sequencing have revolutionized our understanding of the regulatory role of RNAs in cellular functions[190]. For example, RNA can exert its regulatory function through the formation of DNA-RNA hybrids and R-loops, when an invading RNA on a duplex DNA results in the displacement of ssDNA. R-loops were first identified 40 years ago *in vitro*; 20 years later, their existence was demonstrated *in vivo* in the bacteria *Escherichia coli*. However, it was not until the first evidence of their function during immunoglobulin (Ig)-class-switch recombination (CSR) that the research on RNA–DNA hybrids and R-loops gained larger attention[192]. In the last few years, several studies have identified important roles of these structures in gene regulation and DNA repair[191]. However, as by-products of transcription, R-loops can also interfere with the transcription process and contribute to genome instability when their removal by dedicated enzymes fails.

Genome-wide mapping has demonstrated that R-loops form in particular in promoter regions of transcriptional active genes [193, 194]. Generally, in this context, R-loops can form when a nascent transcript re-anneals back on the DNA template: in this case, the R-loop formation is called *in cis*. RNAP pausing at transcriptional start sites or collisions between transcription and replication machinery can also be the cause of *in cis* R-loops. In addition, R-loops can form *in trans* when an RNA molecule transcribed from a distant

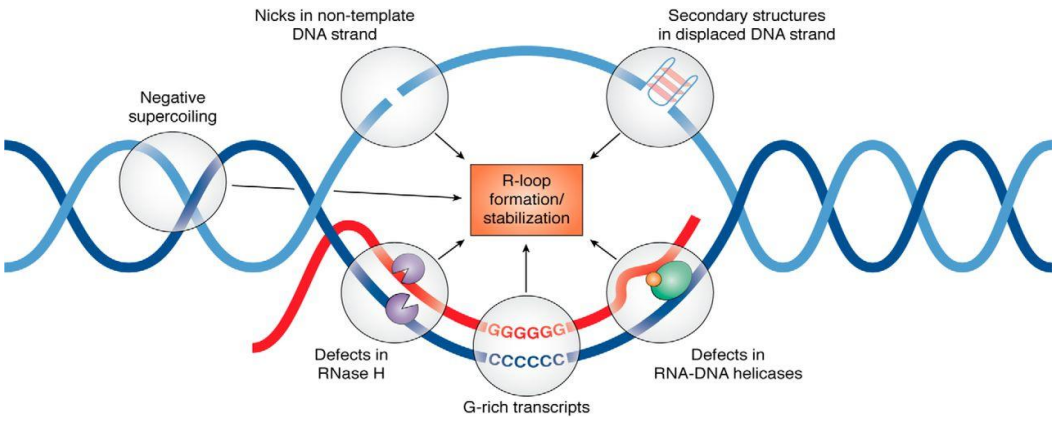

Figure 18. Factors promoting R-loop formation and stabilization: Schematic representation of typical conditions implicated in favouring the formation of R-loops, particularly in the context of transcription. See the text for details. (From *Hegazy, Fernando and Tran, 2020*[192])

genomic locus is used to hybridize with a DNA[192]. Figure 18 highlights most common factors implicated in R-loops generation and stabilization. Several studies have suggested that R-loop formation is strongly promoted by particular DNA conditions and sequence context, for example, the presence of GC-rich DNA sequences. In particular, *in vitro* studies have reported that G-rich transcripts complementary to C-rich DNA strand are responsible for the generation of stable R-loops[195]. Secondary structures generated onto the displaced ssDNA of an R-loop can also favour its stabilization. For instance, it has been shown that G-quadruplex (G4) structures, secondary structures that are composed of quartets of guanine bases held together by Hoogsteen base pairing and base stacking, can form at the ssDNA of the R-loops formed across immunoglobulin loci during CSR and this factor makes them more stable as re-annealing of the two DNA strands is disfavoured[196]. Moreover, topological constraints occurring during transcription can also influence R-loop formation. Negative supercoiling due to dsDNA opening during transcription has been shown to promote the hybrid formation with the nascent transcript. In addition, current mathematical models propose that R-loops can absorb negative supercoiling, thereby relieving topological strain on the overall DNA molecule and stabilizing the R-loop structure[197]. Furthermore, during transcription, the presence of a nick on the non-template DNA strand increases the chances of an R-loop to be formed; indeed, upon unwinding of DNA duplex, a nick on the non-template strand can impede DNA strands to re-anneal and favour DNA-RNA hybrid formation[198]. Finally, beyond factors that can promote R-loop formation, the absence of proteins and enzymes involved in processing these structures can also represent a strong cause for their persistence and stabilization as discussed in the next

section.

1.4.1. R-loops: physiological roles and causes of genome instability

As mentioned above, although it is clear that R-loops can represent a threat for genome integrity, they are also intermediates in several cellular processes regulating genome dynamics (Fig. 19B). For instance, R-loops are essential intermediates in the initiation of DNA replication in mitochondrial DNA, bacterial plasmids and the bacteriophages ColE1. In all these cases, the replication mechanism requires an RNA molecule used as a template for DNA synthesis that will then be processed by an RNAseH enzyme in order to remove the RNA and generate a primer for DNApol to extend and terminate DNA replication[199].

Moreover, among the most known physiological roles of R-loops is their function as a natural sources for Ig-CSR. This process occurs at special regions called repetitive switch (S) regions. They are characterised by high G-content and are targets of the B cells-specific activation-induced cytidine deaminase (AID). In B cells, S regions can form R-loops that are acted upon by AID at the displaced G-rich ssDNA to generate the DSBs responsible for CSR[199]. Finally, R-loops can serve as intermediates for CRISPR-Cas9 activity since the guide-RNA forms a DNA-RNA hybrid to identify the target for Cas9-mediated cleavage[200].

Interestingly, increasing evidence indicates that R-loops play roles in gene expression (Fig. 19C); this is supported by the fact that often R-loops form at promoters or transcription termination sites. For instance, R-loops could avoid methylation and transcription silencing of CpG islands promoter regions when they form in their proximity; indeed, these regions are often associated with unmethylation. It has been proposed that DNA methyl-transferases may bind with more affinity dsDNA than a DNA-RNA hybrid, so R-loops could act preventing their action and transcription silencing[193, 201]. Moreover, it has been shown that R-loops are present at gene promoters of long non-coding RNAs (lncRNAs) involved transcription activation or repression. In response to R-loops presence at these promoters, the binding of transcription factors is affected, thus impeding lncRNAs production and influencing lncRNAs targets transcription activation or repression[202, 203]. In some cases, the lncRNAs can directly form R-loops at promoter regions and regulate gene expression[204, 205]. In addition to localization at promoters in human genes, R-loops can be also enriched over G-rich terminator elements. This situation could facilitate RNAP

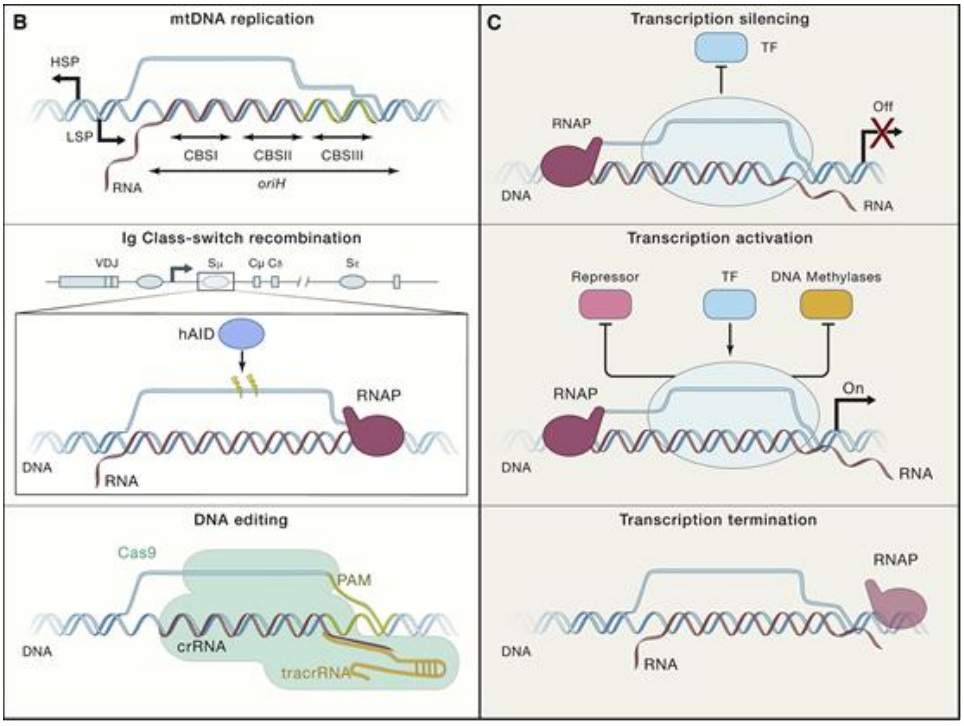

Figure 19. Physiological roles of R-loops in cellular processes and gene regulation: (B) Representation of three examples of typical cellular processes in which R-loops are implicated (from the top to the bottom, replication of mitochondrial DNA, Ig-CSR, and CRISPR-Cas9 activity). (C) Schematic representation of common situation where R-loops are involved in gene regulation and, in particular, impeding transcription factors (TF) binding to promoters, triggering transcription silencing (top), or repressors and DNA methyltransferases, promoting transcription (middle). Finally, presence of R-loops at G-rich transcription termination sites could facilitate RNAP pausing (bottom). (Adapted from *Garcia-Muse and Aguilera, 2019*[191])

pausing before efficient termination. In fact, the DNA-RNA helicase Senataxin (SETX) has been reported to act on R-loops positioned downstream of gene poly(A) signals, removing them and allowing the recruitment of termination factors[206, 207]. The physiological roles of R-loops raise the question of how their formation is regulated. One good example is provided by CRISPR-Cas9 mechanism as mentioned above[200]. Interestingly, an increasing number of factors such as DHX9 and DDX1 have been found involved in this regulation[208, 209]. DDX1 helicase can unwind G4 structures found in the Ig S-region transcript, allowing the RNA to hybridize with the DNA and providing the ssDNA substrate needed for AID action and CSR[209].

Therefore, R-loops are widely exploited in the genome for the regulation of cellular processes such as DNA replication and gene expression.

In spite of their physiological roles however, unscheduled R-loops can lead to DNA damage and ultimately genome instability. The first observations that pointed to R-loops as

being a threat for genome integrity came from studies demonstrating that mutations in genes involved in biogenesis, splicing and export of mRNA exhibited elevated R-loops levels, increased DNA damage and transcription-associated recombination[210, 211, 212]. One explanation for the R-loop-associated genome instability is the possible action that nucleases, DNA modifying enzymes (ex. AID), and genotoxic metabolites could exert on the displaced ssDNA, more susceptible to DNA mutagenic agents than dsDNA (Figure 20A). In addition, it has been proposed that R-loops could be the source of unscheduled DNA-replication if the RNA acts as a primer for highly mutagenic DNA synthesis[199]. However, the most plausible explanation for R-loop-induced genome instability in S-G2 cells is the deleterious effect of these structures on replication fork (RF) progression causing their stalling and, eventually, fork breakage (Fig. 20 B). Indeed, different studies have shown a correlation between DNA damage arising during replication and the presence of R-loops[213, 214, 215]. In fact, R-loops are considered a cause of transcription-replication conflicts (TRCs). In support to this, recent works have shown that RNAseH overexpression can rescue replication-associated damage and fork slowing in condition of active transcription[218, 219]. Moreover, FA pathway factors such as FANCA, FANCD2 and FANCM, that act during replication to repair ICLs, have been shown to suppress or resolve R-loops[216, 217]. Although TRCs are certainly connected to deficiency in R-loops-protecting factors[220, 221], the exact mechanism of how genome instability arises from TRCs is still not clear: one possibility could be that R-loops themselves, or in association with RNA polymerase (RNAP), represent an obstacle for RF progression triggering RF blockage. In favour of this hypothesis, depletion of the FACT chromatin-remodelling complex in yeasts, a factor that exchanges nucleosomes around the RNA polymerase during transcription elongation, leads to the accumulation of R-loops and R-loop-dependent DNA damage suggesting that FACT is important for avoiding R-loop-mediated TRCs[222]. At the present, two models are generally accepted for TRCs formation according to the direction of movement of RNAP related to the replication fork, and each of them leads to different consequences (Fig 20B). In the head-on collision model, RF and RNAP proceed in opposite directions and collide; these R-loops are the ones that preferentially cause DNA breaks[225]. Alternatively, RNAP and RF may travel in the same direction leading to co-directional conflicts.

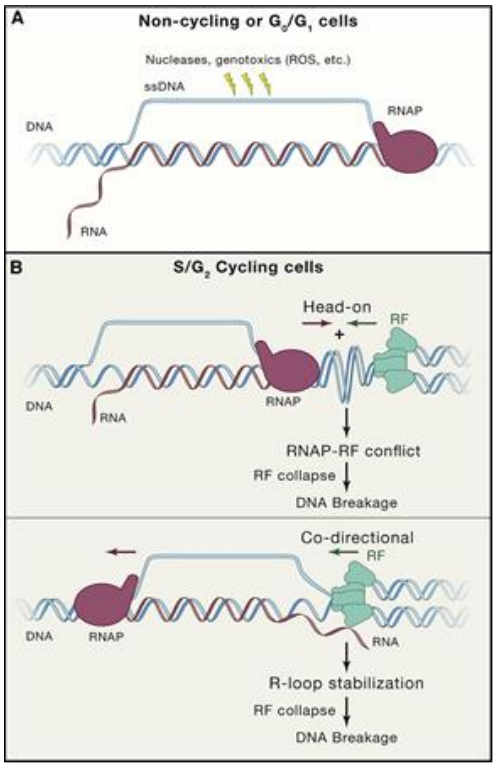

Figure 20. R-loops as a source of genome instability: (A) ssDNA of R-loop is highly susceptible of nucleases and genotoxic agents. (B) Schematic representation of the two accepted models for TCRs: head-on model on top and co-directional model on the bottom. See text for details. (From *Garcia-Muse and Aguilera, 2019*[191])

These TRCs may arise from R-loops stabilized by an DNA-RNA hybrid binding protein[224]. R-loops seem to arise more often from head-on TRCs as reported in yeast and bacteria[223, 224]. In addition, R-loops may cause chromosomal rearrangements, especially in the context of repetitive DNA sequences or common fragile sites (CFS), regions that are difficult to replicate. Indeed, several studies have reported R-loops accumulation at these loci supporting the idea that R-loops can be a source of TRCs in these regions. In agreement with this, the presence of R-loops seems connected to the genome instability at trinucleotide repeat sequences[191] and CFS that can be rescued by R-loop removal[191].

One more threat to genome instability correlated to R-loops is transcriptional stress generated by either stalling, arrest or backtracking of RNAP. R-loops are reported to block transcription *in vitro* and to alter it *in vivo*[226]. However, as previously described, R-loops are known to influence gene expression also via transcription activation. It is still not clear how cells discriminate between these two opposite effects on transcription. It is possible that programmed R-loops are highly regulated in order to be removed by dedicated

enzymes right after having accomplished their regulatory. Transcriptional stress may arise in two different modes: (i) RNAP pausing could be dictated by an associated R-loop; (ii) an R-loop could trigger the stalling of upstream RNAPs[226]. Importantly, transcription-coupled NER (TC-NER), has been involved in the removal of R-loops inducing RNAP stalling. Although the mechanism for R-loops removal in this context has not been fully clarified, recent studies proposed that TC-NER nucleases such as XPG and XPF may excise R-loops that block transcription, leaving a ssDNA gap that could progress to a double-strand break (DSB) with additional strand breaks or DNA replication[188, 227, 228].
In conclusion, these studies have led to identify R-loops as a source of genome instability mainly through DNA breakage occurring at the displaced ssDNA or following transcriptional and/or replication stress.

1.4.2. R-loops preventing and processing factors

The strong association between R-loops and genome instability explains the importance of factors that prevent their formation in cells or process the persistent and potential harmful ones. One first barrier against DNA-RNA hybrids formation is represented by RNA Binding Proteins (RBPs) that through the binding to the nascent mRNA protect it from annealing back to the DNA template during transcription elongation. Several RBPs including the serine/arginine-rich splicing factor 1 (SRSF1), components of the cleavage/polyadenylation machinery, and components of the TREX (mRNA export) complex involved in the coupling of transcription, processing, and nuclear export of transcripts, prevent R loop formation and DNA breaks[199]. To avoid the formation of R-loops, it has been proposed that RBPs may package nascent pre-mRNA and/or promote their co-transcriptional processing thereby avoiding the presence of unprocessed transcripts that could hybridize with the DNA template. Additionally, as mentioned before, negative supercoiling generated by the opening of the DNA duplex during transcription can favour the annealing of the nascent RNA back on the DNA template. Thus, factors like topoisomerases, which reduce topological constrains, are important to counteract this effect[221, 229, 230].
As mentioned above, high levels of transcription are generally associated with R-loop formation. However, several studies suggest that it is not the only cause of R-loops accumulation as demonstrated by R-loops accumulating mutants that exhibit transcription defects[191]. Chromatin state also represents a factor influencing R-loops formation. In yeast,

mutants in histones H3 and H4 exhibit high levels of R-loop[231]. In mammals, different studies have also correlated R-loops accumulation with an "open" state of the chromatin[194, 233]. Along the same lines, human cells deprived of the histone deacetylase SIN3A also accumulate DNA-RNA hybrids [232]. Since SIN3A can interact with mRNA exporting factors, such as the THO complex, it is tempting to speculate that this complex could contribute to R-loops prevention not only by promoting mRNA export, but by also facilitating a close state of the chromatin. In agreement, heterochromatin appears to be an obstacle for R-loops formation[191].

Besides R-loop prevention, cells have developed different mechanisms to resolve these structures and protect genome integrity. Some known factors include nuclease enzymes belonging to RNAseH family, conserved ribonucleases from bacteria to humans that, as already mentioned, are able to degrade the RNA moiety specifically in DNA-DNA hybrid context. Two main types of RNAseH enzymes have been described: RNAseH1 and RNAseH2. Although both are efficient at removing DNA-RNA hybrids, according to recent evidence from yeast, they appear to be differentially regulated: whereas RNAseH2 action is predominant during G2/M phase of cell cycle in both R-loop processing and ribonucleotide excision repair (RER), RNAseH1 can function in a cell cycle-independent manner and it is highly activated in presence of robust R-loop accumulation[234]. Although they act also physiologically removing RNA primer in hybrids at the Okazaki fragments, several studies from bacteria to humans have reported that cells depleted of RNAseH enzymes accumulate R-loops and, in particular, RNAseH1 overexpression can repress phenotypes associated with persistent R-loops[210, 211, 229, 235]. Nevertheless, the removal of DNA-RNA hybrids by degradation of RNA may come with a cost because it often results in the degradation of large chunks of newly synthetized RNA. This is perhaps why a large number of RNA-dependent helicases have evolved to process R-loops. RNA helicases found to be involved in this context include SETX, which, as already mentioned, has been implicated in R-loops resolution also in combination with DNA repair factors like BRCA1, promoting transcription elongation and termination[188, 206, 236, 237, 240]. DEAxQ-like putative RNA/DNA helicase Aquarius (AQR) has also been implicated in R-loops resolution and in preventing R-loops-dependent damage[227]. In addition, many RNA helicases belonging to the DEAD-box (DDX) family have been implicated, directly or indirectly, in R-loops metabolism such as DDX19, DDX23, DDX21, DDX1 and DDX5[206, 209, 227, 238, 239, 241-244, 264].

For instance, DDX19, a nucleopore-associated mRNA export protein, was found to unwind

DNA-RNA hybrids *in vitro* and cells depleted of DDX19 showed an increase in R-loops and DSBs suggesting that it acts on R-loops arising from replication stress or DNA damage[238]. Additionally, phosphorylated DDX23 is recruited to pausing RNAP at R-loops enriched site and mediates R-loops resolution and transcription elongation[242]. A more detailed overview on DEAD-box proteins will be given in section 1.5 (page 58).

But, why cells need all these RNA-helicases for R-loops resolution? One reason could be that each of them is specific for a subset of DNA-DNA hybrids in different cellular contexts; alternatively, they could act as RNA chaperons sequestering RNA and avoiding the possibility of DNA-RNA hybridization. Further studies are required to address this question. For example, proteomic approaches based on DNA-RNA hybrid pull-down have revealed a large number of potential factors implicated in this context[241, 245] and, although the data generated requires further validation, this strategy appears a convincing tool to reveal novel factors involved in R-loop formation or suppression.

1.4.3. R-loops and DDR

As discussed above, R-loops can be the cause of RF stalling and DNA breaks. Thus, R-loops can activate ATM and ATR and trigger the DDR[183]. In particular, a recent study shows that head-on TCRs activate ATR whereas co-directional TCRs preferentially lead to ATM activation[246]. However, ATM activation could arise from the conversion of an R-loop into a DSB, mediated by replication through a gap in the displaced ssDNA or the action of nucleases to process R-loops (Fig. 21A). In turn, ATR activation could derive from the RPA-coated ssDNA present at an R-loop-stalled fork (Fig. 21B)[226].

Nonetheless, R-loops can activate ATM- and ATR- mediated DDR also in absence of DSBs and in non-replicating cells. For instance, it has been shown that RNAP pausing due to DNA lesions blocking transcription triggers R-loops formation, which in turn promote ATM activation in a replication-independent manner[247]. Moreover, recent evidence indicate that RPA colocalizes with R-loops throughout the cell cycle, working as a sensor of these structures[248]. This could stimulate ATR activation independently of DNA replication (Fig. 21C). In support of this hypothesis, a recent work has shown that ATR is activated by the RPA-coated displaced strand of R-loops resulting from the transcription of centromeric proteins during mitosis[249]. Further studies will be needed to explore whether R-loops can activate ATR in a non-canonical manner in other contexts and especially, if

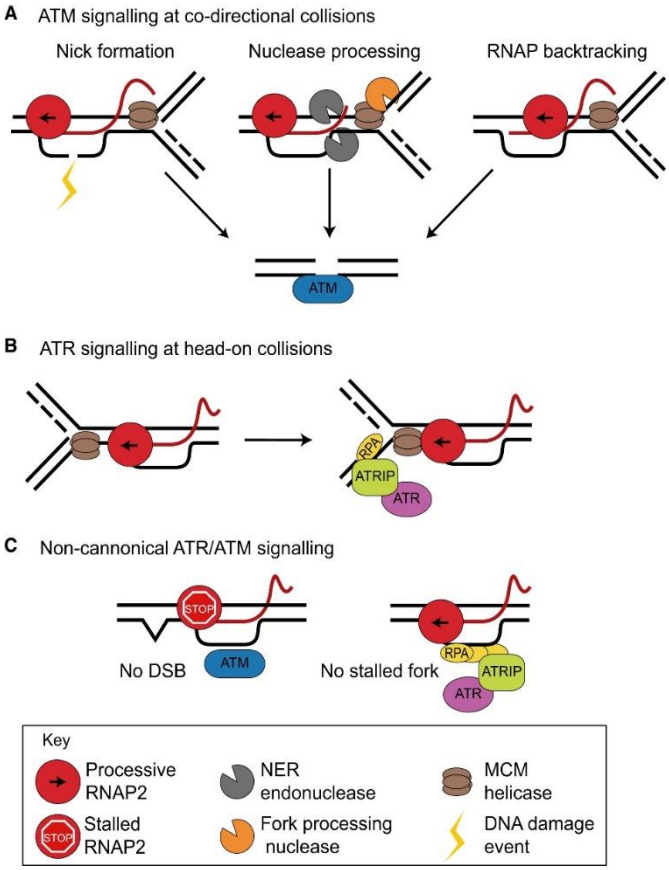

Figure 21. Canonical and non-canonical DDR induced by R-loops. Schematic representation of R-loops-induced ATM activation (A) ATR activation and ATM/ATR non- canonical signaling in absence od DSBs and in non-replicating cells (C). See text for details. (From *Crossley, Bocek and Cimprich, 2019*[226])

this is the case, how this activation is controlled.

1.4.3.1. Interplay between RNA helicases and nucleases involved in RNA metabolism and DNA repair proteins in resolving R-loops

In addition to RNA nucleases and helicases, DDR factors implicated in DNA damage repair pathways have also been involved in the processing of these structures. For instance, in the context of TRCs, ATM and ATR appear to be important for the recruitment of SETX at these sites to promote DNA-RNA hybrids resolution[250]. Another example is ATR activation of DDX19 that promotes its translocation from the nuclear pore to the nucleus in order to resolve DNA-RNA hybrids at TRCs[238].

However, the most important indications of a role of DNA repair pathways in R-loops resolution comes from evidence showing that cells depleted of factors such as BRCA1, BRCA2 and diverse members of FA pathway (FANCD2, FANCA, and FANCM) among

others, accumulate R-loops. For example, overexpression of RNAseH1 in FANCD2-depleted cells lead to a decrease of RF stalling phenotype and reduced DNA damage. Interestingly, although the binding of FANCD2 to R-loops stimulate FANCD2 monoubiquitination and function[180], FANCD2 can also mediate R-loops removal in combination with RNA-processing enzymes such as DDX47[186]. FANCM has also been proposed to remove R-loops by it DNA-RNA unwinding activity demonstrated *in vitro*[181].

Although diverse studies have shown a correlation between BRCA1 and BRCA2 DNA repair proteins with R-loops resolution, a clear mechanism is lacking. As mentioned before, BRCA1 in complex with SETX contributes to R-loop removal in the context of transcription termination sites. In agreement, the disruption of this interaction leads to persistent R-loops and DNA damage at these sites[236]. Another study implicates BRCA1 in transcription elongation indicating that RNAP pausing could induce R-loops accumulation and perhaps tumorigenesis in BRCA1 deficient cells[237].

As described before, BRCA2 depleted cells also accumulate R-loops. Bhatia and colleagues showed that BRCA2 interaction with DSS1 and PCID2, two components of mRNP biogenesis and export complex TREX-2[187]. The authors proposed that in this context, BRCA2 may act as a scaffold protein for the recruitment of other factors involved directly in R-loops processing.

In a recent work, BRCA2 has been proposed as relevant for the transition of RNAP from promoter-proximal pausing (PPP) sites to active transcription elongation. In this scenario, BRCA2 inactivation lead to stalling of RNAP at PPP sites resulting in R-loops accumulation proposing a different model to explain how BRCA2 repair protein could be involved in R-loops metabolism[188]. Thus, both BRCA1 and BRCA2 are able to repress R-loops-induced transcriptional stress by promoting transcription elongation.

A convincing argument for the function of DNA repair factors in resolving DNA-RNA hybrids is suggested by their accumulation upon silencing of very common factors involved in DNA repair pathways such as ATR, ATM, CHK1, CHK2, UBE2B, and RAD18[251].

Finally, because many of the factors discussed above are also involved in DSBs repair, they might also be involved in the removal of R-loops accumulated at sites of DSBs. A more detailed description of this possibility will be provided in the next section.

1.4.3.2. R-loops and DSB repair

Favourable topological conditions such as local negative supercoiling accumulating behind RNAP during transcription, can promote DNA-RNA hybrid formation promoting DNA strands opening and facilitating the hybridization of nascent transcript with the DNA template *in cis*. Therefore, DNA breaks generating a nick could also relieve the topological tension, triggering DNA opening and rotation, and generating ssDNA that will be more prone to anneal with the nascent RNA in transcribed regions, thus inducing DNA-RNA hybrids and R-loops formation[252]. In support of this hypothesis, it has been reported that a ssDNA nick in Ig switch regions as well as treatment with the topoisomerase I (TOPI) inhibitor camptothecin (CPT) (that blocks re-ligation of the ssDNA nicks generated by TOPI), induce DNA-RNA hybrid formation[252]. In human cells, ssDNA nicks and DSBs induced by laser micro-irradiation lead to R-loops formation; in this scenario, the DDR kinases ATM, ATR and DNA-PKcs trigger the exclusion of RBPs from damaged DNA[253]. Also in humans, the DEAD-box protein DDX1 forms foci at DSBs in cells exposed to IR. These foci are sensitive to RNAseH and transcription inhibitors treatment suggesting they are DNA-RNA hybrid dependent[254]. Moreover, DDX1 displays unwinding activity *in vitro* on these substrates suggesting this activity may serve for the removal of DNA-RNA hybrids at DSBs. Other studies in yeast also supported the idea that DNA breakage can induce DNA-RNA hybrids at the sites of the break[255].

Therefore, ssDNA nicks and DSBs represent a driving force for the formation and stabilization of DNA-RNA hybrids at these sites. In addition, several labs have proposed a DSB-induced *de novo* small non-coding RNA (sncRNAs)-transcription in different organisms. Indeed, although canonical transcription of genes flanking DNA breaks is often suppressed[293] several transcription factors as well as RBPs are recruited at DNA damage sites[303]. Whether this event requires specialized mechanisms or is just a consequence of chromatin relaxation upon DNA damage needs further study. As a result of transcription activation at these sites, several species of DNA damage-associated RNAs have been described such as DNA-damage response RNAs (DDRNAs) and DSB-induced RNA (diRNA). Their biogenesis is linked to the RNA interference (RNAi) pathway although the nature of the precursor transcript is still unknown. DDRNAs and diRNAs have been shown to promote DDR activation and DSBs repair by HR[256]. Recently, DSBs-induced-*de novo* transcription of diRNAs has been linked to the formation of DNA-RNA hybrids[257].

All these findings rise the important question of how the presence of DNA-RNA hybrids influence DSB repair.

On the one hand, it has been proposed that DNA-RNA hybrids present at DSBs could

promote their repair: for instance, a study in *S. pombe* refers to these hybrids as intermediates of HR-mediated DSBs repair in which annealing of the RNA to the ssDNA generated upon resection would regulate this step, impeding hyperesection as observed upon RNAseH overexpression. However, for the repair to take place, RNAseH is required to remove these hybrids to allow RPA coating on ssDNA. The same study also reported RNAP stalling at induced DSBs suggesting that formation of DNA-RNA hybrids as intermediates in DSBs repair is a regulated process requiring transcription for the generation of hybrids DNA-RNA and RNAseH action to remove them[255]. On the other hand, a different study in *S. cerevisiae* indicates that RNAseH is not required for efficient DSBs repair, although RNAseH double mutants show R-loops accumulation and forks collapse during replication.

Different studies have shown a decrease of human HR repair factors such as RAD51, RAD52, BRCA1/2 at DSBs in response to RNAseH overexpression suggesting that DNA-RNA hybrids are required for their recruitment[228, 257]. Moreover, HR repair factors are reported to be enriched at induced DSB of actively transcribed regions in human cells[259].

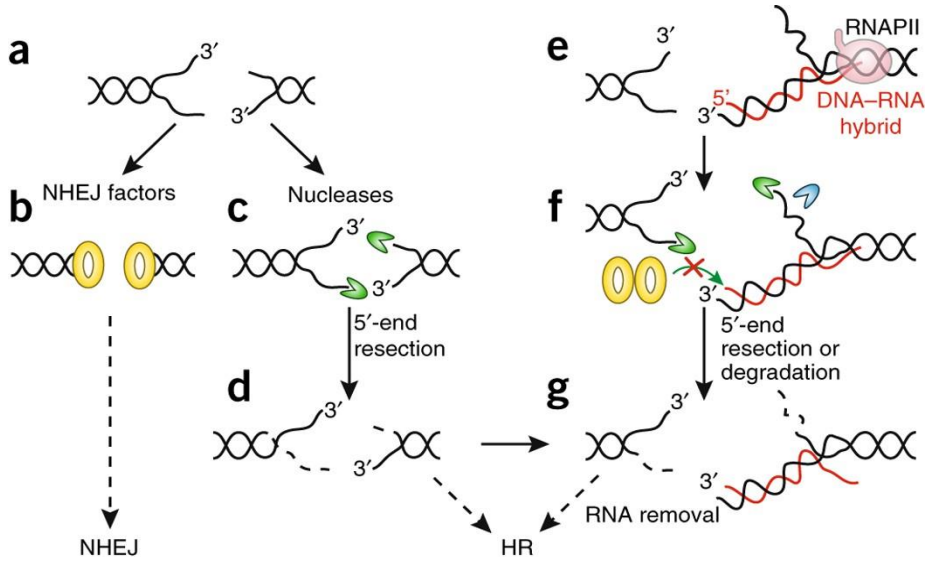

Figure 22. Possible outcomes of DNA-RNA hybrids formation at DSBs sites. When a DSB occur (a) recognition of DNA ends by NHEJ factors (b) or DNA end resection could promote different NHEJ- and HR-mediated repair respectively. However, the formation of a DNA-RNA hybrid before resection (e) could affect normal recognition of DNA ends by NHEJ factors (f) and promote non-template DNA degradation (g) committing DSB repair toward HR pathway, as canonical DNA end resection (d). In the case of DNA-RNA hybrids at DSBs, their removal is necessary for further steps of HR repair pathway. (From *Aguilera and Gomez-Gonzales, 2017*[252])

In spite of these advances, whether DNA-RNA hybrids have a direct role in mediating DSBs repair remains unclear. Indeed, DNA-RNA hybrids may form upon resection by the annealing of RNA on the ssDNA tail generated upon resection or they could be generated at DSBs before resection with the possibility of committing the repair of DSB to HR rather than NHEJ (Fig. 22). If this occurs, the non-template strand would be now prone to degradation by nucleases. The structural alterations caused by the formation of a hybrid before resection (which determines DNA repair pathway choice) could affect the recognition of broken DNA ends by NHEJ factors, thus committing the DSB repair pathway towards HR[252]. In support of this model, DSBs occurring at highly transcribed regions are favourably repaired by HR, whereas NHEJ is more active on DSBs generated in poorly transcribed chromatin[259].

Persistent R-loops flanking DSBs could affect recruitment of DNA repair factors, alter chromatin structure or induce the error-prone repair pathways[226]. In this regard, a recent genome-wide mapping of DNA-RNA hybrids performed in the DSBs inducible cell system (DiVA cells) revealed that R-loops are enriched at regions of the chromatin flanking DSBs and that SETX RNA helicase is recruited at these sites. Importantly, depletion of SETX affected RAD51 recruitment channelling repair through NHEJ[260], reinforcing the idea that the proper removal of DNA-RNA hybrids may promote DSBs repair by HR. Moreover, in yeast, RNAseH mutants have been reported to induce defective breaks repair by BIR pathway or blocking DSBs resection[225, 261]. Along these lines, mammal cells show a decrease in the recruitment of HR factors such as CtIP in response to AQR depletion[262]. Interestingly, a recent study shows that CtIP itself is important for R-loop prevention, although its proposed role in directly processing these structures was presented as independent of DSBs[263].

In conclusion, further studies are required to assess how DNA-RNA hybrid formation at DSBs is regulated and whether they have an active function in DNA repair pathway choice.

1.4.3.3. BRCA2 and R-loop metabolism

A wealth of recent evidence suggest that BRCA2 (as well as also BRCA1) is implicated in the turnover of R-loops structures. BRCA2 was first shown to be involved in R-loops processing or prevention when accumulation of these structures was observed in BRCA2-depleted cells[187]. Whereas BRCA1 role in this context has been associated at R-loops

formed at transcription termination sites (more details on BRCA1 implication in R-loops resolution will be discussed in section 1.4), the origin of R-loop accumulation following BRCA2 inactivation has been less clear. It has been reported that BRCA2 might participate in mRNP biogenesis through the interaction of its partner DSS1, with PCID2 component of the mRNA transcription and export (TREX). Since R-loops are usually co-transcriptional, they could be associated to the exported mRNA and BRCA2 could support the recruitment of proteins and enzymes able to process these structures[187]. Interestingly, human BRCA2 has recently been shown to bind to the RNAP and BRCA2 inactivation was found to trigger RNAP stalling and unscheduled R-loops accumulation at promoter-proximal pausing (PPP) sites in actively transcribed genes. DNA breaks marked by γH2AX formation was increased at these genomic sites in BRCA2-deficient cells, suggesting that unscheduled R-loops formed at PPP sites may be processed into DSBs[188]. Moreover, it has been recently proposed that, in the context of HR-mediated DSBs repair, BRCA2 could recruit RNaseH2 (an enzyme important for the specific degradation of RNA in DNA-RNA structures) to DSBs, where it might regulate the turnover of DNA-RNA hybrids at the damage sites[189]. Finally, a recent paper showed that overexpression of RNaseH1, known to degrade RNA from DNA-RNA hybrids [187], ameliorated the formaldehyde-induced replication stress and chromosomal aberrations of BRCA2 heterozygous cells, suggesting that R-loops might mediate the formaldehyde-induced cellular anomalies following the inactivation of one *BRCA2* allele[138].

Collectively, these observations suggest that unscheduled R-loop accumulation may be a major source of the endogenous DNA damage that leads to spontaneous chromosomal instability following the inactivation of BRCA2.

1.5. DEAD-box (DDX) family of proteins: focus on DDX5

Several RNA helicases belonging to the DEAD-box (DDX) family, including DDX5, have been involved in the processing of DNA-RNA structures.

DEAD-box proteins belong to the superfamily 2 (SF2) helicases and are classified as ATP-dependent RNA helicases that include 38 members in humans, 25 in yeast, and 9 in bacteria[266]. Similar to other SF2 RNA helicases, DEAD-box proteins contain 12 highly conserved motifs that are responsible for RNA-dependent ATPase and ATP-dependent helicase activities. The name “DEAD-box” originates from the single letter amino acid

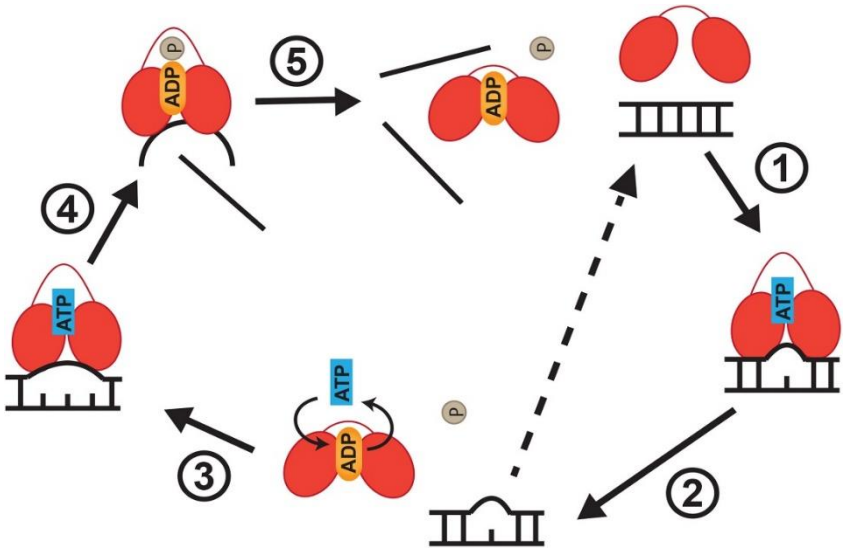

Figure 23. Non-processing unwinding activity of DEAD-box proteins. Schematic representation of the DEAD-box RNA helicases unwinding cycle. Black lines represent RNA strands and the red ovals are the two RecA-like domains connected by a flexible linker. When DEAD-box protein does not bind RNA, the two RecA-like domains are farther apart and exhibit a flexible "opened" conformation. After ATP and dsRNA binding (1) for next unwinding activity, the two RecA-like domains come closer together to form a "closed". This leads to the bending of one RNA strand and results in local duplex destabilization (~6 bp) (2). ATP hydrolysis and inorganic phosphate release convert the two RecA-like domains back to the "opened" conformation (3). In presence of longer than 6 bp duplexes multiple cycles of unwinding are required (4) until the helicase fully disrupts the partially opened duplex (5). (From *Xing, Ma and Tran 2019*[271])

code Asp (D)-Glu (E)-Ala (A)-Asp (D) that is present in the highly conserved motif II. DEAD-box proteins are implicated in all major aspects of RNA metabolism, from synthesis to biological activity, and to inevitable decay[266]. Similar to other RNA helicases, DEAD-box proteins unwind RNA duplexes in an ATP-dependent manner[267] and, as previously mentioned, some of them are reported to unwind also DNA-RNA hybrids [238, 254, 241, 243, 244, 264, 265]. A common unwinding mechanism shared by most of RNA helicases consists in a first binding of the helicase to a single-stranded region next to the duplex and then its translocation in a unidirectional manner. This mechanism is known as translocation-based duplex unwinding[269]. In contrast, DEAD-box proteins do not unwind in a translocation-based fashion but rather, load directly onto the duplex region and separate the two strands by twisting on of the RNA strands. This particular capacity of DEAD-box proteins is linked to the fact that they contain a structurally conserved helicase core that consists of two globular RecA-like domains (RecA_N and RecA_C) which are

connected by a flexible linker to form a characteristic “dumbbell-like” core. During RNA unwinding, the two domains adopt a closed conformation upon cooperative binding of the double strand RNA (dsRNA) and ATP. This allows to bend one strand of the RNA, which results in the destabilization of the dsRNA structure following release of the “unbent” RNA strand[267]. ATP hydrolysis then leads to the helicase dissociation from ssRNA and to the end of a single round of the unwinding cycle. However, a single ATP hydrolysis cycle only unwinds approximately six base pairs of dsRNA; thus, to separate a longer duplex, multiple unwinding cycles are required. Indeed, following the binding of a second ATP molecule, the DEAD-box helicase can recycles back on the same RNA substrate or, alternatively, find a new target[267] (Fig. 23).

One of the main functions of DEAD-box proteins is to act as ribonucleoprotein (RNP) chaperone. This role requires the ability to bind different types of RNAs in a sequence-independent manner, since DEAD-box recognize the phosphate backbone of RNA[267, 269]. In addition, it has been reported that some accessory domains or protein co-factors may confer DEAD-box proteins a specificity for certain substrates[269, 270]. The role of DEAD-box proteins as chaperones relay on their ability to remodel RNA structures using their unwinding and annealing activities, the latter being ATP independent. The remodelling of RNA structures mediated by DEAD-box proteins allow the exposure of RNA motifs required for the interaction with RBPs; on the other hand, DEAD-box proteins themselves can function as platform for the formation of RBPs-RNA structures complexes. Examples of RNA chaperone activity carried out by DEAD-box proteins have been shown in the context of splicing and mRNA export[269].

DDX5 (or p68) RNA helicase was first identified forty years ago; later, analysis of its sequence showed strong similarities with murine translation initiation factor eIF4A, also classified as DEAD-box helicase. A paralog of DDX5, DDX17 (or p72) was also identified, with a level of identity with DDX5 of 69.7%. Several studies have characterized this helicase in humans, Drosophila (Rm62) and yeast (Dbp2), demonstrating a high evolutionary conservation [271]. DDX5 possess a typical DEAD-box helicase core consisting of 12 DEAD-box motifs, whereas the N- and C-terminal are more diverse. For instance, arginine and glycine (RG)-rich regions, important for RNA and protein interaction, that are normally at C-terminal region in other members, can be found at both N- and C-terminus in DDX5. Additionally, DDX5 contains low homology-sequences at C-terminus called C-terminal extensions (CTEs) whereas these extensions are present at both N- and C-terminus in DDX17 and this is one of the most important differences between the two

paralogs[271].

DDX5 unwinding activity was described for the first time thirty years ago. DDX5 recombinant protein was purified from human cells and it showed ATPase and ATP-dependent helicase activity on dsRNA[272]. Recent works based on DDX5 and Dbp2 purified from bacteria, demonstrated the low processivity of both helicases although DDX5 has faster unwinding activity that Dbp2[271, 273]. They also differ on the ATP-dependent annealing activity described for Dbp2 but not for DDX5. Interestingly, the same study showed that a truncated DDX5 lacking CTEs acquires annealing activity suggesting that these extended regions could have an impact on how DDX5 interacts with dsRNA. Importantly, both Dbp2[275] and DDX5 can unwind DNA-RNA hybrids *in vitro*[264]. In this study, DDX5 was found to be methylated by the protein arginine methyltransferase 5 (PRMT5) at the RG-rich motifs which allows its interaction with the exoribonuclease XRN2. This complex is important for the resolution of R-loops at transcription termination sites[264].

As most of DEAD-box proteins, DDX5 also shows a wide range of functions in RNA metabolism ranging from post-transciptional gene regulation to ribosome biogenesis. Several studies have shown a variable localization of DDX5 in the cell according to the cell-cycle status: for instance, in interphase, DDX5 shows a more clear nuclear pattern whereas it locates to the cytoplasmic during G2/M phase. Its localization may dependent on DDX5 post-translational modification and on cell type[271]. Interestingly, DDX5 has been involved in transcription regulation in cancer. Indeed, DDX5 is a co-activator of oncogenic transcription factors such as estrogen receptor (ER) and androgen receptor (AR), which are important in the breast and prostate cancer, respectively. [277, 278]. Importantly, other studies have shown DDX5 as a coactivator of the tumor suppressor p53 in response to DNA damage[279] explaining the sensitivity to γ-irradiation observed in selected tissues following DDX5 depletion. This study suggests that DDX5 has selective coactivator activity for p53 in response to DNA damage and may modulate the decision between cell cycle arrest and apoptosis, favouring cell survival[279]. A more recent analysis in breast cancer context revealed that DDX5-p53 interplay may regulate expression of PLK1. Indeed, it was shown that DDX5 can associate with the promoter of PLK1 and stimulate its expression in p53-deficient breast cancer cells[276]. In addition, it is well established that DDX5 is overexpressed in various types of cancers including colon[280], prostate[277] and breast cancers[278]. Depletion of DDX5 has been shown to inhibits cancer cell growth indicating it may be involved in cancer development. In this regard, a small molecule inhibitor of

DDX5, Supinoxin™ (RX-5902), has been already developed for cancer therapy, and it is in a clinical trial in patients with metastatic triple negative breast cancer (ClinicalTrials.gov identifier: NCT02003092)[271]. This suggests that DDX5 is a promising drug target for cancer.

DDX5 has been found important also in chromatin modification through the regulation of long non-coding RNAs (lncRNAs), essential for their interaction with histone modifiers[271].

A large number of studies have focused on DDX5's role in mRNA processing, especially in splicing and mRNP export. For instance, DDX5 has been reported to interact with the spliceosome and contributes to its catalytic activation[271]. Moreover, DDX5 has been found important in alternative splicing regulation targeting specific sequence elements. Indeed, DDX5 could regulate this process resolving particular RNA structures such as RNA G-quadruplexes, although it is not clear whether DDX5 actively processes these structures[281].

Additional evidence supports a role of DDX5 in mRNA export, mediating not only the association between export factors with the mRNA but, likely, promoting the translocation of the mRNP through the nuclear pores[271]. Other works associate DDX5 to Nonsense-mediated decay (NMD), a surveillance pathway essential to target mRNA for degradation. Common targets for this pathway are mRNAs that exhibit a premature termination codon. DDX5 has been described to stabilize the assembly of the NMD machinery onto the targeted mRNAs[282]. Furthermore, DDX5 appears involved in ribosome biogenesis. Indeed, DDX5 associates with rDNA and its overexpression leads to an increase of rRNA transcripts, suggesting that DDX5 promotes rDNA transcription. Interestingly, R-loops identified in rDNA affect its transcription. Therefore, it is tempting to speculate that DDX5 is required at rDNA to resolve R-loops and facilitate rDNA transcription. On the other hand, DDX5 could also function in ribosome biogenesis promoting the assembly of RBPs on rRNA in order to process it[271]. Additional reported functions of DDX5 are in micro-RNA generation and processing, signalling and glucose metabolism[271].

In conclusion, DDX5 plays important roles in several aspects of RNA metabolism, from RNA processing and export to regulation of RNA levels and gene expression. However, more studies are required to understand how different RNP and RNA conformations regulate the different functions of DDX5.

1.6. Hypothesis and objectives of this thesis project

My thesis project focuses on the role of DDX5 and BRCA2 at DNA-DNA hybrids in the

context of DSBs repair.

Cells have evolved diverse DDR pathway to face both endogenous and exogenous sources of DNA damage and ultimately to prevent tumorigenic transformation. Among the most toxic and mutagenic lesions are DSBs that, if not repaired, lead to chromosome loss or fragmentation, chromosomal rearrangements and genetic instability.

The tumor suppressor BRCA2 participates in the DDR, in particular in HR, the predominant mechanism employed by cells to accurately repair DSBs. A wealth of evidence suggests that mutations affecting this function of BRCA2 lead to genomic instability and tumorigenesis.

BRCA2 is a large protein consisting of 3418 aa (390 KDa) [85]. It comprises several functional domains related to its HR function including the C-terminal DNA binding domain, the BRC repeats that bind RAD51 and DMC1 (RAD51 homolog in meiosis) and a PALB2 (partner and localizer of BRCA2) interacting site at the N-terminus. Recently, our laboratory has described a new DNA binding domain in the N-terminal region that is important for HR[105]. Despite these findings, the function of the N-terminal region of BRCA2, which represent one third of the protein (around 1000 aa), remains poorly understood mainly because of its highly disordered nature which complicates its characterization. Therefore, our laboratory performed an N-terminus "interactome" to shed light on the functions of this region.

OBJECTIVE 1

Biochemical and cell-based confirmation of the BRCA2 interacting RBPs and RNA helicases identified by proteomics screen.

The N-terminus “interactome” revealed that the $BRCA2_{NT}$ interactors are enriched in different categories and one of the most enriched was represented by RNA binding proteins and RNA helicases. Interestingly, some of these proteins have been involved in the DDR and in the case of RNA helicases this seems to be associated to their ability to process R-loops and DNA-RNA hybrids[239, 244, 254].

R-loops and DNA-RNA hybrids formation is concomitant to the process of transcription; however, when unscheduled, these DNA-RNA structures represent a source of genome instability[191]. Interestingly, the formation of R-loops can be enhanced by ssDNA and dsDNA breaks[252] and emerging evidence indicate that DNA-RNA hybrids can accumulate at DSBs [228, 239, 255, 283, 284]. Importantly, BRCA2 deficient cells accumulate R-loops

providing evidence for its role in either R-loop prevention or processing[138, 187]. Additionally, BRCA2 has been found to regulate transcription elongation[188] and in this scenario, BRCA2 inactivation leads to R-loops mediated genome instability. Finally, a recent work report a role of BRCA2 in modulating DNA-RNA hybrid levels at DSBs through its interaction with RNAseH2[189].

All these findings prompted us to ask whether BRCA2 could cooperate with the interacting RNA helicases identified in our MS analysis in preventing or processing DNA-RNA structures.

Thus, the first objective of this PhD project was to confirm by biochemical and cell based tools the results obtained from our proteomics screen. We could confirm the interaction of BRCA2 with the DEAD-box RNA helicase DDX5 by co-immunoprecipitation (co-IP) and pull-downs performed in human cells These preliminary results were further confirmed by in situ Proximity Ligation Assay (PLA), a cell-based technique that allows detecting two proteins that are in close proximity (< 40 nM). Both of these approaches were carried out in presence or absence of DNA damage (irradiation or Mitomycin C treatment) to test whether the interaction was enriched upon DNA damage. We also sought to refine the DDX5 interacting site by co-IP using different truncated fragments of BRCA2. Finally, using the purified proteins and pull-downs assays we determined whether the interaction was direct.

OBJECTIVE 2

Assess the role of the interaction of BRCA2 and DDX5 in DNA-RNA hybrid resolution

The recent findings describing DDX5 unwinding activity on DNA-RNA hybrids *in vitro*[264], together with the proposed role of BRCA2 in R-loops metabolism[138, 187] led us to investigate the role of the confirmed interaction between BRCA2 and DDX5 in the resolution of DNA-RNA hybrids.

Several RNA helicases such as DDX1[239, 254] or DDX21[244] have been described as participating in the DDR: this role seems to be dependent on their unwinding activity on DNA-RNA hybrids or R-loops formed at DNA damage sites that could affect proper DNA repair. Thus, as second objective of this PhD project, we first aimed to characterize DDX5 role in the resolution of DNA-RNA structure in association with BRCA2 in the context of DSBs.

We first aimed to confirm the role of DDX5 in suppressing DNA-RNA structures by looking at the genome-wide spectrum of DNA-RNA hybrids (DNA-RNA Immunoprecipitation (DRIP)) that accumulate upon its depletion. We also sought for evidence for an accumulation of DNA-RNA hybrids at DSBs in these cells using PLA with the DNA-RNA hybrids specific antibody S9.6 and the DNA-damage specific marker γH2AX or at specific R-loop enriched regions, after DSBs induction, exploiting the U2OS DIvA cell system[259]. We then looked for evidence of DDX5 association with DNA-RNA hybrids by PLA and its association with DSB using laser micro-irradiation and Chromatin-Immunoprecipitation (ChIP) and whether this association was dependent on BRCA2.
To get mechanistic information we then used radiolabeled R-loops and purified DDX5 and BRCA2 to test the possible effect of BRCA2 on the unwinding activity of DDX5.

OBJECTIVE 3

Examine the effect of disrupting BRCA2-DDX5 interaction on DNA-RNA resolution and on DSBs repair by HR

To determine the specific role for BRCA2-DDX5 interaction we looked for a mutation that could alter the binding. Following the mapping to the first 250aa of BRCA2, we decided to focus on a BRCA2 missense variants identified in breast cancer patients previously characterized in the lab in the context of mitosis[84] located in this region. Using BRCA2 deficient cells stably complemented with BRCA2 WT or containing the selected variants (stable cell lines previously developed in our lab), we assessed the effect on BRCA2-DDX5 interaction. Once identified a variant altering the interaction, we used cells bearing this variant to study their phenotype, DNA-RNA hybrid levels upon DNA damage and the purified mutated protein to assess its capacity to stimulate DDX5 unwinding activity *in vitro*. Finally, we evaluated whether BRCA2-DDX5 interaction was required for DSBs repair by HR.

CHAPTER 2

BRCA2 is a multidomain and multifunctional protein involved in several pathways throughout the cell cycle, as described in detail in Chapter 1. Over the last years my laboratory has used different approaches to understand the function of BRCA2, focusing especially on those regions of the protein that remain still poorly understood, such as the N-terminal region of BRCA2 ($BRCA2_{NT}$).

This thesis project reveals DDX5 as a new partner of $BRCA2_{NT}$ and contributes to clarify the role of BRCA2 in DNA-RNA hybrids metabolism. In the next Results section, I will give a detailed description of this work outlined in the Objectives section.

Results

To shed light on the function of the highly disordered N-terminal region of BRCA2, Juan Martinez in the lab performed a proteomics mass spectrometry screen on this region. For this purpose, he used a fusion construct composed of a N-terminal tandem of maltose binding protein tags (2xMBP) tag and two nuclear localization signals (NLS) followed by the first 1000 aa of BRCA2 (hereafter $BRCA2_{NT}$). As a control he used 2xMBP-NLS alone (hereafter 2xMBP). The two constructs were transiently expressed in HEK293T cells. Then, he performed an amylose pull-down from nuclear cell extracts and loaded the samples on SDS-PAGE gel. ~24 gel slices of the gel were submitted to trypsin digestion and the peptides extracted from each slice were analizyed by nano-liquid chromatography-coupled to tandem mass spectrometry (MS) at the Mass Spectrometry facility of Institut Curie to identify potential partners (Fig 1A). From this analysis, several factors involved in diverse cellular functions such as DNA damage or chromatin remodelling were identified as possible interactors. Interestingly, several RNA binding proteins (RBPs) and especially RNA helicases appeared particularly enriched in this analysis (Fig. 1B). Importantly, some of these RPBs have already been found involved in DNA damage response (DDR) and in the resolution of DNA-RNA hybrids, such as RNA helicases DDX1[239, 254], DDX5[264], DDX21[244] and the RBP RBMX[285]. Thus, we next aimed to confirm the potential interactions revealed by MS analysis.

2.1. OBJECTIVE 1

Biochemical and cell-based confirmation of the BRCA2 interacting RBPs and RNA helicases identified by proteomics screen

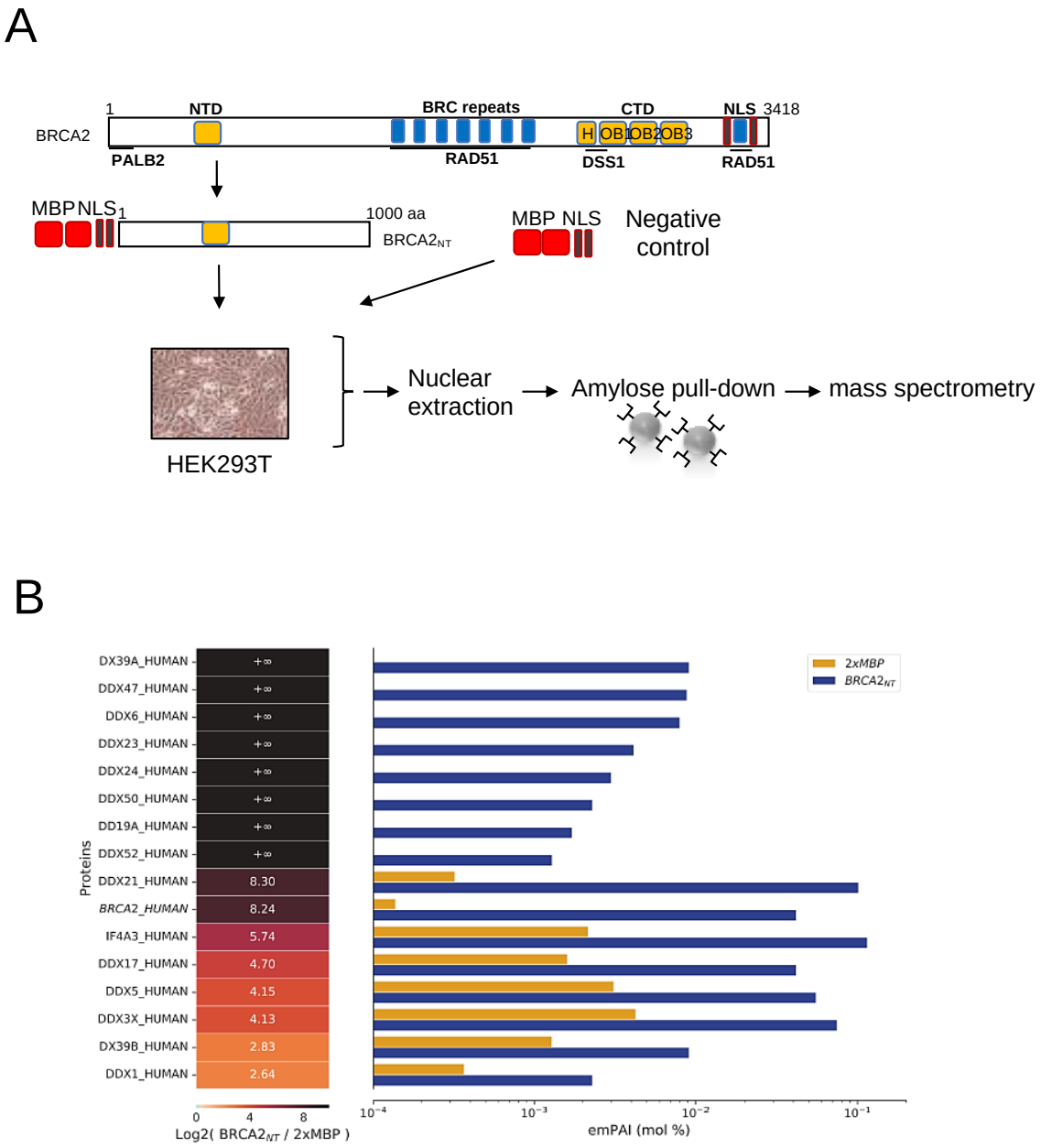

Figure 1. Investigation of potential partners of BRCA2$_{NT}$. (A) Schematic representation of method used for BRCA2$_{NT}$ interactome. HEK293T cells were transfected with 2xMBP-NLS- BRCA2$_{NT}$ and 2xMBP-NLS constructs, subjected to an amylose pull-down, loaded on a SDS-PAGE and processed for mass spectrometry (MS).**(B)** DEAD-box helicases found enriched in the BRCA2$_{NT}$ interactome. Label free protein quantification. (Left) BRCA2 (in italics) and DDX Protein ID present in the MS screen showing the fold enrichment of each protein in BRCA2$_{NT}$/ 2xMBP. Infinite-fold indicates proteins that are only present in BRCA2$_{NT}$ sample. (Right) Quantification of the protein abundance in molar fraction percentage (mol %) in each pull-down as indicated based on label free emPAI quantification as described in *Ishihama et al., 2005*[305].

To confirm these interactions we performed an amylose pull-down with benzonase-treated whole cell extracts of HEK293T cells transfected with the same constructs (2xMBP and $BRCA2_{NT}$) as in the MS. Cells were either left untreated or treated with γ-irradiation (IR, 6Gy) to detect interactions enriched upon DNA damage. Our results revealed that DDX5 and DDX21 could specifically co-purify with $BRCA2_{NT}$ and exposure to IR moderately enhanced the interaction of DDX5 with $BRCA2_{NT}$. In contrast, we were unable to confirm the interaction between RBMX and $BRCA2_{NT}$ (Fig. 2A). Co-Immunoprecipitation (co-IP) using a BRCA2 specific antibody confirmed DDX5 interaction with endogenous BRCA2, whereas we could not validate the same result for DDX21. This analysis confirmed the complex of BRCA2 with DDX5 in benzonase-treated conditions although IR did not enhance the formation of the complex (Fig. 2B).

To further confirm their co-localization of DDX5 and BRCA2 in the cell we performed an *in situ* Proximity Ligation Assay (PLA) with specific antibodies anti-BRCA2 and anti-DDX5 in U2OS cells left untreated or exposed to IR (6Gy) 4 hours before fixation. For every PLA experiment I will present in this thesis, I carried out two single-antibody controls to assess the specificity of the PLA signal. Analysis and quantification of single PLA spots per nucleus showed that BRCA2 and DDX5 colocalized in the cell and their proximity was enhanced in cells exposed to IR (Fig. 2C). As both BRCA2 and, more recently, DDX5 have been shown involved in DNA-RNA hybrids resolution[187, 264] we tested whether BRCA2-DDX5 interaction was dependent on the presence of DNA-RNA hybrids. Overexpression of RNAseH1 (RH), a nuclease able to degrade specifically the RNA molecule in a DNA-DNA hybrid, reduced PLA signal and this was further accentuated in IR conditions (Fig. 2C). Finally, to evaluate the dependence of the interaction on transcription expected from the sensitivity to RH treatment we treated cells with Cordycepin, a transcription inhibitor.

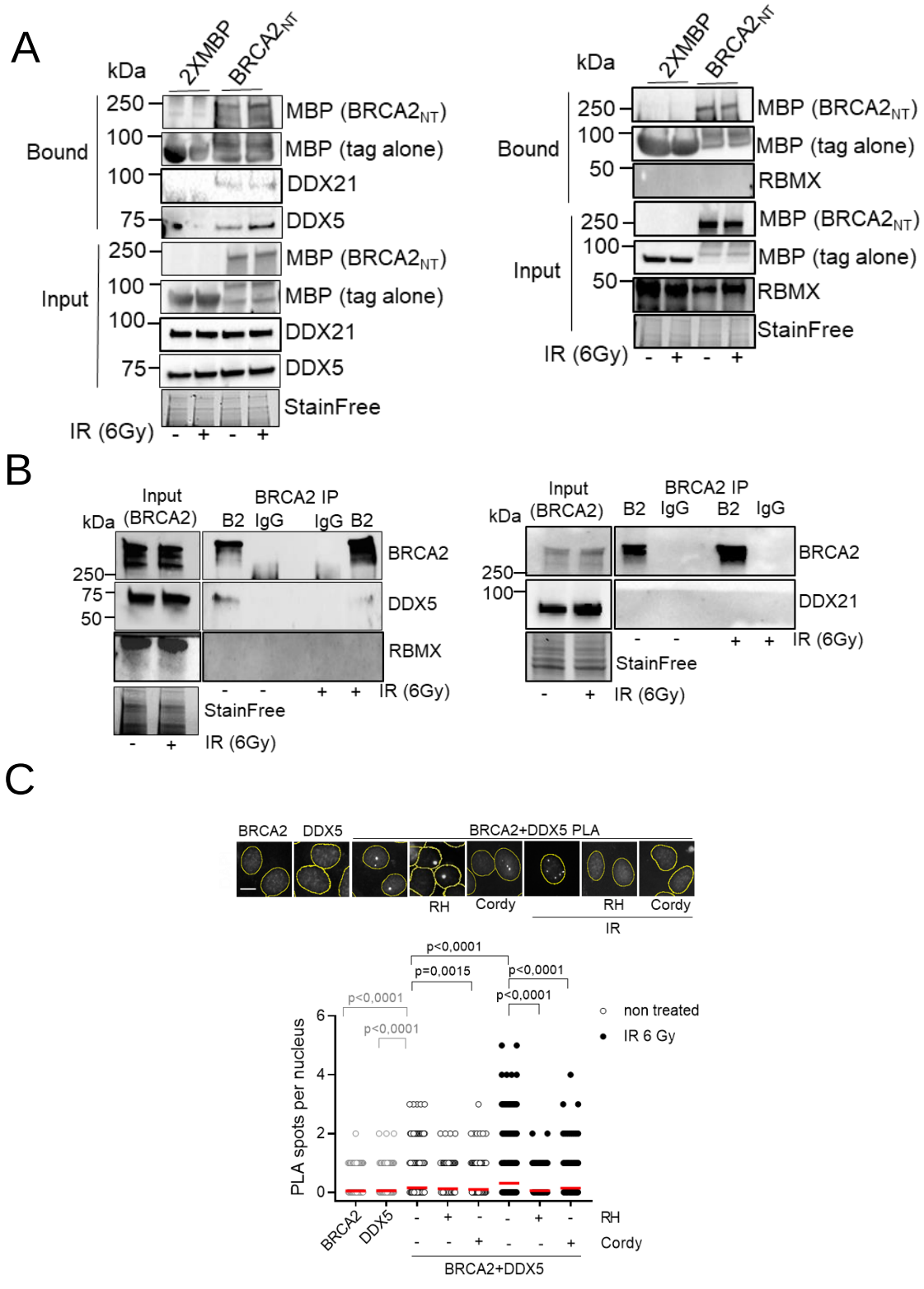
A
kDa
2XMBP
BRCA2NT
Bound
Input
250
100
75
50
MBP (BRCA2NT)
MBP (tag alone)
DDX21
DDX5
RBMX
StainFree
IR (6Gy)
- + - +
B
Input (BRCA2)
BRCA2 IP
B2 IgG IgG B2
BRCA2
DDX5
RBMX
StainFree
IR (6Gy)
C
BRCA2
DDX5
BRCA2+DDX5 PLA
RH
Cordy
IR
p<0,0001
p=0,0015
non treated
IR 6 Gy
PLA spots per nucleus
0
2
4
6
BRCA2+DDX5

Figure 2. BRCA2 interacts with DDX5 (A) Amylose pulldown from HEK293T whole cells extracts expressing 2xMBP-$BRCA2_{NT}$ in untreated or irradiated cells (6Gy; +IR). Lysates treated with Benzonase. DDX5 and $BRCA2_{NT}$ (MBP) detected by immunoblot. StainFree images of the gels before transfer was used as loading control (cropped image is shown). **(B)** Immunoprecipitation (IP) of endogenous BRCA2 from HEK293T cells treated or not with IR (6Gy), as indicated. Lysates treated with Benzonase. Normal mouse IgG was used as negative control. Immunoblot for DDX5 and BRCA2 detection in both Input and IP samples. StainFree images of the gels before transfer was used as loading control (cropped image is shown). **C)** Top: Representative images of *in situ* proximity ligation assay (PLA) between BRCA2 and DDX5 antibodies in U2OS cells either left untreated (-) or irradiated (4h post-IR; 6 Gy). When indicated, cells were transfected with a plasmid expressing RNase H1 (RH) 24h before or treated with Cordycepin (Cordy) for 2h at 37°C before fixation. Single antibody controls from untreated siC cells are shown. Scale bar indicates 10 µm. Bottom: Quantification of the number of PLA spots per nucleus. At least 300 cells per condition were counted from three independent experiments. For statistical comparison of the differences between the samples we applied a Kruskal-Wallis test followed by Dunn's multiple comparison test, the p-values show significant differences. The red line in the plot indicates the median, each symbol represents a single PLA spot.

Similarly to RH overexpression, inhibition of transcription led to a decrease in PLA spots in both untreated and irradiated conditions suggesting that the co-localization of BRCA2 and DDX5 is dependent on transcription (Fig. 2C). Thus, DDX5 interacts with BRCA2 N-terminus; this interaction is enhanced particularly in IR conditions and favoured by DNA-RNA hybrids and transcription.

Next, to define a shorter region of BRCA2 sufficient to bind DDX5 we performed an amylose pull-down in HEK293T cells overexpressing a series of truncated fragments contained in the $BRCA2_{NT}$. The three 2xMBP-NLS-tagged fragments comprised either BRCA2 aa 1-250, 1-500 or 1-750 (hereafter $BRCA2_{T1}$, $BRCA2_{LT2,}$ $BRCA2_{LT3}$,respectively) or the 2xMBP tag as control (Fig. 3A). We found that the three BRCA2 fragments but not the control 2xMBP were able to form a complex with DDX5 that was not sensitive to benzonase treatment included in the reaction (Fig. 3A). These results indicate that the first 250 aa of BRCA2 ($BRCA2_{T1}$) are sufficient to bind DDX5.

Next, to find out whether the interaction was direct, we purified $BRCA2_{T1}$ from HEK293T cells with a protocol already established in the lab[105], and MBP-DDX5-GST as previously described[265]. 2xMBP-NLS-$BRCA2_{T1}$ was purified from HEK293T cells using affinity chromatography followed by a weak ion exchange chromatography. An example of the purification procedure and the fractions obtained in a typical experiment are illustrated in Fig. 3B. MBP-DDX5-GST expression vector (kind gift from E. Tran., Purdue University, US) was expressed in bacteria and was purified using a glutathione resin

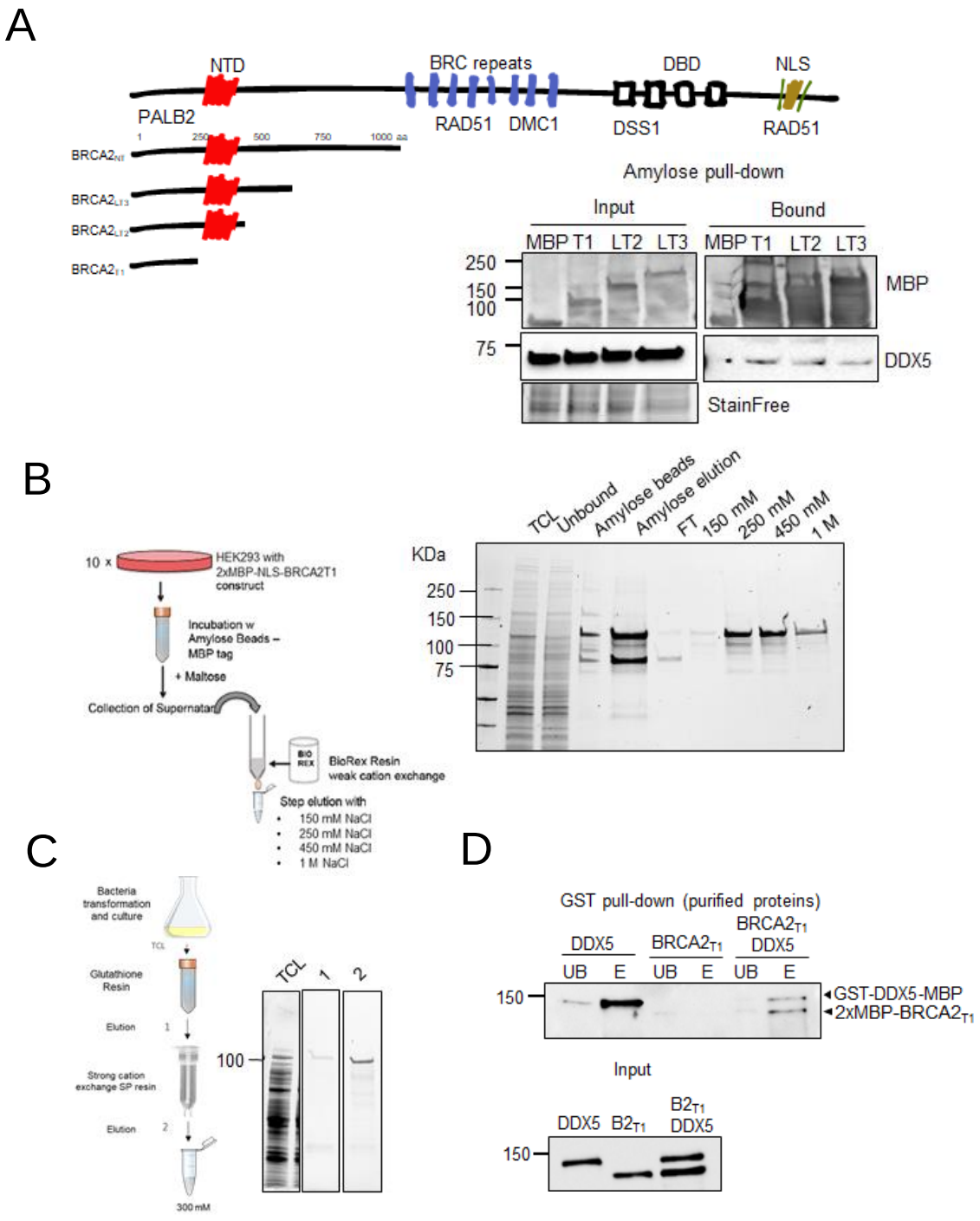

Figure 3. BRCA2$_{T1}$ interacts with DDX5. (A) Top: Diagram showing the BRCA2 N-terminal truncations used in this study. Bottom: Amylose pulldown from HEK293T whole cells extracts overexpressing the indicated BRCA2 N-terminal truncations (BRCA2$_{T1}$, BRCA2$_{LT2}$, BRCA2$_{LT3}$) or the 2xMBP tag. DDX5 and BRCA2$_{NT}$ truncations were detected using specific antibodies against DDX5 and MBP, respectively. StainFree images of the gels before transfer was used as loading control (cropped image is shown). **(B)** Left: Work-flow of 2xMBP-NT-BRCA2 purification. Right: Example of the fractions obtained from one purification experiment. (C) Left: Work-flow of MBP-DDX5-GST purificationand of 2xMBP-tagged BRCA2$_{T1}$ used in (D) See details in the text. **(D)** GST pulldown assay using purified BRCA2$_{T1}$ (B2$_{T1}$) and DDX5; MBP antibody was used for the detection of both proteins. UB: unbound; E: eluate.

followed by cation-exchange chromatography as previously described[265]. The purity of the protein was assessed by SDS-PAGE gel (Fig. 3C).

Equal amount (200 ng) of the two proteins were mixed together and incubated with glutathione resin. Importantly, $BRCA2_{T1}$ was readily eluted from the glutathione resin only in the reaction containing GST-DDX5-MBP indicating that the interaction between BRCA2 and DDX5 is direct (Fig. 3D).

Taken together, these results indicate that DDX5 RNA helicase physically binds BRCA2 and that the interacting site is comprised within the first 250 aa of BRCA2.

2.2. OBJECTIVE 2

Assess the role of the interaction of BRCA2 and DDX5 in DNA-RNA hybrid resolution

Both BRCA2- and DDX5-depleted cells have been reported to accumulate DNA-RNA hybrids[187, 264]. We confirmed these data using U2OS cells transfected with either BRCA2 or DDX5 siRNA. DNA-RNA hybrids accumulated upon DDX5 and BRCA2 depletion as detected by Immunostaining with S9.6 antibody that recognize DNA-RNA hybrids[286] (Fig. 4A). As DDX5 possesses ATP-dependent helicase activity on DNA-RNA hybrids *in vitro*[264, 265] we next tested whether a DDX5-helicase dead mutant (DDX5-HD) could rescue the high levels of DNA-RNA hybrids observed in DDX5-depleted cells. We generated a construct expressing DDX5-GFP WT or a construct in which we introduced an alanine substitution in residue K144 of DDX5, a highly conserved residue previously shown to be required for the unwinding activity of DDX5[265] (DDX5-HD-GFP). DDX5-GFP WT and DDX5-HD-GFP constructs were transfected in U2OS cells depleted of endogenous DDX5 or of BRCA2. As shown in Fig. 4B, DDX5-GFP WT was able to rescue the S9.6 intensity signal in both BRCA2- and DDX5-depleted cells. However, DDX5-HD-GFP was also able to reduce S9.6 intensity signal, indicating that the helicase activity is dispensable for preventing DNA-RNA hybrids in these conditions. It is possible that an excess of RNA binding activity due to the overexpression suffices to suppress the formation of DNA-RNA hybrids (coll. A. Aguilera, CABIMER, Sevilla).

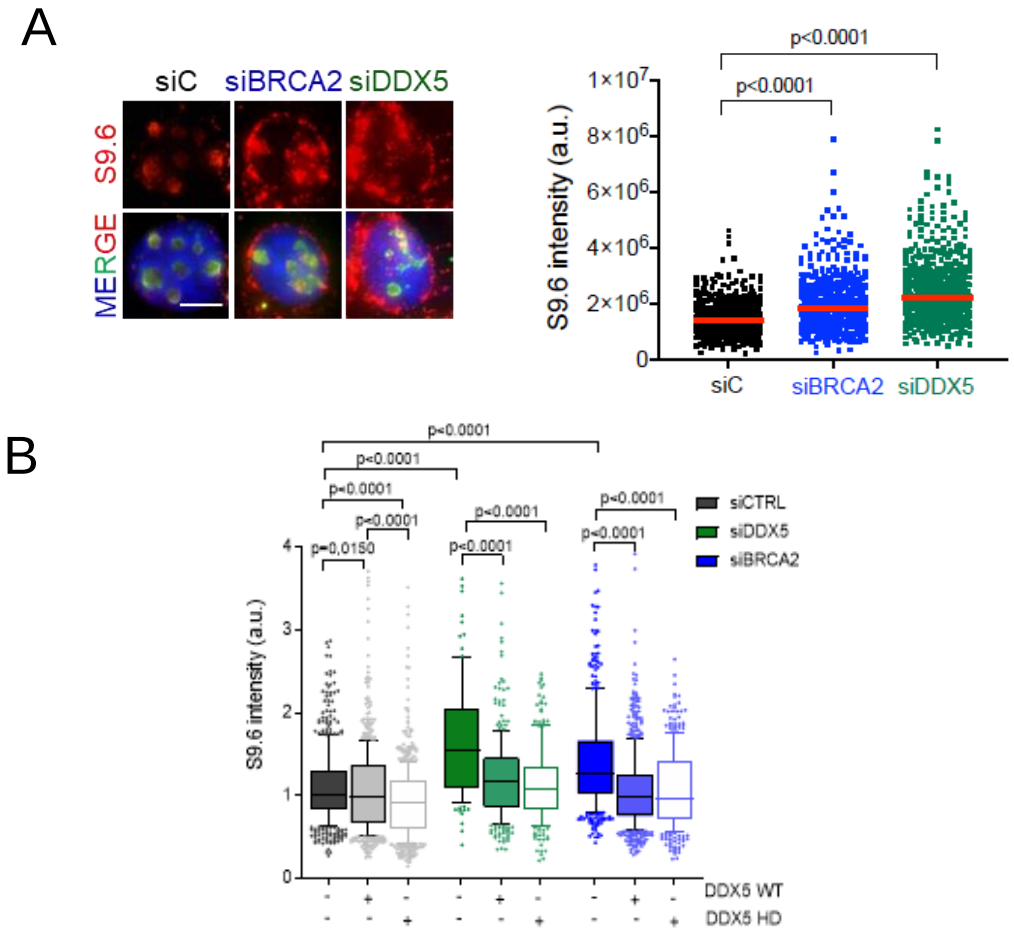

Figure 4. Depletion of BRCA2 and DDX5 leads to accumulation of DNA-RNA hybrids. (A) Representative immunofluorescence images of U2OS cells depleted of DDX5 (siDDX5), BRCA2 (siBRCA2) or control cells (siC) and stained with the DNA-RNA hybrid antibody S9.6. Scale bar indicates 10 µm. Right: Quantification of the relative intensity of S9.6 staining. The data represent at least 500 cells per condition from three independent experiments. The median, 10th to 90th centile range (boxes and whiskers) are plotted. For statistical comparison of the differences between the samples we applied a t test. The p-values show significant differences. **(B)** Quantification of S9.6 immunofluorescence of U2OS cells depleted of BRCA2 (siBRCA2), DDX5 (siDDX5) or control cells (siC) expressing either DDX5-GFP or DDX5-HD-GFP. The red line in the plot indicates the median, each symbol represents the value of a single cell. The statistical significance of the difference was calculated with Mann-Whitney U-test; the p-values show the significant difference. The data represent at least 235 cells per condition from three independent experiments

.

DDX5 depletion have been reported to increase replication stress sensitivity[264]. Because unscheduled DNA-RNA hybrids represent a barrier for replication[182, 218, 219] we tested whether DDX5 associated with DNA-RNA hybrids in replicating cells. We labelled U2OS cells with EdU to monitor replicating cells and performed *in situ* PLA using anti-DDX5 and anti-S9.6 primary antibodies.

Our data revealed that DDX5 associates with DNA-RNA hybrids and this is dependent on transcription (Fig. 5A); However, the association with the hybrids was independent of replication, since both EdU and non-stained cells displayed similar levels of DDX5-S9.6 PLA signal (Fig. 5B). The PLA signal for DNA-RNA hybrids was specific since it was sensitive to RH overexpression.

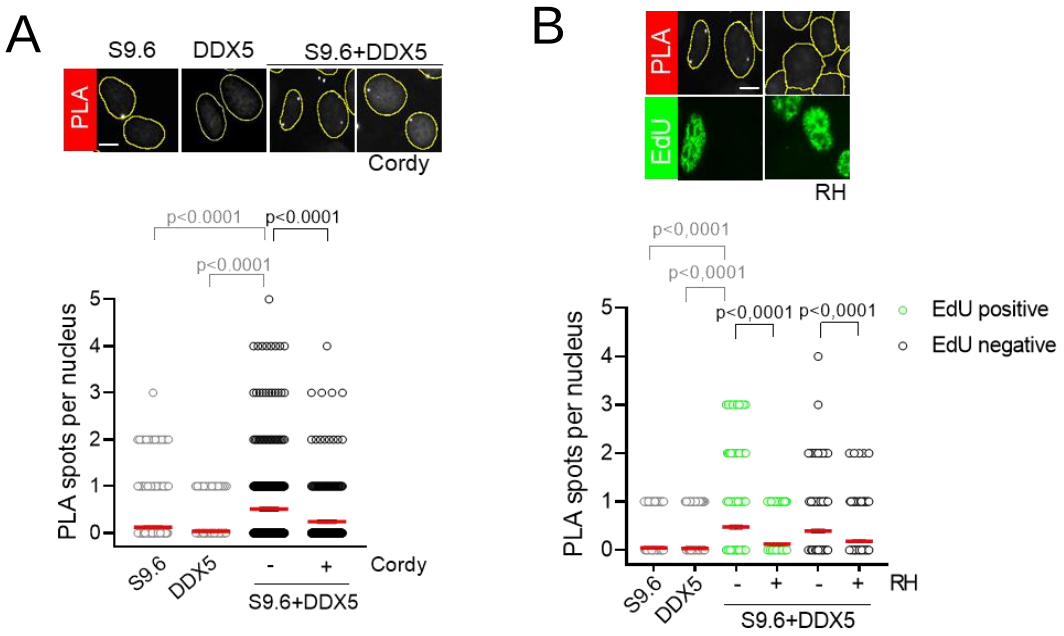

Figure 5. DDX5 associates with DNA-RNA hybrids (A) Representative images of *in situ* PLA experiment performed between DDX5 and S9.6 antibodies in U2OS cells. When indicated, cells were treated with Cordycepin (Cordy) for 2h at 37°C before fixation. Single antibody controls from untreated cells are shown. Scale bar indicates 10 µm. Right: Quantification of the number of PLA spots per nucleus in different conditions, as indicated. The data represent at least 200 cells per condition from three independent experiments. **(B)** Representative images of *in situ* PLA from U2OS cells stained for DDX5 and S9.6 (DNA-RNA hybrids) antibodies in EdU or non-EdU stained cells. Scale bar indicates 10 µm. Bottom: Bottom: Quantification. At least 300 cells per condition were counted from three independent experiments. For **(A)** and **(B)** quantifications statistical comparison of the differences between the samples was performed applying a Kruskal-Wallis test followed by Dunn's multiple comparison test, the p-values show significant differences. The red line in the plot indicates the median, each symbol represents a single PLA

To analyse the genome-wide effect of DDX5 depletion on DNA-RNA hybrids, our collaborators from A. Aguilera's lab (CABIMER, Sevilla) performed a DRIPc-seq experiment providing high-resolution, strand-specific profiling[194].

Meta-plot analysis of the strand-specific composite profile across the average gene body in both Watson and Crick strands in K562 cells (Fig. 6A, B) revealed an enrichment of DNA-

RNA hybrids at the 3' end of the sense strand, corresponding to transcription throughout the gene body, as well as at the promoters, as previously reported [194, 288]. Importantly, DDX5-depleted cells exhibited similar overall distribution pattern of hybrids, but the levels

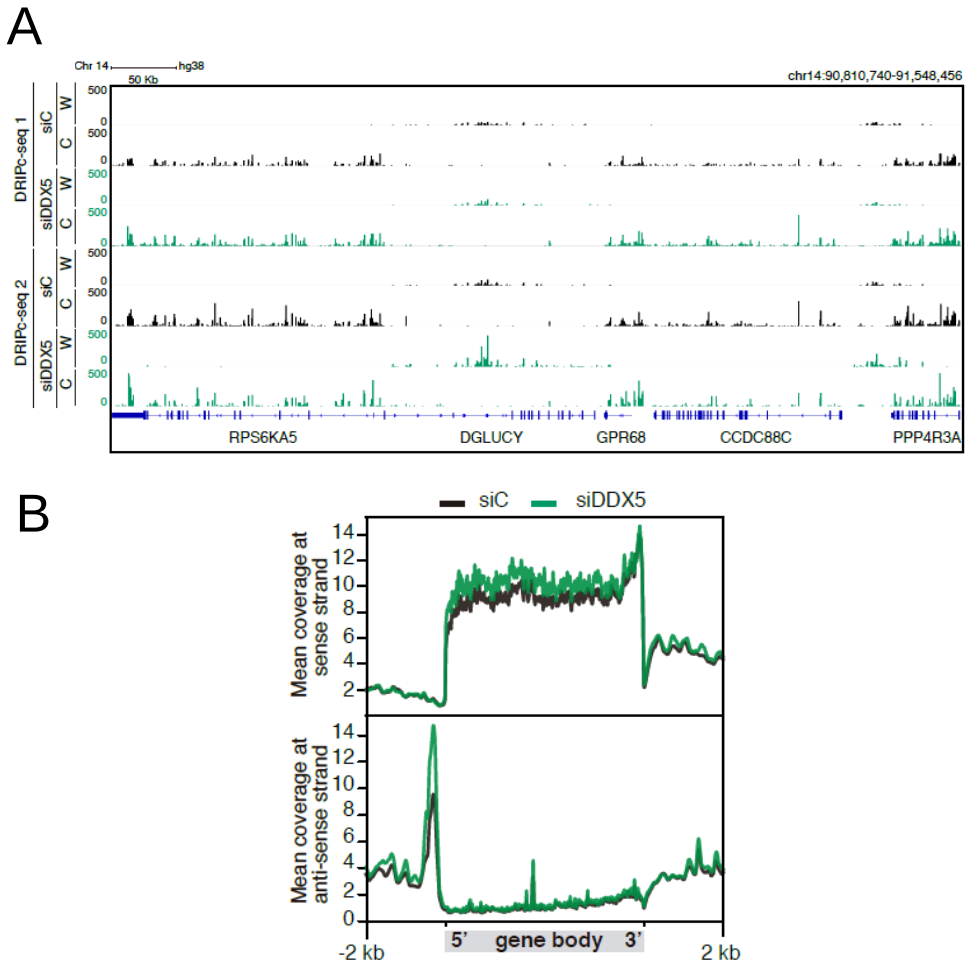

Figure 6. Depletion of DDX5 triggers a genome-wide increses of DNA-RNA hybrids. (A) Representative screenshot of a specific genomic region showing DRIPc-seq profiles at Watson (W) and Crick (C) strands in K562 cells depleted of DDX5 (siDDX5) or control cells (siC) from two independent experiments. The siC data were obtained from (GEO, GSE127979)[288]. **(B)** DNA-RNA hybrid distribution along protein-coding genes. Gene metaplot representing the mean of antisense and sense DRIPc-seq signal from two independent experiments in K562 cells depleted of DDX5 (siDDX5) or control cells (siC).

were consistently higher than those obtained with control cells. Therefore, DDX5 depletion leads to a genome-wide increase in the DNA-RNA hybrids along gene bodies, in agreement with the several RNA metabolism processes in which it is involved[271].

We next wondered whether DNA-RNA hybrids observed in the absence of DDX5 were enriched at DSBs sites. Therefore, our collaborators (coll. A. Aguilera, CABIMER,

Sevilla) compared to a previously reported γH2AX ChIP-seq analysis performed in the same K562 cells[289]. Interestingly, the signal obtained in the DRIPc-seq was enriched in DDX5-depleted cells around γH2AX ChIP-seq peaks (Fig. 7A), suggesting that DNA-RNA hybrid accumulation at break-prone sites is enhanced by the loss of DDX5. Moreover, the overlap of DNA-RNA hybrids and γH2AX -enriched regions was almost two-fold higher in DDX5-depleted cells compared to the control cells (Fig. 7B) (from 12% in siC cells to 22% in siDDX5 cells). These results indicate that DNA-RNA hybrids that arise upon DDX5 depletion are enriched in the vicinity of DSBs.

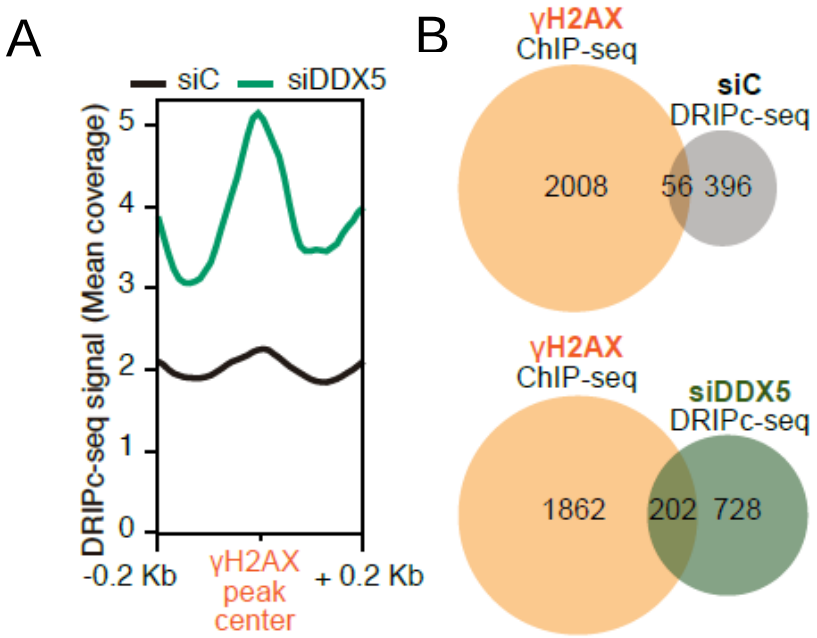

Figure 7. DDX5-depleted cells exhibit DNA-RNA hybrids in the vicinity of DSBs. (A) DNA-RNA hybrid metaplot distribution over γH2AX ChIP-seq peaks, calculated from (GEO, GSE104800)[289]. Peak metaplot shows the mean of the DRIPc-seq signal from two independent experiments in K562 cells depleted of DDX5 (siDDX5) or control cells (siC). **(B)** Venn diagram representing the overlap between γH2AX-positive genes in K562 cells (γH2AX ChIP-seq) and genes that specifically accumulate hybrids in control cells (top) or in DDX5- depleted cells (bottom).

In agreement, *in situ* PLA using S9.6 and anti- γH2AX antibodies performed in DDX5- or BRCA2- depleted U2OS cells showed a two-fold increase in the number of DNA-RNA hybrids associated with DSBs compared to control cells. The signal was sensitive to RH overexpression and Cordycepin treatment (Fig. 8A), suggesting that both BRCA2 and

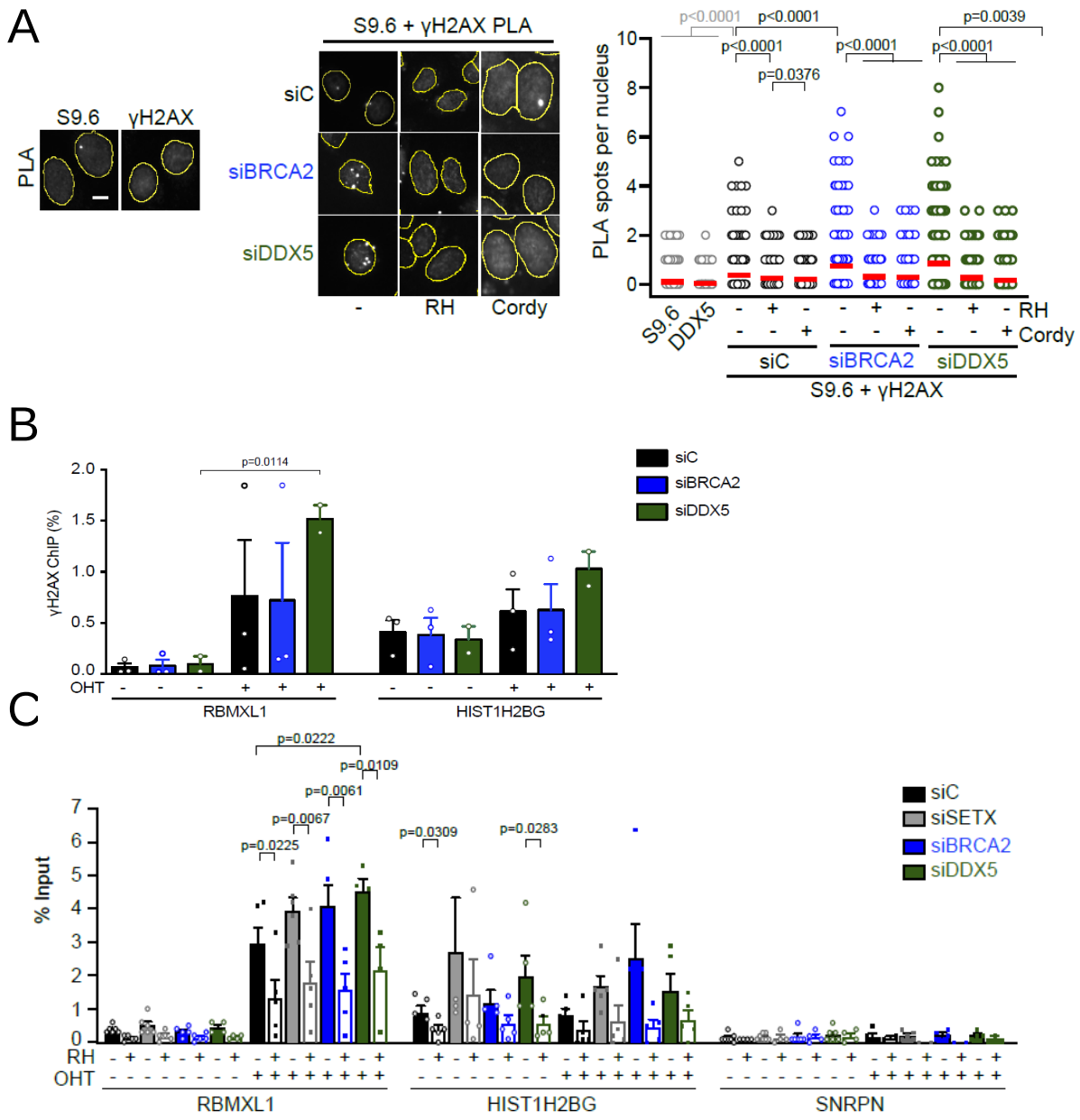

Figure 8. DDX5- and BRCA2-depleted cells accumulate DNA-RNA hybrids at DSBs sites. (A) Left: Representative images of *in situ* PLA between S9.6 and γH2AX antibodies in U2OS cells depleted of BRCA2 (siBRCA2), DDX5 (siDDX5) or control cells (siC). When indicated, cells were transfected with RNase H1 (RH) 24h before or treated with Cordycepin (Cordy) for 2h at 37°C before fixation. Single antibody controls from non-irradiated siC cells are shown. Scale bar indicates 10 µm. Right: Quantification of PLA spots per nucleus in each condition as indicated. At least 300 cells per condition were counted from three independent experiments For statistical comparison of the differences between the samples we applied a Kruskal-Wallis test followed by Dunn's multiple comparison test, the p-values show significant differences. The red line in the plot indicates the median, each symbol represents a single PLA spot. **(B)** γH2AX ChIP-qPCR signal values at RBMXL1 and HIST1H2BG loci in U2OS DiVA cells transfected with the indicated siRNAs and either untreated cells (-OHT) or after tamoxifen addition (+OHT). The data represent the mean ± SEM from at least two independent experiments. The statistical significance of the difference was calculated with unpaired t-Student test; the p-values show the significant difference. **(C)** Relative DRIP-qPCR signal

values at *RBMXL1*, *HIST1H2BG* and *SNRPN* loci in U2OS cells transfected with the indicated siRNAs and treated *in vitro* with RNase H1 (RH) pre-immunoprecipitation where indicated. The experiment was performed in both untreated cells (-OHT) and after tamoxifen addition (+OHT). The data represent the mean ± SEM from at least four independent experiments. The statistical significance of the difference was calculated with unpaired t-test; the p-values show the significant difference.

DDX5 depletion lead to a transcription-dependent increase in DSBs-associated DNA-RNA hybrids. However, these data do not discriminate between DNA-RNA hybrids causing DNA damage from those arising upon DNA break induction thus, we next performed a DRIP experiment in the U2OS DIvA cell system[259] (coll. A. Aguilera, CABIMER, Sevilla). In these cells, around 100 DSBs, marked by γH2AX, are generated by the restriction enzyme AsiSI at specific sites upon treatment with tamoxifen (OHT). The analysis was focused on the *RBMXL1* gene containing an AsiSI cut-site and a control gene, *HIST1H2BG*, not containing an annotated AsiSI cut-site but that was previously shown to accumulate spontaneous DNA-RNA hybrids upon DDX5 loss[264]. Both of these genomic loci are highly transcribed, thus prone to DNA-RNA hybrids. Chromatin-Immunoprecipitation (ChIP) using anti- γH2AX antibody confirmed the induction of DNA damage upon OHT treatment at the *RBMXL1* locus but not at the *HIST1H2BG* locus, as expected (Fig. 8B). In agreement with previous reports, depletion of Senataxin (SETX) or of BRCA2 caused an increase on DNA-RNA hybrids levels in *RBMXL1* locus upon OHT treatment compared to control cells[189, 260]. Interestingly, DDX5- depleted cells also showed a significant increase (Fig. 8C). In all these conditions, RH treatment strongly reduced DRIP signal confirming its specificity. By contrast, no significant increase in hybrids was observed in *HIST1H2BG* gene or at the non-transcribed locus *SNRPN* upon OHT treatment. Altogether, these data indicate that BRCA2- and DDX5-depleted cells accumulate DNA-RNA hybrids particularly at DSB sites.

These results raised the question as to whether DDX5 was recruited to DNA damage sites and if so, whether BRCA2 could affect its retention at these regions. Therefore, we performed a laser micro-irradiation (405 nm) experiment in Hoechst 33258-sensitized U2OS cells transiently expressing DDX5-GFP to follow the localization of DDX5 within the nucleus upon DNA damage induction in real time. This system has been extensively reported in the literature to monitor the recruitment of DDR proteins and RBPs at DNA damage sites[285, 290]. To assess the efficiency of our system, we monitored the recruitment of the early marker of DSBs GFP-53BP1. As expected, GFP-53BP1 signal re-localized at laser tracks within 2 min post-irradiation and the signal at the tracks increased over time

reaching a maximum at around 10 min post-irradiation (Fig. 9). Prior laser irradiation, DDX5-GFP showed a nuclear pattern, as previously reported[291], although some stronger signal could be found at nucleolar regions, probably due to its overexpression (Fig. 9). However, in contrast to GFP-53BP1, DDX5-GFP signal disappeared specifically from the DNA damage tracks in a pattern defined as "anti-stripe" already reported for other RBPs and DEAD-box proteins[285, 292, 294] (Fig. 9) (coll. S. Vagner, Institut Curie, Orsay).

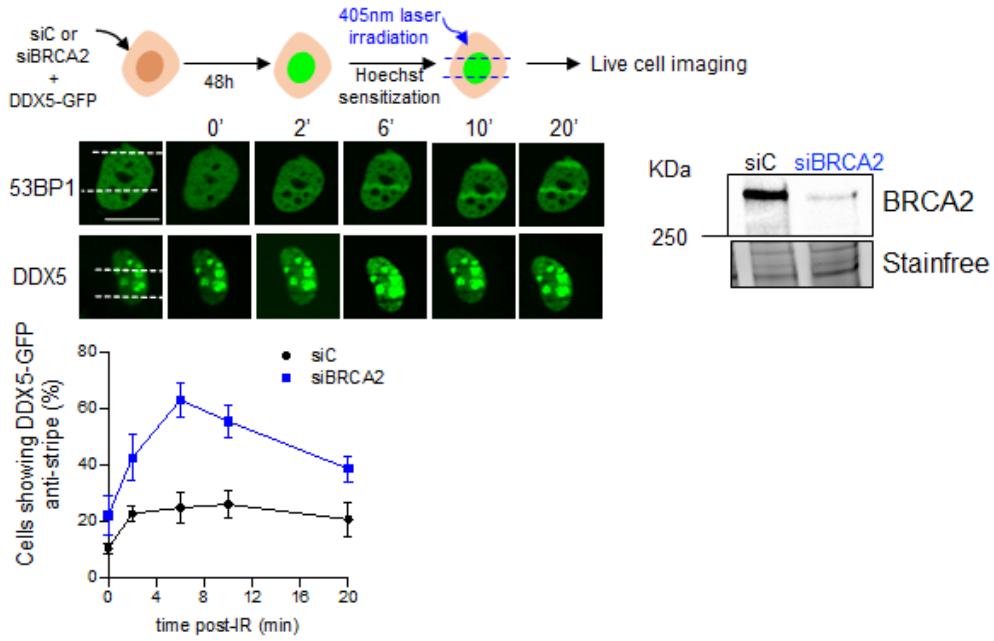

Figure 9. BRCA2 enhances DDX5 retention at DNA damage. Top: Scheme showing the experimental set up for laser irradiation in DDX5-GFP transfected U2OS cells depleted of BRCA2 (siBRCA2) or control cells (siC). Bottom left: Western blot showing the siRNA mediated knock-down of BRCA2 from U2OS cells transfected with DDX5-GFP. Bottom right: Live cell imaging of the recruitment of GFP-53BP1 or DDX5-GFP to DNA damage tracks at different time points as indicated. Exposure and processing were adjusted to best demonstrate stripes and anti-stripes. Scale bar indicates 10 µm. Right: Quantification of the recruitment of DDX5-GFP showing the percentage of transfected cells that exhibit DDX5-GFP "anti-stripe" pattern at DNA damage tracks at the times indicated in cells depleted of BRCA2 (siBRCA2) or treated with control siRNA (siC). The data represent the mean ± SEM from three independent experiments.

The analysis of cells showing anti-stripe pattern out of the total of DDX5-GFP positive cells revealed that up to 25% of the cells showed this pattern 10 min after irradiation whereas the rest of the cells presented pan-nuclear DDX5-GFP staining. Importantly, BRCA2 depletion led to 63% of cells with anti-stripe pattern already at 6 minutes post-irradiation (Fig. 9).Thus, only 37 % of the cells retained DDX5 at the laser tracks in BRCA2- depleted cells compared to the 75% in cells expressing BRCA2. This phenotype could be explained by the fact that DDX5 has been found important for transcription

regulation in response to DNA damage[279]; thus, DDX5 could be excluded from laser tracks following transcription silencing occurring upon induction of DNA damage[293, 294] and BRCA2 could have a role in retaining or re-localizing it at laser-induced DNA damage sites.

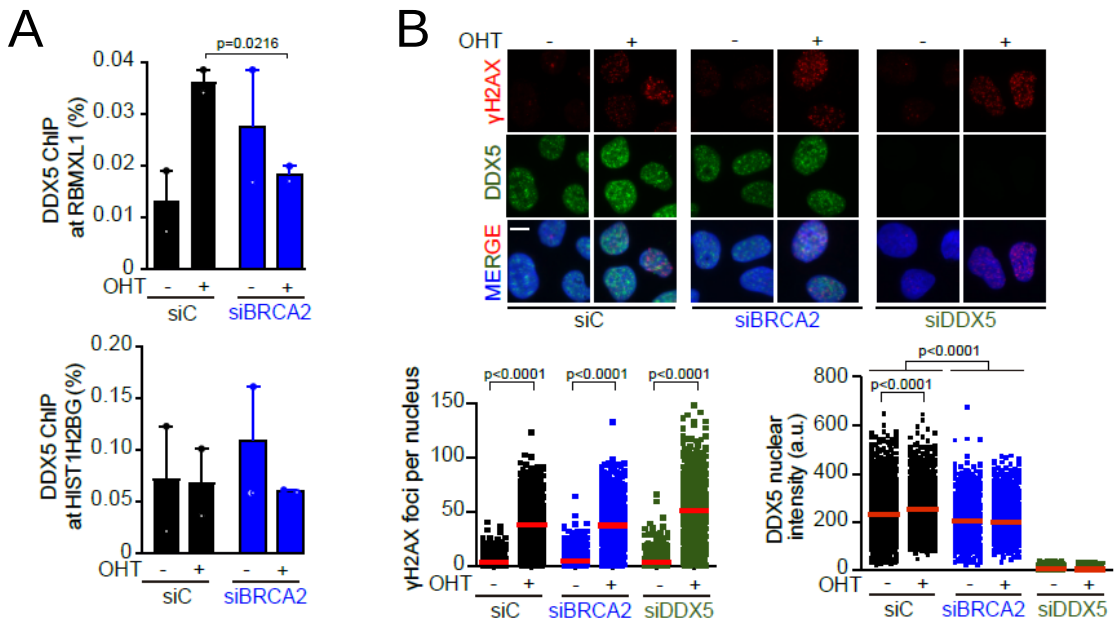

Figure 10. DDX5 localization at induced DSBs is dependent on BRCA2. (A) Relative DDX5 ChIP-qPCR signal values at *RBMXL1* and *HIST1H2BG* loci in U2OS cells transfected with the indicated siRNAs and either untreated cells (-OHT) or after tamoxifen addition (+OHT). The data represent the mean ± SEM from at least four independent experiments. The statistical significance of the difference was calculated with unpaired t-Student test; the p-values show the significant difference. **(B)** Top: Representative images of immunofluorescence of U2OS cells depleted of BRCA2 (siBRCA2), DDX5 (siDDX5) or control cells (siC) and either untreated cells (-OHT) or after tamoxifen addition (+OHT), as indicated. Bottom: Quantification of the number of γH2AX foci per nucleus (left) and DDX5 nuclear intensity (right). The data represent at least 800 cells per condition from three independent experiments. The red line in the plot indicates the median, each symbol represents the value of a single cell. The statistical significance of the difference was calculated with Mann-Whitney U-test; the p-values show the

To further investigate this possibility, we monitored the presence of DDX5 directly at DSBs by ChIP using again the U2OS DIvA cell system[259], (coll. A. Aguilera, CABIMER, Sevilla). Again, the two genomic loci *RBMXL1* and *HIST1H2BG* were used in order to compare DDX5 occupancy at induced DSBs. The occupancy of DDX5 at the *RBMXL1* gene increased upon DSB induction (+OHT) in control cells. Importantly, this increase was not observed in BRCA2-depleted cells (Fig. 10 A). Moreover, DDX5 was not enriched at

the control *HIST1H2BG* gene, where there is no AsiSI cut site (Fig. 10 A). Furthermore, we measured the nuclear fluorescence intensity of endogenous DDX5 in cells depleted of BRCA2 in the same cells to determine any difference upon DNA damage induction. DSB induction via OHT treatment resulted in an increased number of γH2AX foci in all cells; although more γH2AX foci were observed in DDX5-depleted cells compared to control cells in agreement with a previous report[264] (Fig. 10 B). In addition, the nuclear intensity of DDX5 increased upon DSB induction in control cells whereas it remained unchanged in BRCA2-depleted cells (Fig. 10 B). Thus, these results suggest that DDX5 nuclear localization increases upon DNA damage in a BRCA2- dependent manner (coll. A. Aguilera, CABIMER, Sevilla). Taken together, these data indicate a role of BRCA2 in promoting DDX5 retention at DNA damage sites.

The unwinding activity of DDX5 on dsRNA is well documented[272-274], more recently, DDX5 has been shown to unwind R-loops and DNA-RNA hybrids *in vitro*[264, 265] and these findings suggest that the role of DDX5 in processing DNA-RNA hybrids in cells could be mediated by this helicase activity. Thus, we decided to assess whether DDX5 unwinding activity on R-loops could be affected by BRCA2. For this purpose, we used purified MBP-DDX5-GST (Fig. 3C) and we purified full length BRCA2 from HEK293T cells using the construct GFP-MBP-BRCA2 and following our standard protocol, as described above (Fig. 3B left panel) (Fig. 11A. The unwinding assays were performed using synthetic radiolabeled R-loops substrates. Increasing concentrations of DDX5 (1-5 nM) were incubated with the substrate for 30 min in a reaction containing Mg^{2+} and ATP: Our results show that, under these conditions, DDX5 is able to unwind up to 40% of the total R-loop substrate added in the reaction, as measured by the release of free radiolabeled RNA, in agreement with a previous report[264]. Importantly, adding 2 nM of purified full length BRCA2, the unwinding activity of DDX5 was enhanced, reaching 80% of the total R-loop substrate unwound. These results suggest that BRCA2 promotes DDX5 unwinding activity (Fig. 11B). To further investigate whether the DDX5-interacting region of BRCA2 was sufficient to stimulate DDX5 helicase activity, we performed a similar assay, this time adding purified $BRCA2_{T1}$ fragment to the reaction (Fig. 3B). Interestingly, similarly to full length BRCA2, $BRCA2_{T1}$ was able to stimulate DDX5 unwinding activity up to 70% (Fig. 11C). However, higher concentration of $BRCA2_{T1}$ (50 nM) was required compared to BRCA2 full length (2 nM) to get similar stimulation. This is probably due to the disordered

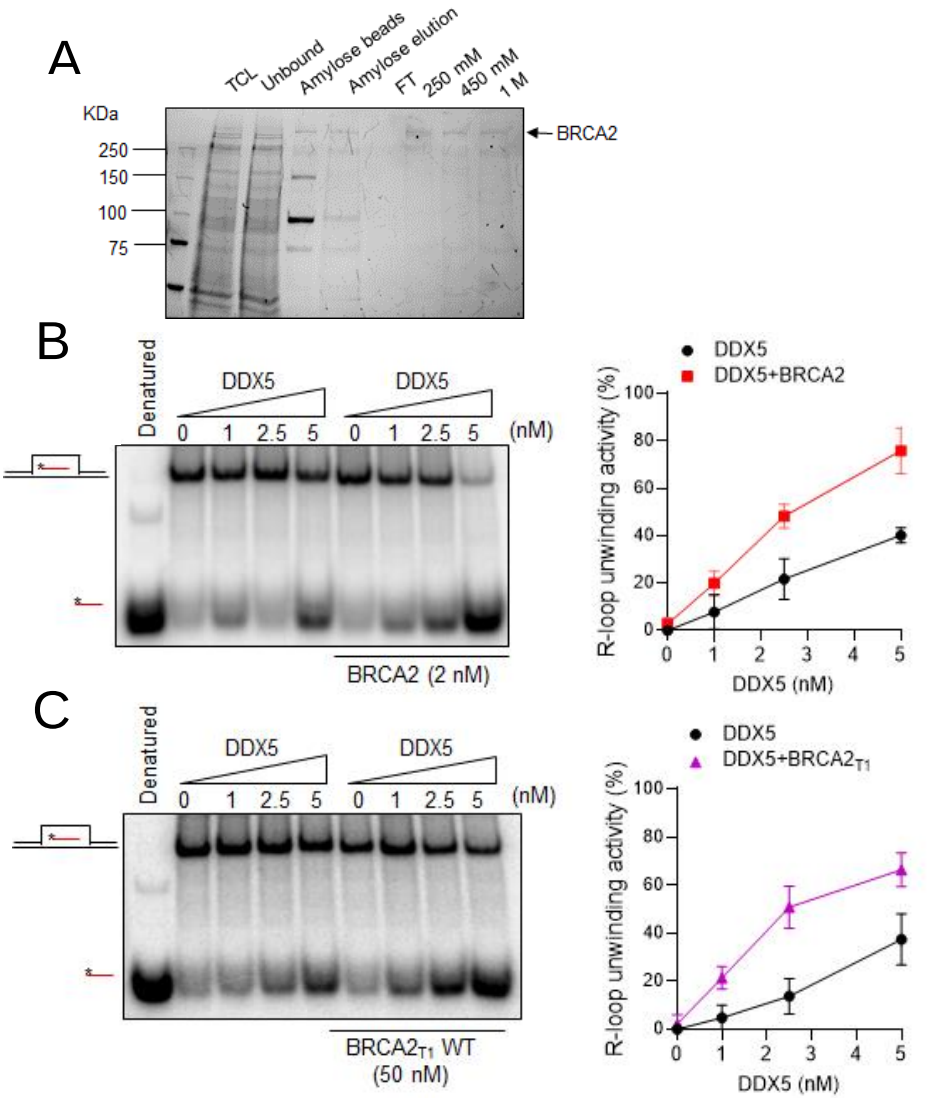

Figure 11. BRCA2 stimulates the R-loop unwinding activity of DDX5. (A) SDS PAGE gel showing purified full-length EGFP-MBP-BRCA2**. (A) (B)** Left: PAGE gel showing a representative unwinding assays in which purified MBP-DDX5-GST (1-5 nM) was incubated with ^{32}P – labelled synthetic R-loop substrate in presence or absence of 2 nM purified EGFP-MBP-BRCA2 **(B)** or 50 nM purified BRCA2$_{T1}$ **(C)**. Right: Quantification of the unwinding experiments showing the percentage of free RNA relative to the R-loop substrate (unwound product) as a function of DDX5 concentration alone (black) or in presence of BRCA2 **(A)** or BRCA2$_{T1}$ **(B)**. The data represent the mean ± SD of at least three independent experiments.

nature of isolated BRCA2 N-terminal region[90]. Altogether, these results demonstrate that BRCA2 is able to stimulate the R-loop unwinding activity of DDX5 and this activity requires the first 250 aa of BRCA2. Moreover, as previously shown in a work from our lab, BRCA2$_{NT}$ contains a N-terminal DNA binding domain comprised in BRCA2$_{T2}$ (250-500 aa). Therefore, the helicase stimulatory function of BRCA2 we observe probably

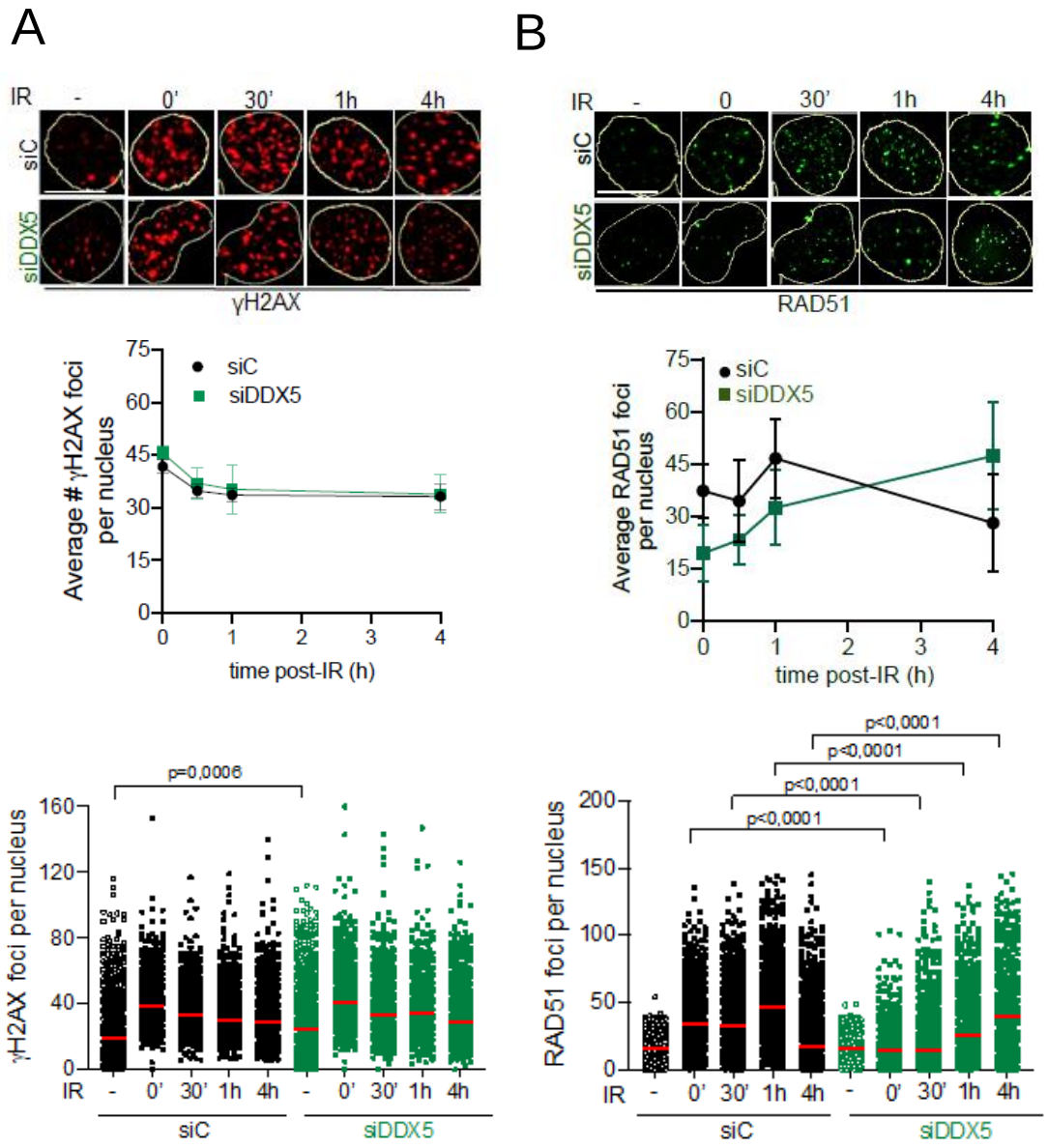

Figure 12. DDX5 favors DSBs repair by homologous recombination. Top: Representative immunofluorescence images of cells stained for γ-H2AX **(A)** and RAD51 **(B)** in U2OS cells depleted of DDX5 (siDDX5) and in control cells (siC) in non-treated (NT) or different time points after exposure to IR (6Gy), as indicated. Scale bar indicates 10 µm. Bottom: Graphs showing the average number of γ-H2AX **(A)** and RAD51 **(B)** repair foci and distribution of number of foci per nucleus in both cell lines. The data represent the mean ± SEM of three independent experiments, whereas in distribution graphs the red line represents the median. At least 500 cells per condition were counted from three independent experiments. For statistical comparison of the differences between the samples we applied a Kruskal-Wallis test followed by Dunn's multiple comparison test, the p-values show significant differences

depends on protein-protein interaction with DDX5 rather than on BRCA2 ability to bind DNA.

Finally, as several studies have reported that DNA-RNA hybrids formed at DSBs could

affect HR-mediated repair, we aimed to assess the possible impact of the DNA-RNA hybrid accumulation at DSBs induced by DDX5 depletion on their repair. For this purpose, DDX5-depleted and control U2OS cells were exposed to γ-irradiation (6 Gy) at different time points. After fixation, an immunostaining for detection of γH2AX and RAD51 was conducted to evaluate the efficiency of DSB repair via HR. As expected, the number of γH2AX foci increased upon irradiation in both control and DDX5-depleted cells (Fig. 12A). Interestingly, DDX5-depleted cells showed an increased number of γH2AX foci in untreated conditions compared to control cells indicating DDX5 depletion triggers DNA damage, as shown above (Fig. 10B) and as reported[264]. Importantly, the kinetics of RAD51 recruitment was strongly altered in DDX5-depleted cells: Control cells reached a maximum of RAD51 foci number 1 hour after irradiation and started recovering 4 hours post-irradiation. In contrast, 4 hours were required to reach the same levels in DDX5-depleted cells indicating a delayed recruitment of RAD51 and HR-mediated DSBs repair (Fig. 12B).

2.3. OBJECTIVE 3

Examine the effect of disrupting BRCA2-DDX5 interaction on DNA-RNA resolution and on DSBs repair by HR

Based on the mapping of BRCA2-DDX5 interaction to the first 250 aa of BRCA2 ($BRCA2_{T1}$) we next seek to find BRCA2 breast cancer variants localized in this region that could alter the interaction to examine its impact in cells and on the helicase activity of DDX5.

We chose T207A, a variant of unknown significance (VUS) that alters a highly conserved residue already characterized in the lab in the context of mitosis[84]. Interestingly, DLD1 cells stably expressing BRCA2-T207A displayed high levels of R-loops as detected by S9.6 fluorescence intensity (Fig. 13A) (coll. with A. Aguilera). This was further confirmed by DNA-RNA hybrid immunoprecipitation (DRIP) at *HIST1H2BG* genomic locus which was sensitive to RH treatment (coll. A. Aguilera) (Fig. 13B). As observed before for U2OS cells depleted of BRCA2 (Fig. 4A) and in agreement with the literature[187], DLD1 BRCA2-deficient cells accumulated DNA-RNA hybrids (Fig. 13C).

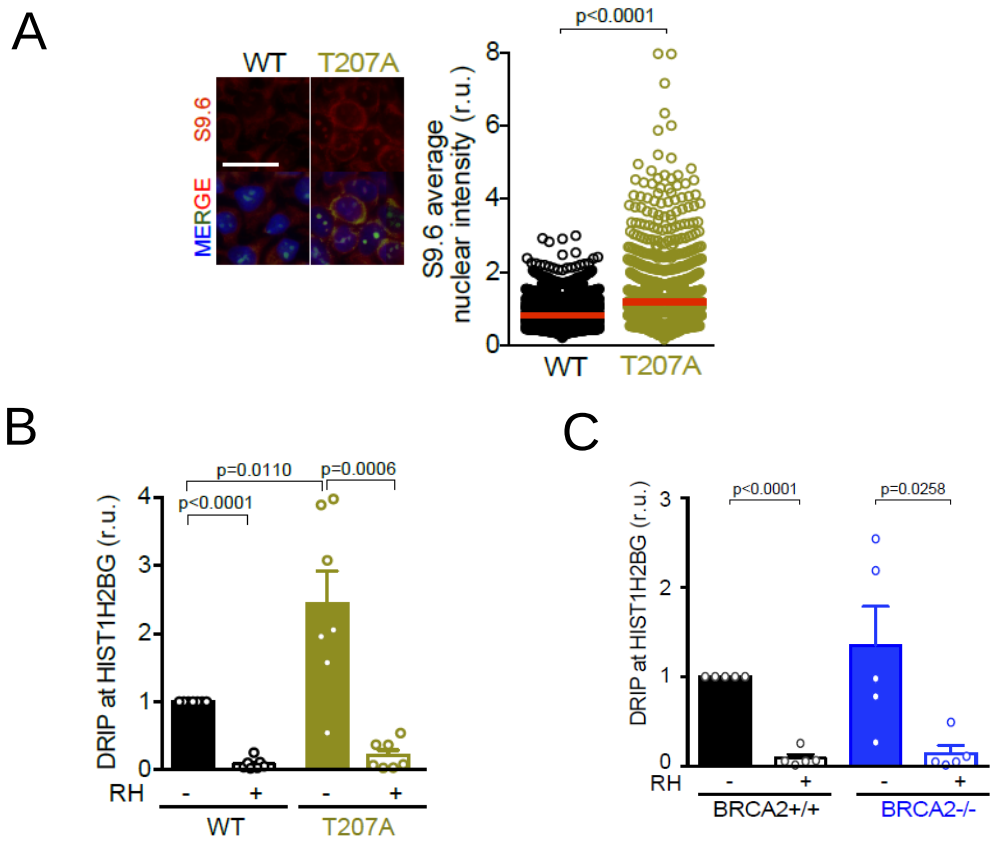

Figure 13. Cells bearing BRCA2 T207A mutation show accumulation of DNA-RNA hybrids. (A) Left: Representative images of S9.6 immunofluorescence of DLD1 cells bearing BRCA2 (WT) or BRCA2-T207A (T207A). The merged images show the signal of S9.6, nucleolin (nucleoli) antibodies and DAPI staining. Scale bar indicates 25 µm. Right: Quantification of the relative intensity of S9.6 staining. The data represent at least 500 cells per condition from three independent experiments. The median, 10th to 90th centile range (boxes and whiskers) are plotted. For statistical comparison of the differences between the samples we applied a t test. The p-values show significant differences. **(B) (C)** Relative DRIP-qPCR signal values at the *HIST1H2BG* loci in DLD1 cells bearing BRCA2 (WT) and BRCA2-T207A (T207A) **(A)** or $BRCA2^{+/+}$ and $BRCA2^{-/-}$ DLD1 cells **(B)**. pre-IP cells were treated *in vitro* with RNase H1 (RH) when indicated. The data represent the mean ± SEM from at least seven independent experiments. The statistical significance of the difference was calculated with unpaired t-Student test; the p-values show the significant difference.

Next, using DLD1 cells stably expressing GFP-tagged BRCA2 WT and BRCA2-T207A we conducted a GFP-trap pull-down from whole cell extracts to assess whether T207A could alter BRCA2-DDX5 interaction.

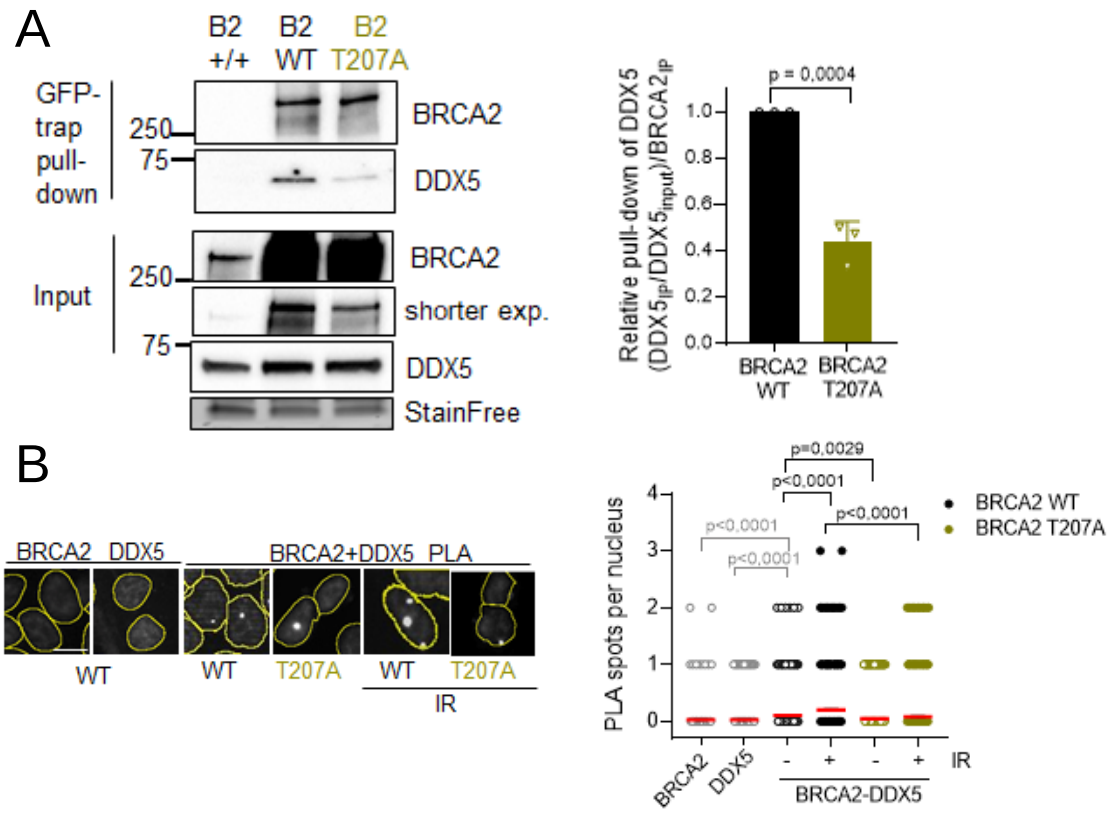

Figure 14. Cells bearing BRCA2-T207A show reduced BRCA2 interaction with DDX5 (A) Left: GFP pull-down assay from whole cells extracts of BRCA2 deficient DLD1 expressing BRCA2 (WT) or the variant T207A (T207A). DLD1 BRCA2$^{+/+}$ (+/+) cell extracts are used as control for the GFP-trap. DDX5 and BRCA2 were detected with specific antibodies against DDX5 and BRCA2, respectively. StainFree images of the gels before transfer was used as loading control (cropped image is shown). Right: Quantification of the GFP-trap pull-down experiments calculated as the co-immunoprecipitated DDX5 with either BRCA2 WT or BRCA2-T207A relative to the input levels of DDX5 and the amount of immunoprecipitated EGFPMBP-BRCA2. Results are presented as the fold change compared to the BRCA2 WT clone. The data represents the mean ± SD of three independent experiments. Statistical significance of the difference was calculated with unpaired t test; the p-values show the significant difference. **(B)** Left: Representative images of *in situ* PLA performed with antibodies for DNA-RNA hybrids (S9.6) and γH2AX in BRCA2 deficient DLD1 cells (BRCA2$^{-/-}$) expressing BRCA2 WT or the variant T207A, as indicated. When indicated, cells were transfected with RNAseH1 (RH) 24h before or treated with Cordycepin (Cordy) for 2h at 37°C before fixation. Single antibody controls from untreated BRCA2 WT cells are shown. Scale bar indicates 10 µm. Right: Quantification of the number of PLA spots per nucleus. At least 400 cells were counted per condition from three independent experiments. For statistical comparison of the differences between the samples we applied a Kruskal-Wallis test followed by Dunn's multiple comparison test, the p-values show significant differences. The red line in the plot indicates the median, each symbol represents a single PLA spot.

As shown in Fig. 14A, although the protein levels of BRCA2 were variable (see INPUT),

the amount of pull-down BRCA2 protein was equivalent in the two samples (GFP-trap pull-down). As a control for specificity we used DLD1 parental cells that express endogenous BRCA2 ($BRCA2^{+/+}$). According to what we demonstrated in HEK293T cells (Fig. 2B), we confirmed that BRCA2 and DDX5 form a complex also in DLD1 cell line. Importantly, the levels of DDX5 pull-down with BRCA2-T207A were reduced to almost half as compared to BRCA2 WT expressing cells, as indicated in the quantification (Fig. 14A). To further confirm these results, we performed an *in situ* PLA using anti-BRCA2 and anti-DDX5 antibodies in DLD1 cells stably expressing BRCA2-WT or BRCA2-T207A left untreated or exposed to IR (6 Gy) 4 hours before fixation. In agreement with the PLA results in U2OS cells (Fig. 2C), we confirmed in DLD1 cell line that BRCA2 and DDX5 are in close proximity in the nucleus and that DNA damage induced by irradiation enhances this co-localization (Fig. 14B). Importantly, PLA analysis also indicated that the co-localization between BRCA2 and DDX5 was reduced in cells bearing BRCA2-T207A variant compared to BRCA2-WT and that the difference was more pronounced upon irradiation.

Taken together, these findings suggest that the interaction of BRCA2 with DDX5 is affected in cells expressing the breast cancer variant of BRCA2-T207A.

Given that BRCA2-T207A expressing cells accumulate R-loops and that BRCA2-DDX5 interaction is reduced in these cells, we tested whether DDX5 association with DNA-RNA hybrids was also affected in these cells which would support an active role of BRCA2 in this context. As shown with U2OS cells, *in situ* PLA with s9.6 and anti-DDX5 antibodies revealed that DDX5 associate with hybrids in DLD1 cells. In contrast, BRCA2-deficient DLD1 cells ($BRCA2^{-/-}$) exhibited very low PLA signal compared to DLD1 BRCA2 WT expressing cells suggesting that BRCA2 may indeed play a role in DDX5 localization at DNA-RNA hybrids (Fig. 15A). More importantly, BRCA2-T207A expressing cells displayed a reduction of PLA spots compared to BRCA2 WT upon irradiation (6Gy, 4h), similar to $BRCA2^{-/-}$, suggesting that the impaired interaction with DDX5 leads to a defect in the association of DDX5 with DNA-RNA hybrids in irradiated conditions. Given that BRCA2- and DDX5-depleted U2OS cells accumulate DNA-RNA hybrids at DSBs (Fig. 8A), we tested if this was the case in DLD1 BRCA2-T207A cells. Interestingly, DLD1 T207A expressing cells also displayed increased levels of DNA-RNA hybrids associated with DSBs as detected by PLA using S9.6 and anti- γH2AX antibodies. The signal was specific as it was sensitive to RH overexpression and Cordycepin treatment (Fig. 15B).

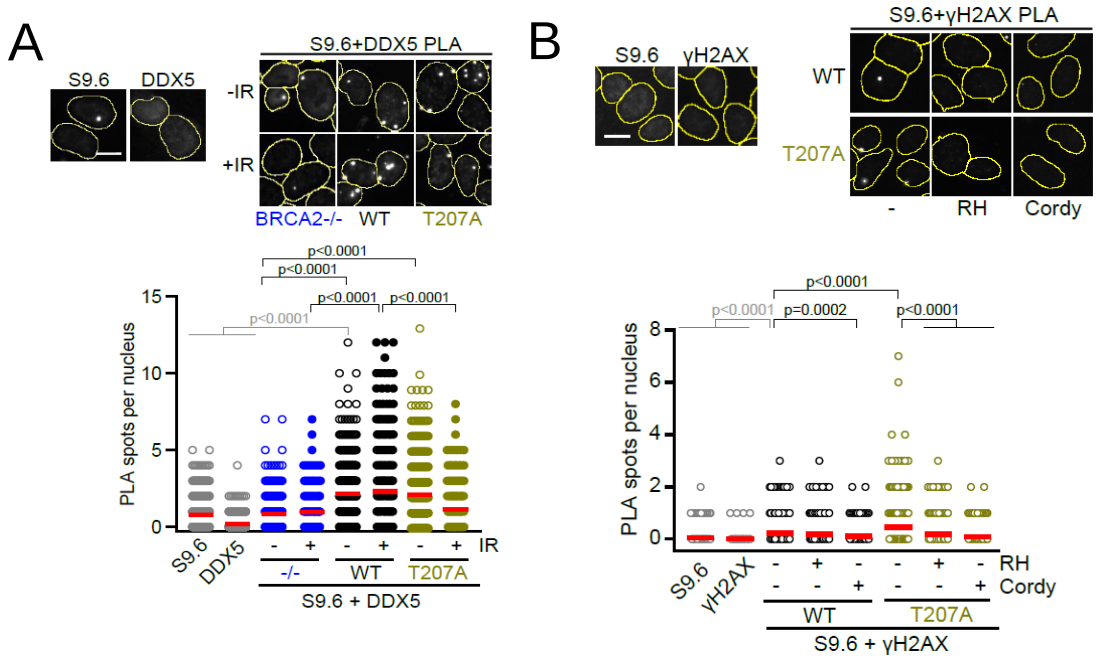

Figure 15 BRCA2-DDX5 disrupted interaction leads to increased DSB-associated DNA-RNA hybrids. (A) Representative images of *In situ* PLA performed between DDX5 and S9.6 (DNA-RNA hybrids) antibodies in BRCA2 deficient DLD1 cells (BRCA2$^{-/-}$) or cells bearing BRCA2 (WT) or BRCA2-T207A (T207A), as indicated. Cells were fixed directly or 4h post-irradiation (6Gy). Single antibody controls in non-irradiated BRCA2 WT cells are shown. Scale bar indicates 10 µm. Bottom**:** Quantification of the number of PLA spots per nucleus. At least 400 cells were counted per condition from three independent experiments. For statistical comparison of the differences between the samples we applied a Kruskal-Wallis test followed by Dunn's multiple comparison test, the p-values show significant differences. The red line in the plot indicates the median, each symbol represents a single PLA spot. **(B)** Top: Representative images of *In situ* PLA performed between γH2AX and S9.6 (DNA-RNA hybrids) antibodies in BRCA2 deficient DLD1 cells (BRCA2$^{-/-}$) bearing BRCA2 (WT) or BRCA2-T207A (T207A). When indicated, cells were transfected/treated with RNase H1 (RH) or Cordycepin (Cordy) prior to fixation. Single antibody controls in non-irradiated BRCA2 WT cells are shown. Scale bar indicates 10 µm. Bottom: Quantification of the number of PLA spots per nucleus. At least 400 cells were counted per condition from three independent experiments. For statistical comparison of the differences between the samples we applied a Kruskal-Wallis test followed by Dunn's multiple comparison test, the p-values show significant differences. The red line in the plot indicates the median, each symbol

To find out whether this increase was due to a defect in the unwinding activity of DDX5 we purified BRCA2$_{T1}$ T207A from human cells as we did for BRCA2$_{T1}$ and tested again the helicase activity of DDX5 now in the presence of this fragment. Interestingly, BRCA2$_{T1}$-T207A inhibited the helicase activity of DDX5 (Fig. 16A) suggesting that the fraction of BRCA2-T207A that binds DDX5 results in a non-productive interaction with DDX5

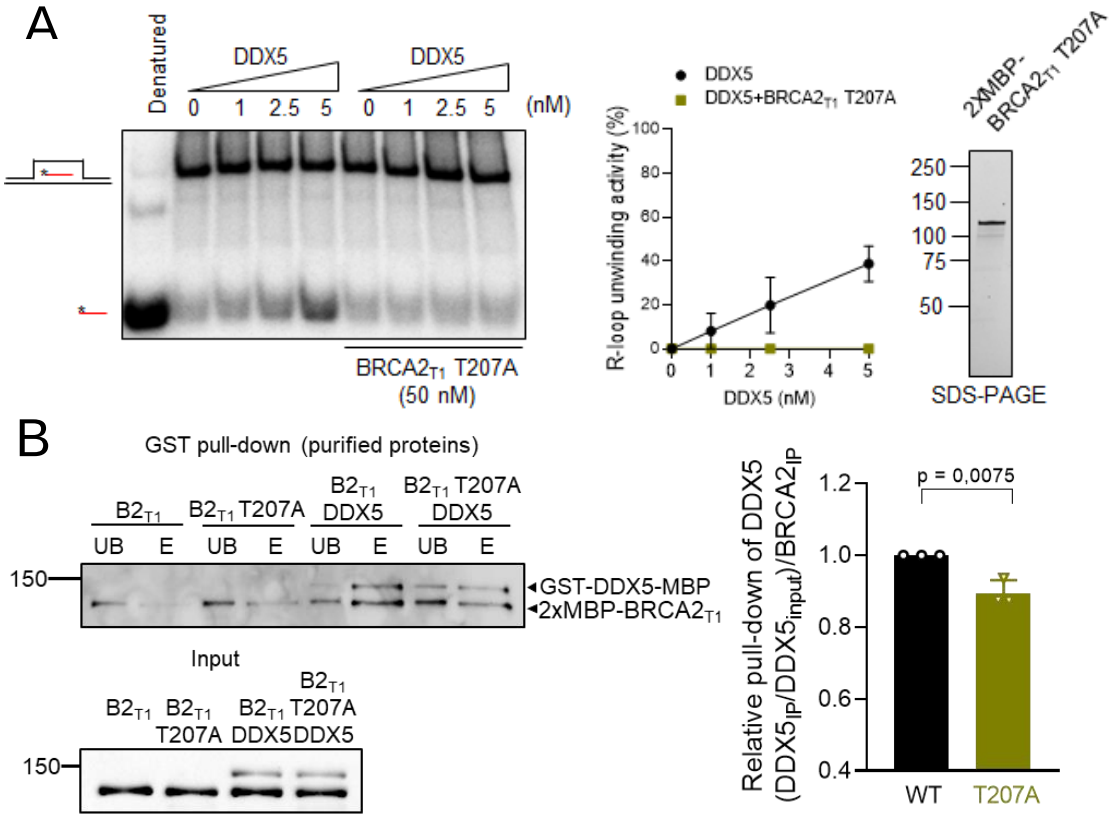

Figure 16. BRCA2 T207A variant affects DDX5 unwinding activity on R-loops. (A) Left: PAGE gel showing a representative unwinding assays in which purified MBP-DDX5-GST (1-5 nM) was incubated with ^{32}P – labelled synthetic R-loop substrate in presence or absence of 50 nM purified $BRCA2_{T1}$ T207A. Middle: Quantification of the unwinding experiments showing the percentage of free RNA relative to the R-loop substrate (unwound product) as a function of DDX5 concentration alone (black) or in presence of $BRCA2_{T1}$ T207A. The data represent the mean ± SD of at least three independent experiments. Right: SDS-PAGE showing 650 ng of purified 2xMBP-$BRCA2_{T1}$ T207A used in the unwinding assay. **(B)** Left: GST pulldown assay using purified $BRCA2_{T1}$ ($B2_{T1}$), $BRCA2_{T1}$ T207A ($B2_{T1}$ T207A) and DDX5; MBP antibody was used for the detection of both proteins. UB: unbound; E: eluate. Right: Quantification of the GST pull-down experiments calculated as the pulled-down DDX5 with either $BRCA2_{T1}$ WT or $BRCA2_{T1}$ T207A relative to the input levels of DDX5 and the amount of pulled-down 2xMBP-$BRCA2_{T1}$. Results are presented as the fold change compared to $BRCA2_{T1}$ WT. The data represents the mean ± SD of three independent experiments. Statistical significance of the difference was calculated with unpaired t test; the p-values show the significant difference.

precluding its unwinding activity. Indeed, GST-pulldown, performed as in figure 3D, revealed that although mildly reduced compared to $BRCA2_{T1}$WT, an important fraction of $BRCA2_{T1}$ T207A can still interact with DDX5 (Fig. 16B), thus likely influencing its unwinding activity on R-loops.

Thus, BRCA2-T207A reduces BRCA2-DDX5 productive interaction, impairing the

localization of DDX5 at DNA-RNA hybrids especially in cells exposed to DNA damage and inhibiting its unwinding activity.

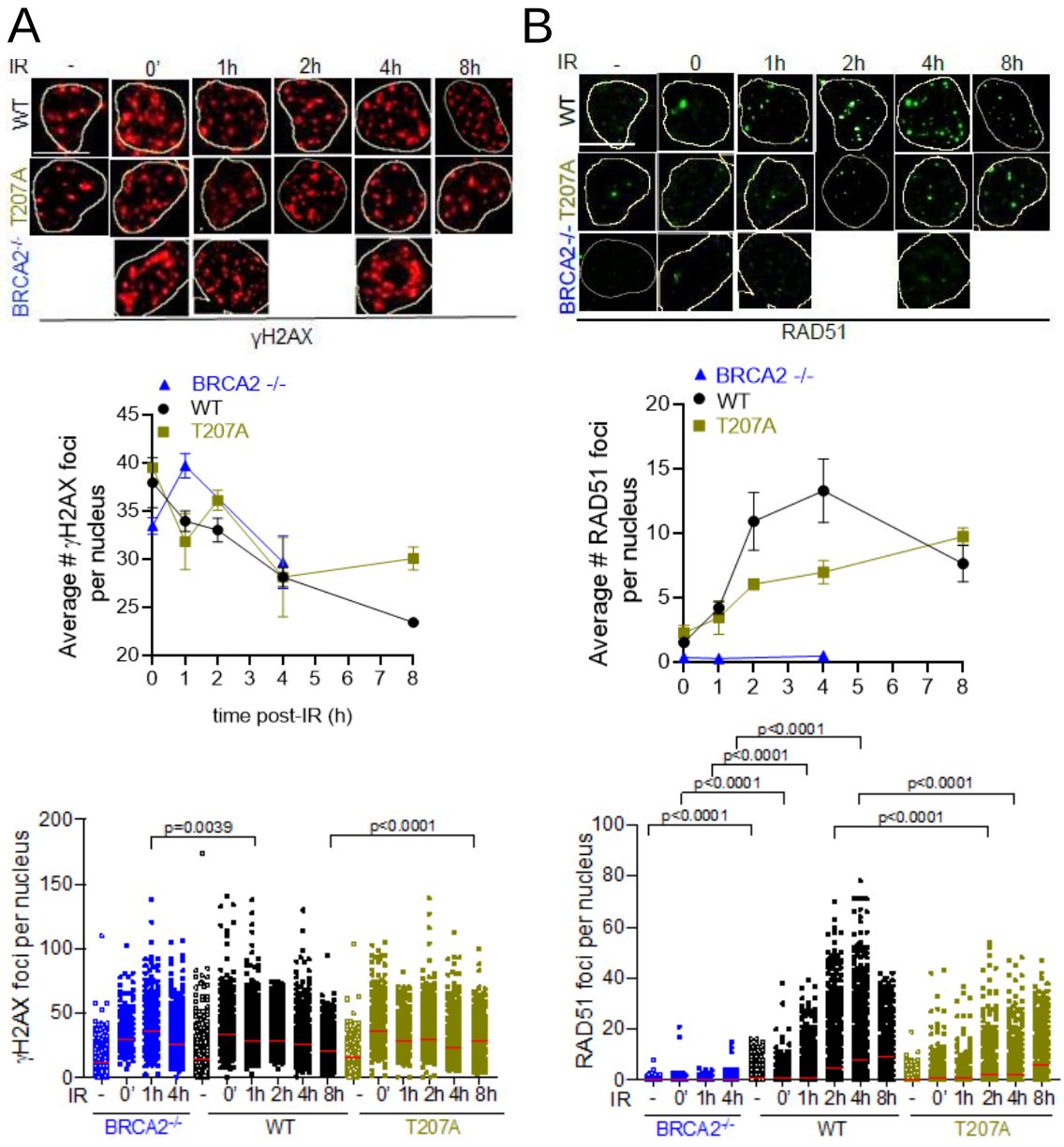

Figure 17. RAD51 kinetics of recruitment is affected in cells bearing T207A mutation. Representative immunofluorescence images of DLD1 BRCA2 deficient cells (BRCA2$^{-/-}$) or BRCA2$^{-/-}$ cells expressing BRCA2 WT or BRCA2-T207A in non-treated (NT) or at different time points post-IR (6 Gy), as indicated; stained for γ-H2AX **(A)** RAD51 **(B)**. Bottom: Graph showing the average number of **(A)** γ-H2AX and **(B)** RAD51 repair foci in the three cell lines and graphs of distributions of γ-H2AX and RAD51 repair foci per nucleus. The data represent the mean ± SEM of three independent experiments whereas in distribution graphs the red line represents the median. At least 500 cells per condition were counted from three independent experiments For statistical comparison of the differences between the samples we applied a Kruskal-Wallis test followed by Dunn's multiple comparison test, the p-values show significant differences

In fig. 12B we showed that DDX5-depleted U2OS cells, exhibited a defect in the kinetics

of RAD51 foci formation upon irradiation compared to control cells. This result suggested a role of DDX5 in facilitating HR-mediated DSBs repair. To find out whether this function was associated with BRCA2 interaction we tested RAD51 foci kinetics in DLD1 cells expressing BRCA2-T207A variant, which affect BRCA2-DDX5 interaction. Thus, we monitored γH2AX and RAD51 foci formation by immunostaining at different time points after γ-irradiation (6Gy) in both BRCA2 WT and T207A expressing DLD1 cells using DLD1 BRCA2-deficient cells as control,. As expected, the number of γH2AX foci increased upon DSBs induction by IR in all three cell lines and subsequently decreased in later time points, in agreement with the repair of DSBs lesions (Fig. 17A). Interestingly, similarly to what we observed for DDX5-depleted U2OS cells, the number of RAD51 foci detected in DLD1 cells bearing BRCA2-T207A was significantly lower than in BRCA2 WT cells, particularly at 2 and 4 h post-irradiation and only reached the same levels as WT at 8h post-IR. These results suggest that the kinetics of RAD51 recruitment at DSBs is defective in cells where BRCA2-DDX5 interaction is altered (Fig. 17B). According to the literature, $BRCA2^{-/-}$ cells showed very low number of RAD51 foci upon IR at all time points (Fig. 17B).

Taken together, these data suggest that BRCA2-DDX5 interaction facilitate DSBs repair by HR pathway.

If the role of BRCA2-DDX5 facilitating repair by HR is dependent on their activity resolving DNA-RNA hybrids, removing these hybrids should rescue the phenotype we observe. For this purpose, we overexpressed RNAse H1 in cells bearing BRCA2-T207A and monitored γH2AX and RAD51 foci formation at 2 hours after irradiation. As expected, untreated cells showed few γH2AX and RAD51 foci, which was not altered by RH overexpression (Fig. 18A). As expected, after irradiation the number of γH2AX foci and RAD51 foci increased. Importantly, overexpression of RNAase H1 in these conditions partially restored the levels of RAD51 foci to almost WT levels whereas the number of γH2AX foci remained unchanged (Fig. 18A). These results strongly suggest that the persistent DNA-RNA hybrids at IR-induced DSBs are at the origin of the delay observed in the kinetics of appearance of RAD51 foci in DLD1 bearing BRCA2-T207A.

Finally, DNA-RNA hybrids forming at DSBs have been shown to influence their repair by either promoting or impeding HR or also regulating DNA end-resection[283, 295, 255]. Our data indicates that DNA-RNA hybrids could have an impact on steps of HR pathway that involve RAD51, i.e., downstream DNA-end resection; however, these hybrids could have

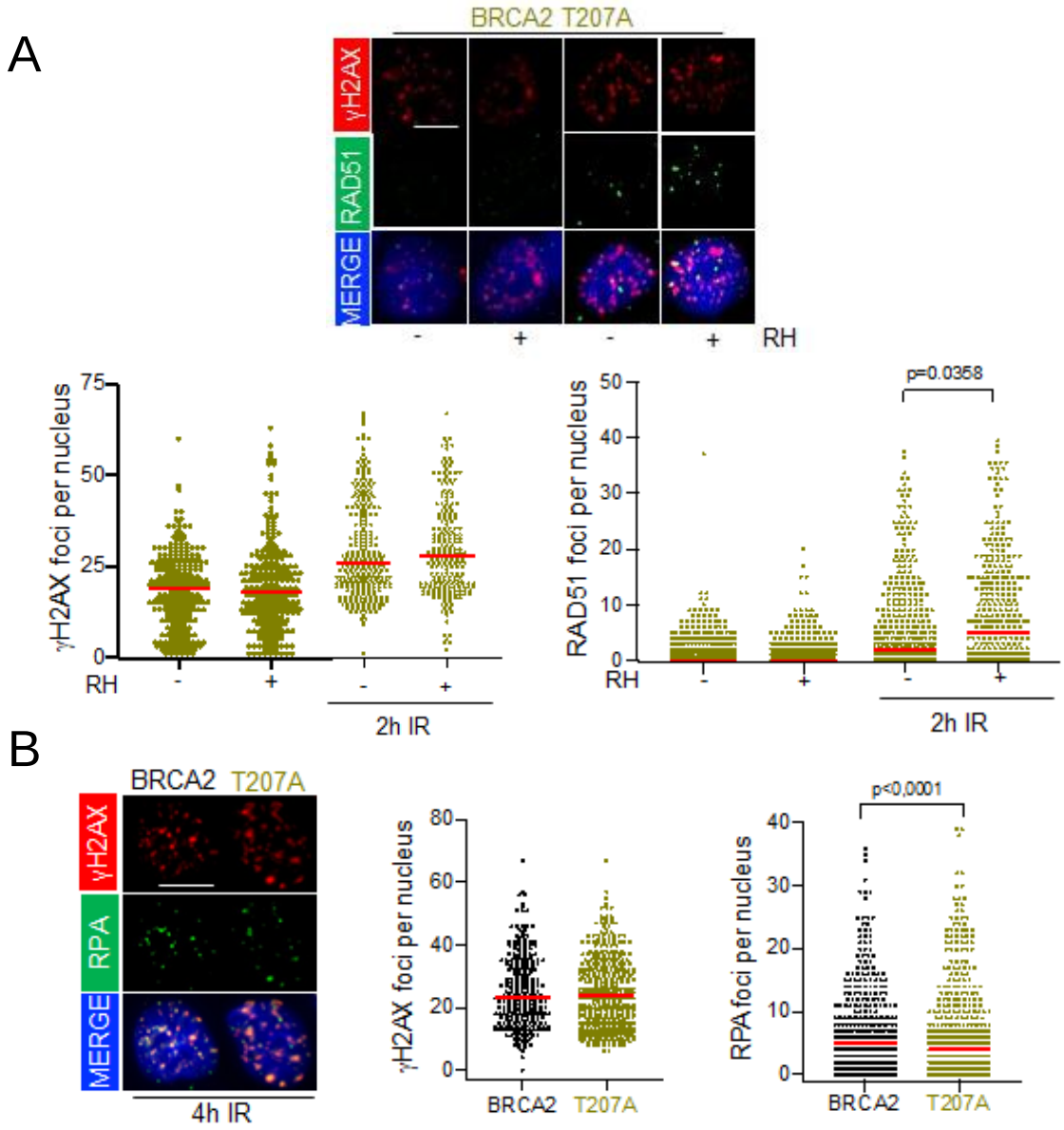

Figure 18. DDX5-BRCA2 interaction favors DSBs repair by homologous recombination. (A) Top: Representative immunofluorescence images of DLD1 BRCA2-T207A cells not treated and 2h post-irradiation (6Gy), as indicated, stained for γH2AX and RAD51. Right: Quantification of the number of γH2AX foci (left) or RAD51 foci (right) per nucleus. When indicated, cells were transfected with plasmid pEGFP-M27 expressing RNaseH1 (RH) 48h prior fixation. The data shown is from at least 400 cells per condition from three independent experiments. For statistical comparison of the differences between the samples we applied a Kruskal-Wallis test followed by Dunn's multiple comparison test, the p-values show significant differences. The red line in the plot indicates the median; each symbol represents a single focus. **(B)** Representative immunofluorescence images of DLD1 BRCA2 WT or BRCA2-T207A cells 4h post-irradiation (6Gy) stained for γH2AX foci and RPA. Right: Quantification of the number of γH2AX and RPA foci per nucleus, as indicated. The data represent at least 400 cells per condition from two independent experiments. For statistical comparison of the differences between the samples we applied a Kruskal-Wallis test followed by Dunn's multiple comparison test, the p-values show significant differences. The red line in the plot indicates the median, each symbol represents a single focus.

also an impact on the resection step. To find out, we monitored the formation of RPA foci in BRCA2 T207A cells exposed to irradiation as a proxy for the presence of ssDNA which is the product of resection. Interestingly, although the number of γH2AX foci number was similar in BRCA2-T207A and BRCA2 WT expressing cells, BRCA2-T207A cells displayed a decreased number of RPA foci compared to BRCA2 WT cells (Fig. 18B). These results suggest that resection is affected in these cells probably due to the persistent DNA-RNA hybrids at DSBs; alternatively, DNA-RNA hybrids formed at the ssDNA overhang generated upon resection may impede normal RPA coating leading to the same outcome. Overall, these results suggest that the DNA-RNA hybrids that accumulate in cells bearing the breast cancer variant T207A interfere with the repair of DSBs by HR.

3. Discussion

In this PhD project, we have identified a novel partner of BRCA2, the RNA helicase DDX5. We demonstrate an important role for this interaction in the resolution of DNA-RNA hybrids that form in the vicinity of DSBs which, in turn, promotes their repair by HR.

Our results reveal a function of DDX5 at DNA-RNA hybrids in the context of DNA damage, either induced at specific sites (DiVA cell system) or upon irradiation, and we demonstrate that this role is supported by BRCA2. More specifically, we show that BRCA2 enhances the retention of DDX5 at DNA damage lesions and the association of DDX5 at DNA-RNA hybrids in irradiated cells.

Mechanistically, we establish that BRCA2 stimulates DDX5 unwinding activity on R-loops *in vitro*, an activity that appears to be driven by protein-protein interaction through the N-terminal region of BRCA2. Importantly, we report that BRCA2-DDX5 interaction favours the kinetics of appearance of RAD51 foci in cells exposed to irradiation.

A previous work showed that DDX5 influences p21 transcription mediating p53 and RNAPII recruitment to p21 promoter[279]. The authors reported that DDX5 depletion leads to sensitivity to γ-irradiation because of this function. Our findings showing the effect of DDX5 depletion on RAD51 foci formation raises the possibility that the sensitivity to γ-irradiation observed in that study could be due, at least in part, to the impaired DNA-RNA hybrid resolution at DSBs following exposure to this treatment.

The role of DDX5 in the resolution of DNA-RNA structures has been studied recently in the context of replication stress[264]. In particular, the authors reported an increase in

sensitivity to replication-stress inducing agents such as hydroxyurea upon depletion of DDX5[264]. Moreover, they showed that PRMT5-mediated methylation of DDX5 is needed for its interaction with XRN2 exoribonuclease and this is required for suppressing R-loops at transcription termination sites in the absence of DNA damage. Although in this thesis project we have focused on a DDX5 role in the resolution of hybrids in the context of DSBs because the interaction we observe with BRCA2 is enhanced in these conditions, we also found that DDX5-depleted cells accumulate DNA-RNA hybrids genome-wide confirming the global role of DDX5 in preventing DNA-RNA structures. Since BRCA2-DDX5 interaction was not restricted to conditions in which DNA damage was induced (Fig. 2A, B) it is possible that BRCA2 could also work in complex with DDX5 or other RNA helicases (see Fig. 1B) to resolve DNA-RNA hybrids outside DSBs.

In this project we could confirm the DDX5 unwinding activity on R-loops as previously reported[264]. Importantly, we found that this activity is stimulated by BRCA2, thus describing a novel role for this important tumor suppressor. However, how this stimulation occurs requires further investigation. One possibility could be that BRCA2 binding influences DDX5 ATP hydrolysis activity, which is indispensable for DDX5 unwinding activity, as shown in previous studies and confirmed in this work[264, 265, 272] (Fig. 11). This mechanism for a stimulatory effect mediated by BRCA2 was already shown for recombinase RAD51[107]. A second possibility is based on the particular mechanism used by DEAD-box proteins to unwind its substrates: instead of translocation-based duplex unwinding, it has been reported that DEAD-box helicases bind to the RNA strand of an RNA duplex (or DNA-RNA hybrids) and trigger the "bending" of RNA strand in order to destabilize the entire structure[267]. Thus, a change in DDX5 conformation induced by the interaction with a partner, such as BRCA2, could modify its affinity for RNA and finally influence the efficiency of its unwinding activity. Moreover, several studies have classified DDX5 as low processive RNA helicase[271, 273, 274]; thus, it is not surprising that in order to increase its unwinding activity rate, DDX5 could rely on interacting partners, such as BRCA2, which could be also enhancing DDX5 specificity for certain substrates[271].

The DDX5 unwinding activity described *in vitro* and stimulated by BRCA2, could be essential for the resolution of DNA-RNA hybrids formed at DSBs and to ensure their proper repair by HR. This idea is supported by our results showing that overexpression of RH in T207A variant-expressing cells that impair BRCA2-DDX5 interaction, partially restores the delayed kinetics of appearance of RAD51 foci in these cells (Fig.18A). Cells bearing this variant also showed increased levels of DSBs-induced DNA-RNA hybrids,

which could explain the delay observed in the formation of RAD51 foci in these cells. Importantly, the fact that $BRCA2_{T1}$ T207A precludes DDX5 unwinding activity on DNA-RNA hybrids *in vitro* (Fig. 16A) strongly supports this idea. These findings also suggest a role of BRCA2 upstream its canonical function in the recombination process as the resolution of DNA-RNA hybrids precedes the loading of RAD51 (Fig. 18A). In agreement with this hypothesis, another study revealed that OB-folds-mediated association between BRCA2 and PAR chains is required for an early recruitment of BRCA2 at DSBs which in turn serves recruit the nuclease EXO1[296].

In this PhD project we shed light on a function of DDX5, never investigated before, in the context of DSBs repair by HR. Although we could not observe a clear recruitment of DDX5 at sites of DNA breaks or detect DDX5 foci, the anti-stripe pattern we observe shortly after laser micro-irradiation strongly suggests that DDX5 is re-localized in the nucleus in response to DNA damage and that this re-localization is supported by BRCA2 (Fig. 9, 10).

This work also contributes to the discussion on the role of RNA and RNA binding proteins in DSB repair. Indeed, a large number of recent studies have identified several RNA binding/processing factors involved in transcription, splicing regulation or miRNA biogenesis as important in the DDR [209, 241, 254, 260, 283, 295, 327-331]. Moreover, RNA binding motifs have been identified in DNA repair factors, suggesting that they could cooperate with RNA processing enzymes at DNA damage sites[209, 241, 332]. In addition, recent meta-analysis studies indicate that RNA processing factors found involved in the DDR, are not only recruited to DNA damage but are also modified in response to DDR, suggesting these modifications are orchestrated by the DDR to regulate the repair outcome[333]. These findings also imply that RNA itself has a role in the DDR: consistent with this, RNAseA treatment, which degrades all RNA species, has been shown to alter the recruitment of DNA repair factors[295, 334]. Likewise, inhibiting transcription leads to similar results[295, 322], suggesting that native RNA transcripts are required for proper DNA repair.

Our results are in agreement with the reports showing that DNA-RNA hybrids form at DNA breaks and impact DSB repair. Some of these studies suggest that hybrids formed at DSBs could be intermediates and/or serve as regulators of repair pathway choice[189, 228, 255, 283]. For example, removal of DNA-RNA hybrids by RH overexpression have been shown to alter the DNA damage recruitment of several DNA repair factors [189, 322]. Moreover, DNA-RNA hybrids also re-localize to DNA damage sites in response to DDR[253, 283], indicating that they could have a role in facilitating DDR signaling propagation.

Importantly, a recent work reveals an interaction between R-loops and DDR factors such as PARP1 and DNA-PKs[241], suggesting that these structures are implicated in canonical DNA repair beyond RNA-mediated DNA repair. Although we have indications that BRCA2 can bind DNA-RNA hybrids *in vitro*, it would be interesting to reveal whether BRCA2 binds DNA-RNA hybrids at DSBs.

Other studies have shown that DNA-RNA hybrids facilitate or impede the HR repair process[239, 260, 261, 262]. In both scenarios however, DNA-RNA hybrids need to be removed to allow DNA repair by HR.

In addition to their role at DSBs, the mechanism of DNA-RNA hybrids generation is also unclear. It is reasonable to think that the opening of the DNA duplex following the generation of a break in a highly transcribed region could promote the annealing of an RNA transcript back to the template strand; consequently, the modification of the DNA ends of the DSB could disfavor their recognition by NHEJ factors and commit DSBs repair towards HR[252]. However, recent investigation reveals that there is no significance difference in the levels of R-loops at HR-repaired sites compared to NHEJ-repaired sites, suggesting that R-loops generation at DSBs is independent of the repair pathway[321]. Importantly, the same study, exploring the transcriptional status of R-loops forming sites, reveals that R-loop formation at DSBs is dependent on the transcriptional activity of the locus via the availability of pre-existing transcripts[321]. Moreover, a fraction of pre-existing RNA transcripts has been shown to serve as homology template in a process similar to HR[208, 322-324]. These reports support the idea that DDR could orchestrate R-loops formation to facilitate repair.

An interesting hypothesis is that R-loop formed at DSBs may result from RNAP pausing due to the transcriptional suppression in response to DNA damage, leading to an increased probability of DNA-RNA hybrids formation around these damaged sites[256, 260]. A more provocative hypothesis suggests that the formation of hybrids may be the consequence of *de novo* transcription triggered by DSB induction. Indeed, the conformational changes in the DNA following a DNA break could promote the recruitment of transcription factors at these sites, and several studies have reported the formation of DNA-damage induced RNAs through DROSHA and DICER activity[283, 284, 295], which were more recently associated with the formation of DNA-RNA hybrids at DSBs[257]. However, this hypothesis remains controversial as a recent study failed detecting any type of small RNAs arising from endogenous DSBs, even though DROSHA and DICER were found essential for DSBs repair. Interestingly, DROSHA has been found implicated in transcription

activation[326] and termination[326], suggesting how it could be implicated in DNA damage-related RNA processing.

DNA-RNA hybrids at DSBs may also form following the resection step, exploiting the ssDNA generated and altering RPA binding. In this case, the HR pathway would be already committed as suggested by the study revealing that the DEAD-box protein DDX1 is involved in the resolution of those DNA-RNA hybrids[239]. Similar to that study, we found that DDX5 interaction with BRCA2 favors RPA coating as cells expressing BRCA2-T207A variant exhibit a decrease in RPA foci compared to BRCA2 WT cells (Fig. 18B). These results can give rise to different interpretations: i) resection could be affected because of the persistence of DNA-RNA hybrids. ii) It is also possible that in the context of a highly transcribed region, RPA coating could be reduced not only if the RNA transcript anneals to the 5' DNA strand, impeding its resection, but also if, regardless of whether resection takes place at the 5' end, RNA anneals on the 3' strand.

In this study we also provide evidence that DDX5- and BRCA2-depleted cells display an enrichment of DNA-RNA hybrids upon DSB induction (Fig. 8C). Moreover, BRCA2-DDX5 interaction as detected by PLA is sensitive to transcription inhibition and RH overexpression, especially in irradiated conditions (Fig. 2C), supporting the idea that this complex could be required for the resolution of hybrids formed at DSBs.

A recent report shows that SETX-depleted cells exhibit a decrease RAD51 foci formation with a concomitant increase in 53BP1 foci upon DSB induction although the kinetics of repair remained unaffected. We found that DDX5 depletion impairs the recruitment of RAD51 after irradiation and observed a clear delay in the kinetics of appearance of RAD51 foci suggesting that the timely repair of DSBs is affected in these conditions (Fig. 12B). Accordingly, cells expressing BRCA2 breast cancer variant T207A, that alters BRCA2-DDX5 interaction, also display a delay in the kinetics of appearance of RAD51 foci (Fig. 17B). Importantly, the fact that the delayed kinetics can be partially rescued by RH overexpression in BRCA2-T207A cells strongly suggests that the DNA-RNA hybrid resolution activity of BRCA2-DDX5 directly impacts HR. Therefore, according to our results, we favor the idea that DNA-RNA hybrids represent an impediment for the HR process.

In this work, we mapped DDX5-interaction site to the first 250 aa of BRCA2 (($BRCA2_{T1}$), (Fig. 3A). Given that the RAD51 binding domain essential for HR-recombination lays in BRCA2 central region (BRC repeats) (Fig. 3A) it is possible that both proteins could bind BRCA2 at the same time to ensure the efficiency of HR-mediated DSB repair.

In addition, it is possible that BRCA2 acts through different interacting partners to remove DNA-RNA hybrids[187]. Indeed, a recent study has described the interaction between BRCA2 and RNAseH2 nuclease for the degradation of DNA-RNA hybrids generated at DSBs[189]. However, the phenotype derived from disruption of BRCA2-RNAseH2 interaction as well as the effects on HR-mediated repair efficiency were not assessed in that study. This example, together with other factors implicated in the resolution of DNA-RNA hybrids at DSBs independently of BRCA2[239, 260, 261, 262], could explain why in absence of DDX5 (Fig. 12B) or in cells expressing BRCA2 T207A variant (Fig. 17B), HR-mediated DSBs repair is still possible, although delayed.

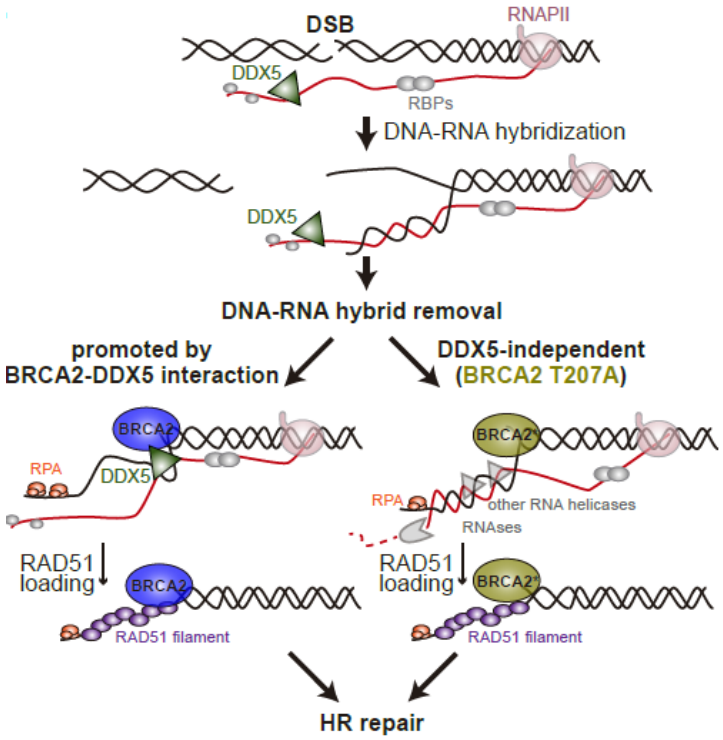

Figure 19. Working model for BRCA2-DDX5 interaction in DSBs repair. When a DSB occurs, resection or the relaxation of the DNA molecule at the break site may induce the formation of DNA-RNA hybrids. DDX5, as well as other RBPs, coating the nascent transcript could therefore be found in proximity to the break. The interaction between BRCA2 and DDX5 could be essential for the removal of the DSB-induced DNA-RNA hybrids, leading to efficient HR-mediated DSB repair (left). In cells were BRCA2-DDX5 interaction is perturbed, DDX5 cannot efficiently resolve DNA-RNA hybrids. Thus, the recruitment of other DNA-RNA hybrids resolving factors might be required leading to a delayed or less efficient HR-mediated DSB repair (right).

Interestingly, the same breast cancer variant characterized here, T207A, was already described in a recent work from the lab in the context of mitosis: we showed that BRCA2-T207A leads to a reduced interaction with PLK1 with detrimental consequences in chromosome alignment, segregation and aneuploidy[84]. Although we showed that the function in chromosome alignment is uncoupled to the DNA repair activity of BRCA2, we

observed a mild sensitivity to MMC that could not be explained from the mitotic phenotype. Our results showing the delay in RAD51 repair foci upon DNA damage in cells bearing T207A may explain this mild sensitivity to DNA damage as we expect a fraction of DNA-RNA hybrids at DSBs to persist in these cells precluding DSB repair.

Importantly, without altering the canonical BRCA2 domains directly implicated in HR function, mainly the BRC repeats and the CTD, this variant has indirect and deleterious effects on RAD51-mediated DSBs repair. To our knowledge, this is the first time this kind of indirect effect is observed in BRCA2 VUS. High levels of R-loops arising from endogenous or exogenous aldehydes have been proposed to be a cause of tumorigenesis in BRCA2-mutation carriers[138]. Thus, our findings may have implications in the evaluation and classification of BRCA1/2 VUS and suggest that testing the levels of DNA-RNA hybrids could be an independent method to reveal the functional impact of missense variants and evaluate their pathogenicity.

In general, revealing BRCA2 dysfunctions correlated with breast cancer mutations, as illustrated by this thesis project, could significantly contribute not only to the discovery of new important functions of BRCA2 but also, to the evaluation of cancer risk in patients bearing these mutations.

In conclusion, our results could be summarized in a model in which the essential role of BRCA2-DDX5 interaction is the removal of DNA-RNA hybrids that form following the induction of DSBs, presumably in the context of actively transcribed regions (Fig. 19): BRCA2 may retain or relocalize DDX5 at DNA damage sites, possibly already in its vicinity due to its role binding at nascent transcripts. Once there, DDX5 could act to resolve DNA-RNA hybrids promoted by BRCA2 enabling the subsequent steps of DSB repair by HR. Other nucleases and/or RNA helicases, interacting or not with BRCA2 or other repair factors, may help the removal of hybrids at DSBs in a delayed or less efficient manner, as observed in the absence of DDX5 or in conditions disrupting BRCA2-DDX5 interaction (BRCA2-T207A expressing cells).

4. Outlook and Perspectives

In this thesis project, we described a new function of BRCA2 repair factor in complex with DDX5 RNA helicase in the context of DSBs repair by HR. This work helps explain why BRCA2-deficient cells[187] accumulate DNA-RNA hybrids and places BRCA2 upstream its canonical step in HR. Our findings also describe a new role for DDX5 in resolving DNA-RNA structures at DSBs sites.

A question raised by this and other works investigating DNA-RNA hybrids and R-loops resolving factors, especially in the context of DNA damage, is why do cells need so many helicases/nucleases to perform the same function. This apparent redundancy may be due to the cellular context such as the type of DNA damage where the DNA-RNA is formed, the levels of transcription or the chromatin status at a given DSB. Consistent with this, cells depleted of Senataxin were found sensitive to etoposide but not IR[260] whereas DDX5 depleted cells are sensitive to IR[279]. We showed in a previous report that cells bearing BRCA2-T207A variant exhibit mild sensitivity to MMC. It would be interesting to know whether cells bearing BRCA2-T207A are sensitive to IR. Our results suggest that transcription favours BRCA2-DDX5 interaction and promotes the accumulation of DSBs-associated DNA-RNA hybrids in DDX5-depleted cells; However, further studies will be required to pinpoint the specificity of BRCA2-DDX5 interaction to resolve DNA-RNA hybrids at DSBs.

We have also suggested that the formation of hybrids at DSBs in the absence of DDX5 or DDX5-BRCA2 interaction impair HR suggesting that the DNA-RNA hybrids associated with DSBs commit the DSBs repair towards HR. Additional studies would be needed to understand the fraction of these DSBs that are channelled to other perhaps error-prone repair pathway which do not necessarily requires an efficient removal of DNA-RNA hybrids such as NHEJ. Along these lines, Senataxin depletion was reported to augment DSB repair by NHEJ[260].

A crucial step in the choice of DSBs repair is DNA resection. Our results do not clearly demonstrate if resection is defective following DNA-RNA hybrids accumulation in T207A bearing cells; however, the fact that the number of RPA foci in BRCA2-T207A cells exposed to IR is reduce suggest that this might be the case. Further analysis to more specifically examine if resection is properly occurring in these conditions (such as measuring amount of ssDNA at breaks as well as search for recruitment of factors, as EXO1, directly involved in this process) could be useful to confirm this hypothesis. Importantly, resection might be a determinant for the choice of RNA helicase operating on hybrids at DSBs.

Our results indicate that BRCA2 stimulates unwinding activity of DDX5 on R-loops *in vitro*. However, as discussed before, the mechanism by which this stimulation is mediated has not been completely elucidated. One hypothesis is that BRCA2, as demonstrated for RAD51[107], could modify the ATP binding or ATP hydrolysis rate of DDX5, since DDX5 helicase activity on these R-loops substrates is dependent on ATP. Assays revealing the

ATP hydrolysis rate associated with DDX5, in presence or not of BRCA2, could confirm this hypothesis. However, my attempts to test this using TLC and monitoring the release of $^{32}P_i$ from [γ^{32}P]-ATP following the addition of purified DDX5 have failed even if I could measure the ATPase of RAD51, our positive control (data not shown in the manuscript). In the future, the use of different conditions or alternative methods such as fluorometric assays would help testing this first hypothesis. Another possibility is based on the fact that DEAD-box proteins including DDX5, unwind RNA duplexes by "bending" one RNA strand, destabilizing the structure. Therefore, a conformational change in DDX5 protein, due to its direct interaction with BRCA2, could increase its ability to bind RNA or drive its specificity for selected substrates explaining the stimulatory activity of BRCA2. For this purpose, we could examine by Electrophoretic Mobility Shift Assay (EMSA) the R-loop and DNA-RNA binding activity of DDX5 following the addition of recombinant BRCA2 to the reaction. To further address the point of specificity f it could be very informative performing both EMSA and unwinding assays with purified DDX5 and BRCA2 proteins incubated with dsRNA as well.

As an RNA binding protein, it is possible that in some contexts, DDX5 RNA binding activity per se leads to the prevention of RNA hybridization to the DNA. Indeed, in the absence of DNA damage, our results show that a helicase dead DDX5 (DDX5-HD) can rescue of DNA-DNA hybrids accumulation observed in DDX5-depleted cells. A previous work has shown that the methylation of DDX5 is required in these conditions. The authors suggested that the unwinding activity of DDX5 on R-loops could be required to relax and facilitate the opening of these structures, favouring XRN2 nuclease activity, however that study did not clearly assess whether the helicase activity of DDX5 was needed[264]. Whether this is the case in the context of DNA-RNA hybrids at DSBs is also unclear; however, the fact that BRCA2-T207A cells accumulate DNA-RNA hybrids and BRCA2$_{T1}$-T207A inhibits DDX5 unwinding activity *in vitro* suggests that the unwinding activity of DDX5 is required to resolve DNA-RNA hybrids at DSBs. To proof this point further we could overexpress DDX5-HD in irradiated cells or in the DiVA cell system monitoring DNA-RNA hybrids upon induction of DSBs.

Finally, BRCA2 has been described to bind RNAseH2 to regulate the levels of DNA-RNA hybrids at DSBs in a scenario where de novo transcription is occuring[189]; whether this interaction takes place in complex with DDX5 or they represent different pools dealing with different subsets of DNA-RNA hybrids at DSBs remains to be elucidated.

5. References

1. Hoeijmakers, J. H. (2009). DNA damage, aging, and cancer. *N Engl J Med* 361, 1475–1485
2. Lindahl, T. (1993) Instability and decay of the primary structure of DNA. *Nature* 362:709-15
3. Cadet, J., Davies, K. J. A. (2017). Oxidative DNA damage & repair: An introduction. *Free Radic Biol Med* 107, 2–12.
4. Ciccia, A., Elledge, S. J. (2010). The DNA Damage Response: Making It Safe to Play with Knives. *Mol. Cell* 40, 179–204
5. Shiloh, Y. (2003). ATM and related protein kinases: safeguarding genome integrity. *Nat.Rev. Cancer* 3, 155–168
6. Andor, N., Maley, C. C., Ji, H. P. (2017). Genomic instability in cancer: Teetering on the limit of tolerance. *Cancer Res* 77, 2179–2185
7. Zhou, B. S., Elledge, S. J. (2000). The DNA damage response: putting checkpoints in perspective. *Nature* 408, 433–439
8. Lanz, M. C., Dibitetto, D., Bustamante Smolka, M. (2019). DNA damage kinase signaling: checkpoint and repair at 30 years. *The EMBO Journal* 38: e101801
9. Awasthi, P., Foiani, M., Kumar, A., (2015) ATM and ATR signaling at a glance. *Journal of Cell Science* 128, 4255-4262
10. Syed, A., Tainer, J.A. (2018). The MRE11-RAD50-NBS1 Complex Conducts the Orchestration of Damage Signaling and Outcomes to Stress in DNA Replication and Repair. *Annu Rev Biochem.* 20;87:263-294
11. Blackford, A. N., Jackson, S. (2017). ATM, ATR, and DNA-PK: The Trinity at the Heart of the DNA Damage Response. *Molecular Cell* 66(6):801-817
12. Chen, J. (2016). The cell-cycle arrest and apoptotic functions of p53 in tumor initiation and progression. *Cold Spring Harb Perspect Med* 6: a026104
13. Sulli, G., Di Micco, R., di Fagagna, F. d'Adda. (2012). Crosstalk between chromatin state and DNA damage response in cellular senescence and cancer. *Nat. Rev. Cancer* 12, 709–720
14. Hoeijmakers, J. H. J. (2001). Genome maintenance mechanisms for preventing cancer *DNA Repair (Amst).* 411, 366–374
15. Fu, D., Calvo, J. A., Samson, L. D. (2012) Balancing repair and tolerance of DNA damage
    caused by alkylating agents. *Nat. Rev. Cancer* 12, 104–20

16. Begley, T. J., Samson, L. D. (2004) Reversing DNA damage with a directional bias. *Nat Struct Mol Biol*. 11(8):714-20
17. Wallace, S.S. (2014) Base excision repair: A critical player in many games. *DNA Repair (Amst).* 19: 14–26
18. Spivak, G. (2015). Nucleotide excision repair in humans. *DNA Repair (Amst)*. 36:13-18.
19. Lans, H., Hoeijmakers, J.H.J., Vermeulen, W., Marteijn, J.A. (2019) The DNA damage response to transcription stress. *Nat Rev Mol Cell Biol.* 20(12):766-784
20. Marteijn, J. A., Lans, H., Vermeulen, W., Hoeijmakers, J. H. J. (2014) Understanding nucleotide excision repair and its roles in cancer and ageing. *Nat. Rev. Mol. Cell. Biol*. 15, 465–81 (2014).
21. Jiricny, J. (2006). The multifaceted mismatch-repair system. *Nature Reviews Molecular Cell Biology*. 7, 335–346
22. Peña-Diaz, J., Jiricny, J. (2012) Mammalian mismatch repair: error-free or error-prone? *Trends Biochem Sci.* 37(5):206-14
23. Iyer, R.R., Pluciennik, A., Napierala, M., Wells, R.D. (2015). DNA triplet repeat expansion and mismatch repair. *Annu Rev Biochem.* 84:199-226.
24. Germano, G., Amirouchene-Angelozzi, N., Rospo, G., Bardelli, A. (2018). The Clinical Impact of the Genomic Landscape of Mismatch Repair-Deficient Cancers. *Cancer Discov.* 8(12):1518-1528.
25. Berti, M., Vindigni, A. (2016). Replication stress: getting back on track. *Nat Struct Mol Biol.* 23(2):103-9
26. Zeman, M.K., Cimprich, K.A. (2014). Causes and consequences of replication stress. *Nat Cell Biol.* 16(1):2-9
27. Heyer, W.D., Ehmsen, K. T., Liu, J. (2010). Regulation of homologous recombination in eukaryotes. *Annu. Rev. Genet.* 44, 113–39
28. Leung, W., Baxley, R.M., Moldovan, G.L., Bielinsky, A.K. (2018) Mechanisms of DNA Damage Tolerance: Post-Translational Regulation of PCNA. *Genes (Basel)* 24;10(1)
29. Kolinjivadi, A.M., Sannino, V., de Antoni, A., Técher, H., Baldi, G., Costanzo, V. (2017) Moonlighting at replication forks - a new life for homologous recombination proteins BRCA1, BRCA2 and RAD51. *FEBS Lett.* 591 (8):1083-1100

30. Carr, A.M., Lambert, S. (2013) Replication stress-induced genome instability: the dark side of replication maintenance by homologous recombination. *J Mol Biol.* 29;425(23):4733-44.
31. Schlacher, K., Christ, N., Siaud, N., Egashira, A., Wu, H., Jasin, M. (2011). Double-strand break repair independent role for BRCA2 in blocking stalled replication fork degradation by MRE11. *Cell* 145,529–542.
32. Schlacher, K., Wu, H., Jasin, M. (2012). A distinct replication fork protection pathway connects Fanconi anemia tumor suppressors to RAD51-BRCA1/2. *Cancer Cell*, 22, 106–116
33. Abe, T., Branzei, D., Hirota, K. (2018). DNA Damage Tolerance Mechanisms Revealed from the Analysis of Immunoglobulin V Gene Diversification in Avian DT40 Cells. *Genes* 9(12), 614
34. Clauson C., Schärer O.D., Niedernhofer L.(2013) Advances in Understanding the Complex Mechanisms of DNA Interstrand Cross-Link Repair. *Cold Spring Harb Perspect Biol* 5:a012732
35. Zhang, J., Walter, J.C. (2014) Mechanism and regulation of incisions during DNA interstrand cross-link repair. *DNA Repair (Amst).* 19:135-42
36. Muniandy, P.A., Liu, J., Majumdar, A., Liu, S.T., Seidman, M.M. (2010) DNA interstrand crosslink repair in mammalian cells: step by step. *Crit Rev Biochem Mol Biol.* 45(1):23-49
37. Ceccaldi, R., Sarangi, P., D'Andrea, A.D. (2016) The Fanconi anaemia pathway: new players and new functions. *Nat Rev Mol Cell Biol.* 17(6):337-49
38. Michl, J., Zimmer, J., Tarsounas, M. (2016). Interplay between Fanconi anemia and homologous recombination pathways in genome integrity. *EMBO J.* 2;35(9):909-23
39. Hossain, M.A., Lin, Y., Yan, S. (2018). Single-Strand Break End Resection in Genome Integrity: Mechanism and Regulation by APE2. *Int J Mol Sci*. 14;19(8)
40. Caldecott, K.W. (2014) DNA single-strand break repair. *Exp Cell Res.* 15;329(1):2-8
41. Pascal, J.M. (2018). The comings and goings of PARP-1 in response to DNA damage. *DNA Repair (Amst).* 71:177-182
42. Caldecott, K.W. (2019). XRCC1 protein; Form and function. *DNA Repair (Amst).* 81:102664.

43. Liao, H., Ji, F., Helleday, T., Ying, S. (2018). Mechanisms for stalled replication fork stabilization: new targets for synthetic lethality strategies in cancer treatments. *EMBO Rep.* 19(9). pii: e46263
44. Shibata, A., Jeggo, P. A. (2014). DNA double-strand break repair in a cellular context. *Clin.Oncol (R Coll Radiol)* 26, 243–249.
45. Scully, R., Panday, A., Elango, R., Willis, N.A. (2019). DNA double-strand break repair-pathway choice in somatic mammalian cells. *Nat Rev Mol Cell Biol.* 20(11):698-714
46. Rich, T., Allen, R.L., Wyllie, A.H. (2000) Defying death after DNA damage. *Nature.* 12;407(6805):777-83
47. Cannan, W. J., Pederson, D. S. (2016) Mechanisms and Consequences of Double-strand DNA Break Formation in Chromatin. *J Cell Physiol.* 231(1): 3–14
48. Mehta, A. Haber, J.E. (2014). Sources of DNA Double-Strand Breaks and Models of Recombinational DNA Repair. *Cold Spring Harb Perspect Biol.* 6(9): a016428
49. Woodbine, L., Brunton, H., Goodarzi, A. A., Shibata, A., & Jeggo, P. A. (2011). Endogenously induced DNA double strand breaks arise in heterochromatic DNA regions and require ataxia telangiectasia mutated and Artemis for their repair. *Nucleic Acids Res.* 39, 6986–6997.
50. Aksenova, A. Y., Mirkin, S. M. (2019). At the beginning of the end and in the middle of the beginning: structure and maintenance of telomeric DNA repeats and interstitial telomeric sequences. Genes (Basel) 10.
51. So, A., Le Guen, T., Lopez, B. S., Guirouilh-Barbat, J. (2017) Genomic rearrangements induced by unscheduled DNA double strand breaks in somatic mammalian cells. *FEBS J.* 284(15):2324-2344
52. Bétermier, M., Borde, V., Villartay, J. P. (2019). Coupling DNA Damage and Repair: an Essential Safeguard during Programmed DNA Double-Strand Breaks? *Trends Cell Biol.* 6. pii: S0962-8924(19)30201-6
53. Ceccaldi, R., Rondinelli, B., D'Andrea, A.D. (2016) Repair Pathway Choices and Consequences at the Double-Strand Break. *Trends Cell Biol.* 26(1):52-64
54. Chang, H. H. Y., Pannunzio, N. R., Adachi, N., Lieber, M. R. (2017). Non-homologous DNA end joining and alternative pathways to double-strand break repair. *Nat Rev Mol Cell Biol*. 18, 495–506.

55. Dinkelmann,M., Spehalski, E., Stoneham, T., Buis, J.,Wu, Y., Sekiguchi, J.M., & Ferguson, D.O. (2009). Multiple functions of MRN in end-joining pathways during isotype class switching. *Nat Struct Mol Biol.* 16, 808–813.
56. Rulten, S. L., Fisher, A. E., Robert, I., Zuma, M. C., Rouleau, M., Ju, L., Poirier, G., Reina-San-Martin, B., Caldecott, K.W. (2011) PARP-3 and APLF function together to accelerate nonhomologous end-joining. Mol Cell. 7;41(1):33-45
57. Grundy, G. J., Rulten, S. L., Arribas-Bosacoma, R., Davidson, K., Kozik, Z., Oliver, A. W., Caldecott, K.W. (2016). The Ku-binding motif is a conserved module for recruitment and stimulation of non-homologous end-joining proteins. *Nat Commun.* 7, 11242.
58. Sallmyr, A., Tomkinson, A.E. (2018) Repair of DNA double-strand breaks by mammalian alternative end-joining pathways. *J Biol Chem.* 6;293(27):10536-10546
59. Seol, J.H., Shim, E.Y., Lee S. E. (2018) Microhomology-mediated end joining: Good, bad and ugly. *Mutat Res.* ;809:81-87
60. Bhargava, R., Onyango, D. O., Stark, J. M. (2016). Regulation of single-strand annealing and its role in genome maintenance. *Trends Genet*. 32, 566–575.
61. Hanamshet, K., Mazina, O. M., & Mazin, A. V. (2016). Reappearance from obscurity:Mammalian Rad52 in homologous recombination. Genes (Basel) 7
62. Marnef, A., and Legube, G. (2017). Organizing DNA repair in the nucleus: DSBs hit the road. Curr. Opin. Cell Biol. 46, 1–8.
63. Cejka, P. (2015). DNA End Resection: Nucleases Team Up with the Right Partners to Initiate Homologous Recombination. *J Biol Chem.* 18;290(38):22931-8
64. Himmels, S. F., Sartori, A. A. (2016). Controlling DNA-End Resection: An Emerging Task for Ubiquitin and SUMO. *Front Genet.* 23;7:152
65. Piazza, A., Heyer, W. D. (2019) Homologous Recombination and the Formation of Complex Genomic Rearrangements. *Trends Cell Biol.* 29(2):135-149
66. Chen, C. C, Feng, W., Lim, P. X., Kass, E. M., Jasin, M. (2018). Homology-Directed Repair and the Role of BRCA1, BRCA2, and Related Proteins in Genome Integrity and Cancer. *Annu Rev Cancer Biol.* 2: 313–336
67. Jensen, R. B., Carreira, A., Kowalczykowski, S. C. (2010). Purified human BRCA2 stimulates RAD51-mediated recombination. *Nature* 467, 678–83
68. Liu, J., Doty, T., Gibson, B., Heyer, W. D. (2010). Human BRCA2 protein promotes RAD51 filament formation on RPA-covered single-stranded DNA. *Nat. Struct. Mol. Biol.* 17, 1260–2

69. Thorslund, T., McIlwraith, M., Compton, S. A., Lekomtsev, S., Petronczki, M., Griffith, J. D., West, S. C. (2010). The breast cancer tumor suppressor BRCA2 promotes the specific targeting of RAD51 to single-stranded DNA. *Nat. Struct. Mol. Biol.* 17, 1263–5
70. Byrum, A. K., Vindigni, A., Mosammaparast, N. (2019) Defining and Modulating 'BRCAness'. *Trends Cell Biol*. 29(9):740-751
71. Haber, J. E. (2018) DNA Repair: The Search for Homology. *Bioessays* 40(5):e1700229
72. Wright, W. D., Shah, S. S., Heyer, W. D. (2018). Homologous recombination and the repair of DNA double-strand breaks. *J Biol Chem* 6;293(27):10524-10535
73. Schwartz, E.K. and Heyer, W.D. (2011) Processing of joint molecule intermediates by structure-selective endonucleases during homologous recombination in eukaryotes. *Chromosoma* 120, 109–127
74. Kramara, J., Osia, B., & Malkova, A. (2018). Break-induced replication: The Where, The Why, and The How. *Trends Genet* 34, 518–531
75. Nathanson K. N., Wooster R., Weber B. L. (2001). Breast cancer genetics: what we know and what we need. *Nat. Med.* 7 552–556.
76. Venkitaraman, A. R. (2019) How do mutations affecting the breast cancer genes BRCA1 and BRCA2 cause cancer susceptibility? *DNA Repair (Amst)* 81:102668
77. Lord, C. J., Ashworth, A. (2016). BRCAness revisited. *Nat Rev Cancer.* 16(2):110-20
78. Sharan, S. K., Morimatsu, M., Albrecht, U., Lim, D. S., Regel, E., Dinh, C., Sands, A., Eichele, G., Hasty, P., Bradley, A. (1997). Embryonic lethality and radiation hypersensitivity mediated by Rad51 in mice lacking Brca2. *Nature* 386: 804–810.
79. Connor, F., Bertwistle, D., Mee, P. J., Ross, G. M., Swift, S., Grigorieva, E., Tybulewicz, V. L., Ashworth, A. (1997). Tumorigenesis and a DNA repair defect in mice with a truncating Brca2 mutation. *Nat Genet* 17: 423–430.
80. Wong, A. K. C., Pero, R., Ormonde, P. A., Tavtigian, S. V., Bartel, P. L.(1997) RAD51 Interacts with the Evolutionarily Conserved BRC Motifs in the Human Breast. *J Biol Chem* 272: 31941–31944
81. Patel, K., Yu, V. P., Lee, H., Corcoran, A., Thistlethwaite, F. C., Evans, M. J., Colledge, W. H., Friedman, L. S., Ponder, B. A., Venkitaraman, A. R. (1998) Involvement of Brca2 in DNA repair. *Mol. Cell* 1, 347–57

82. Moynahan, M. E., Pierce, A. J., Jasin, M. (2001). BRCA2 is required for homology-directed repair of chromosomal breaks. *Molecular Cell* 7, 263–272
83. Daniels, M. J., Wang, Y., Lee, M., Venkitaraman, A. R. (2004). Abnormal cytokinesis in cells deficient in the breast cancer susceptibility protein BRCA2. *Science* 306, 876–879.
84. Ehlén, Å., Martin, C., Miron, S., Julien, M., Theillet, F. X., Ropars, V., Sessa, G., Beaurepere, R., Boucherit, V., Duchambon, P., El Marjou, A., Zinn-Justin, S., Carreira, A. (2020). Proper chromosome alignment depends on BRCA2 phosphorylation by PLK1. *Nat Commun*14;11(1):1819
85. Lo, T., Pellegrini, L., Venkitaraman, A. R, Blundell, T. L. (2003) Sequence fingerprints in BRCA2 and RAD51: implications for DNA repair and cancer. *DNA Repair (Amst)*. 2, 1015–1028
86. Martinez, J. S., Baldeyron, C., Carreira, A. (2015) Molding BRCA2 function through its interacting partners. *Cell Cycle* 14, 3389–3395
87. Carreira, A., Kowalczykowski, S. C. (2009). Shining light on the regulation of DNA-binding selectivity by RAD51. *Cell Cycle*1;8(21):3445-7
88. Yang, H., Li, Q., Fan, J., Holloman, W.K., Pavletich, N.P. (2005) The BRCA2 homologue Brh2 nucleates RAD51 filament formation at a dsDNA-ssDNA junction. *Nature.* 10;433(7026):653-7
89. Sánchez, H., Paul, M. W., Grosbart, M., van Rossum-Fikkert, S.E., Lebbink, J. H. G., Kanaar, R.,4, Houtsmuller, A. B., Wyman, C. (2017) Architectural plasticity of human BRCA2-RAD51 complexes in DNA break repair. *Nucleic Acids Res.* 5;45(8):4507-4518
90. Julien, M., Miron, S., Carreira, A., Theillet, F. X., Zinn-Justin, S. (2020). 1H, 13C and 15N backbone resonance assignment of the human BRCA2 N-terminal region. *Biomol NMR Assign.* 14(1):79-85
91. Xia, B., Sheng, Q., Nakanishi, K., Ohashi, A., Wu, J., Christ, N. Livingston, D. M. (2006). Control of BRCA2 cellular and clinical functions by a nuclear partner, PALB2. *Mol Cell* 22, 719–729.
92. Sy, S. M., Huen, M. S., Zhu, Y., & Chen, J. (2009). PALB2 regulates recombinational repair through chromatin association and oligomerization. *J Biol Chem* 284, 18302–18310.

93. Sy, S. M., Huen,M. S., Chen, J. (2009). PALB2 is an integral component of the BRCA complex required for homologous recombination repair. *Proc Natl Acad Sci U S A* 106, 7155–7160
94. Buisson, R., Dion-Cote, A.M., Coulombe, Y., Launay, H., Cai, H., Stasiak, A. Z. Masson, J. Y. (2010). Cooperation of breast cancer proteins PALB2 and piccolo BRCA2 in stimulating homologous recombination. *Nat Struct Mol Biol* 17, 1247–1254.
95. Hou, J., Wang, Z., Yang, L., Guo, X., Yang, G. (2014). The function of EMSY in cancer development. *Tumour Biol. J. Int. Soc. Oncodev. Biol. Med.* 35, 5061–5066
96. Zitouni, S., Nabais, C., Jana, S. C., Guerrero, A., Bettencourt-Dias, M. (2014) Polo-like kinases: structural variations lead to multiple functions. *Nat Rev Mol Cell Biol* 15, 433–452
97. Lin, H.-R., Ting, N. S. Y., Qin, J. & Lee, W.-H. (2003). M phase-specific phosphorylation of BRCA2 by Polo-like kinase 1 correlates with the dissociation of the BRCA2-P/CAF complex. *J Biol Chem* 278, 35979–35987
98. Lee, M., Daniels, M. J. & Venkitaraman, A. R. (2004). Phosphorylation of BRCA2 by the Polo-like kinase Plk1 is regulated by DNA damage and mitotic progression. *Oncogene* 23, 865–872
99. Takaoka, M., Saito, H., Takenaka, K., Miki, Y., Nakanishi A. (2014) BRCA2 phosphorylated by PLK1 moves to the midbody to regulate cytokinesis mediated by nonmuscle myosin IIC. *Cancer Res* 74:1518-28
100. Yata, K., Bleuyard, J. Y., Nakato, R., Ralf, C., Katou, Y., Schwab, R.A., Niedzwiedz, W., Shirahige, K., Esashi, F. (2014) BRCA2 coordinates the activities of cell-cycle kinases to promote genome stability. *Cell Reports* 7:1547-59
101. Suijkerbuijk, S. J. E., Vleugel, M., Teixeira, A., Kops, G. J. P. L. (2012) Integration of kinase and phosphatase activities by BUBR1 ensures formation of stable kinetochore-microtubule attachments. *Developmental Cell* 23, 745–755
102. Choi, E., Park, P. G., Lee, H. O, Lee, Y.K. , Kang, G. H., Lee, J. W., Han, W., Lee, H. C., Noh, D. Y., Lekomtsev, S. et al. (2012). BRCA2 fine-tunes the spindle assembly checkpoint through reinforcement of BubR1 acetylation. *Developmental Cell* 22:295-308
103. Shin, S., Verma, I. M. (2003) BRCA2 cooperates with histone acetyltransferases in androgen receptor-mediated transcription. *Proc Natl Acad Sci USA* 100:7201-6

104. Mondal, G., Rowley, M., Guidugli, L., Wu, J., Pankratz, V.S., Couch, F.J. (2012). BRCA2 localization to the midbody by filamin A regulates cep55 signaling and completion of cytokinesis. *Developmental Cell* 23:137-52
105. von Nicolai, C., Ehlén, Å., Martin, C., Zhang, X., Carreira, A. (2016). A second DNA binding site in human BRCA2 promotes homologous recombination. *Nat Commun.* 15;7:12813.
106. Yuan, S. S., Lee, S. Y., Chen, G., Song, M., Tomlinson, G. E., Lee, E. Y. (1999) BRCA2 is required for ionizing radiation-induced assembly of Rad51 complex in vivo. *Cancer Res.* 1;59(15):3547-51
107. Carreira, A., Hilario, J., Amitani, I., Baskin, R., Shivji, M. K., Venkitaraman, A.R., Kowalczykowski, S.C. (2009) The BRC repeats of BRCA2 modulate the DNA-binding selectivity of RAD51. *Cell.* 20;136(6):1032-43
108. Carreira, A. & Kowalczykowski, S. C. (2011), Two classes of BRC repeats in BRCA2 promote RAD51 nucleoprotein filament function by distinct mechanisms. Proc. Natl. Acad. Sci. U. S. A. 108, 10448–53.
109. Han, X., Saito, H., Miki, Y., Nakanishi, A. A. (2008). CRM1-mediated nuclear export signal governs cytoplasmic localization of BRCA2 and is essential for centrosomal localization of BRCA2. *Oncogene* 27:2969-77
110. Lee, M., Daniels, M. J., Garnett, M. J., Venkitaraman, A. R. (2011) A mitotic function for the high-mobility group protein HMG20b regulated by its interaction with the BRC repeats of the BRCA2 tumor suppressor. *Oncogene* 2011; 30:3360-9
111. Yang, H., Jeffrey, P. D., Miller, J., Kinnucan, E., Sun, Y., Thoma, N. H., Zheng, N., Chen, P. L., Lee, W. H., Pavletich N. P. (2002) BRCA2 function in DNA binding and recombination from a BRCA2-DSS1-ssDNA structure. *Science* 297:1837-48
112. San Filippo, J., Chi, P., Sehorn, M.G., Etchin, J., Krejci, L., Sung, P. (2006). Recombination mediator and Rad51 targeting activities of a human BRCA2 polypeptide. *J Biol Chem* 281:11649-57
113. Li, J., Zou, C., Bai, Y., Wazer, D. E., Band, V., Gao, Q. (2005) DSS1 is required for the stability of BRCA2. *Oncogene* 25:1186-94
114. Jeyasekharan, A.D., Liu, Y., Hattori, H., Pisupati, V., Jonsdottir, A.B., Rajendra, E., Lee, M., Sundaramoorthy, E., Schlachter, S., Kaminski, C.F. et al. (2013) A

cancer-associated BRCA2 mutation reveals masked nuclear export signals controlling localization. *Nat Struct Mol Biol* 20:1191-8

115. Liu, J., Doty, T., Gibson, B., Heyer, W. D. (2010) Human BRCA2 protein promotes RAD51 filament formation on RPA-covered single-stranded DNA. *Nat. Struct. Mol. Biol.* 17:1260–1262
116. Zhao, W., Vaithiyalingam, S., San Filippo, J., Maranon, D.G., Jimenez-Sainz, J., Fontenay, G.V., Kwon, Y., Leung, S.G., Lu, L., Jensen R.B. et al. (2015). Promotion of BRCA2-dependent homologous recombination by DSS1 via RPA targeting and DNA mimicry. *Mol. Cell.* 59:176–187
117. Thorslund, T., Esashi, F., West, S.C. (2007) Interactions between human BRCA2 protein and the meiosis-specific recombinase DMC1. *EMBO J* 20;26(12):2915-22
118. Martinez, J. S., von Nicolai, C., Kim, T., Ehlén, Å., Mazin, A.V., Kowalczykowski, S. C., Carreira, A. BRCA2 regulates DMC1-mediated recombination through the BRC repeats. (2016) *Proc Natl Acad Sci U S A* 29;113(13):3515-20
119. Rajagopalan, S., Andreeva, A., Rutherford, T.J., Fersht, A.R.(2010) Mapping the physical and functional interactions between the tumor suppressors p53 and BRCA2. *Proc Natl Acad Sci USA* 107:8587-92
120. Esashi, F., Christ, N., Gannon, J., Liu, Y., Hunt, T., Jasin, M., West, S.C. (2005) CDK-dependent phosphorylation of BRCA2 as a regulatory mechanism for recombinational repair. *Nature* 434:598-604
121. Spain, B.H., Larson, C.J., Shihabuddin, L.S., Gage, F.H., Verma, I.M. (1999) Truncated BRCA2 is cytoplasmic: implications for cancer-linked mutations. *Proc Natl Acad Sci USA* 96:13920-5
122. Rahman, N., Stratton, M.R. (1998) The genetics of breast cancer susceptibility. *Annu. Rev. Genet.* 32:95–121.
123. Welcsh, P.L., King, M.C. (2001) BRCA1 and BRCA2 and the genetics of breast and ovarian cancer. *Hum. Mol. Genet.* 10:705–713
124. Cline, M.S., Liao, R.G., Parsons, M.T., Paten, B., Alquaddoomi, F., Antoniou, A. Baxter, S., Brody, L., Cook-Deegan, R., Coffin, A. et al. (2018) BRCA Challenge: BRCA Exchange as a global resource for variants in BRCA1 and BRCA2. *PLoS Genet.* 14:e1007752
125. ClinVar, https://www.ncbi.nlm.nih.gov/clinvar
126. Anczuków, O., Ware, M. D., Buisson, M., Zetoune, A. B., Stoppa-Lyonnet, D., Sinilnikova, O. M., Mazoyer, S. (2008) Does the nonsense-mediated mRNA de-

cay mechanism prevent the synthesis of truncated BRCA1, CHK2, and p53 proteins? *Hum Mutat*. 29(1):65-73.

127. Friedman, L.S., Thistlethwaite, F.C., Patel, K.J., Yu, V.P., Lee, H., Venkitaraman, A.R., Abel, K.J., Carlton, M.B., Hunter, S.M., Colledge, W.H. et al. (1998) Thymic lymphomas in mice with a truncating mutation in Brca2, *Cancer Res.* 58:1338–1343.
128. Chen, P. L., Chen, C. F., Chen, Y., Xiao, J., Sharp, Z. D. Lee, W. H. (1998). The BRC repeats in BRCA2 are critical for RAD51 binding and resistance to methyl methanesulfonate treatment. *Proc Natl Acad Sci U S A.* 28;95(9):5287-92
129. Yu, V. P., Koehler, M., Steinlein, C., Schmid, M., Hanakahi, L. A., van Gool, A. J., West, S. C., Venkitaraman, A. R. (2000) Gross chromosomal rearrangements and genetic exchange between nonhomologous chromosomes following BRCA2 inactivation. *Genes Dev.* 1;14(11):1400-6
130. Xia, F., Taghian, D. G., DeFrank, J. S., Zeng, Z. C., Willers, H., Iliakis, G., Powell, S. N. (2001). Deficiency of human BRCA2 leads to impaired homologous recombination but maintains normal nonhomologous end joining. *Proc Natl Acad Sci U S A.* 17;98(15):8644-9
131. Tutt, A., Bertwistle, D., Valentine, J., Gabriel, A., Swift, S., Ross, G., Griffin, C., Thacker, J., Ashworth, A. (2001). Mutation in Brca2 stimulates error-prone homology-directed repair of DNA double-strand breaks occurring between repeated sequences. *EMBO J.* 3;20(17):4704-16
132. Alexandrov, L. B. et al. (2013) Signatures of mutational processes in human cancer. *Nature.* 22;500(7463):415-21.
133. Lomonosov, M., Anand, S., Sangrithi, M., Davies, R., and Venkitaraman, A.R. (2003). Stabilization of stalled DNA replication forks by the BRCA2 breast cancer susceptibility protein. *Genes Dev.* 17, 3017-3022.
134. Daly, P.A., Ford, D., Easton, D.F. et al. (1995) Consistent loss of the wild type allele in breast cancers from a family linked to the BRCA2 gene on chromosome 13q12-13 *Oncogene* 10:1673–1675
135. Gudmundsson, J., Johannesdottir, G., Bergthorsson, J.T., Arason, A., Ingvarsson, S., Egilsson, V., Barkardottir, R.B. (1995) Different tumor types from BRCA2 carriers show wild-type chromosome deletions on 13q12-q13. *Cancer Res.* 55:4830–4832.

136. Merajver, S.D., Frank, T.S., Xu, J., Pham, T.M., Calzone, K.A., Bennett-Baker, P., Chamberlain, J., Boyd, J., Garber, J.E., Collins, F.S. (1995) Germline BRCA1 mutations and loss of the wild-type allele in tumors from families with early onset breast and ovarian cancer. *Clin. Cancer Res. Off. J. Am. Assoc. Cancer Res.* 1:539–544

137. Maxwell, K. N., Wubbenhorst, B., Wenz, B. M., De Sloover, D., Pluta, J., Emery, L. et al. (2017). BRCA locus-specific loss of heterozygosity in germline BRCA1 and BRCA2 carriers. *Nat Commun.* 22;8(1):319

138. Tan, S.L., Chadha, S., Liu, Y., Gabasova, E., Perera, D., Ahmed, K., Constantinou, S., Renaudin, X., Lee, M.Y., Aebersold, R., et al. (2017). A class of environmental and endogenous toxins induces BRCA2 haploinsufficiency and genome instability. *Cell* 169, 1105–1118 e15.

139. Goldgar, D. E., Easton, D. F., Deffenbaughm A. M., Monteiro, A. N., Tavtigian, S. V., Couch, F. J., et al. (2004) Integrated evaluation of DNA sequence variants of unknown clinical significance: application to BRCA1 and BRCA2. *Am J Hum Genet.* 75(4):535–44

140. Spurdle, A. B., Healey, S., Devereau, A., Hogervorst, F. B., Monteiro, A. N., Nathanson, K. L., et al. (2012). ENIGMA--evidence-based network for the interpretation of germline mutant alleles: an international initiative to evaluate risk and clinical significance associated with sequence variation in BRCA1 and BRCA2 genes. *Hum Mutat.* 33(1):2–7

141. Parsons, M. T., Tudini, E., Li, H., Hahnen, E., Wappenschmidt, B., Feliubadaló, L., et al. (2019) Large scale multifactorial likelihood quantitative analysis of BRCA1 and BRCA2 variants: an ENIGMA resource to support clinical variant classification. *Hum Mutat.* 40(9):1557–78

142. Goldgar, D. E., Easton, D. F., Byrnes, G. B., Spurdle, A. B., Iversen, E. S., Greenblatt, M. S., et al. (2008) Genetic evidence and integration of various data sources for classifying uncertain variants into a single model. *Hum Mutat.* 29(11):1265–72.

143. Cline, M. S., Liao, R. G., Parsons, M. T., Paten, B., Alquaddoomi, F., Antoniou, A., et al.(2018). BRCA challenge: BRCA exchange as a global resource for variants in BRCA1 and BRCA2. *PLoS Genet.* 14(12):e1007752.

144. MacArthur, D. G., Manolio, T. A., Dimmock, D. P., Rehm, H. L., Shendure, J., Abecasis, G. R., et al. (2014) Guidelines for investigating causality of sequence variants in human disease. *Nature.* 508(7497):469–76

145. Guidugli, L., Carreira, A., Caputo, S. M., Ehlen, A., Galli, A., Monteiro, A. N., et al. (2014) Functional assays for analysis of variants of uncertain significance in BRCA2. *Hum Mutat.* 35(2):151–64.

146. Toland, A. E., Andreassen, P. R. (2017) DNA repair-related functional assays for the classification of BRCA1 and BRCA2 variants: a critical review and needs assessment. *J Med Genet.* 54(11):721–31.

147. Farmer, H., McCabe, N., Lord, C. J., Tutt, A. N. J., Johnson, D. A., Richardson, T. B., Santarosa, M., Dillon, K. J., Hickson, I. D., Knights, C., Martin, N. M .B., Jackson, S. P., Smith, G. C. M., Ashworth, A. (2005). Targeting the DNA repair defect in BRCA mutant cells as a therapeutic strategy. *Nature* 434, 917–921.

148. Bryant, H. E., Schultz, N., Thomas, H. D., Parker, K. M., Flower, D., Lopez, E., Kyle, S., Meuth, M., Curtin, N. J., Helleday, T. (2005). Specific killing of BRCA2-deficient tumours with inhibitors of poly(ADP-ribose) polymerase. *Nature* 434, 913–917.

149. Guidugli, L., Pankratz, V. S., Singh, N., Thompson, J., Erding, C. A., Engel, C., et al. (2013) A classification model for BRCA2 DNA binding domain missense variants based on homology-directed repair activity. *Cancer Res.* 73(1):265–75.

150. Mesman, R. L. S., Calléja, F. M. G. R., Hendriks, G., Morolli, B., Misovic, B., Devilee, P., et al. (2019) The functional impact of variants of uncertain significance in BRCA2. *Genet Med.* 21(2):293–302.

151. Kuznetsov, S. G., Liu, P., Sharan, S. K. (2008) Mouse embryonic stem cell-based functional assay to evaluate mutations in BRCA2. *Nat Med.* 14(8):875–81.

152. Farrugia, D. J., Agarwal, M. K., Pankratz, V. S., Deffenbaugh, A. M., Pruss, D., Frye, C., et al. (2008) Functional assays for classification of BRCA2 variants of uncertain significance. *Cancer Res.* 68(9):3523–31.

153. Wu, K., Hinson, S. R., Ohashi, A., Farrugia, D., Wendt, P., Tavtigian, S. V., et al. (2005) Functional evaluation and cancer risk assessment of BRCA2 unclassified variants. *Cancer Res.* 65(2):417–26.

154. Barwell, J., Pangon, L., Georgiou, A., Kesterton, I., Langman, C., Arden-Jones, A., et al. (2007). Lymphocyte radiosensitivity in BRCA1 and BRCA2 mutation

carriers and implications for breast cancer susceptibility. *Int J Cancer.* 121(7):1631–6.

155. Lim, D.S. & Hasty, P. (1996). A mutation in mouse rad51 results in an early embryonic lethal that is suppressed by a mutation in p53. *Mol. Cell. Biol.* 16, 7133–7143
156. Ludwig, T., Chapman, D.L., Papaioannou, V.E. & Efstratiadis, A. (1997) Targeted mutations of breast cancer susceptibility gene homologs in mice: lethal phenotypes of Brca1, Brca2, Brca1/Brca2, Brca1/p53, and Brca2/p53 nullizygous embryos. *Genes Dev.* 11, 1226–1241
157. Chen, C. F., Chen, P. L., Zhong, Q., Sharp, Z. D. & Lee, W. H.(1999). Expression of BRC repeats in breast cancer cells disrupts the BRCA2-Rad51 complex and leads to radiation hypersensitivity and loss of G(2)/M checkpoint control. *J. Biol. Chem.* 274, 32931–32935
158. Morimatsu, M., Donoho, G. & Hasty, P. (1998). Cells deleted for Brca2 COOH terminus exhibit hypersensitivity to gamma-radiation and premature senescence. *Cancer Res.* 58,3441–3447
159. Pellegrini, L. , Yu, D. S., Lo, T., Anand, S., Lee, M., Blundell, T. L., Venkitaraman, A. R. (2002). Insights into DNA recombination from the structure of a RAD51-BRCA2 complex. *Nature* 420, 287–293
160. Saeki, H., Siaud, N., Christ, N., Wiegant, W. W., van Buul, P. P., Han, M., Zdzienicka M. Z., Stark, J. M., Jasin, M. (2006). Suppression of the DNA repair defects of BRCA2-deficient cells with heterologous protein fusions. *Proc Natl Acad Sci U S A.* 6;103(23):8768-73
161. Shivji, M. K., Davies, O. R., Savill, J. M., Bates, D. L., Pellegrini, L., Venkitaraman, A. R. (2006) A region of human BRCA2 containing multiple BRC repeats promotes RAD51-mediated strand exchange. *Nucleic Acids Res.* 34(14):4000-11
162. Shivji, M. K., Mukund, S. R., Rajendra, E., Chen, S., Short, J. M., Savill, J., Klenerman, D., Venkitaraman, A. R. (2009) The BRC repeats of human BRCA2 differentially regulate RAD51 binding on single- versus double-stranded DNA to stimulate strand exchange. *Proc Natl Acad Sci U S A.* 11;106(32):13254-9
163. Shahid, T., Soroka, J., Kong, E., Malivert, L., McIlwraith, M., Pape, T., West, S. C., Zhang, X. (2014) Structure and mechanism of action of the BRCA2 breast cancer tumor suppressor. *Nat Struct Mol Biol.* 21(11):962-968

164. Hashimoto, Y., Ray Chaudhuri, A., Lopes, M., Costanzo, V. (2010). Rad51 protects nascent DNA from Mre11-dependent degradation and promotes continuous DNA synthesis. *Nat Struct Mol Biol.* 17(11):1305-11

165. Ray Chaudhuri, A. et al. (2016). Replication fork stability confers chemoresistance in BRCA-deficient cells. *Nature* 535, 382–387

166. Ying, S., Hamdy, F. C., Helleday, T. (2012). Mre11-dependent degradation of stalled DNA replication forks is prevented by BRCA2 and PARP1. *Cancer Res.* 1;72(11):2814-21

167. Kolinjivadi, A.M., Sannino, V., De Antoni, A., Zadorozhny, K., Kilkenny, M., Técher, H., Baldi, G., Shen, R., Ciccia, A., Pellegrini, L., Krejci, L., Costanzo, V. (2017). Smarcal1-mediated fork reversal triggers Mre11-dependent degradation of nascent DNA in the absence of Brca2 and stable Rad51 nucleofilaments. *Mol. Cell* 67, 867–881.e7

168. Lemacon, .D., Jackson, J., Quinet, A., Brickner, J. R., Li, S., Yazinski, S., You, Z., Ira, G., Zou, L., Mosammaparast, N., Vindigni, A. (2017). MRE11 and EXO1 nucleases degrade reversed forks and elicit MUS81-dependent fork rescue in BRCA2-deficient cells. *Nat. Commun.* 8, 860

169. Mijic, S., Zellweger, R., Chappidi, N., Berti, M., Jacobs, K., Mutreja, K., Ursich, S., Ray Chaudhuri, A., Nussenzweig, A., Janscak, P., Lopes, M. (2017). Replication fork reversal triggers fork degradation in BRCA2-defective cells. *Nat. Commun.* 8, 859

170. Taglialatela, A., Alvarez, S., Leuzzi, G., Sannino, V., Ranjha, L., Huang, J. W., Madubata, C., Anand, R., Levy, B., Rabadan, R., Cejka, P., Costanzo, V., Ciccia, A. (2017). Restoration of replication fork stability in BRCA1- and BRCA2-deficient cells by inactivation of SNF2- family fork remodelers. *Mol. Cell* 68, 414–430.e8

171. Neelsen, K. J. and Lopes, M. (2015). Replication fork reversal in eukaryotes: from dead end to dynamic response. *Nat. Rev. Mol. Cell Biol.* 16, 207–220

172. Przetocka, S., Porro, A., Bolck, H., Walker, C., Lezaja, A., Trenner, A., von Aesch, C., Himmels, S. F., D'Andrea, A. D., Ceccaldi, R., Altmeyer, M., Sartori, A. A. (2018). CtIP-mediated fork protection synergizes with BRCA1 to suppress genomic instability upon DNA replication stress. *Mol. Cell.* 72, 568–582

173. Rondinelli, B., Gogola, E., Yücel, H., Duarte, A. A., van de Ven, M., van der Sluijs, R., Konstantinopoulos, P. A., Jonkers, J., Ceccaldi, R., Rottenberg, S.,

D'Andrea, A. D. (2017) EZH2 promotes degradation of stalled replication forks by recruiting MUS81 through histone H3 trimethylation. *Nat Cell Biol.* 19(11):1371-1378.

174. Auerbach, A. D. (2009). Fanconi anemia and its diagnosis. *Mutat Res.* 31;668(1-2):4-10
175. Niraj, J., Färkkilä, A., D'Andrea, A. D. (2019). The Fanconi Anemia Pathway in Cancer. *Annu Rev Cancer Biol.* 3:457-478
176. Howlett, N. G., Taniguchi, T., Olson, S., Cox, B., Waisfisz, Q., De Die-Smulders, C., Persky, N., Grompe, M., Joenje, H., Pals, G., et al. (2002). Biallelic inactivation of BRCA2 in Fanconi anemia. *Science* 297:606-9
177. Cipak, L., Watanabe, N., Bessho, T. (2006). The role of BRCA2 in replication-coupled DNA interstrand cross-link repair in vitro. *Nat Struct Mol Biol* 13:729-33
178. Ciccia, A., Ling, C., Coulthard, R., Yan, Z. J., Xue, Y. T., Meetei, A. R., Laghmani, E. H., Joenje, H., McDonald, N., de Winter, J. P., Wang, W. D., West, S. C. (2007) Identification of FAAP24, a Fanconi anemia core complex protein that interacts with FANCM. *Mol Cell* 25: 331 – 343
179. Collis, S. J., Ciccia, A., Deans, A. J., Horejsi, Z., Martin, J. S., Maslen, S. L., Skehel, J. M., Elledge, S. J., West, S. C. Boulton, S. J. (2008). FANCM and FAAP24 function in ATRmediated checkpoint signaling independently of the Fanconi anemia core complex. *Mol Cell* 32: 313 – 324
180. Garcìa-Rubio, M. L., Perez-Calero, C., Barroso, S.I., Tumini, E., Herrera-Moyano, E., Rosado, I. V., and Aguilera, A. (2015). The Fanconi anemia pathway protects genome integrity from R-loops. *PLoS Genet.* 11, e1005674
181. Schwab, R. A., Nieminuszczy, J., Shah, F., Langton, J., Lopez-Martinez, D., Liang, C.-C., Cohn, M.A., Gibbons, R.J., Deans, A.J., and Niedzwiedz, W. (2015) The Fanconi anemia pathway maintains genome stability by coordinating replication and transcription. *Mol. Cell* 60, 351-361
182. Garcia-Muse, T. and Aguilera, A. (2016). Transcription-replication conflicts: how they occur and how they are resolved. *Nat. Rev.Mol. Cell Biol.* 17, 553-563
183. Sollier, J. and Cimprich, K.A. (2015) Breaking bad: R-loops and genome integrity. *Trends Cell Biol.* 25, 514-522
184. Okamoto, Y., et al. (2018). Replication stress induces accumulation of FANCD2 at central region of large fragile genes. *Nucleic Acids Res.* 46, 2932-2944

185. Liang, Z., Liang, F., Teng, Y., Chen, X., Liu, J., Longerich, S., Rao, T., Green, A.M., Collins, N.B., Xiong, Y., Lan, L., Sung, P., and Kupfer, G. M. (2019) Binding of FANCI-FANCD2 complex to RNA and Rloops stimulates robust FANCD2 monoubiquitination. *Cell Rep.* 26, 564-572.e5

186. Okamoto, Y., Abe, M., Itaya, A., Tomida, J., Ishiai, M., Takaori-Kondo, A., Taoka, M., Isobe, T., and Takata, M. (2019). FANCD2 protects genome stability by recruiting RNA processing enzymes to resolve R-loops during mild replication stress. *FEBS J.* 286, 139-150

187. Bhatia, V., Barroso, S. I., García-Rubio, M. L., Tumini, E., Herrera-Moyano, E., Aguilera, A. (2014) BRCA2 prevents R-loop accumulation and associates with TREX-2 mRNA export factor PCID2. *Nature.* 17;511(7509):362-5

188. Shivji, M. K. K., Renaudin, X., Williams, Ç. H., Venkitaraman, A. R. (2018). BRCA2 Regulates Transcription Elongation by RNA Polymerase II to Prevent R-Loop Accumulation. *Cell Rep.* 23;22(4):1031-1039

189. D'Alessandro, G., Whelan, D.R., Howard, S. M., Vitelli, V., Renaudin, X., Adamowicz, M., Iannelli, F., Jones-Weinert, C. W., Lee, M., Matti, V., Lee, W. T. C., Morten, M. J., Venkitaraman, A. R., Cejka, P., Rothenberg, E., d'Adda di Fagagna, F. (2018). BRCA2 controls DNA:RNA hybrid level at DSBs by mediating RNase H2 recruitment. *Nat Commun.* 18;9(1):5376

190. Morris, K. V. & Mattick, J. S. (2014). The rise of regulatory RNA. *Nat. Rev. Genet.* 15, 423–437.

191. Garcia-Muse, T. & Aguilera, A. (2019). R. Loops: from physiological to pathological roles. *Cell* 179, 604–618

192. Hegazy, Y. A., Fernando, C. M., Tran, E. J. (2020). The balancing act of R-loop biology: The good, the bad, and the ugly. *J Biol Chem.* 24;295(4):905-913

193. Ginno, P. A., Lott, P. L., Christensen, H. C., Korf, I., and Chédin, F. (2012). R-loop formation is a distinctive characteristic of unmethylated human CpG island promoters. *Mol. Cell* 45, 814–825

194. Sanz, L. A., Hartono, S. R., Lim, Y. W., Steyaert, S., Rajpurkar, A., Ginno, P. A., Xu, X., and Chédin, F. (2016). Prevalent, dynamic, and conserved R-loop structures associate with specific epigenomic signatures in mammals. *Mol. Cell* 63, 167–178

195. Roy, D., and Lieber, M. R. (2009). G clustering is important for the initiation of transcription-induced R-loops in vitro, whereas high G density without clustering is sufficient thereafter. *Mol. Cell. Biol.* 29, 3124–3133

196. Rhodes, D., and Lipps, H. J. (2015). G-quadruplexes and their regulatory roles in biology. *Nucleic Acids Res.* 43, 8627–8637

197. Chedin, F., Benham, C. J. (2020). Emerging roles for R-loop structures in the management of topological stress. *J Biol Chem.* 3;295(14):4684-4695

198. Roy, D., Zhang, Z., Lu, Z., Hsieh, C. L., and Lieber, M. R. (2010). Competition the RNA transcript and the nontemplate DNA strand during during R-loop formation in vitro: a nick can serve as a strong R-loop initiation site. *Mol. Cell. Biol.* 30, 146–159

199. Aguilera, A., García-Muse, T. (2012). R loops: from transcription byproducts to threats to genome stability. *Mol Cell.* 27;46(2):115-24

200. Jinek, M., Chylinski, K., Fonfara, I., Hauer, M., Doudna, J.A., Charpentier, E. (2012). A programmable dual-RNA-guided DNA endonuclease in adaptive bacterial immunity. *Science* 337, 816–821.

201. Grunseich, C., Wang, I. X., Watts, J. A., Burdick, J. T., Guber, R. D., Zhu, Z., Bruzel, A., Lanman, T., Chen, K., Schindler, A. B., Edwards, N., Ray-Chaudhury, A., Yao, J., Lehky, T., Piszczek, G., Crain, B., Fischbeck, K. H., Cheung, V. G. (2018) Senataxin Mutation Reveals How R-Loops Promote Transcription by Blocking DNA Methylation at Gene Promoters. *Mol Cell*. 1;69(3):426-437.

202. Sun, Q., Csorba, T., Skourti-Stathaki, K., Proudfoot, N. J., Dean, C. (2013). R-loop stabilization represses antisense transcription at the Arabidopsis FLC locus. *Science* 340, 619–621.

203. Cloutier, S. C., Wang, S., Ma, W. K., Al Husini, N., Dhoondia, Z., Ansari, A., Pascuzzi, P. E., Tran, E. J. (2016). Regulated Formation of lncRNA-DNA Hybrids Enables Faster Transcriptional Induction and Environmental Adaptation. *Mol. Cell* 61, 393–404.

204. Boque-Sastre, R., Soler, M., Oliveira-Mateos, C., Portela, A., Moutinho, C., Sayols, S., Villanueva, A., Esteller, M., Guil, S. (2015). Head-to-head antisense transcription and R-loop formation promotes transcriptional activation. *Proc. Natl. Acad. Sci. USA* 112, 5785–5790.

205. Arab, K., Karaulanov, E., Musheev, M., Trnka, P., Schafer, A., Grummt, I., Niehrs, C. (2019). GADD45A binds R-loops and recruits TET1 to CpG island promoters. *Nat. Genet.* 51, 217–223.
206. Skourti-Stathaki, K., Proudfoot, N. J., Gromak, N. (2011). Human senataxin resolves RNA/DNA hybrids formed at transcriptional pause sites to promote Xrn2-dependent termination. *Mol. Cell* 42, 794–805.
207. Morales, J. C., Richard, P., Patidar, P. L., Motea, E. A., Dang, T. T., Manley, J. L. Boothman, D.A. (2016). XRN2 Links Transcription Termination to DNA Damage and Replication Stress. *PLoS Genet.* 12, e1006107.
208. Chakraborty, P., Huang, J. T. J., and Hiom, K. (2018). DHX9 helicase promotes R-loop formation in cells with impaired RNA splicing. *Nat. Commun*. 9, 4346.
209. Ribeiro de Almeida, C., Dhir, S., Dhir, A., Moghaddam, A. E., Sattentau, Q., Meinhart, A., and Proudfoot, N.J. (2018). RNA Helicase DDX1 Converts RNA G-Quadruplex Structures into R-Loops to Promote IgH Class Switch Recombination. *Mol. Cell* 70, 650–662.
210. Huertas, P., and Aguilera, A. (2003). Cotranscriptionally formed DNA:RNA hybrids mediate transcription elongation impairment and transcription-associated recombination. *Mol. Cell* 12, 711–721.
211. Li, X., and Manley, J. L. (2005). Inactivation of the SR protein splicing factor ASF/SF2 results in genomic instability. *Cell* 122, 365–378.
212. Paulsen, R .D., Soni, D. V., Wollman, R., Hahn, A. T., Yee, M. C., Guan, A., Hesley, J. A., Miller, S. C., Cromwell, E. F., Solow-Cordero, D. E., et al. (2009). A genome-wide siRNA screen reveals diverse cellular processes and pathways that mediate genome stability. *Mol. Cell* 35, 228–239.
213. Gan, W., Guan, Z., Liu, J., Gui, T., Shen, K., Manley, J. L., and Li, X. (2011). Rloop-mediated genomic instability is caused by impairment of replication fork progression. *Genes Dev.* 25, 2041–2056.
214. Wellinger, R. E., Prado, F., Aguilera, A. (2006). Replication fork progression is impaired by transcription in hyperrecombinant yeas cells lacking a functional THO complex. *Mol Cell Biol* 26:3327–3334
215. Gómez-González, B., García-Rubio, M., Bermejo, R., Gaillard, H., Shirahige, K., Marín, A., Foiani, M., Aguilera, A. (2011). Genomewide function of THO/TREX in active genes prevents Rloop-dependent replication obstacles. *EMBO J* 30: 3106–3119

216. García-Rubio, M. L., Pérez-Calero, C., Barroso, S. I., Tumini, E., Herrera-Moyano, E., Rosado, I. V., Aguilera, A. (2015). The Fanconi anemia pathway protects genome integrity from R-loops. *PLoS Genet* 11: e1005674
217. Schwab, R. A., Nieminuszczy, J., Shah, F., Langton, J., Lopez Martinez, D., Liang, C. C., Cohn, M. A., Gibbons, R. J., Deans, A. J., and Niedzwiedz, W. (2015). The Fanconi Anemia Pathway Maintains Genome Stability by Coordinating Replication and Transcription. *Mol. Cell* 60, 351–361.
218. Stork, C. T., Bocek, M., Crossley, M. P., Sollier, J., Sanz, L. A., Chedin, F., Swigut, T., and Cimprich, K. A. (2016). Co-transcriptional R-loops are the main cause of estrogen-induced DNA damage. *eLife* 5, e17548.
219. Kotsantis, P., Silva, L. M., Irmscher, S., Jones, R. M., Folkes, L., Gromak, N., and Petermann, E. (2016). Increased global transcription activity as a mechanism of replication stress in cancer. *Nat. Commun*. 7, 13087.
220. Domínguez-Sánchez, M. S., Barroso, S., Gómez-González, B., Luna, R., Aguilera, A. (2011). Genome instability and transcription elongation impairment in human cells depleted of THO/TREX. *PLoS Genet.* 7(12):e1002386
221. Tuduri, S., Crabbé, L., Conti, C., Tourrière, H., Holtgreve-Grez, H., Jauch, A., Pantesco, V., De Vos, J., Thomas, A., Theillet, C., et al. (2009). Topoisomerase I suppresses genomic instability by preventing interference between replication and transcription. *Nat Cell Biol* 11: 1315–1324
222. Herrera-Moyano, E., Mergui, X., Garcıa-Rubio, M. L., Barroso, S., and Aguilera, A. (2014). The yeast and human FACT chromatin-reorganizing complexes solve R-loop-mediated transcription-replication conflicts. *Genes Dev.* 28,735–748.
223. Lang, K. S., Hall, A. N., Merrikh, C. N., Ragheb, M., Tabakh, H., Pollock, A. J., Woodward, J. J., Dreifus, J. E., and Merrikh, H. (2017). Replication-Transcription Conflicts Generate R-Loops that Orchestrate Bacterial Stress Survival and Pathogenesis. *Cell* 170, 787–799.
224. Garcıa-Rubio, M., Aguilera, P., Lafuente-Barquero, J., Ruiz, J. F., Simon, M. N., Geli, V., Rondon, A. G., and Aguilera, A. (2018). Yra1-bound RNA-DNA hybrids cause orientation-independent transcription-replication collisions and telomere instability. *Genes Dev.* 32, 965–977.
225. Costantino, L., and Koshland, D. (2018). Genome-wide Map of R-Loop Induced Damage Reveals How a Subset of R-Loops Contributes to Genomic Instability. *Mol. Cell* 71, 487–497.

226. Crossley, M. P., Bocek, M., Cimprich, K. A. (2019). R-Loops as Cellular Regulators and Genomic Threats. *Mol Cell.* 7;73(3):398-411

227. Sollier, J., Stork, C. T., Garcıa-Rubio, M. L., Paulsen, R. D., Aguilera, A., and Cimprich, K.A. (2014). Transcription-coupled nucleotide excision repair factors promote R-loop-induced genome instability. *Mol. Cell* 56, 777–785.

228. Yasuhara, T., Kato, R., Hagiwara, Y., Shiotani, B., Yamauchi, M., Nakada, S., Shibata, A., and Miyagawa, K. (2018). Human Rad52 Promotes XPG-Mediated R-loop Processing to Initiate Transcription-Associated Homologous Recombination Repair. *Cell* 175, 558–570.e11.

229. Drolet, M., Phoenix, P., Menzel, R., Masse, E., Liu, L. F., and Crouch, R. J. (1995). Overexpression of RNase H partially complements the growth defect of an Escherichia coli delta topA mutant: R-loop formation is a major problem in the absence of DNA topoisomerase I. *Proc. Natl. Acad. Sci. USA* 92, 3526–3530.

230. El Hage, A., French, S. L., Beyer, A. L., and Tollervey, D. (2010). Loss of Topoisomerase I leads to R-loop-mediated transcriptional blocks during ribosomal RNA synthesis. *Genes Dev.* 24, 1546–1558.

231. Garcia-Pichardo, D., Canas, J. C., Garcia-Rubio, M. L., Gomez-Gonzalez, B., Rondon, A. G., and Aguilera, A. (2017). Histone Mutants Separate R Loop Formation from Genome Instability Induction. *Mol. Cell* 66, 597–609.

232. Salas-Armenteros, I., Perez-Calero, C., Bayona-Feliu, A., Tumini, E., Luna, R. and Aguilera, A. (2017). Human THO-Sin3A interaction reveals new mechanisms to prevent R-loops that cause genome instability. *EMBO J.* 36,3532–3547

233. Chen, L., Chen, J. Y., Zhang, X., Gu, Y., Xiao, R., Shao, C., Tang, P., Qian, H., Luo, D., Li, H., et al. (2017). R-ChIP Using Inactive RNase H Reveals Dynamic Coupling of R-loops with Transcriptional Pausing at Gene Promoters. *Mol. Cell* 68, 745–757.

234. Lockhart, A., Pires, V. B., Bento, F., Kellner, V., Luke-Glaser, S., Yakoub, G., Ulrich, H. D., Luke, B. (2019) RNase H1 and H2 Are Differentially Regulated to Process RNA-DNA Hybrids. *Cell Rep.* 26;29(9):2890-2900.e5

235. Wahba, L., Amon, J.D., Koshland, D., and Vuica-Ross, M. (2011). RNase H and multiple RNA biogenesis factors cooperate to prevent RNA:DNA hybrids from generating genome instability. *Mol. Cell* 44, 978–988.

236. Hatchi, E., Skourti-Stathaki, K., Ventz, S., Pinello, L., Yen, A., Kamieniarz-Gdula, K., Dimitrov, S., Pathania, S., McKinney, K. M., Eaton, M. L., et al.

(2015). BRCA1 recruitment to transcriptional pause sites is required for R-loop-driven DNA damage repair. *Mol. Cell* 57, 636–647.

237. Zhang, X., Chiang, H. C., Wang, Y., Zhang, C., Smith, S., Zhao, X., Nair, S. J., Michalek, J., Jatoi, I., Lautner, M., et al. (2017). Attenuation of RNA polymerase II pausing mitigates BRCA1-associated R-loop accumulation and tumorigenesis. *Nat. Commun*. 8, 15908.
238. Hodroj, D., Recolin, B., Serhal, K., Martinez, S., Tsanov, N., Abou Merhi, R., and Maiorano, D. (2017). An ATR-dependent function for the Ddx19 RNA helicase in nuclear R-loop metabolism. *EMBO J*. 36, 1182–1198.
239. Li, L., Germain, D.R., Poon, H.Y., Hildebrandt, M.R., Monckton, E.A., McDonald, D., Hendzel, M.J., and Godbout, R. (2016). DEAD Box 1 Facilitates Removal of RNA and Homologous Recombination at DNA Double Strand Breaks. *Mol. Cell. Biol.* 36, 2794–2810.
240. Mischo, H.E., Gomez-Gonzalez, B., Grzechnik, P., Rondo´ n, A.G., Wei, W., Steinmetz, L., Aguilera, A., and Proudfoot, N.J. (2011). Yeast Sen1 helicase protects the genome from transcription-associated instability. *Mol. Cell* 41, 21–32.
241. Cristini, A., Groh, M., Kristiansen, M.S., and Gromak, N. (2018). RNA/DNA Hybrid Interactome Identifies DXH9 as a Molecular Player in Transcriptional Termination and R-Loop-Associated DNA Damage. *Cell Rep.* 23, 1891–1905.
242. Sridhara, S. C., Carvalho, S., Grosso, A. R., Gallego-Paez, L. M., Carmo-Fonseca, M., and de Almeida, S. F. (2017). Transcription Dynamics Prevent RNA-Mediated Genomic Instability through SRPK2-Dependent DDX23 Phosphorylation. *Cell Rep.* 18, 334–343.
243. Tedeschi, F. A., Cloutier, S. C., Tran, E. J., and Jankowsky, E. (2018). The DEADbox protein Dbp2p is linked to noncoding RNAs, the helicase Sen1p, and R-loops. *RNA* 24, 1693–1705
244. Song, C., Hotz-Wagenblatt, A., Voit, R., Grummt, I. (2017) SIRT7 and the DEAD-box helicase DDX21 cooperate to resolve genomic R loops and safeguard genome stability. *Genes Dev.* 1;31(13):1370-1381
245. Wang, I. X., Grunseich, C., Fox, J., Burdick, J., Zhu, Z., Ravazian, N., Hafner, M., and Cheung, V. G. (2018). Human proteins that interact with RNA/DNA hybrids. *Genome Res.* 28, 1405–1414

246. Hamperl, S., Bocek, M. J., Saldivar, J. C., Swigut, T., and Cimprich, K. A. (2017). Transcription-Replication Conflict Orientation Modulates R-Loop Levels and Activates Distinct DNA Damage Responses. *Cell* 170, 774–786.e19.

247. Tresini, M., Warmerdam, D. O., Kolovos, P., Snijder, L., Vrouwe, M. G., Demmers, J. A., van IJcken, W. F., Grosveld, F. G., Medema, R. H., Hoeijmakers, J. H., et al. (2015). The core spliceosome as target and effector of non-canonical ATM signalling. *Nature* 523, 53–58.

248. Nguyen, H.D., Yadav, T., Giri, S., Saez, B., Graubert, T.A., and Zou, L. (2017). Functions of Replication Protein A as a Sensor of R Loops and a Regulator of RNaseH1. *Mol. Cell* 65, 832–847.e4.

249. Kabeche, L., Nguyen, H. D., Buisson, R., and Zou, L. (2018). A mitosis-specific and R loop-driven ATR pathway promotes faithful chromosome segregation. *Science* 359, 108–114.

250. Yuce, O., and West, S. C. (2013). Senataxin, defective in the neurodegenerative disorder ataxia with oculomotor apraxia 2, lies at the interface of transcription and the DNA damage response. *Mol. Cell. Biol.* 33, 406–417.

251. Barroso, S., Herrera-Moyano, E., Munoz, S., Garcıa-Rubio, M., Gomez-Gonzalez, B., and Aguilera, A. (2019). The DNA damage response acts as a safeguard against harmful DNA-RNA hybrids of different origins. *EMBO Rep*. 20,e47250.

252. Aguilera, A., and Gomez-Gonzalez, B. (2017). DNA-RNA hybrids: the risks of DNA breakage during transcription. *Nat. Struct. Mol. Biol.* 24, 439–443

253. Britton, S. Dernoncourt, E., Delteil, C., Froment, C., Schiltz, O., Salles, B., Frit, P., Calsou, P. (2014). DNA damage triggers SAF-A and RNA biogenesis factors exclusion from chromatin coupled to R-loops removal. *Nucleic Acids Res.* 42, 9047–9062

254. Li, L., Monckton, E. A. & Godbout, R. (2008). A role for DEAD box 1 at DNA double-strand breaks. *Mol. Cell. Biol.* 28, 6413–6425

255. Ohle, C., Tesorero, R., Schermann, G., Dobrev, N., Sinning, I., and Fischer, T. (2016). Transient RNA-DNA Hybrids Are Required for Efficient Double-Strand Break Repair. *Cell* 167, 1001–1013.e7.

256. D'Alessandro, G., d'Adda di Fagagna, F. (2017) Transcription and DNA Damage: Holding Hands or Crossing Swords? *J Mol Biol.* 27;429(21):3215-3229

257. D'Alessandro, G., Whelan, D. R., Howard, S. M., Vitelli, V., Renaudin, X., Adamowicz, M., Iannelli, F., Jones-Weinert, C. W., Lee, M., Matti, V., et al. (2018).

BRCA2 controls DNA:RNA hybrid level at DSBs by mediating RNase H2 recruitment. *Nat. Commun.* 9, 5376.

258. Zhao, H., Zhu, M., Limbo, O., and Russell, P. (2018). RNase H eliminates R-loops that disrupt DNA replication but is nonessential for efficient DSB repair. *EMBO Rep.* 19, e45335.
259. Aymard, F., Bugler, B., Schmidt, C. K., Guillou, E., Caron, P., Briois, S., Iacovoni, J. S., Daburon, V., Miller, K. M., Jackson, S. P., and Legube, G. (2014). Transcriptionally active chromatin recruits homologous recombination at DNA double-strand breaks. *Nat. Struct. Mol. Biol.* 21, 366–374.
260. Cohen, S., Puget, N., Lin, Y. L., Clouaire, T., Aguirrebengoa, M., Rocher, V., Pasero, P., Canitrot, Y., and Legube, G. (2018). Senataxin resolves RNA:DNA hybrids forming at DNA double-strand breaks to prevent translocations. *Nat. Commun.* 9, 533.
261. Amon, J. D., and Koshland, D. (2016). RNase H enables efficient repair of R-loop induced DNA damage. *eLife* 5, e20533.
262. Makharashvili, N., Arora, S., Yin, Y., Fu, Q., Wen, X., Lee, J. H., Kao, C. H., Leung, J. W., Miller, K. M., and Paull, T. T. (2018). Sae2/CtIP prevents R-loop accumulation in eukaryotic cells. *eLife* 7, e42733.
263. Sakasai, R., Isono, M., Wakasugi, M., Hashimoto, M., Sunatani, Y., Matsui, T., Shibata, A., Matsunaga, T., and Iwabuchi, K. (2017). Aquarius is required for proper CtIP expression and homologous recombination repair. *Sci. Rep.* 7, 13808.
264. Mersaoui, S. Y., Yu, Z., Coulombe, Y., Karam, M., Busatto, F. F., Masson, J. Y., and Richard, S. (2019) Arginine methylation of the DDX5 helicase RGG/RG motif by PRMT5 regulates resolution of RNA:DNA hybrids. *EMBO J.* 38, e100986
265. Xing, Z., Wang, S., & Tran, E. J. (2017). Characterization of the mammalian DEAD-box protein DDX5 reveals functional conservation with S. cerevisiae ortholog Dbp2 in transcriptional control and glucose metabolism. *RNA*, 23(7), 1125–1138.
266. Linder, P., & Jankowsky, E. (2011). From unwinding to clamping—The DEAD box RNA helicase family. *Nature Reviews Molecular Cell Biology* 12(8), 505–516.
267. Rudolph, M. G., & Klostermeier, D. (2015). When core competence is not enough: Functional interplay of the DEAD-box helicase core with ancillary do-

mains and auxiliary factors in RNA binding and unwinding. *Biological Chemistry* 396(8), 849–865.

268. Jankowsky, E., Gross, C. H., Shuman, S., & Pyle, A. M. (2000). The DExH protein NPH-II is a processive and directional motor for unwinding RNA. *Nature* 403(6768), 447–451.
269. Jarmoskaite, I., & Russell, R. (2014). RNA helicase proteins as chaperones and remodelers. *Annual Review of Biochemistry* 83, 697–725.
270. Young, C. L., Khoshnevis, S., & Karbstein, K. (2013). Cofactor-dependent specificity of a DEAD-box protein. *Proceedings of the National Academy of Sciences of the USA* 110(29), E2668–E2676.
271. Xing, Z., Ma, W. K., Tran, E. J. (2019). The DDX5/Dbp2 subfamily of DEAD-box RNA helicases. *Wiley Interdiscip Rev RNA* 10(2):e1519
272. Hirling, H., Scheffner, M., Restle, T., & Stahl, H. (1989). RNA helicase activity associated with the human p68 protein. *Nature* 339(6225), 562–564
273. Huang, Y., & Liu, Z. R. (2002). The ATPase, RNA unwinding, and RNA binding activities of recombinant p68 RNA helicase. *Journal of Biological Chemistry* 277(15), 12810–12815.
274. Rossler, O. G., Straka, A., & Stahl, H. (2001). Rearrangement of structured RNA via branch migration structures catalysed by the highly related DEAD-box proteins p68 and p72. *Nucleic Acids Research* 29(10), 2088–2096.
275. Ma, W. K., Cloutier, S. C., and Tran, E. J. (2013). The DEAD-box protein Dbp2 functions with the RNA-binding protein Yra1 to promote mRNP assembly. *J. Mol. Biol.* 425, 3824–3838
276. Iyer, R. S., Nicol, S. M., Quinlan, P. R., Thompson, A. M., Meek, D. W., Fuller-Pace, F. V. (2014). The RNA helicase/transcriptional co-regulator, p68 (DDX5), stimulates expression of oncogenic protein kinase, Polo-like kinase-1 (PLK1), and is associated with elevated PLK1 levels in human breast cancers. *Cell Cycle* 13(9):1413-23
277. Clark, E. L., Hadjimichael, C., Temperley, R., Barnard, A., Fuller-Pace, F. V., & Robson, C. N. (2013). p68/DdX5 supports beta-catenin & RNAP II during androgen receptor mediated transcription in prostate cancer. *PLoS One* 8(1), e54150.
278. Wortham, N. C., Ahamed, E., Nicol, S. M., Thomas, R. S., Periyasamy, M., Jiang, J. et al. (2009). The DEAD-box protein p72 regulates ERalpha-/oestrogen- de-

pendent transcription and cell growth, and is associated with improved survival in ERalpha-positive breast cancer. *Oncogene* 28(46), 4053–4064.

279. Nicol, S. M., Bray, S. E., Black, H. D., Lorimore, S. A., Wright, E. G., Lane, D. P. et al. (2013). The RNA helicase p68 (DDX5) is selectively required for the induction of p53-dependent p21 expression and cell-cycle arrest after DNA damage. *Oncogene* 32(29), 3461–3469.
280. Causevic, M., Hislop, R. G., Kernohan, N. M., Carey, F. A., Kay, R. A., Steele, R. J., & Fuller-Pace, F. V. (2001). Overexpression and poly-ubiquitylation of the DEAD-box RNA helicase p68 in colorectal tumours. *Oncogene* 20(53), 7734–7743.
281. Dardenne, E., Polay Espinoza, M., Fattet, L., Germann, S., Lambert, M.-P., Neil, H. et al. (2014). RNA helicases DDX5 and DDX17 dynamically orchestrate transcription, miRNA, and splicing programs in cell differentiation. *Cell Reports* 7(6), 1900–1913
282. Geißler, V., Altmeyer, S., Stein, B., Uhlmann-Schiffler, H., & Stahl, H. (2013). The RNA helicase Ddx5/p68 binds to hUpf3 and enhances NMD of Ddx17/p72 and Smg5 mRNA. *Nucleic Acids Research* 41(16), 7875–7888.
283. Lu, W.-T., Hawley, B. R., Skalka, G. L., Baldock, R. A., Smith, E. M., Bader, A. S., Malewicz, M., Watts, F. Z., Wilczynska, A., Bushell, M. (2018). Drosha drives the formation of DNA:RNA hybrids around DNA break sites to facilitate DNA repair. *Nat Commun* 9, 532.
284. Michelini, F., Pitchiaya, S., Vitelli, V., Sharma, S., Gioia, U., Pessina, F., Cabrini, M., Wang, Y., Capozzo, I., Iannelli, F., Matti, V., Francia, S., Shivashankar, G. V., Walter, N. G., d'Adda di Fagagna, F. (2017). Damage-induced lncRNAs control the DNA damage response through interaction with DDRNAs at individual double-strand breaks. *Nat Cell Biol* 19, 1400–1411
285. Adamson, B., Smogorzewska, A., Sigoillot, F. D., King, R. W., Elledge, S.J. (2012). A genome-wide homologous recombination screen identifies the RNA-binding protein RBMX as a component of the DNA-damage response. *Nat Cell Biol.* 19;14(3):318-28
286. Boguslawski, S.J., Smith, D.E., Michalak, M.A., Mickelson, K.E., Yehle, C.O., Patterson, W.L., Carrico, R.J. (1986). Characterization of monoclonal antibody to DNA.RNA and its application to immunodetection of hybrids. *J Immunol Methods* 89, 123–130.

287. Sanz, L. A., Chédin, F. (2019). High-resolution, strand-specific R-loop mapping via S9.6-based DNA-RNA immunoprecipitation and high-throughput sequencing. *Nat Protoc* 14, 1734–1755

288. Pérez-Calero, C.,Bayona-Feliu, A., Xue, X., Barroso, S., Muñoz, S., González-Basallote, V.M., Sung. P., Aguilera, A. UAP56/DDX39B is a major co-transcriptional RNA-DNA helicase that unwinds harmful R loops genome-wide. *Genes Dev. In press*

289. Kim, J., Sturgill, D., Sebastian, R., Khurana, S., Tran, A.D., Edwards, G.B., Kruswick, A., Burkett, S., Hosogane, E.K., Hannon, W.W., Weyemi, U., Bonner, W.M., Luger, K., Oberdoerffer, P. (2018). Replication Stress Shapes a Protective Chromatin Environment across Fragile Genomic Regions. *Mol. Cell* 69, 36–47.e7

290. Bekker-Jensen, S., Lukas, C., Kitagawa, R., Melander, F., Kastan, M. B., Bartek, J., Lukas, J. (2006). Spatial organization of the mammalian genome surveillance machinery in response to DNA strand breaks. *J Cell Biol* 173, 195–206.

291. Wang, H., Gao, X., Huang, Y., Yang, J., Liu, Z.-R. (2009). P68 RNA helicase is a nucleocytoplasmic shuttling protein. *Cell Res* 19, 1388–1400.

292. Britton, S., Dernoncourt, E., Delteil, C., Froment, C., Schiltz, O., Salles, B., Frit, P., Calsou, P. (2014). DNA damage triggers SAF-A and RNA biogenesis factors exclusion from chromatin coupled to R-loops removal. *Nucleic Acids Res.* 42(14):9047-62

293. Shanbhag, N. M., Greenberg, R. A. (2010). Neighborly DISCourse: DNA double strand breaks silence transcription. *Cell Cycle*15;9(18):3635-6

294. Chou, D.M., Adamson, B., Dephoure, N.E., Tan, X., Nottke, A.C., Hurov, K.E., Gygi, S.P., Colaiácovo, M.P., Elledge, S.J. (2010). A chromatin localization screen reveals poly (ADP ribose)-regulated recruitment of the repressive poly-comb and NuRD complexes to sites of DNA damage. *Proc Natl Acad Sci USA* 107, 18475–18480

295. Francia, S., Michelini, F., Saxena, A., Tang, D., de Hoon, M., Anelli, V., Mione, M., Carninci, P., d'Adda di Fagagna, F. (2012). Site-specific DICER and DROSHA RNA products control the DNA-damage response. *Nature* 488, 231–235.

296. Zhang, F., Shi, J., Bian, C., Yu, X. (2015). Poly(ADP-Ribose) Mediates the BRCA2-Dependent Early DNA Damage Response. *Cell Rep.* 27;13(4):678-689

297. Schlacher, K., Wu, H., Jasin, M. (2012) A distinct replication fork protection pathway connects Fanconi anemia tumor suppressors to RAD51-BRCA1/2. *Cancer Cell.* 10;22(1):106-16

298. Ait Saada, A., Teixeira-Silva, A., Iraqui, I., Costes, A., Hardy, J., Paoletti, G., Fréon, K., Lambert, S. A. E. (2017) Unprotected Replication Forks Are Converted into Mitotic Sister Chromatid Bridges. *Mol Cell.* 4;66(3):398-410.e4.

299. Anderson, T. et al. (2015). A dominant mutation in human RAD51 reveals its function in DNA interstrand crosslink repair independent of homologous recombination. *Mol Cell.* 6; 59(3): 478–490.

300. Rickman, K. A., Noonan, R. J., Lach, F. P., Sridhar, S., Wang, A. T., Abhyankar, A., Huang, A., Kelly, M., Auerbach, A. D., Smogorzewska, A. (2020). Distinct roles of BRCA2 in replication fork protection in response to hydroxyurea and DNA interstrand cross-links. *Genes Dev.* 34:1–15

301. Wooster, R., Bignell, G., Lancaster, J., Swift, S., Seal, S., Mangion, J., Collins, N., Gregory, S., Gumbs, C., Micklem, G. (1995) Identification of the breast cancer susceptibility gene BRCA2. *Nature* 21-28;378(6559):789-92.

302. Shimelis, H. et al. (2017). BRCA2 Hypomorphic Missense Variants Confer Moderate Risks of Breast Cancer. *Cancer Res.* 1;77(11):2789-2799

303. Izhar, L., Adamson, B., Ciccia, A., Lewis, J., Pontano-Vaites, L., Leng, Y., Liang, A. C., Westbrook, T. F., Harper, J. W., Elledge, S. J. (2015). A Systematic Analysis of Factors Localized to Damaged Chromatin Reveals PARP-Dependent Recruitment of Transcription Factors. *Cell Rep.* 9;11(9):1486-500

304. Ranjha, L., Howard, S. M. & Cejka, P. (2018). Main steps in DNA double-strand break repair: an introduction to homologous recombination and related processes. *Chromosoma* 127,187–214(2018)

305. Ishihama, Y., Oda, Y., Tabata, T., Sato, T., Nagasu, T., Rappsilber, J. & Mann, M. (2005). Exponentially modified protein abundance index (emPAI) for estimation of absolute protein amount in proteomics by the number of sequenced peptides per protein. *Mol Cell Proteomics* 4, 1265–1272

306. Hucl, T., Rago, C., Gallmeier, E., Brody, J. R., Gorospe, M. & Kern, S. E. (2008). A syngeneic variance library for functional annotation of human variation: application to BRCA2. *Cancer Res* 68, 5023–5030

307. Asbroek, ten, A. L. M. A., van Groenigen, M., Nooij, M. & Baas, F. (2002). The involvement of human ribonucleases H1 and H2 in the variation of response of

cells to antisense phosphorothioate oligonucleotides. *Eur. J. Biochem.* 269, 583–592

308. Cerritelli, S. M., Frolova, E. G., Feng, C., Grinberg, A., Love, P. E. & Crouch, R. J. (2003). Failure to produce mitochondrial DNA results in embryonic lethality in Rnaseh1 null mice. *Mol. Cell* 11, 807–815
309. Mazurek, A., Luo, W., Krasnitz, A., Hicks, J., Powers, R. S. & Stillman, B. (2012). DDX5 regulates DNA replication and is required for cell proliferation in a subset of breast cancer cells. *Cancer Discov* 2, 812–825
310. Poullet, P., Carpentier, S. & Barillot, E. (2007). myProMS, a web server for management and validation of mass spectrometry-based proteomic data. *Proteomics* **7,** 2553–2556
311. Spivak, M., Weston, J., Bottou, L., Käll, L. & Noble, W. S. (2009). Improvements to the percolator algorithm for Peptide identification from shotgun proteomics data sets. *J. Proteome Res.* **8,** 3737–3745
312. Perez-Riverol, et al. (2019) The PRIDE database and related tools and resources in 2019: improving support for quantification data. *Nucleic Acids Research* 47, D442–D450
313. Langmead, B. & Salzberg, S. L. (2012). Fast gapped-read alignment with Bowtie 2. *Nat Meth* 9, 357–359
314. Li, H., Handsaker, B., Wysoker, A., Fennell, T., Ruan, J., Homer, N., Marth, G., Abecasis, G., Durbin. (2009) R.1000 Genome Project Data Processing Subgroup. The Sequence Alignment/Map format and SAMtools. *Bioinformatics* 25, 2078–2079
315. Ramírez, F., Ryan, D. P., Grüning, B., Bhardwaj, V., Kilpert, F., Richter, A. S., Heyne, S., Dündar, F. & Manke, T. (2016). deepTools2: a next generation web server for deep-sequencing data analysis. *Nucleic Acids Research* 44, W160–5
316. Zhang, Y., Liu, T., Meyer, C. A., Eeckhoute, J., Johnson, D. S., Bernstein, B. E., Nusbaum, C., Myers, R. M., Brown, M., Li, W. & Liu, X. S. (2008). Model-based analysis of ChIP-Seq (MACS). *Genome Biology* 9, R137–9
317. Quinlan, A. R. & Hall, I. M. (2010). BEDTools: a flexible suite of utilities for comparing genomic features. *Bioinformatics* 26, 841–842
318. Yu, G., Wang, L.-G. & He, Q.-Y. (2015). ChIPseeker: an R/Bioconductor package for ChIP peak annotation, comparison and visualization. *Bioinformatics* 31, 2382–2383

319. Zerbino, D. R.,et al. (2018). Ensembl 2018. *Nucleic Acids Research* 46, D754–D761
320. Knudson, A. G. and Strong, L. C. (1972). Mutation and cancer: neuroblastoma and pheochromocytoma. *Am J Hum Genet.* 24(5): 514–532.
321. Bader, A. S., Bushell M. (2020). DNA:RNA Hybrids Form at DNA Double-Strand Breaks in Transcriptionally Active Loci. *Cell Death Dis.* 24;11(4):280
322. Welty, S. et al. (2018). RAD52 is required for RNA-templated recombination repair in post-mitotic neurons. *J. Biol. Chem.* 293, 1353–1362
323. Teng, Y. et al. (2018). ROS-induced R loops trigger a transcription-coupled but BRCA1/ 2-independent homologous recombination pathway through CSB. *Nat. Commun.* 9, 4115
324. Keskin, H. et al.(2014). Transcript-RNA-templated DNA recombination and repair. *Nature* 515, 436 (2014).
325. Dhir, A., Dhir, S., Proudfoot, N. J. & Jopling, C. L. (2015). Microprocessor mediates transcriptional termination of long noncoding RNA transcripts hosting microRNAs. *Nat. Struct. Mol. Biol.* 22, 319–327
326. Gromak, N. et al. (2013). Drosha regulates gene expression independently of RNA cleavage function. *Cell Rep.* 5, 1499–1510
327. Francia, S., Cabrini, M., Matti, V., Oldani, A. & d'Adda di Fagagna, F. (2016). DICER, DROSHA and DNA damage response RNAs are necessary for the secondary recruitment of DNA damage response factors. *J. Cell Sci.* 129, 1468–1476
328. Krietsch, J., Caron, M., Gagné, J., Ethier, C., Vignard, J., Vincent, M. et al. (2012). PARP activation regulates the RNA-binding protein NONO in the DNA damage response to DNA double-strand breaks. *Nucleic Acids Res.* 40, 10287–10301
329. Beli, P., Lukashchuk, N., Wagner, S. A., Weinert, B. T., Olsen, J. V., Baskcomb, L. et al. (2012). Proteomic investigations reveal a role for RNA processing factor THRAP3 in the DNA damage response. *Mol. Cell* 46, 212–225
330. Becherel, O. J., Yeo, A. J., Stellati, A., Heng, E. Y. H., Luff, J., Suraweera, A. M. et al. (2013). Senataxin plays an essential role with DNA damage response protein meiotic recombination and gene silencing. *PLOS Genet*. 9, e1003435
331. Jain, A., Bacolla, A., del Mundo, I. M., Zhao, J., Wang, G. & Vasquez, K. M.(2013). DHX9 helicase is involved in preventing genomic instability induced

by alternatively structured DNA in human cells. *Nucleic Acids Res* 41, 10345–10357

332. Mazina, O. M., Keskin, H., Hanamshet, K., Storici, F. & Mazin, A. V. (2017). Rad52 inverse strand exchange drives RNA-templated DNA double-strand break repair. *Mol. Cell* 67,1–29.e3
333. Bader, A. S., Hawley, B. R., Wilczynska A. and Bushell M. (2020). The roles of RNA in DNA double-strand break repair. *British Journal of Cancer* 122:613–623
334. Pryde, F., Khalili, S., Robertson, K., Selfridge, J., Ritchie, A., Melton, D. W. et al. (2005). 53BP1 exchanges slowly at the sites of DNA damage and appears to require RNA for its association with chromatin. *J. Cell Sci.* 118, 2043–2055

6. Matherials and Methods

Cell lines

The human cell lines HEK293T and U2OS cells (kind gift from Dr. Mounira Amor-Gueret) were cultured in DMEM (Eurobio Abcys, Courtaboeuf, France) media containing 25 mM sodium bicarbonate and 2 mM L-Glutamine supplemented with 10% heat inactive FCS (EuroBio Abcys). The BRCA2 deficient colorectal adenocarcinoma cell line DLD1 BRCA2$^{-/-}$ [306] (HD 105-007) and the parental cell line DLD1 BRCA2$^{+/+}$ (HD-PAR-008) was purchased from Horizon Discovery (Cambridge, England). The cells were cultured in RPMI media containing 25 mM sodium bicarbonate and 2 mM L-Glutamine (EuroBio Abcys) supplemented with 10% heat inactivated fetal calf serum (EuroBio Abcys). The DLD1 BRCA2$^{-/-}$ cells were maintained in growth media containing 0.1 mg/ml hygromycin B (Thermo Fisher Scientific). The stable cell lines of DLD1$^{-/-}$ BRCA2 deficient cells expressing BRCA2 WT or T207A generated as described[84] were cultured in growth media containing 0.1 mg/ml hygromycin B and 1 mg/ml G418 (Sigma-Aldrich). DIvA cells (AsiSI-ER-U2OS) (kind gift from G. Legube) were cultured in DMEM (Gibco) supplemented with antibiotics, 10% FBS and 1 μg/ml puromycin. For AsiSI-dependent induction of DSBs, cells were incubated for 4h in medium containing 300 nM trans-4-Hydroxytamoxifen (4OHT) (Sigma, H7904). K562 cells (ATCC, CCL-243) were cultured in Iscove's Modified Dulbecco's medium (IMDM; GIBCO) supplemented with 10% heat inactivated fetal bovine serum (Sigma Aldrich) and 1% antibiotic-antimycotic (BioWEST). All cells were cultured at 37°C with 5% CO_2 in a humidified incubator and all cell lines

used in this study have been regularly tested negatively for mycoplasma contamination (MycoAlert, Lonza).

Plasmids, transfections and inhibitors

All BRCA2 N-terminal expression constructs containing the sequence coding for BRCA2 amino acids 1–250 ($BRCA2_{T1}$), 1–500 ($BRCA2_{LT2}$), 1–750 ($BRCA2_{LT3}$) or 1-1000 ($BRCA2_{NT}$) and EGFP-MBP-BRCA2 subcloning in phCMV1 expression vector were generated as described[105].

The point mutation T207A in the 2xMBP-$BRCA2_{T1}$ and EGFP-MBP-BRCA2 have been described before[84].

The point mutation K144A in the were introduced in the pcDNA 6.2 CMV EmGFP-DDX5 vector using QuikChange II site-directed mutagenesis kit (Agilent Technologies) using primers oAC965 and oAC966 (see APPENDIX, Table 3)

GFP-53BP1 construct was obtained by Gateway cloning (Thermo Fisher Scientific) into pCDNA6.2-GFP of a construct comprising the coding sequence of 53BP1 (kind gift of P. Bertrand, CEA, FR).

DDX5-GFP WT and HD constructs were obtained by the insertion of DDX5 sequence (either WT or K144A mutated) from a pcDNA 6.2 CMV EmGFP vector in a pEGFP-N3 vector (kind gift from Carsten Janke, Institut Curie, FR) using oAC953/967 primers (see APPENDIX, Table 3).

MBP-DDX5-GST construct for purification of human DDX5 was a kind gift from Elizabeth Tran (Purdue University, US).

pCDNA3 CMV expressing RNAseH1 has been previously reported[307]; pEGFP-M27 has been previously reported[308].

Transfection of either U2OS or DLD1 cells with pCDNA3 CMV expressing RNAseH1 was performed with Turbofect (ThermoFisher Scientific) 24h before fixation (48h before fixation in case of Fig. 18A).

Transfection of U2OS with DDX5-GFP and of DLD1 BRCA2 WT and BRCA2-T207A clones with either pEGFP-C1 (-RH) or pEGFP-M27 (+RH) was performed with Lipofectamin 3000 (Life Technologies) 24h before fixation.

For transcription inhibition in cells, cordycepin (100 μM, Sigma-Aldrich C3394-25MG) was added to the growth media for a 2 h treatment at 37°C.

Ionizing radiation-induced DNA damage

Cells were exposed to a ^{137}Cs source (GSR D1; dose rate: 0.9 Gy/min) and subsequently incubated at 37°C for the indicated time.

siRNA transfections

For U2OS cells, siRNA transfections were performed using jetPRIME (Ozyme) with 100 nM of the indicated siRNAs following manufacturer's instructions, except for Fig. 4B, in which Lipofectamin 3000 (Life Technologies) was used. For BRCA2 depletion we transfected a combination of the BRCA2 siRNA (SI00000966, Qiagen) and BRCA2 siRNA (Dharmacon D-003462-04) (100 nM each) (Fig. 4A and 8A) or the ON-TARGETplus SMARTpool human BRCA2 (L-021420-00) (Dharmacon) (Fig. 4B). For DDX5 depletion we used siRNA targeting $DDX5^{309}$ (Fig. 4B, 8A, and 12) (see APPENDIX, Table 1). Experiments were performed 30h or 72h (Fig. 4B) after transfection.

For experiments using K562 cells (Fig. 6 and 7) siRNA transfections were performed using Lipofectamin 3000 (Life Technologies) according to manufacturer's instructions with 100 nM siRNA targeting $DDX5^{309}$ (see APPENDIX, Table 1) and experiments were performed 72h after transfection.

For experiments using DIvA cells (Fig. 8C and 10), siRNA transfections were performed using Lipofectamin 3000 (Life Technologies) according to manufacturer's instructions with 100 nM of the indicated siRNAs (ON-TARGETplus SMARTpool human SETX (L-003462-00) (Dharmacon), ON-TARGETplus SMARTpool human BRCA2 (L-021420-00) (Dharmacon), or siRNA targeting $DDX5^{309}$ (see APPENDIX, Table 1) and experiments were performed 72h after transfection.

The non-targeting oligonucleotide (Dharmacon D-001810-04-20, 100 nM) was used as control (siC) in all cells.

Expression and purification of 2xMBP-BRCA2$_{1-250}$ and EGFP-MBP-BRCA2 2xMBP-$BRCA2_{1-250}$ and EGFP-MBP-BRCA2 were purified as previously described[105]. Briefly, ten to twenty 150 mm plates of HEK293 were transiently transfected with the 2xMBP-$BRCA2_{1-250}$ ($BRCA2_{T1}$) or the EGFP-MBP-BRCA2 using TurboFect (Thermo Fisher Scientific). The cells were harvested 30 h post transfection, lysed in lysis buffer H (50 mM HEPES (pH 7.5), 250 mM NaCl, 1% NP-40, 5 mM EDTA, 1 mM ATP and 3 mM $MgCl_2$, 1 mM DTT, 1 mM PMSF and EDTA-free Protease Inhibitor Cocktail (Roche)) and incubated with amylose resin (NEB) for 3h at 4°C. The lysate was extensively washed with

buffer H including 250 mM (EGFP-MBP-BRCA2) or 500 mM ($BRCA2_{T1}$) NaCl and the protein was eluted with 20 mM maltose. The eluate was further purified with Bio-Rex 70 cation-exchange resin (Bio-Rad) by NaCl step elution. For the purification of 2xMBP-BRCA2T1-T207A, we followed the same steps as above except for the Bio-Rex resin that was substituted by a HiTrap Q HP strong anion exchange column (GE Healthcare). The size and purity of the final nuclease-free fractions were analysed by SDS-PAGE and western blotting using anti-MBP antibody or anti-BRCA2 antibody in the case of full-length BRCA2 purification. Pooled protein was snap frozen in N_2 and stored at -80°C. Concentrations were calculated measuring the intensity of the band on a StainFree gel (Bio-Rad) via ImageLab software and using the same protein at known concentration as a reference.

Expression and purification of MBP-DDX5-GST

MBP-DDX5-GST was purified as described[265]. Briefly, expression of MBP-DDX5-GST in *E. coli* BL21 (DE3) Star cells was induced using 0.2 mM IPTG at 16°C overnight. Cells were lysed in a buffer containing 50 mM HEPES (pH 7.5), 250 mM NaCl and 1% NP-40 and disrupted using a French press. The crude lysate was clarified by centrifugation in a Beckmann Ti45 rotor at 35,000 rpm, 60 min, and the MBP-DDX5-GST was purified from the soluble lysate using glutathione resin (GE healthcare) followed by cation-exchange chromatography (SP sepharose, Sigma-Aldrich). The protein was eluted with elution buffer 1 (50 mM Tris– HCl [pH 8.0], 300 mM NaCl, 20% glycerol). StainFree images of the gels before transfer were used as loading control for the input and cropped image are shown in the figure. Nuclease-free aliquots were snap frozen in N_2 and stored at -80°C. Concentration was calculated measuring intensity of the band on stain-free gel via ImageLab software and using Bradford assay.

Amylose and GFP pull-down from whole cell extracts

For amylose pull-down, cell pellets were resuspended in lysis buffer (50 mM HEPES pH7.5, 250 mM NaCl) supplemented with 1 x protease inhibitor cocktail (Complete, EDTA-free; Roche), 1 mM PMSF, 1 % NP-40, 1 mM DTT, 1 mM $MgCl_2$ and 250 units/ml benzonase (1.5 ml lysis buffer/2.5 x 10^7 cells). Cell suspension was sonicated and cleared by centrifugation. The supernatant was then incubated for O/N at 4°C with 60 µl amylose resin (New England Biolabs) per 2.5 x 10^7 cells. After 4 washes with washing buffer (50 mM HEPES pH7.5, 500 mM NaCl, EDTA 5 mM), the bound proteins were eluted in

washing buffer supplemented with 10 mM maltose (Sigma). Eluted proteins were separated by SDS-PAGE and analysed by western blotting. For all Western blots, the protein bands were visualized with ChemiDoc XRS+ System (BioRad). StainFree images of the gels before transfer were used as loading control for the input and cropped image is shown in the figure.

For GFP-pull-down, DLD1 BRCA2$^{+/+}$ parental cells and DLD1 BRCA2$^{-/-}$ stable clones expressing EGFP-MBP-BRCA2 (WT or T207A) pellets were re-suspended in lysis buffer (50 mM HEPES pH7.5, 100 mM NaCl) supplemented with 1 x protease inhibitor cocktail (Complete, EDTA-free; Roche), 1 mM PMSF, 1 % NP-40, 1 mM DTT, 1 mM $MgCl_2$ and BSA 100 µg/ml. Cell suspension was sonicated and cleared by centrifugation. The supernatant was then incubated for 1, 5h at 4°C with 25 µl of pre-equilibrated GFP-TRAP beads (Chromotek) to pull-down EGFP-MBP-BRCA2. The beads were washed 3 times in lysis buffer with 250 mM NaCl. Bound proteins were eluted by boiling the samples for 4 min in 3x SDS-PAGE sample loading buffer (SB), eluted proteins were separated by SDS-PAGE and analysed by western blotting. For all Western blots, the protein bands were visualized with ChemiDoc XRS+ System (BioRad) and quantified by Image LabTM5.2.1 Software (BioRad). To calculate the relative co-immunoprecipitation (co-IP)/co-pull-down of a protein of interest, the intensity of the band in the co-IP was divided by the intensity of the band in the input (ImageQuantTMTL software), the ratio co-IP: input of the protein of interest was then divided by the intensity of the band of the immunoprecipitated protein. StainFree images of the gels before transfer were used as loading control for the input and cropped image is shown in the figure.

Amylose pull-down from nuclear cell extracts

Four plates of HEK293T exponentially growing cells were harvested and the cell pellets were gently resuspended in nuclear isolation buffer (NIB; 10 mM HEPES pH 7.5, 10 mM KCl, 1.5 mM $MgCl_2$, 10 % glycerol, 350 mM sucrose) supplemented with 1 x protease inhibitor cocktail (Complete, EDTA-free; Roche), 1 mM PMSF and 1 mM DTT (1.5 mL lysis buffer/2.5 x 10^7 cells). Samples were kept on ice for 10 min and centrifuged at 1300 *x g* for 5 min at 4^{o}C. The pellet (nuclear fraction) was washed with NIB and sonicated. The pull-down was performed as that of the whole cell extracts above.

Mass spectrometry

Amylose-isolated samples were separated by SDS-PAGE and stained with colloidal blue

(LabSafe Gel Blue GBiosciences). In-gel digestion was performed, according to standard protocols. Briefly, 23 to 24 gel slices were excised, washed, and the proteins were reduced with 10 mM DTT (Sigma) and alkylated with 55 mM iodoacetamide (Sigma). The gel pieces were washed with 100% acetonitrile and incubated overnight with trypsin (Roche Diagnostics) in 25 mM ammonium bicarbonate at 30 °C. Peptides extracted from each gel slice were used directly and analyzed by nano-liquid chromatography-coupled to tandem mass spectrometry (nanoLC-MS/MS) for protein identification. Each sample was concentrated and then separated on a C18 reverse phase column, with a linear acetonitrile gradient (UltiMate 3000 System, Dionex, and column 75 μm inner diameter × 15 cm, packed with C18 PepMapTM, 3 μm, 100 Å; LC Packings) before MS and MS/MS. Spectra were recorded on an LTQ-Orbitrap XL mass spectrometer (Thermo Electron). For identification, data were searched against the Swiss-Prot "Homo sapiens" database using Mascot^{TM} (version 2.5.1) one by one band or merged per conditions for emPAI abundance evaluation. Enzyme specificity was set to trypsin and a maximum of two-missed cleavage sites were allowed. Oxidized methionine, carbamidomethyl cysteine and N-terminal acetylation were set as variable modifications. Maximum allowed mass deviation was set to 2 ppm for monoisotopic precursor ions and 0.8 Da for MS/MS peaks. Result files were further processed using myProMS software[310]. FDR calculation used Percolator[311] and was set to 1% at the peptide level for the whole study. To calculate protein abundance we used the label free exponentially modified protein abundance index (emPAI) and molar % values obtained in the merged Mascot from each replicate as described[305]. Mascot uses only peptides identified with score at or above homology or identity thresholds for the calculation of the emPAI values. Fold change ratios for identified proteins were calculated by dividing the calculated molar percentage value for an individual protein in the $BRCA2_{NT}$ condition with the cognate 2XMBP condition value.

The Mass Spectrometry datasets generated during this study are available at ProteomeXchange Consortium via the PRIDE[312] partner repository. Project Name: BRCA2-N-terminus interacting proteins in HEK293T cells

Project accession: PXD018979

Reviewer account details: (Username: reviewer16179@ebi.ac.uk, Password: GcRskLia)

Co-immunoprecipitation

Cell pellets were resuspended in lysis buffer (50 mM HEPES pH7.5, 250 mM NaCl, 5 mM EDTA) supplemented with 1 x protease inhibitor cocktail (Complete, EDTA-free;

Roche), 1 mM PMSF, 1 % NP-40, 1 mM DTT, 1 mM $MgCl_2$ and 250 units/ml benzonase (1.5 ml lysis buffer/2.5 x 10^7 cells). The cell suspension was sonicated and cleared by centrifugation. The supernatant was then incubated for 2 h in a rotator at 4°C with 1 µg Dynabeads Protein G (Life Technologies) and 1 µg primary antibody(or normal IgG where indicated) per 2.5 x 10^7 cells. The beads were collected using a magnet and washed 4 times with washing buffer (50 mM HEPES pH7.5, 250 mM NaCl, EDTA 5 mM). Proteins were eluted with 50 µl 0.2 M glycine pH 2.2 per sample. 3 µl of 1.5 M Tris-HCl pH 8.8 was added. Eluted proteins were separated by SDS-PAGE and analysed by western blotting. For all Western blots, the protein bands were visualized with ChemiDoc XRS+ System(BioRad). StainFree images of the gels before transfer were used as loading control for the input and cropped image is shown in the figure.

In vitro pull-down

Glutathione resin (GE healthcare) was equilibrated with binding buffer: 50 mM HEPES (pH 7.5), 250 mM NaCl, 1mM DTT. Purified MBP-DDX5-GST (200 ng) was incubated with 200 ng of purified 2XMBP-$BRCA2_{T1}$ (either WT or T207A) for 30 min at 37 °C and then batch bound to 30 µl of glutathione resin for 1h at 4 °C under rotation. The complexes were washed 3 times with washing buffer (50mM HEPES (pH 7.5), 500mM NaCl, 1mM DTT) containing 0.1% Triton-X 100. Bound proteins were eluted with 30 µl 20mM reduced Glutathione in binding buffer, resuspended in 3X SDS sample buffer, heated at 54 °C for 5 min and loaded onto a 10% SDS–PAGE gel. Proteins were analysed by western blotting. For all Western blots, the protein bands were visualized with ChemiDoc XRS+ System (BioRad).

Antibodies used for Western Blotting

mouse anti-MBP (1:5000, R29, Cat. #MA5-14122, Thermo Fisher Scientific), mouse anti-BRCA2 (1:1000, OP95, EMD Millipore), mouse anti-DDX5 (1:100 or 1:500, Cat. # sc-166167 Santa Cruz Biotechnology). Horseradish peroxidase (HRP) conjugated secondary antibodies used: mouse-IgGκ BP-HRP (IB: 1:5000, Cat. #sc-516102, Santa Cruz), goat anti-mouse IgG-HRP (1:10 000, Cat.# 115-035-003, Interchim).

In situ Proximity Ligation Assay (PLA)

Cells were seeded on coverslips precoated with 1 µg/ml fibronectin (Sigma) and 20 µg/ml collagen (Sigma). In case of EdU incorporation, a pulse-label nascent DNA was performed

with 10 µM EdU for 5 min before fixation. Cells were washed with PBS and cytoskeleton (CSK) buffer (10 mM PIPES pH 6.8, 100 mM NaCl, 300 mM sucrose, 3 mM $MgCl_2$ and 1 x protease inhibitor cocktail (Complete, EDTA-free; Roche)) and permeabilized with CSK-T buffer (CSK supplemented with 0.5 % Triton-X100). After washes in CSK and PBS, the cells were fixed with 2 % para-formaldehyde (PFA) for 20 minutes at room temperature (RT). The cells were then washed 3 times with PBS. . In case of EdU labelling, before incubation with primary antibodies, samples were incubated for 30 minutes at RT with a Click-mix solution (Biotin-azide 6nM, Sodium ascorbate 10 mM, CuSO4 2 mM, diluted in PBS 1X) in order to allow EdU-biotin conjugation. In this case, IF was combined to PLA, adding a primary antibody anti-biotin (1:3000, Bethyl laboratories, Cat. # BETA150-109A) together with primary antibodies for PLA and secondary antibody (donkey anti rabbit Alexa-488, 1:1000, Cat. # A-21206, Life Technologies) together with PLA probes.

In situ PLA was performed following the manufacturer's specifications (Duolink™, Sigma) except that the primary antibody was incubated for 1h at 37°C. For quantification, particle analysis was done using ImageJ software (NIH Image). The nucleus was defined by an auto-threshold (Huang, Image J) on DAPI, a mask was generated and applied onto the Texas-Red2 picture to count PLA spots within the nucleus using the plugin Find Maxima with a prominence of 2000 for Fig. 2C, of 5000 Fig. 5, 8A, 14B and 15. Primary antibodies used for PLA: BRCA2 (1:2000 OP95 EMD Millipore), DDX5 (1:3000 Cat. # ab10261 Abcam), S9.6 (1:100000, Protein Expression and Purification Core facility, Institut Curie), γ-H2AX (1:3000 Cat. # 07-164, EMD Millipore).

Immunofluorescence microscopy

For immunofluorescence experiments in Fig. 4A, 12, 17, 18, cells were seeded on coverslips pre-coated with 1 µg/ml fibronectin (Sigma) and 20 µg/ml collagen (Sigma) the day before 6 Gy γ−irradiation. At the time indicated after irradiation the coverslips were washed twice in PBS followed by one wash in CSK Buffer (10 mM PIPES, pH 6.8, 0.1 M NaCl, 0.3 M sucrose, 3 mM $MgCl_2$, EDTA-free Protease Inhibitor Cocktail (Roche)). The cells were permeabilized for 5 minutes at room temperature in CSK buffer containing 0.5% Triton X-100 (CSK-T) followed by one rinse in CSK buffer and one rinse in PBS before fixation for 20 minutes at room temperature with 2% PFA in PBS. After one rinse in PBS and one in PBS-T, the cells were blocked for 5 minutes at room temperature with 5% BSA in PBS-T.

For immunofluorescence experiments in Fig. 4B, 10B and 13A, cells grown on glass coverslips coated with poly-L-Lysine (Sigma) were rinsed with cold PBS and treated for 3 minutes with a TritonX-100 extraction buffer (0.1% TritonX-100, 20mM HEPES-KOH pH7.9, 50mM NaCl, 3mM $MgCl_2$, 300mM sucrose). In the case of figures 4B and 13A and C, after extraction, cells were fixed for 8 minutes with methanol at -20ºC; coverslips were then washed three times with PBS and blocked overnight at 4ºC in blocking solution (PBS with 2% BSA). In the case of Fig. 10B, after extraction, DIvA cells were fixed in 4% FA/2% sucrose in PBS for 10 minutes at room temperature (RT), washed twice in PBS and re-permeabilized with PBS-TritonX-100 0.5% for 10 minutes at RT. Then were then blocked at RT for 1h in blocking solution (3% BSA, 0.1% TritonX-100 in PBS).
For all immunofluorescence experiments, cells were incubated overnight at 4°C in blocking solution with primary antibodies, except in case of Fig. 4A, when cells were incubated for 1h at 37°C with S9.6 (1:500, Protein Expression and Purification Core facility, Institut Curie) and anti-nucleolin (1:1000 Cat. # ab22758, Abcam) antibodies. For Fig. 12, 17 and 18, cells were incubated with anti-γH2AX (1:1000 Cat. # 05-636, EMD Millipore) anti-RAD51 (1:100 for DLD1 cells, 1:1000 for U2OS cells, Cat. # sc-8349, Santa Cruz Biotechnology) or anti-RPA (1:1000, Cat. # 2208S, Ozyme (Cell Signaling) antibodies. For Fig. 4B and 13A the mouse S9.6 (1:2000) and rabbit anti-nucleolin (1:1000 Cat. # ab50279, Abcam) primary antibodies were used on un-transfected cells or S9.6 (1:2000) and rabbit anti-GFP (1:200, Cat. # ab6556 Abcam) were used in the case of transfected cells. For Fig. 10B anti-γH2AX (1:1000, Cat. # ab2893, Abcam) or anti-DDX5 (1:500, Cat. # sc-166167 Santa Cruz) were used. After primary antibody incubation, the coverslips were rinsed in PBS-T followed by two washes of 10 minutes in PBS-T and blocked for 5 minutes at room temperature with 5% BSA in PBS-T. Cells were incubated with appropriate secondary antibodies (conjugated with Alexa Fluor 488, 546, 568, 594 or 647), diluted in blocking solution for 1h at RT. After rinsing, coverslips were mounted onto slides using ProLong Gold Antifade reagent (Invitrogen). Images in Fig. 4B, 10B and 13A were acquired using a Leica DM6000 wide-field microscope equipped with a DFC390 camera (Leica) at x63 magnification using the LAS AF software (Leica). For Fig. 12, 17 and 18 the camera used was a Hamamatsu Flash 4.0 sCMOS controlled with MetaMorph2.1 software (Molecular Devices).

The quantification of S9.6 intensity was performed in the area of the nucleus as determined by DAPI and subtracting the intensity of S9.6 in nucleoli (stained with an antibody specific for nucleolin, see above).

For Fig. 4B, 10B and 13A automated quantification of foci and fluorescence intensities was performed using the Metamorph v7.5.1.0 software (Molecular Probes).
For Fig. 12, 17 and 18 Z-stacks were taken at 0.5 μm intervals to generate a Z-projection image using ImageJ. For the analysis of γ-H2AX, RAD51 and RPA foci, 26 Z-stacks were taken at 0.2 μm intervals to generate a maximal intensity projection using Image J. The number of γH2AX foci per nucleus were counted with a customized macro using a semi-automated procedure; the nucleus was defined by an auto-threshold (Otsu, Image J) on DAPI, a mask was generated and applied onto the Z-projection to count foci within the nucleus. For the definition of foci we applied the threshold plugin IsoData (ImageJ) and for the quantification of foci we used the tool Analyze Particles (ImageJ) setting a range of 5-100 pixels^2 for Fig. 12A and a range of 5-1000 for Fig. 17A and 18 to select only particles that correspond to the size of a focus. RAD51 and RPA foci were quantified using the plugin Find Maxima onto the Z-projection with a prominence of 1000 for Fig. 12B and of 5000 for Fig. 17B and 18.

Protein recruitment after laser-induced damage

U2OS cells were seeded on glass coverslips precoated with 1 μg/ml fibronectin (Sigma) and 20 μg/ml collagen (Sigma). Cells were then co-transfected with 2 μg of a DDX5-GFP construct and BRCA2 siRNA and ON-TARGET plus Non-targeting oligonucleotide (as described in siRNA section) 48h prior to imaging; or with 2 μg of a construct expressing GFP-53BP1 also 48h prior imaging. Cells were pre-sensitized by adding 10 mg/ml of Hoechst dye 33258 to the medium for 5 min at 37°C. Live cell imaging of DDX5-GFP or GFP-53BP1 at laser tracks was carried out using an inverted Leica confocal laser scanning SP5 system equipped with a 37°C heating chamber attached to a DMI6000 stand using 63x/1.4 oil objective. DNA damage was generated using a 405 nm laser diode focused onto a single line (thickness: 1 pixel) within the nucleus to generate the damage. Specifically, we set the laser output to 70% of maximum power and the scan speed at 10 Hz. GFP signal was detected between 500-550nm on PM detector. All recordings were performed using the indicated sampling frequency (512 x 512 image size, line average of 4 and zooming set to 7.94). To reduce the time of image acquisition, the scan was used in bidirectional regime and the scan speed was set at 10Hz (10 000 lines by second). The whole system was driven by LAS AF software (Leica). Images were collected at 2, 4, 6, 8, 10, 15 and 20 minutes after the DNA damage using a 488 nm argon laser.

The quantification of cells showing a DDX5-GFP "anti-stripe" pattern at DNA damage tracks (reduced GFP signal at the laser tracks compared to the rest of the nucleus) was performed by manual counting in images visualized in ImageJ.

In vitro unwinding assay

DNA substrates were purchased PAGE-purified from MWG Eurofins and the RNA substrate was purchased from Sigma. The RNA oligonucleotide oAC864 (see APPENDIX, Table 2) was 5′ end- labeled with T4 polynucleotide kinase and [γ-^{32}P]ATP. R loops substrates were prepared by annealing 1 pmol of labeled oAC864 (RNA) to 2.5 pmol of DNA oligo oAC862 (see Table S3) and 2.5 pmol of DNA oligo oAC863 (see APPENDIX, Table 2) in annealing buffer (1 mM EDTA, 10 mM Tris-HCl at pH 7.6) by heating for 2 min at 95°C followed by slow cooling to room temperature. To assess unwinding activity, 1.5 nM molecules of R loop substrate was incubated with the indicated concentrations of purified MBP-DDX5-GST in 25 mM TrisAcO, 5mM $MgCl_2$,1mM DTT, 5mM ATP, 100μg/mL and 40U RNAse OUT (ThermoFisher Scientific) alone or with the indicated concentration of purified 2XMBP-BRCA2 or 2XMBP-BRCA2$_{T1}$. The mixture was incubated at 37°C for 30 min and the reaction products were resolved on 10% PAGE in 1% TAE buffer (40mM Tris Acetate, 0.5mM EDTA) at 110V for 45 min at room temperature. The gels were dried, visualized by phosphorimaging (Typhoon, GE Healthcare) and analysed on Image Quant software (GE Healthcare). In all *in vitro* unwinding assays, DDX5 unwinding activity was calculated as the percentage of free radiolabelled RNA relative to the R loop signal.

DNA-RNA immunoprecipitation (DRIP)

DRIP was performed in enzymatically digested DNA from U2OS DIvA cells after 72h transfection, with or without 4h treatment with 4OHT for DSB induction, and treated or not with RNase H *in vitro* as previously described[222]. Analysis was performed by qPCR using primers located at each of the regions of interest: RBMXL1-fw (GATTGGCTATGGGTGTGGAC; RBMXL1-rv (CATCCTTGCAAACCAGTCCT), HIST1H2BG-Fw (TGTGACCAAGGCGCAGAAGA), HIST1H2BG-rv (GAGCGCTTGTTGTAGTGGGC), SNRNP-fw (GCCAAATGAGTGAGGATGGT) and SNRNP-rv (TCCTCTCTGCCTGACTCCAT). Means and SEM from 4-5 independent experiments were calculated and statistical significance was analysed using unpaired t-test.

Chromatin immunoprecipitation (ChIP)

Cells were crosslinked with a formaldehyde solution added to the culture medium (1% formaldehyde final concentration) for 10 min at room temperature, with gentle agitation. Glycine (0.125 M) was added for 5 min to stop the reaction. Cells were washed twice with cold PBS in the presence of complete protease inhibitor cocktail (Roche) and PMSF and harvested by. Pelleted cells were lysed in two steps, first using 0.5% NP-40 buffer for nucleus isolation followed by nuclear lysis in 1% SDS lysis buffer. Sonication was performed using Bioruptor (Diagenode, UCD-200) at high intensity and two cycles of 8 min (30" sonication, 30" pause) to achieve DNA fragments of about 200–1000 bp and chromatin was clarified by centrifugation (13,000 × g, 30 min, 4 °C). For each IP, 20 µg of chromatin were diluted in IP buffer (0.01% SDS, 1.1% Triton X-100, 1.2 mM EDTA pH 8, 16.7 mM Tris pH 8, 167 mM NaCl) and incubated overnight at 4 °C on a rotating wheel with 4 µg antibody (anti-DDX5 Santa Cruz sc-166167; anti-γH2AX Abcam ab2893; rabbit IgG SIGMA I8140; and mouse IgG SIGMA I8765 as controls), followed by 2h incubation with 30 µl pre-cleared Dynabeads protein A and Dynabeads protein G (ThermoFisher). Beads were sequentially washed with increasing salt concentrations (150-500 mM NaCl, 0.1% SDS, 1% Triton X-100, 2 mM EDTA pH 8, 20 mM Tris pH 8), and LiCl buffer (0.25 M LiCl, 1% NP-40, 1% sodium deoxycholate, 1 mM EDTA, 10 mM Tris pH8). Immunoprecipitated complexes were resuspended in elution buffer (Tris 10 mM pH 8, EDTA 0.5 mM pH 8, 1% SDS) and incubated for 20 min at 65°C shaking. After removal of the beads, SDS concentration was brought to 0.5% by addition of 1x TE and samples were further incubated overnight at 65°C to revert crosslinking. After 1h proteinase K treatment, immunoprecipitated and input DNA were purified with phenol/chloroform and precipitated in ethanol at -20°C. Samples were resuspended in 50 µl water.

Quantitative PCR analysis

All real-time (RT)–qPCR analysis was performed with iTaq Universal SYBR Green Supermix (Bio-Rad) and analyzed on 7500 FAST Real-Time PCR system (Applied Biosystems, Carlsbad, CA).

DRIPc-seq

For genome-wide detection of DNA-RNA hybrids, DRIPc-seq was performed essentially as described[287]. Briefly, after DRIP, the eluted DNA from five immunoprecipitations of each sample was treated with 6 U of DNase I (New England BioLabs) for 45 min at 37°C to degrade all DNA. The resulting RNA was subjected to library construction using the

TruSeq Stranded Total RNA protocol (Illumina) from the fragmentation step. The quality of the libraries was checked on a 2100 Agilent Bioanalyzer prior to sequencing on an Illumina NextSeq500 platform.

DRIPc-seq read mapping, peak calling and annotation

Sequenced paired-ends reads were subjected to quality control pipeline using the FASTQ Toolkit v.1.0.0 software (Illumina) and aligned to the human reference genome hg38 with Bowtie2[313]. Reads were separated into Watson and Crick strand using SAMTools[314]. Genome signal tracks were obtained using bamCoverage command from Deeptools[315].

DRIPc-seq peaks were called using MACS2[316] setting default parameters and FRD<0.01 allowing broad region detection with a 0.1 cutoff. Next, regions covered by peaks in both replicates in both conditions were merged and fused when closer than 5kb distance for comparative analysis using BEDtools[317]. Then, number of counts per peak was calculated using FeatureCounts and RPKM normalized. For further comparative analysis, R loop-gain peaks were established selecting peaks whose DRIPc signal fold change was higher than 2.5X in siDDX5 respect to the siC control cells in both replicates and *vice versa* for R loop-gain peaks in siC cells. Finally, peaks were annotated to genes using ChIPseeker[318] and genes retrieved from Ensembl release 94 2018[319]. Our analyses were

mainly focus on protein-coding genes considering promoter as -2 Kb from the transcription start site (TSS) and downstream as +2 Kb from the transcription termination site (TTS).

For γH2AX peak metaplot, the mean DRIPc-seq signal (mean coverage) from the two replicates in K562 cells was superimposed on the plot of γH2AX peaks from previously reported γH2AX ChIP-seq analysis (GSE 104800)[289] performed in the same cells.

The DRIPc-seq datasets generated in this study are available at GEO repository (GSE150163)

QUANTIFICATION AND STATISTICAL ANALYSIS

The total number of replicates, mean and error bars in graphs are explained in the figure legends. Statistical significance of differences was calculated with unpaired two-tailed t-test, one/two-way ANOVA with Tukey's multiple comparisons test or Mann-Whitney two-tailed test as indicated in the figure legends. All analyses were conducted using GraphPad Prism (version Mac OS X 8.4.2).

7. APPENDIX

Table 1. siRNA used in this study

SiRNA		
TARGET AND SEQUENCES (5'-3')	SOURCE	IDENTIFIER
BRCA2 CAGCGTTTGTGTATCGGGCAA	Qiagen	Cat# SI00000966
BRCA2 ON-TARGETplus SMARTpool	Dharmacon	Cat# L-021420-00
BRCA2 GAAGAAUGCAGGUUUAAUA	Dharmacon	Cat# D-003462-04
DDX5 GCUCUUUAUAUUGUGUGUUAU	Mazurek et al., 2012 (Ref. 309)	N/A
SETX ON-TARGETplus SMARTpool	Dharmacon	Cat# L-003462-00
Non targeting oligonucleotide (siC)	Dharmacon	Cat# D-001810-01-20

Table 3. Primers for sequencing, cloning quantitative PCR analysis

Primers		
NAME AND SEQUENCES (5'-3')	SOURCE	IDENTIFIER
oAC914 (sequencing of DDX5-GFP plasmid): ATGTCGGGTTATTCGAGTGACCGAG	Eurofins MWG	N/A
oAC149 (sequencing of $BRCA2_{1-250}$ plasmid) TTATTTGCTAGCCCTATTGGATCCAAAGAG	Eurofins MWG	N/A
oAC953 (for DDX5-GFP cloning): CGTGTCGACATGTCGGGTTATTCGAGTGACCGAGAC	Eurofins MWG	N/A
oAC967 (for DDX5-GFP cloning): CGTACCGGTCCTTGGGAATATCCTGTTGGCATTGGATAACC	Eurofins MWG	N/A
oAC965 (for insertion of K144A mutation in DDX5 sequence): GTGGCACAGACTGGATCTGGGGCAACATTGTCTTATTTGCTT	Eurofins MWG	N/A
oAC966 (for insertion of K144A mutation in DDX5 sequence): AAGCAAATAAGACAATGTTGCCCCAGATCCAGTCTGTGCCAC	Eurofins MWG	N/A
RBMXL1-fw: GATTGGCTATGGGTGTGGAC	Aymard *et al*., 2014 (Ref.259)	N/A
RBMXL1-rv: CATCCTTGCAAACCAGTCCT	Aymard *et al*., 2014 (Ref.259)	N/A
HIST1H2BG-Fw: TGTGACCAAGGCGCAGAAGA	Mersaoui *et al*., 2019 (Ref.264)	N/A
HIST1H2BG-rv: GAGCGCTTGTTGTAGTGGGC	Mersaoui *et al*., 2019 (Ref.264)	N/A
SNRNP-fw: GCCAAATGAGTGAGGATGGT	Bhatia *et al.*, 2014 (Ref.187)	N/A
SNRNP-rv: TCCTCTCTGCCTGACTCCAT	Bhatia *et al.*, 2014 (Ref.187)	N/A

Table 3. Oligonucleotides for generation of R-loop generation

Oligonucleotides		
NAME AND SEQUENCES (5'-3')	SOURCE	IDENTIFIER
oAC862 (PAGE purified) GTACCCGGGGATCCTCTAGAGTCGAGCG TCGATCCGAAACTTGGCACTGGCCGTCGT TTTACAAC	Song et al. 2017 (Ref.244)	N/A
oAC863 (PAGE purified) GTTGTAAAACGACGGCCAGTGCCTTTTCC CAGCCTCAATCTCATCACTCTAGAGGATC CCCGGGTAC	Song et al. 2017 (Ref.244)	N/A
oAC864 (PAGE purified) GUUUCGGAUCGACGC	Song et al. 2017 (Ref.244)	N/A

Primary and secondary antibodies

Antibodies		
anti-MBP (R29) (mouse, immunoblot (IB): 1:5000)	Thermo Fisher Scientific	Cat# MA5-14122
anti-BRCA2 (OP95) (mouse, (co-IP): 1µg , (IB): 1:1000 (PLA); 1:2000)	EMD Millipore	OP95
anti-DDX5 (mouse, (IB): 1:100 or 1:500 (ChIP): 4 µg (IF): 1:500)	Santa Cruz Biotechnology	Cat# sc-166167
anti-DDX5 (goat, (PLA)1:3000)	Abcam	Cat# ab10261
anti-pSer139-γ-H2AX (rabbit, (PLA):1:3000)	EMD Millipore	Cat# 07-164
anti-pSer139- γH2AX (clone JBW301) (mouse, IF: 1:1000)	EMD Millipore	Cat #05-636
anti--pSer139- γH2AX (rabbit (IF):1:1000) (ChIP): 4 µg	Abcam	Cat # ab2893
anti-RAD51 (clone H-92) (rabbit, (IF): 1:100 or 1:1000 clone H-92)	Santa Cruz Biotechnology	Cat#sc-8349
anti-RPA32 (rat, (IF):1:1000)	Ozyme (Cell Signaling)	Cat# 2208S
anti-DNA-RNA hybrids (S9.6) (mouse, (PLA):1:100000 (IF): 1:500)	Protein Expression and Purification Core facility, Institut Curie	
anti-DNA-RNA hybrids (S9.6) ((IF): 1:2000	Purified from hybridoma cell line HB-8730	N/A
anti-nucleolin (rabbit, (IF):1:1000)	Abcam	Cat#ab50279
anti-nucleolin (rabbit, (IF):1:1000)	Abcam	Cat#ab22758

anti-GFP (rabbit (IF):1:200)	Abcam	Cat#ab6556
anti-biotin (rabbit (IF): 1:3000)	Bethyl Laboratories	Cat# BETA150-109A
anti-rabbit IgG (ChIP): 4 µg	SIGMA	Cat# I8140
anti-Mouse IgG (ChIP): 4 µg	SIGMA	Cat# I8765
goat anti mouse IgG-HRP: (co-IP): 1µg	Santa Cruz Biotechnology	Cat# sc-2055
mouse-IgGκ BP-HRP (IB: 1:5000)	Santa Cruz Biotechnology	Cat#sc-516102
goat anti-mouse IgG-HRP (IB: 1:10 000)	Interchim	Cat#115-035-003
chicken anti-rat Alexa Flour 647 (IF): 1:1000	Life Technologies	Cat#A-21472
donkey anti-mouse Alexa-594 (IF): 1:1000	Thermo Fisher Scientific	Cat#A-21203
donkey anti-rabbit Alexa-488 (IF): 1:1000	Thermo Fisher Scientific	Cat#A-21206
goat anti-human Alexa-555 (IF: 1:1000)	Thermo Fisher Scientific	Cat#A-21433
donkey anti-mouse Alexa-488 (IF: 1:1000)	Thermo Fisher Scientific	Cat#A-21202
chicken anti-mouse Alexa-594 (IF): 1:1000	Thermo Fisher Scientific	Cat#A-21201
chicken anti-mouse Alexa-488 (IF): 1:1000	Thermo Fisher Scientific	Cat#A-21200
goat anti-mouse Alexa-546 (IF): 1:1000	Thermo Fisher Scientific	Cat#A-11030
goat anti-rabbit Alexa-568 (IF): 1:1000	Thermo Fisher Scientific	Cat#A-11011
goat anti-mouse Alexa-488 (IF): 1:1000	Thermo Fisher Scientific	Cat#A-11029

Bacterial and virus strains

Bacterial and Virus Strains		
E. coli DH5α electrocompetent cells	Protein Expression and Purification Core Facility, Institut Curie	N/A
E. coli BL21 (DE3) Star cells	Protein Expression and Purification Core Facility, Institut Curie	N/A

Chemical and reagents

Chemicals, Peptides, and Recombinant Proteins		
Fibronectin from bovine plasma	Sigma-Aldrich	Cat.F1141-1MG
Collagen	Sigma-Aldrich	Cat#C3867-1VL

Hygromycin B	Thermo Fisher Scientific	Cat#10687010
Puromycin	Sigma-Aldrich	Cat#P8833
G 418 Disulfate salt	Sigma-Aldrich	Cat#G5013
EdU (5 -ethynyl-2’ -desoxyuridine)	Thermo Fisher Scientific	Cat#A10044
Biotin Azide	Thermo Fisher Scientific	Cat#B10184
Turbofect	Thermo Fisher Scientific	Cat#R0532
Lipofectamine™ 3000 Transfection Reagent	Thermo Fisher Scientific	Cat#L3000015
jetPRIME®	Ozyme	Cat#POL114-15
cOmplete, EDTA-free Protease Inhibitor Cocktail	Sigma-Aldrich	Cat#000000011873580001
Maltose monohydrate	Carlo Erba	Cat#459865
Glycine	Sigma-Aldrich	Cat#G7126-1KG
IPTG	Sigma-Aldrich	Cat#16758
L-glutathione	Sigma-Aldrich	Cat#G6529
Kanamycin	Sigma-Aldrich	Cat#K4000
Ampicillin	Sigma-Aldrich	Cat# A9518-5G
Chloramphenicol	AppliChem	Cat#A18060025
Benzonase nuclease	Merck Millipore	Cat#70664-3
RNAseOUT™	Invitrogen	Cat# 10777019
RNase I	Thermo Fisher Scientific	Cat# AM2294
DNase I	New England Biolabs (NEB)	Cat# M0303S
RNase A	Thermo Fisher Scientific	Cat# EN0531
RNase H	New England Biolabs (NEB)	Cat# M0297L
Hexokinase	Millipore Sigma	Cat#11426362001
T4 Polynucleotide Kinase	New England Biolabs (NEB)	Cat# M0201S
ATP, [γ-32P]- 3000Ci/mmol 10mCi/ml EasyTide	Perkin Elmer	BLU502A250UC
Amersham Protran Nitrocellulose Blotting Membrane	GE Healthcare Life Science	Cat#10600008
Amersham ECL Prime Western Blotting Detection Reagent	GE Healthcare Life Science	Cat#RPN2236
Cordycepin, from *Cordyceps militaris*	Sigma-Aldrich	Cat# C3394-25MG
trans-4-Hydroxytamoxifen (4OHT)	Sigma	Cat#H7904
penicillin/streptomycin	Eurobio Abcys	CABPES01-04
Bovine Serum Albumin	Sigma-Aldrich	Cat#A4503

Hoechst 33258	Sigma-Aldrich	Cat# 861405-100MG
ProLong Diamond Antifade Mountant with DAPI	Thermo Fisher Scientific	Cat#P36962
ProLong™ Gold Antifade Mountant	Thermo Fisher Scientific	Cat#P36930
iTaq Universal SYBR Green Supermix	Bio Rad	Cat# 172-5125SP1
Purified MBP-DDX5-GST protein	This study	N/A
Purified 2xMBP-BRCA2 (1-250 aa) WT protein	This study	N/A
Purified EGFP-MBP-BRCA2 protein	This study	N/A

Commercial kits

Critical Commercial Assays		
Bio-Rad Protein Assay Dye Reagent Concentrate	Bio-Rad	Cat#500-0006
Duolink® In Situ PLA® Probe Anti-Rabbit PLUS	Sigma-Aldrich	Cat#DUO92002-100RXN
Duolink® In Situ PLA® Probe Anti-Mouse MINUS	Sigma-Aldrich	Cat#DUO92004-100RXN
Duolink® In Situ PLA® Probe Anti-Goat PLUS	Sigma-Aldrich	Cat# DUO92003-100RXN
Duolink® In Situ Detection Reagents Red	Sigma-Aldrich	Cat#DUO92008-100RXN
QuikChange II Site-Directed Mutagenesis Kit	Agilent Technologies	Cat. #200523
NextSeq 500 kit	Illumina	Cat# 20024906

Cell lines

Experimental Models: Cell Lines		
U2OS (human osteosarcoma epithelial cell line)	Kind gift from Mounira Amor-Gueret	N/A
HEK293T (human embryonic kidney cell line)	Kind gift from Mounira Amor-Gueret	N/A
K562 (Erythromyeloblastoid leukemia cell line)	ATCC	CCL-243
DLD1 (human colorectal adenocarcinoma cell line)	Horizon Discovery	HD-PAR-008
DLD1 BRCA2$^{-/-}$	Horizon Discovery Hucl, T. *et al* 2008 (Ref. 306)	HD 105-007
DLD1 BRCA2$^{-/-}$ GFPMBPBRCA2 WT clone C1	Ehlen *et al.*2020 (Ref. 84)	N/A
DLD1 BRCA2$^{-/-}$ GFPMBPBRCA2 T207A clone B1	Ehlen *et al.*2020 (Ref. 84)	N/A
DIvA cells (AsiSI-ER-U2OS)	Kind gift from Gaelle Legube	N/A

Plasmids

Recombinant DNA		
Plasmid 2XMBP-BRCA2 (aa 1-250) in phCMV1	Nicolai *et al*., 2016 (Ref. 105)	N/A
Plasmid 2XMBP-BRCA2 (aa 1-500) in phCMV1	Nicolai *et al*., 2016 (Ref. 105)	N/A
Plasmid 2XMBP-BRCA2 (aa 1-750) in phCMV1	Nicolai *et al*., 2016 (Ref. 105)	N/A
Plasmid 2XMBP-BRCA2 (aa 1-1000) in phCMV1	Nicolai *et al*., 2016 (Ref. 105)	N/A
Plasmid EGFPMBP-BRCA2 in phCMV1	Nicolai *et al*., 2016 (Ref. 105)	N/A
Plasmid EGFPMBP-BRCA2 T207A in phCMV1	Ehlen *et al.* 2020 (Ref. 84)	N/A
Plasmid DDX5-GFP	This study	N/A
Plasmid MBP-DDX5-GST	Xing *et al.*, 2017 (Ref. 265)	N/A
Plasmid pCDNA3 CMV RNaseH1	Asbroek *et al*., 2002 (Ref. 307)	N/A
Plasmid pEGFP-M27 (GFP-RNase H1)	Cerritelli *et al*., 2003 (Ref. 308)	N/A
Plasmid pCDNA6.2-GFP-53BP1	This study	N/A

Softwares

Software and Algorithms		
ImageQuant TL Software	GE Healthcare	N/A
Image Lab 5.2.1 Software	Bio-Rad	N/A
MetaMorph2.1 software	Molecular Devices	N/A
Graph Pad Prism (version Mac OS X 8.4.2)	GraphPad Software	www.graphpad.com
ImageJ	1.51s, NIH	https://imagej.nih.gov
Fiji	1.51s, NIH	https://imagej/Fiji.nih.gov
LAS AF SP8 software (FRAP Wizard module)	Leica	N/A
Bowtie2	Langmead and Salzberg, 2012 (Ref. 313)	http://bowtie-bio.sourceforge.net/bowtie2/index.shtml
SAMTools	Li *et al*., 2009 (Ref. 314)	http://samtools.sourceforge.net/

Deeptools2	Ramirez *et al*., 2016 (Ref. 315)	
MACS2	Zhang *et al.*, 2008 (Ref. 316)	
ChIPseeker	Yu *et al*., 2015 (Ref. 318)	

Others

Other		
Amylose resin	NEB	Cat#E8021S
Bio-Rex 70 cation-exchange resin	Bio Rad	Cat#1435832
Glutathione Sepharose 4B	GE Healthcare	Cat#17-0756-01
GFP-TRAP beads	Chromotek	Cat#gta-20
Dynabeads® Protein G for Immunoprecipitation	Life Technologies	Cat#10003D
Dynabeads® Protein A for Immunoprecipitation	Thermo Fisher	Cat#10008D
SP Sepharose Fast Flow	Sigma-Aldrich	Cat#S1799-100ML
Mini-PROTEAN TGX Stain-Free gels 4-15%	Bio Rad	Cat#456-8084
Acrylamide/ Bis-Acrylamide 40% Ratio 29/1	Euromedex	Cat# EU0063-B
Ammonium Persulfate (APS)	Bio Rad	Cat# 161-0700
TEMED	Bio Rad	Cat# 161-0800

8. Manuscript and publications

BRCA2 promotes DNA-RNA hybrid resolution by DDX5 at DNA double-strand breaks to facilitate homologous recombination

Gaetana Sessa[1, 2, #], Belen Gómez-González[3, 4, #], Sonia Silva[3, 4], Carmen Pérez-Calero[3, 4], Romane Beaurepere[1, 2], Sonia Barroso[3, 4], Sylvain Martineau[1, 2], Åsa Ehlén[1, 2], Juan S. Martínez[1, 2], Charlotte Martin[1, 2], Bérangère Lombard[5], Damarys Loew[5], Stephan Vagner[1, 2], Andrés Aguilera[3,4, *], Aura Carreira[1, 2, 6, *]

[1]Institut Curie, PSL Research University, CNRS, UMR3348, F-91405, Orsay, France

[2]Paris Sud University, Paris-Saclay University CNRS, UMR3348, F-91405 Orsay, France

[3]Andalusian Molecular Biology and Regenerative Medicine Centre-CABIMER, University of Seville-CSIC, 41092 Seville, Spain

[4]Departamento de Genética, Facultad de Biología, University of Seville, 41012 Seville, Spain

[5]Institut Curie, PSL Research University, Laboratoire de Spectrométrie de Masse Protéomique, 26 rue d'Ulm, 75248 Cedex 05 Paris, France

[#] Equal contributors

*Correspondence: aguilo@us.es and aura.carreira@curie.fr

Abstract

The BRCA2 tumor suppressor is a DNA double-strand break repair factor essential to maintain genome integrity. BRCA2-deficient cells spontaneously accumulate DNA-RNA hybrids, a known source of genome instability. However, the specific role of BRCA2 on these structures remains poorly understood. Here we identified the DEAD-box RNA helicase DDX5 as a BRCA2 interacting partner. DDX5 associates with DNA-RNA hybrids that form in the vicinity of DSBs and this association is enhanced by BRCA2. Notably, BRCA2 stimulates the DNA-RNA hybrid helicase activity of DDX5. An impaired BRCA2-DDX5 interaction, as observed in cells bearing the breast cancer variant BRCA2-T207A, reduces the association of DDX5 with DNA-RNA hybrids, decreases the number of RPA foci and alters the kinetics of appearance of RAD51 foci upon irradiation. Our findings are consistent with DNA-RNA hybrids being an impediment for the repair of DSBs by homologous recombination and reveal BRCA2 and DDX5 as active players in their removal.

BRCA2 tumor suppressor protein is involved in genome maintenance mechanisms including DNA repair by homologous recombination (HR) [1,2], protection of stalled replication forks (RFs) [3] and faithful segregation of chromosomes [4,5]. Recent reports have revealed that BRCA2-deficient cells accumulate DNA-RNA hybrids or R loops [6,7]. Unscheduled hybrids may form during transcription representing an important source of genome instability by either the subsequent action of nucleases acting on the displaced ssDNA strand or, mainly, by blocking RF progression leading to transcription-replication conflicts [8]. On the other hand, DNA-RNA hybrid accumulation is enhanced by both single (SSBs) and double strand DNA breaks (DSBs) [9] and recent reports indicate that DNA-RNA hybrids accumulate in the proximity of DSBs [10-15].

Given the ability of R loops to compromise genome integrity, cells have developed different strategies to prevent the detrimental accumulation of these structures. Among these are particularly relevant nucleases such as RNases H1 and H2 and a number of recently characterized RNA helicases [8]. The latter include, in addition to Senataxin [16], members of the DEAD-box family of RNA helicases such as DDX1 [17], DDX5 [18], DDX21 [19], DDX19 [20] or UAP56/DDX39B[21]. Arguably, their mechanism of action is not completely elucidated and their functional specificity might be determined by the nucleic acid structural context and the co-factors they interact with.

Several DNA repair proteins have been proposed to act in concert with helicases and nucleases to direct DNA-RNA hybrid resolution. For example, BRCA2 and other related proteins such as BRCA1 or the Fanconi anemia (FA) canonical factors FANCD2, FANCJ and FANCM reduce DNA-RNA hybrids at transcription-replication conflicts [22-24]. Both BRCA1 and BRCA2 have also been reported to regulate RNA pol II transcription elongation [25] or termination [26], which

when defective result in R loop-mediated DNA breaks. Interestingly, a connection between FA factors and splicing has been recently revealed [27].

In this study we find that BRCA2 interacts with DDX5, a known DEAD-box RNA helicase [28,29], and their association is particularly enriched in DNA damage conditions. BRCA2 stimulates the DNA-RNA hybrid unwinding activity of DDX5 *in vitro* and promotes its association with DNA-RNA hybrids located in the vicinity of DSBs. Both DDX5-depleted cells and cells bearing a breast cancer missense variant (T207A), that reduces BRCA2 interaction with DDX5, exhibit increased DNA damage-associated DNA-RNA hybrids and delays kinetics of HR-mediated DSB repair. Our results indicate that DNA-RNA hybrids are an impediment for the repair of DSBs and reveal that BRCA2 and DDX5 are active players in their removal.

Results

BRCA2 physically interacts with DDX5

The N-terminal region of BRCA2 is highly disordered [30]. To get insight on its function we used a mass spectrometry screen to identify interacting partners using HEK293T cells overexpressing a fusion protein comprising the first 1000 aa of BRCA2 fused to a N-terminal 2xMBP tag followed by two nuclear localization signals (NLS) (hereafter $BRCA2_{NT}$) or the 2xMBP-NLS alone. Among the potential protein partners we found several RNA helicases including the DEAD-box RNA helicase DDX5 [29], recently reported to suppress R loops [18](Supplementary Figure 1a, Supplementary Table 1). In order to validate the interaction between BRCA2 and DDX5, we performed a pull-down assay and Western blot that showed an interaction between overexpressed $BRCA2_{NT}$ and endogenous DDX5 (Figure 1a). Exposure of HEK293T cells to DNA damage induced by γ-irradiation (6Gy)

enhanced the interaction although the increase was moderate (Figure 1a). We then confirmed the interaction of the endogenous proteins BRCA2 and DDX5 by co-immunoprecipitation (co-IP) in both unchallenged and irradiated conditions (γ-irradiation, 6 Gy) (Figure 1b). The association of the endogenous BRCA2 and DDX5 was not mediated by DNA or RNA as was not affected by benzonase (Figure 1b). Consistently, using *in situ* proximity ligation assay (PLA) and specific antibodies, we found that BRCA2 and DDX5 colocalized in U2OS cells and that their proximity was enhanced in cells exposed to γ-irradiation (Figure 1c).

Given that both BRCA2- and DDX5-deficient cells accumulate DNA-RNA hybrids [6,18], we assessed whether the interaction could be promoted by DNA-RNA hybrids. As shown in Figure 1c, the proximity of BRCA2 and DDX5 in both untreated and irradiated cells was reduced after overexpression of RNase H1, a nuclease that specifically degrades the RNA moiety of DNA-RNA hybrids, the effect being stronger under irradiated conditions. In addition, inhibition of transcription with cordycepin led to a substantial reduction in the proximity of BRCA2 and DDX5 in both untreated and irradiated conditions suggesting that their colocalization is transcription-dependent (Figure 1c).

Next, to define a smaller region of BRCA2 sufficient to bind DDX5 we used a series of truncated fragments contained in the $BRCA2_{NT}$ used in the proteomic mass spectrometry screen. We overexpressed three 2xMBP-NLS-tagged fragments comprising either BRCA2 aa 1-250, 1-500 or 1-750 or the 2XMBP-NLS alone as control and performed an amylose pull-down for the detection of DDX5 in complex with these fragments of BRCA2 (Figure 1d). Three BRCA2 fragments but not the control 2xMBP-NLS were able to form a benzonase-resistant complex with DDX5 indicating that the first 250 aa of BRCA2 (hereafter $BRCA2_{T1}$) are sufficient to bind DDX5 (Figure 1d). To find out if the interaction was direct, we purified

2XMBP-BRCA2$_{T1}$ from HEK293T cells as we previously reported [31] and MBP-DDX5-GST from bacteria as previously described [32] and performed a GST pull-down assay. Importantly, BRCA2$_{T1}$ was readily eluted from the glutathione resin only in the reaction containing GST-DDX5-MBP indicating that the interaction between BRCA2 and DDX5 is direct (Figure 1e).

Altogether, these results indicate that BRCA2 and DDX5 interact directly through the first 250 aa of BRCA2 and suggest that the interaction is enhanced particularly at DNA-RNA hybrids and in cells exposed to γ-irradiation.

DDX5 depletion leads to a genome-wide increase of DNA-RNA hybrids

As demonstrated previously [6,18], depleting BRCA2 or DDX5 lead to DNA-RNA hybrids accumulation, visualized by immunofluorescence (IF) using the DNA-RNA hybrid marker S9.6 in U2OS cells [33] (Supplementary Figure 1b). Consistently, DDX5 overexpression rescued the DNA-RNA hybrid accumulation observed in DDX5-depleted cells but also of BRCA2-depleted cells (Figure 2a) confirming its role suppressing these hybrids.

To test whether DDX5 associates with DNA-RNA hybrids, we performed *in situ* PLA experiments and found that DDX5 was indeed in close proximity to them (Figure 2b). As expected for an association with DNA-RNA hybrids, the proximity was reduced in cells transfected with a plasmid expressing RNAse H1 (Figure 2b). Given that (i) DDX5 depletion leads to increased sensitivity to replication stress [18] and (ii) unscheduled DNA-RNA hybrids represent a barrier for replication [34-36], we next asked whether this association was particularly enriched in replicating cells. However, in our conditions, DDX5 association with hybrids was independent of replication, since both EdU and non-EdU stained cells displayed similar levels of DDX5-S9.6 PLA signal (Figure 2b), but was dependent on transcription

(Supplementary Figure 1c).

To analyse the genome-wide effect of DDX5 depletion on DNA-RNA hybrids, we performed a DRIPc-seq experiment providing high-resolution and strand-specific profiling of hybrids [37] in K562 cells. Consistent with the reliability of this method [38], the data obtained from two biological replicates were reproducible (Figure 2c). Meta-plot analysis of the strand-specific composite profile across the average gene body revealed an enrichment of DNA-RNA hybrids at the 3' end of the template strand (Figure 2d), corresponding to sense transcription throughout the gene body, as well as an enrichment of DNA-RNA hybrids at the 5' end of the non-template strand, corresponding to antisense transcription at the promoters at the non-template strand, as previously reported [21,37]. DDX5-depleted cells exhibited similar overall distribution pattern of hybrids, but the levels were consistently higher than those obtained with control cells (GEO, GSE127979) [21]. Therefore, DDX5 depletion leads to a genome-wide increase in the DNA-RNA hybrids along gene bodies, consistent with a role in RNA processing [28].

DDX5 and BRCA2-depleted cells accumulate DNA-RNA hybrids at DSBs

Since BRCA2 and DDX5 interaction was enhanced after γ-irradiation, we wondered whether DNA-RNA hybrids were enriched at DSB sites in DDX5-depleted cells. We compared our DRIPc-seq data to a previously reported γH2AX ChIP-seq analysis performed in the same cell line (GEO, GSE104800) [39]. Interestingly, the signal of DRIPc-seq was enriched in DDX5-depleted cells around γH2AX ChIP-seq peaks (Figure 2e). Moreover, the overlap of DNA-RNA hybrids and γH2AX-enriched regions was almost two-fold higher in DDX5-depleted cells compared to the control cells (22% in DDX5-depleted cells compared to 12% in control cells) (Figure 2f). These results suggest that, in addition to the genome-

wide accumulation of DNA-RNA hybrids along gene bodies presumably independent of damage, DDX5 depletion leads to an enrichment of DNA-RNA hybrids in the vicinity of DSBs. Furthermore, DDX5-depletion caused a two-fold increase in the number of PLA spots observed with the S9.6 and anti-γH2AX antibodies that was reduced by RNase H1 and cordycepin (Figure 3a). Similar results were obtained for BRCA2-depleted cells suggesting that both DDX5 and BRCA2 depletion cause a transcription-dependent increase in DNA-RNA hybrids associated with DNA breaks.

These results, however, do not discriminate whether the DNA-RNA hybrid leads to the break or vice versa. To add some light to this conundrum, we determined DNA-RNA hybrid levels at DSBs induced in the U2OS DIvA cell system [40]. In these cells, around 100 DSBs (detectable by γH2AX) are generated by the restriction enzyme *Asi*SI at specific sites upon treatment with tamoxifen (OHT), (Supplementary Figure 2). We focused the analysis on two loci: (i) the *RBMXL1* gene containing an *Asi*SI cut-site and (ii) *HIST1H2BG* gene that does not contain an annotated *Asi*SI cut-site but was previously shown to accumulate DNA-RNA hybrids upon DDX5 loss [18]. In addition, we used *SNRPN* gene, which is not prone to DNA-RNA hybrids, as a negative control [41] (Figure 3b).

Monitoring DNA-RNA hybrids in these cells by DNA-RNA hybrid immunoprecipitation (DRIP), revealed that, as expected, control cells strongly accumulated DNA-RNA hybrids at the *RBMXL1* gene especially after DSB induction (+OHT) (Figure 3b). As a control, we confirmed that depletion of the Senataxin (SETX) DNA-RNA helicase increased hybrids at the cut-sites compared to the control cells, as previously reported [12]. BRCA2-depleted cells also showed a similar trend, consistent with a previous report [41]. Importantly, DDX5-depleted cells showed an enrichment of DNA-RNA hybrids upon induction of DSBs (Figure 3b).

The levels of DNA-RNA hybrids were strongly reduced by RNase H1 treatment demonstrating the specificity of the signal. The levels of DNA-RNA hybrids were not significantly affected by OHT addition in the *HIST1H2BG* gene, nor in a non-transcribed region (*SNRPN*) (Figure 3b), indicating that the effect observed depends on the induction of the break and transcription. Altogether, these results suggest that BRCA2 and DDX5 depleted cells exhibit increased levels of DNA-RNA hybrids at DSBs sites.

BRCA2 helps retain DDX5 at DNA damage sites

To determine whether BRCA2 could modulate DDX5 retention at damaged sites we performed laser irradiation (405 nm) in U2OS live cells sensitized by Hoechst 33258 transfected with DDX5-GFP and monitored the recruitment of DDX5 at DNA damage tracks as described before for DNA repair proteins [42] and RBPs [43]. We verified the efficiency of our system to specifically recruit DSB repair proteins by monitoring under the same conditions the recruitment of the early DSB marker GFP-53BP1. As expected, GFP-53BP1 signal re-localized at laser tracks within 2 min post-irradiation and the signal at the tracks increased over time reaching a maximum at around 10 min post-irradiation (Figure 4a). Before laser irradiation, DDX5-GFP exhibited a predominant nuclear staining as previously reported [44], although with some accumulation of signal at the nucleoli probably due to its overexpression (Figure 4a). In contrast to GFP-53BP1, DDX5-GFP signal decreased specifically at the DNA damage tracks, detected in 11% of the cells upon laser microirradiation (Figure 4a). This “anti-stripe” pattern already reported before for other RBPs and DEAD-box proteins [43,45,46] started within the first 2 min post-irradiation and reached 25% of the cells at 10 min post-irradiation whereas the rest of the cells showed DDX5 pan-nuclear staining. Interestingly, depletion of

BRCA2 resulted in a widespread “anti-stripe” pattern of DDX5-GFP in the cell population reaching 63% of the cells at 6 min (Figure 4a). Thus, only 37% of the cells retained DDX5 at the laser tracks in BRCA2-depleted cells compared to the 75% in cells expressing BRCA2.

Since DDX5 has been involved in transcription regulation in response to DNA damage [47], the “anti-stripe” pattern observed here suggests that DDX5 is excluded from the DNA damage sites probably due to the local repression of transcription concomitant to DNA damage [46,48], and that BRCA2 retains or re-localizes DDX5 at laser-induced DNA damage tracks. To confirm this possibility, we took advantage again of the U2OS DIvA cell system [40] and measured directly the presence of DDX5 at DSBs by ChIP. The occupancy of DDX5 at the *RBMXL1* gene increased upon DSB induction (+OHT) in control cells. Importantly, this increase was not observed in cells depleted of BRCA2 (Figure 4b). Furthermore, DDX5 was not enriched at the control *HIST1H2BG* gene, where there is no *Asi*SI cut-site (Figure 4b). We also monitored the nuclear fluorescence intensity of DDX5 to determine any difference upon DNA damage induction. As expected, DSB induction with OHT treatment resulted in a robust increase of γH2AX foci in all conditions (Figure 4c). Endogenous DDX5 displayed a distinct granular nuclear pattern as previously reported in interphase cells [49] (Figure 4c). In addition, DDX5 nuclear intensity increased upon DSB induction in control cells whereas it remained unchanged in BRCA2-depleted cells (Figure 4c). These results suggest that DDX5 nuclear localization increases upon DNA damage in a BRCA2-dependent manner and that BRCA2 helps retain DDX5 at DNA damage sites.

BRCA2 stimulates the R loop unwinding activity of DDX5

DDX5 can unwind R loops and DNA-RNA hybrids *in vitro* [18 32] suggesting that its

helicase activity might be required to process DNA-RNA hybrids in cells. Thus, we next assessed whether DDX5 R loop unwinding activity was altered by BRCA2. We purified GFP-MBP-BRCA2 from human HEK293T cells following our standard protocol [50] and assessed the unwinding activity of DDX5 on synthetic radiolabeled R loops substrates *in vitro*. The incubation of increasing concentrations of DDX5 (1-5 nM) with the R loop substrate for 30 min reached up to 40% of unwound product in a reaction that required ATP and Mg^{2+} (Figure 5), consistent with a previous report [18]. Importantly, the addition of nearly-stoichiometric concentration of purified BRCA2 relative to DDX5 (2 nM) stimulated DDX5 helicase activity up to two-fold reaching 80% of unwound product (Figure 5). To find out whether the region of interaction, $BRCA2_{T1}$ (Figure 1d, e), was sufficient to stimulate this activity, we conducted the same unwinding assay now in the presence of $BRCA2_{T1}$. Interestingly, as with full-length BRCA2, $BRCA2_{T1}$ was able to stimulate DDX5 unwinding of R loops, although the concentration of $BRCA2_{T1}$ required to achieve similar stimulation as the full-length BRCA2 was ~25-fold higher (Figure 5). This is perhaps not surprising given the disordered nature of the N-terminal region in isolation [30].

Taken together, these results reveal that nearly-stoichiometric amounts of BRCA2 stimulate the R loop unwinding activity of DDX5. We previously showed that the region from 250-500aa of BRCA2 contains a DNA binding domain [31], which is not comprised in the DDX5 binding region (Figure 1d, e). Therefore, the stimulatory function of BRCA2 depends primarily on direct protein-protein interaction through the first 250 aa of BRCA2 and not on its DNA binding activity.

BRCA2-T207A cells show reduced interaction with DDX5 leading to increased DNA-RNA hybrids

Following the mapping of the interaction and the helicase stimulatory activity to the first 250 aa of BRCA2 ($BRCA2_{T1}$) we searched for BRCA2 missense variants identified in breast cancer patients that could disrupt the interaction with DDX5. We selected T207A, a breast cancer variant of unknown clinical significance (VUS) (clinvar/variation/VCV000052028.2) affecting a highly conserved residue in the region of $BRCA2_{T1}$ that we had characterized previously in the context of mitosis [5]. Using DLD1 BRCA2-deficient cells stably complemented with GFP-tagged BRCA2 WT or BRCA2-T207A, we performed a GFP-trap pull-down assay to detect bound DDX5. Although the levels of BRCA2 WT and BRCA2-T207A were variable (see input levels in Figure 6a), the amount of pull-down BRCA2 protein was equivalent in the two samples (GFP-trap pull-down). BRCA2-T207A association with DDX5 was consistently reduced by two-fold as compared to BRCA2 (Figure 6a).

We next wondered whether cells bearing the T207A variant accumulated DNA-RNA hybrids. In agreement with a previous report using BRCA2-depleted cells [6] and reproduced in U2OS cells here (Supplementary Figure 1b) we found that DLD1 BRCA2-deficient cells ($BRCA2^{-/-}$) accumulated DNA-RNA hybrids, as detected by an increase in S9.6 nuclear IF signal, compared to the DLD1 cells bearing endogenous BRCA2 ($BRCA2^{+/+}$)(Supplementary Figure 3a). This was also confirmed by DRIP at the *HIST1H2BG* locus (Supplementary Figure 3b). Importantly, $BRCA2^{-/-}$ cells stably expressing BRCA2-T207A augmented the levels of DNA-RNA hybrids by 1.5-fold compared to the cells complemented with BRCA2 WT (Figure 6b). Consistently, a 2.4-fold increase in the levels of DNA-RNA hybrids was detected by DRIP at the *HIST1H2BG* locus (Figure 6c). These increased levels were specific to DNA-RNA hybrids as they were dramatically reduced upon RNase H1 treatment (Figure 6c, Supplementary Figure 3c).

Given that BRCA2 interaction with DDX5 seemed relevant upon DNA damage, we analyzed whether these conditions would promote DDX5 retention or localization to damaged sites by *in situ* PLA (Figure 6d). As shown before in U2OS cells (Figure 1c), the proximity between BRCA2 and DDX5 was enhanced by irradiation in DLD1 cells bearing BRCA2 WT. In contrast, cells bearing BRCA2-T207A displayed consistently reduced proximity of BRCA2 and DDX5 in both conditions (Figure 6d).

Importantly, BRCA2-T207A cells also exhibited a clear reduction of DDX5-S9.6 PLA signal compared to the BRCA2 WT cells. The signal in BRCA2-T207A cells exposed to DNA damage was equivalent to that of $BRCA2^{-/-}$ cells (Figure 6e). These results confirm that BRCA2-DDX5 interaction promotes localization/retention of DDX5 to DNA-RNA hybrids at DNA breaks. Moreover, T207A bearing cells increased the levels of DNA-RNA hybrids associated with DNA breaks as manifested by an increased levels of S9.6-γH2AX PLA spots compared to control cells (Figure 6f). The effect was transcription-dependent and specific to DNA-RNA hybrids as shown by the dramatic signal reduction caused by cordycepin and RNase H1 treatments, respectively (Figure 6f).

To find out whether this increase was due to a defect in the unwinding activity of DDX5 we purified $BRCA2_{T1}$-T207A from human cells as for $BRCA2_{T1}$ and tested again the helicase activity of DDX5 now in the presence of this fragment. Interestingly, $BRCA2_{T1}$-T207A inhibited the helicase activity of DDX5 (Figure 6g) suggesting that the fraction of BRCA2-T207A that binds DDX5 results in a non-productive interaction with DDX5 precluding its unwinding activity.

Thus, BRCA2-T207A reduces BRCA2-DDX5 productive interaction, impairing the localization of DDX5 at DNA-RNA hybrids especially in cells exposed to DNA damage and inhibiting its unwinding activity.

DDX5-BRCA2 interaction favors DSBs repair by homologous recombination

Finally, we assessed the possible impact of the DNA-RNA hybrids observed in DDX5-depleted cells or BRCA2-T207A cells on the repair of DSBs by HR. We used cells exposed to γ-irradiation (6 Gy) at different time points and quantified the number of γH2AX foci, as a marker of DSBs, and RAD51 foci, as a marker of HR repair. As expected, the number of γH2AX foci increased upon irradiation in both control and DDX5-depleted U2OS cells (Supplementary Figure 4a). Interestingly, although the number of RAD51 foci gradually increased upon exposure to irradiation in both cell lines, the kinetics was clearly affected in DDX5-depleted cells (Figure 7a). In control cells, the number of RAD51 foci reached a maximum 1-hour after the irradiation and started recovering 4 hours post-irradiation, consistent with the repair of the damage. In contrast, 4 hours were required to reach the same maximum levels in DDX5-depleted cells. A delay in the kinetics of appearance of RAD51 foci post-irradiation was also observed in DLD1 cells stably expressing BRCA2-T207A variant versus BRCA2 WT (Figure 7b, Supplementary Figure 4b). Of note, in agreement with the slower growth rate we observed in DLD1 cells compared to U2OS cells, the peak of RAD51 foci was observed only at 4 hours post-irradiation in DLD1 BRCA2 WT cells and was not reached even at 8 hours post-irradiation in BRCA2-T207A cells. Consistent with previous reports [51], the number of RAD51 foci was severely reduced in $BRCA2^{-/-}$ cells exposed to IR as compared to the BRCA2 WT cells (Figure 7b).

DNA-RNA hybrids that form at DSBs have been shown to alter the outcome of their repair by either promoting or impeding DNA end-resection [13,52], one of the early steps of HR pathway. To test the consequences of the observed DNA-RNA hybrid accumulation due to the lack of BRCA2-DDX5 interaction on DNA-end

resection, we monitored the formation of RPA foci, a protein that coats ssDNA immediately upon resection [53], in irradiated DLD1 cells bearing BRCA2 WT or BRCA2-T207A. Interestingly, cells bearing T207A mutation showed reduced number of RPA foci after γ-irradiation compared to BRCA2 WT cells even if the levels of γH2AX were equivalent in both cell lines (Figure 7c) suggesting that end-resection might be affected in these cells.

If the increased levels of DNA-RNA hybrids observed in T207A cells is causing the delay observed in the appearance of RPA and RAD51 repair foci, reducing the DNA-RNA hybrids should rescue this delay. To test this hypothesis, we overexpressed RNase H1 in cells bearing T207A and monitored the number of RAD51 foci upon γ-irradiation as compared to non-irradiated cells. Importantly, overexpression of RNase H1 partially restored the levels of RAD51 foci at 2h after treatment without significantly changing the number of DSBs, as monitored by γH2AX foci (Figure 7d, Supplementary Figure 4c). Overall, these results suggest that the DNA-RNA hybrids that accumulate in cells bearing T207A variant interfere with the repair of the DNA damage by HR.

Discussion

In this work, we establish that BRCA2 physically binds the RNA helicase DDX5 and demonstrate that this interaction plays an active role in the resolution of DNA-RNA hybrids associated with DSBs that favors their repair by HR.

BRCA2 retains DDX5 at DNA damage sites and stimulates its DNA-RNA hybrid unwinding activity *in vitro*. We show that either depleting DDX5 or precluding the interaction of BRCA2 and DDX5, as observed in the breast cancer variant BRCA2-T207A, reduce the efficiency of HR repair by altering the kinetics of RAD51 repair foci.

Our findings suggest that DDX5 functions at DNA-RNA hybrids that form in the vicinity of DSBs and its association with these structures is enhanced by BRCA2. Several observations support this interpretation: (1) DDX5-depleted cells accumulate DNA-RNA hybrids genome-wide and particularly at DSBs; (2) BRCA2 is required to retain/relocalize DDX5 at induced-DSBs and laser micro-irradiation tracks, and (3) the proximity of DDX5 to DNA-RNA hybrids under DNA damage conditions (IR) decreases in cells bearing a BRCA2 missense variant that impairs BRCA2-DDX5 interaction.

Although enhanced, BRCA2 interaction with DDX5 is not restricted to DNA damage conditions. DDX5 has been recently reported to suppress spontaneous R loops at R loop-prone loci, an activity that requires DDX5 methylation by PRMT5 [18]. Here we show that the role of DDX5 preventing DNA-RNA hybrids is ubiquitous, since the increase in DNA-RNA hybrids after depletion of DDX5 is observed genome-wide. Whether BRCA2 acts in concert with DDX5 or other RNA helicases to resolve spontaneous DNA-RNA hybrids needs further study.

As its homolog in yeast Dbp2, DDX5 can unwind DNA-RNA hybrids both alone or in the context of R loops *in vitro* [18,32]. Notably, we found that BRCA2 stimulates the unwinding activity of DDX5 on R loops *in vitro*, thus defining a novel function for BRCA2. Mechanistically, it is possible that BRCA2 binding modifies the ATP hydrolysis rate of DDX5, as shown for the recombination enzyme RAD51 [54]. Unlike canonical RNA helicases, DEAD-box proteins unwind duplex RNA by “bending” one of the RNA strands [28]. Thus, it is also conceivable that BRCA2 interaction changes the conformation of DDX5 so that it binds with different affinity to RNA. An altered ATPase or RNA binding affinities of DDX5 may also explain why BRCA2$_{T1}$-T207A precludes DDX5 DNA-RNA helicase activity. Besides, it is not surprising that this type of non-processive helicases rely on co-factors for

substrate specificity, whether an RNA or a DNA-RNA hybrid, and/or to enhance their activity [28]. Interestingly, these findings suggest a role of BRCA2 upstream its canonical position in the recombination process as the resolution of DNA-RNA hybrids precedes the loading of RAD51 (Figure 7e). Regarding this possibility, a previous report showed that BRCA2 is recruited early to DNA damage sites through PolyADP-ribose (PAR) binding [55].

The consequences of DNA-RNA hybrids at the break are controversial: whereas some reports suggest that hybrids formed at DSBs may preclude the subsequent steps of the HR repair process [11,12], others have suggested that these structures could act as intermediates of the pathway [13,15,41]. In both scenarios however, DNA-RNA hybrids need to be removed to license DNA repair by HR. DNA-RNA hybrid resolution could be required at different stages. On the one hand, DNA-RNA hybrids may form at the breaks before resection facilitated by the dsDNA rotation freedom conferred by a DSB [9], with the possibility of channeling repair towards NHEJ as it was shown in cells depleted of Senataxin [12]. On the other hand, DNA-RNA hybrids may form at the ssDNA generated upon resection impeding RPA binding, in a scenario in which long-range end-resection, required for HR, is already committed, as described for DDX1-depleted cells [11]. Interestingly, DDX5 interaction with BRCA2 favors RPA coating and the timely repair of DSBs, as measured by RAD51 foci formation, which are not altered by Senataxin [12]. Moreover, the reduced RAD51 foci formation can be partially rescued by RNase H1 suggesting that the DNA-RNA hybrid resolution activity of BRCA2-DDX5 directly impacts HR. Thus, our results are consistent with DNA-RNA hybrids associated with DNA damage being an impediment for the HR process and BRCA2-DDX5 being active players in their resolution. Because the domains of interaction of RAD51 and of DDX5 on BRCA2 are separated, it is

conceivable that the two proteins transiently co-exist bound to BRCA2, presumably enabling the efficient repair of DSBs by HR.

Based on the number of RNA helicases that came out in our mass spectrometry screen and a previous report [6], it is possible that BRCA2 acts with other proteins to remove DNA-RNA hybrids. Along these lines, a recent work has reported the association of BRCA2 with the nuclease RNase H2 at DNA-RNA hybrids at DSBs [41], although the phenotype of disrupting the interaction was not assessed in that study.

We show here that a single missense mutation in BRCA2 reduces the interaction of BRCA2 with DDX5 resulting in increased DNA-damage dependent DNA-RNA hybrids. BRCA2-T207A is a breast cancer variant previously characterized as being defective in the alignment of chromosomes due to its altered phosphorylation by PLK1 [5]. In that study, a mild sensitivity of BRCA2-T207A bearing cells to MMC was shown that could not be explained by the defect observed in mitosis. It is possible that that sensitivity results from the fraction of DNA-RNA hybrids at DSBs not resolved in BRCA2-T207A cells. The fact that T207A alters DDX5 interaction and the removal of DNA-RNA hybrids at DSBs with consequences in RAD51-mediated repair exemplifies a missense BRCA2 variant that indirectly affects HR without impairing the canonical HR functional domains of BRCA2; that is, the BRC repeats and the C-terminal DNA binding domain, previously associated with breast cancer risk [56,57]. This, and the cumulative impact of this variant on the functions of BRCA2 may have potential implications for cancer risk assessment.

In summary, our results are in agreement with a model in which the removal of DNA-RNA hybrids formed as a consequence of DSBs is favored by the direct interaction between the DSB repair factor BRCA2 and the RNA helicase DDX5

(Figure 7e). We envision a scenario in which BRCA2 interacts with and retains DDX5 at the DSB site at a DNA transcribed region harboring a DNA-RNA hybrid, thus promoting its DNA-RNA helicase activity to enable HR repair. Other proteins, such as RNA helicases or RNases might also contribute to DNA-RNA hybrid removal but, when BRCA2-DDX5 interaction is impaired, as exemplified by the BRCA2-T207A breast cancer variant, the reaction would either be delayed or less efficient.

Methods

Cell lines

The human cell lines HEK293T and U2OS cells (kind gift from Dr. Mounira Amor-Gueret) were cultured in DMEM (Eurobio Abcys, Courtaboeuf, France) media containing 25 mM sodium bicarbonate and 2 mM L-Glutamine supplemented with 10% heat inactive FCS (EuroBio Abcys). The BRCA2 deficient colorectal adenocarcinoma cell line DLD1 BRCA2$^{-/-}$ [58](HD 105-007) and the parental cell line DLD1 BRCA2$^{+/+}$ (HD-PAR-008) was purchased from Horizon Discovery (Cambridge, England). The cells were cultured in RPMI media containing 25 mM sodium bicarbonate and 2 mM L-Glutamine (EuroBio Abcys) supplemented with 10% heat inactivated fetal calf serum (EuroBio Abcys). The DLD1 BRCA2$^{-/-}$ cells were maintained in growth media containing 0.1 mg/ml hygromycin B (Thermo Fisher Scientific). The stable cell lines of DLD1$^{-/-}$ BRCA2 deficient cells expressing BRCA2 WT or T207A generated as described [5] were cultured in growth media containing 0.1 mg/ml hygromycin B and 1 mg/ml G418 (Sigma-Aldrich). DIvA cells (AsiSI-ER-U2OS) (kind gift from G. Legube) were cultured in DMEM (Gibco) supplemented with antibiotics, 10% FBS and 1 μg/ml puromycin. For AsiSI-dependent induction of DSBs, cells were incubated for 4h in medium containing

300 nM trans-4-Hydroxytamoxifen (4OHT) (Sigma, H7904). K562 cells (ATCC, CCL-243) were cultured in Iscove's Modified Dulbecco's medium (IMDM; GIBCO) supplemented with 10% heat inactivated fetal bovine serum (Sigma Aldrich) and 1% antibiotic-antimycotic (BioWEST).

All cells were cultured at 37°C with 5% CO_2 in a humidified incubator and all cell lines used in this study have been regularly tested negatively for mycoplasma contamination (MycoAlert, Lonza).

Plasmids, transfections and inhibitors

All BRCA2 N-terminal expression constructs containing the sequence coding for BRCA2 amino acids 1–250 ($BRCA2_{T1}$), 1–500 ($BRCA2_{LT2}$), 1–750 ($BRCA2_{LT3}$) or 1-1000 ($BRCA2_{NT}$) and EGFP-MBP-BRCA2 subcloning in phCMV1 expression vector were generated as described [31].

The point mutation T207A in the 2xMBP-$BRCA2_{T1}$ and EGFP-MBP-BRCA2 have been described before [5].

GFP-53BP1 construct was obtained by Gateway cloning (Thermo Fisher Scientific) into pCDNA6.2-GFP of a construct comprising the coding sequence of 53BP1 (kind gift of P. Bertrand, CEA, FR).

DDX5-GFP construct was obtained by the insertion of DDX5 sequence from a pcDNA 6.2 CMV EmGFP vector) in a pEGFP-N3 vector (kind gift from Carsten Janke, Institut Curie, FR) using oAC953/967 primers (see Supplementary Table 2).

MBP-DDX5-GST construct for purification of human DDX5 was a kind gift from Elizabeth Tran (Purdue University, US).

pCDNA3 CMV expressing RNAseH1 has been previously reported[59]; pEGFP-M27 has been previously reported[60].

Transfection of either U2OS or DLD1 cells with pCDNA3 CMV expressing RNAseH1 was performed with Turbofect (ThermoFisher Scientific) 24h before fixation (48h before fixation in case of Figure 7d).

Transfection of U2OS with DDX5-GFP and of DLD1 BRCA2 WT and BRCA2-T207A clones with either pEGFP-C1 (-RH) or pEGFP-M27 (+RH) was performed with Lipofectamin 3000 (Life Technologies) 24h before fixation.

For transcription inhibition in cells, cordycepin (100 µM, Sigma-Aldrich C3394-25MG) was added to the growth media for a 2 h treatment at 37°C.

Ionizing radiation-induced DNA damage

Cells were exposed to a ^{137}Cs source (GSR D1; dose rate: 0.9 Gy/min) and subsequently incubated at 37˚C for the indicated time.

siRNA transfections

For U2OS cells, siRNA transfections were performed using jetPRIME (Ozyme) with 100 nM of the indicated siRNAs following manufacturer's instructions, except for Figure 2a, in which Lipofectamin 3000 (Life Technologies) was used. For BRCA2 depletion we transfected a combination of the BRCA2 siRNA (SI00000966, Qiagen) and BRCA2 siRNA (Dharmacon D-003462-04) (100 nM each) (Figure 3a and Supplementary Figure 1b) or the ON-TARGETplus SMARTpool human BRCA2 (L-021420-00) (Dharmacon) (Figure 2a). For DDX5 depletion we used siRNA targeting DDX5 [61] (Figure 3a, 7a and Supplementary Figure 1b) (see Supplementary Table 3). Experiments were performed 30h or 72h (Figure 2a) after transfection.

For experiments using K562 cells (Figure 2c-f) siRNA transfections were performed using Lipofectamin 3000 (Life Technologies) according to

manufacturer's instructions with 100 nM siRNA targeting DDX5 [61] (see Supplementary Table 3) and experiments were performed 72h after transfection. For experiments using DIvA cells (Figures 3b, 4b and 4c), siRNA transfections were performed using Lipofectamin 3000 (Life Technologies) according to manufacturer's instructions with 100 nM of the indicated siRNAs (ON-TARGETplus SMARTpool human SETX (L-003462-00) (Dharmacon), ON-TARGETplus SMARTpool human BRCA2 (L-021420-00) (Dharmacon), or siRNA targeting DDX5 [61] (see Supplementary Table 3) and experiments were performed 72h after transfection.

The non-targeting oligonucleotide (Dharmacon D-001810-04-20, 100 nM) was used as control (siC) in all cells.

Expression and purification of 2xMBP-BRCA2$_{T1}$ (WT and T207A) and EGFP-MBP-BRCA2

2xMBP-BRCA2$_{1-250}$ and EGFP-MBP-BRCA2 were purified as previously described[31]. Briefly, ten to twenty 150 mm plates of HEK293 were transiently transfected with the 2xMBP-BRCA2$_{1-250}$ (BRCA2$_{T1}$) or the EGFP-MBP-BRCA2 using TurboFect (Thermo Fisher Scientific). The cells were harvested 30 h post transfection, lysed in lysis buffer H (50 mM HEPES (pH 7.5), 250 mM NaCl, 1% NP-40, 5 mM EDTA, 1 mM ATP and 3 mM $MgCl_2$, 1 mM DTT, 1 mM PMSF and EDTA-free Protease Inhibitor Cocktail (Roche)) and incubated with amylose resin (NEB) for 3h at 4°C. The lysate was extensively washed with buffer H including 250 mM (EGFP-MBP-BRCA2) or 500 mM (BRCA2$_{T1}$) NaCl and the protein was eluted with 20 mM maltose. The eluate was further purified with Bio-Rex 70 cation-exchange resin (Bio-Rad) by NaCl step elution. For the purification of 2xMBP-BRCA2$_{T1}$-T207A, we followed the same steps as above except for the Bio-Rex

resin that was substituted by a HiTrap Q HP strong anion exchange column (GE Healthcare). The size and purity of the final nuclease-free fractions were analysed by SDS-PAGE and western blotting using anti-MBP antibody or anti-BRCA2 antibody in the case of full-length BRCA2 purification. Pooled protein was snap frozen in N_2 and stored at -80°C. Concentrations were calculated measuring the intensity of the band on a StainFree gel (Bio-Rad) via ImageLab software and using the same protein at known concentration as a reference.

Expression and purification of MBP-DDX5-GST

MBP-DDX5-GST was purified as described [32]. Briefly, expression of MBP-DDX5-GST in *E. coli* BL21 (DE3) Star cells was induced using 0.2 mM IPTG at 16°C overnight. Cells were lysed in a buffer containing 50 mM HEPES (pH 7.5), 250 mM NaCl and 1% NP-40 and disrupted using a French press. The crude lysate was clarified by centrifugation in a Beckmann Ti45 rotor at 35,000 rpm, 60 min, and the MBP-DDX5-GST was purified from the soluble lysate using glutathione resin (GE healthcare) followed by cation-exchange chromatography (SP sepharose, Sigma-Aldrich). The protein was eluted with elution buffer 1 (50 mM Tris– HCl [pH 8.0], 300 mM NaCl, 20% glycerol). StainFree images of the gels before transfer were used as loading control for the input and cropped image are shown in the figure. Nuclease-free aliquots were snap frozen in N_2 and stored at -80°C. Concentration was calculated measuring intensity of the band on stain-free gel via ImageLab software and using Bradford assay.

Amylose and GFP pull-down from whole cell extracts

For amylose pull-down, cell pellets were resuspended in lysis buffer (50 mM HEPES pH7.5, 250 mM NaCl) supplemented with 1 x protease inhibitor cocktail

(Complete, EDTA-free; Roche), 1 mM PMSF, 1 % NP-40, 1 mM DTT, 1 mM $MgCl_2$ and 250 units/ml benzonase (1.5 ml lysis buffer/2.5 x 10^7 cells). Cell suspension was sonicated and cleared by centrifugation. The supernatant was then incubated for O/N at 4°C with 60 µl amylose resin (New England Biolabs) per 2.5 x 10^7 cells. After 4 washes with washing buffer (50 mM HEPES pH7.5, 500 mM NaCl, EDTA 5 mM), the bound proteins were eluted in washing buffer supplemented with 10 mM maltose (Sigma). Eluted proteins were separated by SDS-PAGE and analysed by western blotting. For all Western blots, the protein bands were visualized with ChemiDoc XRS+ System (BioRad). StainFree images of the gels before transfer were used as loading control for the input and cropped image is shown in the figure.

For GFP-pull-down, DLD1 BRCA2$^{+/+}$ parental cells and DLD1 BRCA2$^{-/-}$ stable clones expressing EGFP-MBP-BRCA2 (WT or T207A) pellets were re-suspended in lysis buffer (50 mM HEPES pH7.5, 100 mM NaCl) supplemented with 1 x protease inhibitor cocktail (Complete, EDTA-free; Roche), 1 mM PMSF, 1 % NP-40, 1 mM DTT, 1 mM $MgCl_2$ and BSA 100 µg/ml. Cell suspension was sonicated and cleared by centrifugation. The supernatant was then incubated for 1, 5h at 4°C with 25 µl of pre-equilibrated GFP-TRAP beads (Chromotek) to pull-down EGFP-MBP-BRCA2. The beads were washed 3 times in lysis buffer with 250 mM NaCl. Bound proteins were eluted by boiling the samples for 4 min in 3x SDS-PAGE sample loading buffer (SB), eluted proteins were separated by SDS-PAGE and analysed by western blotting. For all Western blots, the protein bands were visualized with ChemiDoc XRS+ System (BioRad) and quantified by Image LabTM5.2.1 Software (BioRad). To calculate the relative co-immunoprecipitation (co-IP)/co-pull-down of a protein of interest, the intensity of the band in the co-IP was divided by the intensity of the band in the input (ImageQuantTMTL software),

the ratio co-IP: input of the protein of interest was then divided by the intensity of the band of the immunoprecipitated protein. StainFree images of the gels before transfer were used as loading control for the input and cropped image is shown in the figure.

Amylose pull-down from nuclear cell extracts

Four plates of HEK293T exponentially growing cells were harvested and the cell pellets were gently resuspended in nuclear isolation buffer (NIB; 10 mM HEPES pH 7.5, 10 mM KCl, 1.5 mM $MgCl_2$, 10 % glycerol, 350 mM sucrose) supplemented with 1 x protease inhibitor cocktail (Complete, EDTA-free; Roche), 1 mM PMSF and 1 mM DTT (1.5 mL lysis buffer/2.5 x 10^7 cells). Samples were kept on ice for 10 min and centrifuged at 1300 *x g* for 5 min at 4ºC. The pellet (nuclear fraction) was washed with NIB and sonicated. The pull-down was performed as that of the whole cell extracts above.

Mass spectrometry

Amylose-isolated samples were separated by SDS-PAGE and stained with colloidal blue (LabSafe Gel Blue GBiosciences). In-gel digestion was performed, according to standard protocols. Briefly, 23 to 24 gel slices were excised, washed, and the proteins were reduced with 10 mM DTT (Sigma) and alkylated with 55 mM iodoacetamide (Sigma). The gel pieces were washed with 100% acetonitrile and incubated overnight with trypsin (Roche Diagnostics) in 25 mM ammonium bicarbonate at 30 °C. Peptides extracted from each gel slice were used directly and analyzed by nano-liquid chromatography-coupled to tandem mass spectrometry (nanoLC-MS/MS) for protein identification. Each sample was concentrated and then separated on a C18 reverse phase column, with a linear

acetonitrile gradient (UltiMate 3000 System, Dionex, and column 75 µm inner diameter × 15 cm, packed with C18 PepMapTM, 3 µm, 100 Å; LC Packings) before MS and MS/MS. Spectra were recorded on an LTQ-Orbitrap XL mass spectrometer (Thermo Electron). For identification, data were searched against the Swiss-Prot "Homo sapiens" database using Mascot^{TM} (version 2.5.1) one by one band or merged per conditions for emPAI abundance evaluation. Enzyme specificity was set to trypsin and a maximum of two-missed cleavage sites were allowed. Oxidized methionine, carbamidomethyl cysteine and N-terminal acetylation were set as variable modifications. Maximum allowed mass deviation was set to 2 ppm for monoisotopic precursor ions and 0.8 Da for MS/MS peaks. Result files were further processed using myProMS software [62]. FDR calculation used Percolator[63] and was set to 1% at the peptide level for the whole study. To calculate protein abundance we used the label free exponentially modified protein abundance index (emPAI) and molar % values obtained in the merged Mascot from each replicate as described[64]. Mascot uses only peptides identified with score at or above homology or identity thresholds for the calculation of the emPAI values. Fold change ratios for identified proteins were calculated by dividing the calculated molar percentage value for an individual protein in the $BRCA2_{NT}$ condition with the cognate 2XMBP condition value.

The Mass Spectrometry datasets generated during this study are available at ProteomeXchange Consortium via the PRIDE [65] partner repository. Project Name: BRCA2-N-terminus interacting proteins in HEK293T cells

Project accession: PXD018979

Reviewer account details: (Username: reviewer16179@ebi.ac.uk, Password: GcRskLia)

Co-immunoprecipitation

Cell pellets were resuspended in lysis buffer (50 mM HEPES pH7.5, 250 mM NaCl, 5 mM EDTA) supplemented with 1 x protease inhibitor cocktail (Complete, EDTA-free; Roche), 1 mM PMSF, 1 % NP-40, 1 mM DTT, 1 mM $MgCl_2$ and 250 units/ml benzonase (1.5 ml lysis buffer/2.5 x 10^7 cells). The cell suspension was sonicated and cleared by centrifugation. The supernatant was then incubated for 2 h in a

rotator at 4°C with 1 µg Dynabeads Protein G (Life Technologies) and 1 µg primary antibody(or normal IgG where indicated) per 2.5 x 10^7 cells. The beads were collected using a magnet and washed 4 times with washing buffer (50 mM HEPES pH7.5, 250 mM NaCl, EDTA 5 mM). Proteins were eluted with 50 µl 0.2 M glycine pH 2.2 per sample. 3 µl of 1.5 M Tris-HCl pH 8.8 was added. Eluted proteins were separated by SDS-PAGE and analysed by western blotting. For all Western blots, the protein bands were visualized with ChemiDoc XRS+ System(BioRad). StainFree images of the gels before transfer were used as loading control for the input and cropped image is shown in the figure.

In vitro pull-down

Glutathione resin (GE healthcare) was equilibrated with binding buffer: 50 mM HEPES (pH 7.5), 250 mM NaCl, 1mM DTT. Purified MBP-DDX5-GST (200 ng) was incubated with 200 ng of purified 2XMBP-$BRCA2_{T1}$ for 30 min at 37 °C and then batch bound to 30 µl of glutathione resin for 1h at 4 °C under rotation. The

complexes were washed 3 times with washing buffer (50mM HEPES (pH 7.5), 500mM NaCl, 1mM DTT) containing 0.1% Triton-X 100.

Bound proteins were eluted with 30 µl 20mM reduced Glutathione in binding buffer,

resuspended in 3X SDS sample buffer, heated at 54 °C for 5 min and loaded onto a

10% SDS–PAGE gel. Proteins were analysed by western blotting.

For all Western blots, the protein bands were visualized with ChemiDoc XRS+ System(BioRad).

Antibodies used for Western Blotting

mouse anti-MBP (1:5000, R29, Cat. #MA5-14122, Thermo Fisher Scientific), mouse anti-BRCA2 (1:1000, OP95, EMD Millipore), mouse anti-DDX5 (1:100 or 1:500, Cat. # sc-166167 Santa Cruz Biotechnology). Horseradish peroxidase (HRP) conjugated secondary antibodies used: mouse-IgGκ BP-HRP (IB: 1:5000, Cat. #sc-516102, Santa Cruz), goat anti-mouse IgG-HRP (1:10 000, Cat.# 115-035-003, Interchim).

In situ Proximity Ligation Assay (PLA)

Cells were seeded on coverslips precoated with 1 µg/ml fibronectin (Sigma) and 20 µg/ml collagen (Sigma). In case of EdU incorporation, a pulse-label nascent DNA was performed with 10 µM EdU for 5 min before fixation. Cells were washed with PBS and cytoskeleton (CSK) buffer (10 mM PIPES pH 6.8, 100 mM NaCl, 300 mM sucrose, 3 mM $MgCl_2$ and 1 x protease inhibitor cocktail (Complete, EDTA-free; Roche)) and permeabilized with CSK-T buffer (CSK supplemented with 0.5 % Triton-X100). After washes in CSK and PBS, the cells were fixed with 2 % para-formaldehyde (PFA) for 20 minutes at room temperature (RT). The cells were then washed 3 times with PBS. . In case of EdU labelling, before incubation with primary antibodies, samples were incubated for 30 minutes at RT with a Click-mix solution (Biotin-azide 6nM, Sodium ascorbate 10 mM, CuSO4 2 mM, diluted in

PBS 1X) in order to allow EdU-biotin conjugation. In this case, IF was combined to PLA, adding a primary antibody anti-biotin (1:3000, Bethyl laboratories, Cat. # BETA150-109A) together with primary antibodies for PLA and secondary antibody (donkey anti rabbit Alexa-488, 1:1000, Cat. # A-21206, Life Technologies) together with PLA probes.

In situ PLA was performed following the manufacturer's specifications (Duolink^{TM}, Sigma) except that the primary antibody was incubated for 1h at 37°C. For quantification, particle analysis was done using ImageJ software (NIH Image). The nucleus was defined by an auto-threshold (Huang, Image J) on DAPI, a mask was generated and applied onto the Texas-Red2 picture to count PLA spots within the nucleus using the plugin Find Maxima with a prominence of 2000 for Fig. 1C, of 5000 Fig. 2c, 3a, 6b, e, f and Supplementary Figure 1d. Primary antibodies used for PLA: BRCA2 (1:2000 OP95 EMD Millipore), DDX5 (1:3000 Cat. # ab10261 Abcam), S9.6 (1:100000, Protein Expression and Purification Core facility, Institut Curie), γ-H2AX (1:3000 Cat. # 07-164, EMD Millipore).

Immunofluorescence microscopy

For immunofluorescence experiments in figures 7a-d Supplementary Figure 1b and 4c, cells were seeded on coverslips pre-coated with 1 µg/ml fibronectin (Sigma) and 20 µg/ml collagen (Sigma) the day before 6 Gy γ−irradiation. At the time indicated after irradiation the coverslips were washed twice in PBS followed by one wash in CSK Buffer (10 mM PIPES, pH 6.8, 0.1 M NaCl, 0.3 M sucrose, 3 mM $MgCl_2$, EDTA-free Protease Inhibitor Cocktail (Roche)). The cells were permeabilized for 5 minutes at room temperature in CSK buffer containing 0.5% Triton X-100 (CSK-T) followed by one rinse in CSK buffer and one rinse in PBS before fixation for 20 minutes at room temperature with 2% PFA in PBS. After one rinse in

PBS and one in PBS-T, the cells were blocked for 5 minutes at room temperature with 5% BSA in PBS-T.

For immunofluorescence experiments in figures 2a, 4c, 6b, Supplementary Figure 3a and c, cells grown on glass coverslips coated with poly-L-Lysine (Sigma) were rinsed with cold PBS and treated for 3 minutes with a TritonX-100 extraction buffer (0.1% TritonX-100, 20mM HEPES-KOH pH7.9, 50mM NaCl, 3mM $MgCl_2$, 300mM sucrose). In the case of figures 2a, 6b, Supplementary Figure 3a and c, after extraction, cells were fixed for 8 minutes with methanol at -20ºC; coverslips were then washed three times with PBS and blocked overnight at 4ºC in blocking solution (PBS with 2% BSA). In the case of figure 4c, after extraction, DIvA cells were fixed in 4% FA/2% sucrose in PBS for 10 minutes at room temperature (RT), washed twice in PBS and re-permeabilized with PBS-TritonX-100 0.5% for 10 minutes at RT. Then were then blocked at RT for 1h in blocking solution (3% BSA, 0.1% TritonX-100 in PBS).

For all immunofluorescence experiments, cells were incubated overnight at 4°C in blocking solution with primary antibodies, except in case of figure S1B, when cells were incubated for 1h at 37°C with S9.6 (1:500, Protein Expression and Purification Core facility, Institut Curie) and anti-nucleolin (1:1000 Cat. # ab22758, Abcam) antibodies. For figures 7a-d and Supplementary Figure 4c, cells were incubated with anti-γH2AX (1:1000 Cat. # 05-636, EMD Millipore) anti-RAD51 (1:100 for DLD1 cells, 1:1000 for U2OS cells, Cat. # sc-8349, Santa Cruz Biotechnology) or anti-RPA (1:1000, Cat. # 2208S, Ozyme (Cell Signaling) antibodies. For figures 2a, 6b, Supplementary Figure 3a and c the mouse S9.6 (1:2000) and rabbit anti-nucleolin (1:1000 Cat. # ab50279, Abcam) primary antibodies were used on untransfected cells or S9.6 (1:2000) and rabbit anti-GFP (1:200, Cat. # ab6556

Abcam) were used in the case of transfected cells. For figure 4c anti-γH2AX (1:1000, Cat. # ab2893, Abcam) or anti-DDX5 (1:500, Cat. # sc-166167 Santa Cruz) were used. After primary antibody incubation, the coverslips were rinsed in PBS-T followed by two washes of 10 minutes in PBS-T and blocked for 5 minutes at room temperature with 5% BSA in PBS-T. Cells were incubated with appropriate secondary antibodies (conjugated with Alexa Fluor 488, 546, 568, 594 or 647), diluted in blocking solution for 1h at RT. After rinsing, coverslips were mounted onto slides using ProLong Gold Antifade reagent (Invitrogen). Images in figures 2a, 4c, 6b, Supplementary Figure 3a and c were acquired using a Leica DM6000 wide-field microscope equipped with a DFC390 camera (Leica) at x63 magnification using the LAS AF software (Leica). For figures 7a-d, Supplementary Figure 1b and 4c the camera used was a Hamamatsu Flash 4.0 sCMOS controlled with MetaMorph2.1 software (Molecular Devices).

The quantification of S9.6 intensity was performed in the area of the nucleus as determined by DAPI and subtracting the intensity of S9.6 in nucleoli (stained with an antibody specific for nucleolin, see above).

For figures 2a, 4c, 6b, Supplementary Figure 3a, c automated quantification of foci and fluorescence intensities was performed using the Metamorph v7.5.1.0 software (Molecular Probes).

For figures 7a-d and Supplementary Figure 4c Z-stacks were taken at 0.5 µm intervals to generate a Z-projection image using ImageJ. For the analysis of γ-H2AX, RAD51 and RPA foci, 26 Z-stacks were taken at 0.2 µm intervals to generate a maximal intensity projection using Image J. The number of γH2AX foci per nucleus were counted with a customized macro using a semi-automated procedure; the nucleus was defined by an auto-threshold (Otsu, Image J) on

DAPI, a mask was generated and applied onto the Z-projection to count foci within the nucleus. For the definition of foci we applied the threshold plugin IsoData (ImageJ) and for the quantification of foci we used the tool Analyze Particles (ImageJ) setting a range of 5-100 pixels^2 for Supplementary Figure 4a and a range of 5-1000 for Fig. 7d, Supplementary Figure 4b to select only particles that correspond to the size of a focus. RAD51 and RPA foci were quantified using the plugin Find Maxima onto the Z-projection with a prominence of 1000 for Fig. 7a and of 5000 for Fig. 7b, c.

Protein recruitment after laser-induced damage

U2OS cells were seeded on glass coverslips precoated with 1 µg/ml fibronectin (Sigma) and 20 µg/ml collagen (Sigma). Cells were then co-transfected with 2 µg of a DDX5-GFP construct and BRCA2 siRNA and ON-TARGET plus Non-targeting oligonucleotide (as described in siRNA section) 48h prior to imaging; or with 2 µg of a construct expressing GFP-53BP1 also 48h prior imaging. Cells were pre-sensitized by adding 10 mg/ml of Hoechst dye 33258 to the medium for 5 min at 37°C. Live cell imaging of DDX5-GFP or GFP-53BP1 at laser tracks was carried out using an inverted Leica confocal laser scanning SP5 system equipped with a 37°C heating chamber attached to a DMI6000 stand using 63x/1.4 oil objective. DNA damage was generated using a 405 nm laser diode focused onto a single line (thickness: 1 pixel) within the nucleus to generate the damage. Specifically, we set the laser output to 70% of maximum power and the scan speed at 10 Hz. GFP signal was detected between 500-550nm on PMdetector. All recordings were performed using the indicated sampling frequency (512 x 512 image size, line average of 4 and zooming set to 7.94). To reduce the time of image acquisition, the scan was used in bidirectional regime and the scan speed was set at 10Hz (10

000 lines by second). The whole system was driven by LAS AF software (Leica). Images were collected at 2, 4, 6, 8, 10, 15 and 20 minutes after the DNA damage using a 488 nm argon laser.

The quantification of cells showing a DDX5-GFP “anti-stripe” pattern at DNA damage tracks (reduced GFP signal at the laser tracks compared to the rest of the nucleus) was performed by manual counting in images visualized in ImageJ.

In vitro unwinding assay

DNA substrates were purchased PAGE-purified from MWG Eurofins and the RNA substrate was purchased from Sigma. The RNA oligonucleotide oAC864 (see Supplementary Table 4) was 5′ end- labeled with T4 polynucleotide kinase and [γ-^{32}P]ATP. R loops substrates were prepared by annealing 1 pmol of labeled oAC864 (RNA) to 2.5 pmol of DNA oligo oAC862 (see Supplementary Table 4) and 2.5 pmol of DNA oligo oAC863 (see Supplementary Table 4) in annealing buffer (1 mM EDTA, 10 mM Tris-HCl at pH 7.6) by heating for 2 min at 95°C followed by slow cooling to room temperature. To assess unwinding activity, 1.5 nM molecules of R loop substrate was incubated with the indicated concentrations of purified MBP-DDX5-GST in 25 mM TrisAcO, 5mM $MgCl_2$,1mM DTT, 5mM ATP, 100µg/mL and 40U RNAse OUT (ThermoFisher Scientific) alone or with the indicated concentration of purified 2XMBP-BRCA2 or 2XMBP-BRCA2$_{T1}$. The mixture was incubated at 37°C for 30 min and the reaction products were resolved on 10% PAGE in 1% TAE buffer (40mM Tris Acetate, 0.5mM EDTA) at 110V for 45 min at room temperature. The gels were dried, visualized by phosphorimaging (Typhoon, GE Healthcare) and analysed on Image Quant software (GE Healthcare). In all *in*

vitro unwinding assays, DDX5 unwinding activity was calculated as the percentage of free radiolabelled RNA relative to the R loop signal.

DNA-RNA immunoprecipitation (DRIP)

DRIP was performed in enzymatically digested DNA from U2OS DIvA cells after 72h transfection, with or without 4h treatment with 4OHT for DSB induction, and treated or not with RNase H *in vitro* as previously described [66]. Analysis was performed by qPCR using primers located at each of the regions of interest: RBMXL1-fw (GATTGGCTATGGGTGTGGAC; RBMXL1-rv (CATCCTTGCAAACCAGTCCT), HIST1H2BG-Fw (TGTGACCAAGGCGCAGAAGA), HIST1H2BG-rv (GAGCGCTTGTTGTAGTGGGC), SNRNP-fw (GCCAAATGAGTGAGGATGGT) and SNRNP-rv (TCCTCTCTGCCTGACTCCAT). Means and SEM from 4-5 independent experiments were calculated and statistical significance was analysed using unpaired t-test.

Chromatin immunoprecipitation (ChIP)

Cells were crosslinked with a formaldehyde solution added to the culture medium (1% formaldehyde final concentration) for 10 min at room temperature, with gentle agitation. Glycine (0.125 M) was added for 5 min to stop the reaction. Cells were washed twice with cold PBS in the presence of complete protease inhibitor cocktail (Roche) and PMSF and harvested by. Pelleted cells were lysed in two steps, first using 0.5% NP-40 buffer for nucleus isolation followed by nuclear lysis in 1% SDS lysis buffer. Sonication was performed using Bioruptor (Diagenode, UCD-200) at high intensity and two cycles of 8 min (30” sonication, 30” pause) to achieve DNA fragments of about 200–1000 bp and chromatin was clarified by centrifugation (13,000 × g, 30 min, 4 °C). For each IP, 20 µg of chromatin were diluted in IP buff-

er (0.01% SDS, 1.1% Triton X-100, 1.2 mM EDTA pH 8, 16.7 mM Tris pH 8, 167 mM NaCl) and incubated overnight at 4 °C on a rotating wheel with 4 µg antibody (anti-DDX5 Santa Cruz sc-166167; anti-γH2AX Abcam ab2893; rabbit IgG SIGMA I8140; and mouse IgG SIGMA I8765 as controls), followed by 2h incubation with 30 µl pre-cleared Dynabeads protein A and Dynabeads protein G (ThermoFisher). Beads were sequentially washed with increasing salt concentrations (150-500 mM NaCl, 0.1% SDS, 1% Triton X-100, 2 mM EDTA pH 8, 20 mM Tris pH 8), and LiCl buffer (0.25 M LiCl, 1% NP-40, 1% sodium deoxycholate, 1 mM EDTA, 10 mM Tris pH8). Immunoprecipitated complexes were resuspended in elution buffer (Tris 10 mM pH 8, EDTA 0.5 mM pH 8, 1% SDS) and incubated for 20 min at 65°C shaking. After removal of the beads, SDS concentration was brought to 0.5% by addition of 1x TE and samples were further incubated overnight at 65°C to revert crosslinking. After 1h proteinase K treatment, immunoprecipitated and input DNA were purified with phenol/chloroform and precipitated in ethanol at -20°C. Samples were resuspended in 50 µl water.

Quantitative PCR analysis

All real-time (RT)–qPCR analysis was performed with iTaq Universal SYBR Green Supermix (Bio-Rad) and analyzed on 7500 FAST Real-Time PCR system (Applied Biosystems, Carlsbad, CA).

DRIPc-seq

For genome-wide detection of DNA-RNA hybrids, DRIPc-seq was performed essentially as described (Sanz and Chedin 2019). Briefly, after DRIP, the eluted DNA from five immunoprecipitations of each sample was treated with 6 U of DNase I (New England BioLabs) for 45 min at 37°C to degrade all DNA. The

resulting RNA was subjected to library construction using the TruSeq Stranded Total RNA protocol (Illumina) from the fragmentation step. The quality of the libraries was checked on a 2100 Agilent Bioanalyzer prior to sequencing on an Illumina NextSeq500 platform.

DRIPc-seq read mapping, peak calling and annotation

Sequenced paired-ends reads were subjected to quality control pipeline using the FASTQ Toolkit v.1.0.0 software (Illumina) and aligned to the human reference genome hg38 with Bowtie2[67]. Reads were separated into Watson and Crick strand using SAMTools[68]. Genome signal tracks were obtained using bamCoverage command from Deeptools[69].

DRIPc-seq peaks were called using MACS2[70] setting default parameters and FRD<0.01 allowing broad region detection with a 0.1 cutoff. Next, regions covered by peaks in both replicates in both conditions were merged and fused when closer than 5kb distance for comparative analysis using BEDtools [71]. Then, number of counts per peak was calculated using FeatureCounts and RPKM normalized. For further comparative analysis, R loop-gain peaks were established selecting peaks whose DRIPc signal fold change was higher than 2.5X in siDDX5 respect to the siC control cells in both replicates and *vice versa* for R loop-gain peaks in siC cells. Finally, peaks were annotated to genes using ChIPseeker [72] and genes retrieved from Ensembl release 94 2018[73]. Our analyses were mainly focus on protein-coding genes considering promoter as -2 Kb from the transcription start site (TSS) and downstream as +2 Kb from the transcription termination site (TTS).

For γH2AX peak metaplot, the mean DRIPc-seq signal (mean coverage) from the two replicates in K562 cells was superimposed on the plot of γH2AX

peaks from previously reported γH2AX ChIP-seq analysis (GSE 104800) [39] performed in the same cells.

The DRIPc-seq datasets generated in this study are available at GEO repository (GSE150163)

QUANTIFICATION AND STATISTICAL ANALYSIS

The total number of replicates, mean and error bars in graphs are explained in the figure legends. Statistical significance of differences was calculated with unpaired two-tailed t-test, one/two-way ANOVA with Tukey's multiple comparisons test or Mann-Whitney two-tailed test as indicated in the figure legends except for Figure 3b where one-tailed t-test was used. All analyses were conducted using GraphPad Prism (version Mac OS X 8.4.2).

Acknowledgments

We thank Elizabeth Tran (Purdue Univ., US) and Gaelle Legube (Toulouse, FR) for kindly providing the plasmid expressing DDX5 and the U2OS DIvA cell system, respectively; Laetitia Besse from the Cell and Tissue Imaging Facility of the Institut Curie (PICT), a member of the France BioImaging National Infrastructure (ANR-10-INBS-04), Patricia Duchambon from the Protein Core Facility of Institut Curie (Orsay, FR) for helping with protein purification; Victor Laigle from the Mass Spectrometry facility of Institut Curie for helping with the graphical representation of the mass spectrometry data; Eloisa Andújar and Mónica Pérez from the Genomic Unit of CABIMER for DNA sequencing of the DRIPc-seq samples. Research was funded by grants from the Agence National de Recherche (ANR-17-CE12-0016), Institut National du Cancer (INCa-DGOS_8706), Association pour la Recherche sur le Cancer (ARC), Ligue contre le Cancer and the Prix "Avenir" from the French Cancer Association Cancer du Sein: Parlons-en! to A.C.; grants

from the European Research Council (ERC2014 AdG669898 TARLOOP), the Spanish Ministry of Economy and Competitiveness (BFU2016-75058-P) and the European Union (FEDER) to A.A; and grants from Institut Curie and CNRS to S.V. G. S. was supported by a predoctoral Fellowship from Association pour la Recherche sur le Cancer (ARC). B. G—G. was recipient of a grant from the Asociación Española Contra el Cancer (AECC), S.S. and C.P-C were the recipients of a Juan de la Cierva-Incorporation grant and a predoctoral FPI fellowship, respectively, from the Spanish Ministry of Economy, Industry, and Competitiveness, and J.S.M. was supported by a postdoctoral Fellowship from Fondation de France.

Author contributions

Conceptualization: G.S., B.G.-G., S. V., A.A. and A.C. Methodology: G.S., B.G.-G, S.S., C.P.-C., S.V, A.A. and A.C.; Investigation: G.S., B.G.-G, S.S., C.P.-C., R.B., S.B., S.M., A.E., J.S.M., C. M., B.L. and D.L.; Visualization and formal analysis: G.S., B.G.-G, C.P.-C, A.A and A.C. Writing-Original Draft., G.S., B.G.-G, A.A. and A.C. Funding Acquisition, S.V., A.A., A.C. Supervision, A.A. and A.C.

Competing interests

The authors declare no competing interests.

Data availability

Correspondence and requests for materials should be addressed to A.A. or A. C.

Mass Spectrometry source data for Supplementary Table 1 and Supplementary Figure 1 is accesible at ProteomeXchange Consortium (accesion PXD018979). The DRIPc-seq source data used in figure 2c-f are available in GEO: GSE150163

for siDDX5 samples (this study), GSE127979 for siC samples (Pérez-Calero et al 2020) and GSE104800 for H2AX ChIP-seq data (Kim et al 2018).

References

1. Moynahan, M. E., Pierce, A. J. & Jasin, M. BRCA2 is required for homology-directed repair of chromosomal breaks. *Molecular Cell* **7,** 263–272 (2001).
2. Jensen, R. B., Carreira, A. & Kowalczykowski, S. C. Purified human BRCA2 stimulates RAD51-mediated recombination. *Nature* **467,** 678–683 (2010).
3. Schlacher, K., Christ, N., Siaud, N., Egashira, A., Wu, H. & Jasin, M. Double-Strand Break Repair-Independent Role for BRCA2 in Blocking Stalled Replication Fork Degradation by MRE11. *Cell* **145,** 529–542 (2011).
4. Daniels, M. J., Wang, Y., Lee, M. & Venkitaraman, A. R. Abnormal cytokinesis in cells deficient in the breast cancer susceptibility protein BRCA2. *Science* **306,** 876–879 (2004).
5. Ehlen, A., Martin, C., Miron, S., Julien, M., Theillet, F.-X., Ropars, V., Sessa, G., Beaurepere, R., Boucherit, V., Duchambon, P., Marjou, El, A., Zinn-Justin, S. & Carreira, A. Proper chromosome alignment depends on BRCA2 phosphorylation by PLK1. *Nat Commun* **11,** 1819 (2020).
6. Bhatia, V., Barroso, S. I., García-Rubio, M. L., Tumini, E., Herrera-Moyano, E. & Aguilera, A. BRCA2 prevents R-loop accumulation and associates with TREX-2 mRNA export factor PCID2. *Nature* **511,** 362–365 (2014).
7. Tan, S. L. W., Chadha, S., Liu, Y., Gabasova, E., Perera, D., Ahmed, K., Constantinou, S., Renaudin, X., Lee, M., Aebersold, R. & Venkitaraman, A. R. A Class of Environmental and Endogenous Toxins Induces BRCA2 Haploinsufficiency and Genome Instability. *Cell* **169,** 1105–1118.e15 (2017).
8. García-Muse, T. & Aguilera, A. R Loops: From Physiological to Pathological Roles. *Cell* **179,** 604–618 (2019).
9. Aguilera, A. & Gómez-González, B. DNA-RNA hybrids: the risks of DNA breakage during transcription. *Nat Struct Mol Biol* **24,** 439–443 (2017).
10. Michelini, F., Pitchiaya, S., Vitelli, V., Sharma, S., Gioia, U., Pessina, F., Cabrini, M., Wang, Y., Capozzo, I., Iannelli, F., Matti, V., Francia, S., Shivashankar, G. V., Walter, N. G. & d'Adda di Fagagna, F. Damage-induced lncRNAs control the DNA damage response through interaction with DDRNAs at individual double-strand breaks. *Nat Cell Biol* **19,** 1400–1411 (2017).
11. Li, L., Germain, D. R., Poon, H.-Y., Hildebrandt, M. R., Monckton, E. A., McDonald, D., Hendzel, M. J. & Godbout, R. DEAD Box 1 Facilitates Removal of RNA and Homologous Recombination at DNA Double-Strand Breaks. *Mol. Cell. Biol.* **36,** 2794–2810 (2016).
12. Cohen, S., Puget, N., Lin, Y.-L., Clouaire, T., Aguirrebengoa, M., Rocher, V., Pasero, P., Canitrot, Y. & Legube, G. Senataxin resolves RNA:DNA hybrids forming at DNA double-strand breaks to prevent translocations. *Nature*

Communications **9,** 533 (2018).
13. Lu, W.-T., Hawley, B. R., Skalka, G. L., Baldock, R. A., Smith, E. M., Bader, A. S., Malewicz, M., Watts, F. Z., Wilczynska, A. & Bushell, M. Drosha drives the formation of DNA:RNA hybrids around DNA break sites to facilitate DNA repair. *Nat Commun* **9,** 532–13 (2018).
14. Yasuhara, T., Kato, R., Hagiwara, Y., Shiotani, B., Yamauchi, M., Nakada, S., Shibata, A. & Miyagawa, K. Human Rad52 Promotes XPG-Mediated R-loop Processing to Initiate Transcription-Associated Homologous Recombination Repair. *Cell* **175,** 558–570.e11 (2018).
15. Ohle, C., Tesorero, R., Schermann, G., Dobrev, N., Sinning, I. & Fischer, T. Transient RNA-DNA Hybrids Are Required for Efficient Double-Strand Break Repair. *Cell* **167,** 1001–1013.e7 (2016).
16. Skourti-Stathaki, K., Proudfoot, N. J. & Gromak, N. Human Senataxin Resolves RNA/DNA Hybrids Formed at Transcriptional Pause Sites to Promote Xrn2-Dependent Termination. *Molecular Cell* **42,** 794–805 (2011).
17. Li, L., Monckton, E. A. & Godbout, R. A role for DEAD box 1 at DNA double-strand breaks. *Mol. Cell. Biol.* **28,** 6413–6425 (2008).
18. Mersaoui, S. Y., Yu, Z., Coulombe, Y., Karam, M., Busatto, F. F., Masson, J.-Y. & Richard, S. Arginine methylation of the DDX5 helicase RGG/RG motif by PRMT5 regulates resolution of RNA:DNA hybrids. *EMBO J* **38,** e100986 (2019).
19. Song, C., Hotz-Wagenblatt, A., Voit, R. & Grummt, I. SIRT7 and the DEAD-box helicase DDX21 cooperate to resolve genomic R loops and safeguard genome stability. *Genes Dev* **31,** 1370–1381 (2017).
20. Hodroj, D., Recolin, B., Serhal, K., Martinez, S., Tsanov, N., Abou Merhi, R. & Maiorano, D. An ATR-dependent function for the Ddx19 RNA helicase in nuclear R-loop metabolism. *EMBO J* **36,** 1182–1198 (2017).
21. Pérez-Calero, C.,Bayona-Feliu, A., Xue, X., Barroso, S., Muñoz, S., González- Basallote, V.M., Sung. P., Aguilera, A. UAP56/DDX39B is a major co- transcriptional RNA-DNA helicase that unwinds harmful R loops genome-wide. Genes Dev. *In press*
22. García-Rubio, M. L., Pérez-Calero, C., Barroso, S. I., Tumini, E., Herrera-Moyano, E., Rosado, I. V. & Aguilera, A. The Fanconi Anemia Pathway Protects Genome Integrity from R-loops. *PLoS Genet* **11,** e1005674–e1005674 (2015).
23. Madireddy, A., Kosiyatrakul, S. T., Boisvert, R. A., Herrera-Moyano, E., García-Rubio, M. L., Gerhardt, J., Vuono, E. A., Owen, N., Yan, Z., Olson, S., Aguilera, A., Howlett, N. G. & Schildkraut, C. L. FANCD2 Facilitates Replication through Common Fragile Sites. *Mol. Cell* **64,** 388–404 (2016).
24. Schwab, R. A., Nieminuszczy, J., Shah, F., Langton, J., Lopez Martinez, D., Liang, C.-C., Cohn, M. A., Gibbons, R. J., Deans, A. J. & Niedzwiedz, W. The Fanconi Anemia Pathway Maintains Genome Stability by Coordinating Replication and Transcription. *Mol. Cell* **60,** 351–361 (2015).
25. Shivji, M. K. K., Renaudin, X., Williams, Ç. H. & Venkitaraman, A. R. BRCA2 Regulates Transcription Elongation by RNA Polymerase II to Prevent R-Loop Accumulation. *CellReports* **22,** 1031–1039 (2018).
26. Hatchi, E., Skourti-Stathaki, K., Ventz, S., Pinello, L., Yen, A., Kamieniarz-Gdula, K., Dimitrov, S., Pathania, S., McKinney, K. M., Eaton, M. L., Kellis, M., Hill, S. J., Parmigiani, G., Proudfoot, N. J. & Livingston, D. M. BRCA1 recruitment to transcriptional pause sites is required for R-loop-driven DNA damage repair. *Mol. Cell* **57,** 636–647 (2015).

27. Moriel-Carretero, M., Ovejero, S., Gérus-Durand, M., Vryzas, D. & Constantinou, A. Fanconi anemia FANCD2 and FANCI proteins regulate the nuclear dynamics of splicing factors. *The Journal of Cell Biology* **216,** 4007–4026 (2017).
28. Xing, Z., Ma, W. K. & Tran, E. J. The DDX5/Dbp2 subfamily of DEAD-box RNA helicases. *Wiley Interdiscip Rev RNA* **10,** e1519 (2019).
29. Hirling, H., Scheffner, M., Restle, T. & Stahl, H. RNA helicase activity associated with the human p68 protein. *Nature* **339,** 562–564 (1989).
30. Julien, M., Miron, S., Carreira, A., Theillet, F.-X. & Zinn-Justin, S. 1H, 13C and 15N backbone resonance assignment of the human BRCA2 N-terminal region. *Biomol NMR Assign* **14,** 79–85 (2020).
31. Nicolai, von, C., Ehlen, A., Martin, C., Zhang, X. & Carreira, A. A second DNA binding site in human BRCA2 promotes homologous recombination. *Nature Communications* **7,** 12813 (2016).
32. Xing, Z., Wang, S. & Tran, E. J. Characterization of the mammalian DEAD-box protein DDX5 reveals functional conservation with S. cerevisiae ortholog Dbp2 in transcriptional control and glucose metabolism. **23,** 1125–1138 (2017).
33. Boguslawski, S. J., Smith, D. E., Michalak, M. A., Mickelson, K. E., Yehle, C. O., Patterson, W. L. & Carrico, R. J. Characterization of monoclonal antibody to DNA.RNA and its application to immunodetection of hybrids. *J Immunol Methods* **89,** 123–130 (1986).
34. Kotsantis, P., Silva, L. M., Irmscher, S., Jones, R. M., Folkes, L., Gromak, N. & Petermann, E. Increased global transcription activity as a mechanism of replication stress in cancer. *Nature Communications* **7,** 13087–13 (2016).
35. Gómez-González, B. & Aguilera, A. Transcription-mediated replication hindrance: a major driver of genome instability. *Genes Dev* **33,** 1008–1026 (2019).
36. Stork, C. T., Bocek, M., Crossley, M. P., Sollier, J., Sanz, L. A., Chédin, F., Swigut, T. & Cimprich, K. A. Co-transcriptional R-loops are the main cause of estrogen-induced DNA damage. *Elife* **5,** e17548 (2016).
37. Sanz, L. A., Hartono, S. R., Lim, Y. W., Steyaert, S., Rajpurkar, A., Ginno, P. A., Xu, X. & Chédin, F. Prevalent, Dynamic, and Conserved R-Loop Structures Associate with Specific Epigenomic Signatures in Mammals. *Mol. Cell* **63,** 167–178 (2016).
38. Sanz, L. A. & Chédin, F. High-resolution, strand-specific R-loop mapping via S9.6-based DNA-RNA immunoprecipitation and high-throughput sequencing. *Nat Protoc* **14,** 1734–1755 (2019).
39. Kim, J., Sturgill, D., Sebastian, R., Khurana, S., Tran, A. D., Edwards, G. B., Kruswick, A., Burkett, S., Hosogane, E. K., Hannon, W. W., Weyemi, U., Bonner, W. M., Luger, K. & Oberdoerffer, P. Replication Stress Shapes a Protective Chromatin Environment across Fragile Genomic Regions. *Mol. Cell* **69,** 36–47.e7 (2018).
40. Aymard, F., Bugler, B., Schmidt, C. K., Guillou, E., Caron, P., Briois, S., Iacovoni, J. S., Daburon, V., Miller, K. M., Jackson, S. P. & Legube, G. Transcriptionally active chromatin recruits homologous recombination at DNA double-strand breaks. *Nat Struct Mol Biol* **21,** 366–374 (2014).
41. D'Alessandro, G., Whelan, D. R., Howard, S. M., Vitelli, V., Renaudin, X., Adamowicz, M., Iannelli, F., Jones-Weinert, C. W., Lee, M., Matti, V., Lee, W. T. C., Morten, M. J., Venkitaraman, A. R., Cejka, P., Rothenberg, E. & d'Adda di Fagagna, F. BRCA2 controls DNA:RNA hybrid level at DSBs by

mediating RNase H2 recruitment. *Nature Communications* **9,** 5376 (2018).
42. Bekker-Jensen, S., Lukas, C., Kitagawa, R., Melander, F., Kastan, M. B., Bartek, J. & Lukas, J. Spatial organization of the mammalian genome surveillance machinery in response to DNA strand breaks. *J Cell Biol* **173,** 195–206 (2006).
43. Adamson, B., Smogorzewska, A., Sigoillot, F. D., King, R. W. & Elledge, S. J. A genome-wide homologous recombination screen identifies the RNA-binding protein RBMX as a component of the DNA-damage response. *Nat Cell Biol* **14,** 318–328 (2012).
44. Wang, H., Gao, X., Huang, Y., Yang, J. & Liu, Z.-R. P68 RNA helicase is a nucleocytoplasmic shuttling protein. *Cell Res* **19,** 1388–1400 (2009).
45. Britton, S., Dernoncourt, E., Delteil, C., Froment, C., Schiltz, O., Salles, B., Frit, P. & Calsou, P. DNA damage triggers SAF-A and RNA biogenesis factors exclusion from chromatin coupled to R-loops removal. *Nucleic Acids Research* **42,** 9047–9062 (2014).
46. Chou, D. M., Adamson, B., Dephoure, N. E., Tan, X., Nottke, A. C., Hurov, K. E., Gygi, S. P., Colaiácovo, M. P. & Elledge, S. J. A chromatin localization screen reveals poly (ADP ribose)-regulated recruitment of the repressive polycomb and NuRD complexes to sites of DNA damage. *Proc Natl Acad Sci USA* **107,** 18475–18480 (2010).
47. Nicol, S. M., Bray, S. E., Black, H. D., Lorimore, S. A., Wright, E. G., Lane, D. P., Meek, D. W., Coates, P. J. & Fuller-Pace, F. V. The RNA helicase p68 (DDX5) is selectively required for the induction of p53-dependent p21 expression and cell-cycle arrest after DNA damage. *Oncogene* **32,** 3461–3469 (2013).
48. Shanbhag, N. M., Rafalska-Metcalf, I. U., Balane-Bolivar, C., Janicki, S. M. & Greenberg, R. A. ATM-dependent chromatin changes silence transcription in cis to DNA double-strand breaks. *Cell* **141,** 970–981 (2010).
49. Iggo, R. D., Jamieson, D. J., MacNeill, S. A., Southgate, J., McPheat, J. & Lane, D. P. p68 RNA helicase: identification of a nucleolar form and cloning of related genes containing a conserved intron in yeasts. *Mol. Cell. Biol.* **11,** 1326–1333 (1991).
50. Nicolai, von, C., Ehlen, A., Martinez, J. S. & Carreira, A. Dissecting the Recombination Mediator Activity of BRCA2 Using Biochemical Methods. *Meth Enzymol* **600,** 479–511 (2018).
51. Yuan, S. S., Lee, S. Y., Chen, G., Song, M., Tomlinson, G. E. & Lee, E. Y. BRCA2 is required for ionizing radiation-induced assembly of Rad51 complex in vivo. *Cancer Res* **59,** 3547–3551 (1999).
52. Francia, S., Michelini, F., Saxena, A., Tang, D., de Hoon, M., Anelli, V., Mione, M., Carninci, P. & d'Adda di Fagagna, F. Site-specific DICER and DROSHA RNA products control the DNA-damage response. *Nature* **488,** 231–235 (2012).
53. Chen, H., Lisby, M. & Symington, L. S. RPA coordinates DNA end resection and prevents formation of DNA hairpins. *Mol. Cell* **50,** 589–600 (2013).
54. Carreira, A., Hilario, J., Amitani, I., Baskin, R. J., Shivji, M. K. K., Venkitaraman, A. R. & Kowalczykowski, S. C. The BRC Repeats of BRCA2 Modulate the DNA-Binding Selectivity of RAD51. *Cell* **136,** 1032–1043 (2009).
55. Zhang, F., Shi, J., Bian, C. & Yu, X. Poly(ADP-Ribose) Mediates the BRCA2-Dependent Early DNA Damage Response. *CellReports* **13,** 678–689 (2015).

56. Shimelis, H., Mesman, R. L. S., Nicolai, von, C., Ehlen, A., Guidugli, L., Martin, C., Calléja, F. M. G. R., Meeks, H., Hallberg, E., Hinton, J., Lilyquist, J., Hu, C., Aalfs, C. M., Aittomäki, K., Andrulis, I., Anton-Culver, H., Arndt, V., Beckmann, M. W., Benítez, J., Bogdanova, N. V., Bojesen, S. E., Bolla, M. K., Børresen-Dale, A.-L. L., Brauch, H., Brennan, P., Brenner, H., Broeks, A., Brouwers, B., Brüning, T., Burwinkel, B., Chang-Claude, J., Chenevix-Trench, G., Cheng, C.-Y., Choi, J.-Y., Collée, J. M., Cox, A., Cross, S. S., Czene, K., Darabi, H., Dennis, J., Dörk, T., Santos Silva, Dos, I., Dunning, A. M., Fasching, P. A., Figueroa, J., Flyger, H., Garcia-Closas, M., Giles, G. G., Glendon, G., Guénel, P., Haiman, C. A., Hall, P., Hamann, U., Hartman, M., Hogervorst, F. B., Hollestelle, A., Hopper, J. L., Ito, H., Jakubowska, A., Kang, D., Kosma, V.-M., Kristensen, V., Lai, K.-N., Lambrechts, D., Marchand, L. L., Li, J., Lindblom, A., Lophatananon, A., Lubiński, J., Machackova, E., Mannermaa, A., Margolin, S., Marme, F., Matsuo, K., Miao, H., Michailidou, K., Milne, R. L., Muir, K., Neuhausen, S. L., Nevanlinna, H., Olson, J. E., Olswold, C., Oosterwijk, J. J. C., Osorio, A., Peterlongo, P., Peto, J., Pharoah, P. D. P., Pylkäs, K., Radice, P., Rashid, M. U., Rhenius, V., Rudolph, A., Sangrajrang, S., Sawyer, E. J., Schmidt, M. K., Schoemaker, M. J., Seynaeve, C., Shah, M., Shen, C.-Y., Shrubsole, M., Shu, X.-O., Slager, S., Southey, M. C., Stram, D. O., Swerdlow, A., Teo, S. H., Tomlinson, I., Torres, D., Truong, T., van Asperen, C. J., van der Kolk, L. E., Wang, Q., Winqvist, R., Wu, A. H., Yu, J.-C., Zheng, W., Zheng, Y., Leary, J., Walker, L., Foretova, L., Fostira, F., Claes, K. B. M., Varesco, L., Moghadasi, S., Easton, D. F., Spurdle, A., Devilee, P., Vrieling, H., Monteiro, A. N. A., Goldgar, D. E., Carreira, A., Vreeswijk, M. P. G., Couch, F. J., for kConFab/AOCS Investigatorsfor NBCS Collaborators. BRCA2 Hypomorphic Missense Variants Confer Moderate Risks of Breast Cancer. *Cancer Res* **77,** 2789–2799 (2017).
57. Guidugli, L., Pankratz, V. S., Singh, N., Thompson, J., Erding, C. A., Engel, C., Schmutzler, R., Domchek, S., Nathanson, K., Radice, P., Singer, C., Tonin, P. N., Lindor, N. M., Goldgar, D. E. & Couch, F. J. A classification model for BRCA2 DNA binding domain missense variants based on homology-directed repair activity. *Cancer Res* **73,** 265–275 (2013).
58. Hucl, T., Rago, C., Gallmeier, E., Brody, J. R., Gorospe, M. & Kern, S. E. A syngeneic variance library for functional annotation of human variation: application to BRCA2. *Cancer Res* **68,** 5023–5030 (2008).
59. Asbroek, ten, A. L. M. A., van Groenigen, M., Nooij, M. & Baas, F. The involvement of human ribonucleases H1 and H2 in the variation of response of cells to antisense phosphorothioate oligonucleotides. *Eur. J. Biochem.* **269,** 583–592 (2002).
60. Cerritelli, S. M., Frolova, E. G., Feng, C., Grinberg, A., Love, P. E. & Crouch, R. J. Failure to produce mitochondrial DNA results in embryonic lethality in Rnaseh1 null mice. *Mol. Cell* **11,** 807–815 (2003).
61. Mazurek, A., Luo, W., Krasnitz, A., Hicks, J., Powers, R. S. & Stillman, B. DDX5 regulates DNA replication and is required for cell proliferation in a subset of breast cancer cells. *Cancer Discov* **2,** 812–825 (2012).
62. Poullet, P., Carpentier, S. & Barillot, E. myProMS, a web server for management and validation of mass spectrometry-based proteomic data. *Proteomics* **7,** 2553–2556 (2007).
63. Spivak, M., Weston, J., Bottou, L., Käll, L. & Noble, W. S. Improvements to the percolator algorithm for Peptide identification from shotgun proteomics

data sets. *J. Proteome Res.* **8,** 3737–3745 (2009).
64. Ishihama, Y., Oda, Y., Tabata, T., Sato, T., Nagasu, T., Rappsilber, J. & Mann, M. Exponentially modified protein abundance index (emPAI) for estimation of absolute protein amount in proteomics by the number of sequenced peptides per protein. *Mol Cell Proteomics* **4,** 1265–1272 (2005).
65. Perez-Riverol, Y., Csordas, A., Bai, J., Bernal-Llinares, M., Hewapathirana, S., Kundu, D. J., Inuganti, A., Griss, J., Mayer, G., Eisenacher, M., Pérez, E., Uszkoreit, J., Pfeuffer, J., Sachsenberg, T., Yilmaz, S., Tiwary, S., Cox, J., Audain, E., Walzer, M., Jarnuczak, A. F., Ternent, T., Brazma, A. & Vizcaíno, J. A. The PRIDE database and related tools and resources in 2019: improving support for quantification data. *Nucleic Acids Research* **47,** D442–D450 (2019).
66. Herrera-Moyano, E., Mergui, X., García-Rubio, M. L., Barroso, S. & Aguilera, A. The yeast and human FACT chromatin-reorganizing complexes solve R-loop-mediated transcription-replication conflicts. *Genes Dev* **28,** 735–748 (2014).
67. Langmead, B. & Salzberg, S. L. Fast gapped-read alignment with Bowtie 2. *Nat Meth* **9,** 357–359 (2012).
68. Li, H., Handsaker, B., Wysoker, A., Fennell, T., Ruan, J., Homer, N., Marth, G., Abecasis, G., Durbin, R.1000 Genome Project Data Processing Subgroup. The Sequence Alignment/Map format and SAMtools. *Bioinformatics* **25,** 2078–2079 (2009).
69. Ramírez, F., Ryan, D. P., Grüning, B., Bhardwaj, V., Kilpert, F., Richter, A. S., Heyne, S., Dündar, F. & Manke, T. deepTools2: a next generation web server for deep-sequencing data analysis. *Nucleic Acids Research* **44,** W160–5 (2016).
70. Zhang, Y., Liu, T., Meyer, C. A., Eeckhoute, J., Johnson, D. S., Bernstein, B. E., Nusbaum, C., Myers, R. M., Brown, M., Li, W. & Liu, X. S. Model-based analysis of ChIP-Seq (MACS). *Genome Biology* **9,** R137–9 (2008).
71. Quinlan, A. R. & Hall, I. M. BEDTools: a flexible suite of utilities for comparing genomic features. *Bioinformatics* **26,** 841–842 (2010).
72. Yu, G., Wang, L.-G. & He, Q.-Y. ChIPseeker: an R/Bioconductor package for ChIP peak annotation, comparison and visualization. *Bioinformatics* **31,** 2382–2383 (2015).
73. Zerbino, D. R., Achuthan, P., Akanni, W., Amode, M. R., Barrell, D., Bhai, J., Billis, K., Cummins, C., Gall, A., Girón, C. G., Gil, L., Gordon, L., Haggerty, L., Haskell, E., Hourlier, T., Izuogu, O. G., Janacek, S. H., Juettemann, T., To, J. K., Laird, M. R., Lavidas, I., Liu, Z., Loveland, J. E., Maurel, T., McLaren, W., Moore, B., Mudge, J., Murphy, D. N., Newman, V., Nuhn, M., Ogeh, D., Ong, C. K., Parker, A., Patricio, M., Riat, H. S., Schuilenburg, H., Sheppard, D., Sparrow, H., Taylor, K., Thormann, A., Vullo, A., Walts, B., Zadissa, A., Frankish, A., Hunt, S. E., Kostadima, M., Langridge, N., Martin, F. J., Muffato, M., Perry, E., Ruffier, M., Staines, D. M., Trevanion, S. J., Aken, B. L., Cunningham, F., Yates, A. & Flicek, P. Ensembl 2018. *Nucleic Acids Research* **46,** D754–D761 (2018).

Figure Legends

Figure 1. BRCA2 physically interacts with DDX5

(a) Amylose pulldown from benzonase-treated HEK293T cell lysates expressing 2xMBP-BRCA2$_{NT}$ in untreated or irradiated cells (6Gy; +IR). DDX5 and BRCA2$_{NT}$ (MBP) detected by immunoblot. StainFree images of the gels before transfer was used as loading control (cropped image is shown). **(b)** Immunoprecipitation (IP) of endogenous BRCA2 from benzonase-treated HEK293T cell lysates treated or not with IR (6Gy), as indicated. Normal mouse IgG was used as negative control. Immunoblot of DDX5 and BRCA2. StainFree images of the gels before transfer was used as loading control (cropped image is shown). **(c)** Top: Representative images of *in situ* proximity ligation assay (PLA) between BRCA2 and DDX5 antibodies in U2OS cells either left untreated (-) or irradiated (4h post-IR; 6 Gy). When indicated, cells were transfected with a plasmid expressing RNase H1 (RH) 24h before or treated with Cordycepin (Cordy) for 2h at 37°C before fixation. Single antibody controls from untreated siC cells are shown. Scale bar indicates 10 µm. Bottom: Quantification of the number of PLA spots per nucleus. For statistical comparison of the differences between the samples we applied a Kruskal-Wallis test followed by Dunn's multiple comparison test, the p-values show significant differences. The red line in the plot indicates the median, each symbol represents a single PLA spot. **(d)** Top: Diagram showing the BRCA2 N-terminal truncations used in this study. Bottom: Amylose pulldown from HEK293T whole cells extracts overexpressing the indicated BRCA2 N-terminal truncations (BRCA2$_{T1}$, BRCA2$_{LT2}$, BRCA2$_{LT3}$) or the 2xMBP tag. DDX5 and BRCA2$_{NT}$ truncations were detected using specific antibodies against DDX5 and MBP, respectively. StainFree images of the gels before transfer was used as loading control (cropped image is shown). **(e)** Left: GST pulldown assay using purified BRCA2$_{T1}$ (B2$_{T1}$) and DDX5; MBP antibody was used for the detection of both proteins. UB: unbound; E: eluate. Right: SDS-PAGE showing 300 ng of purified

MBP-DDX5-GST and of 2xMBP-tagged BRCA2$_{T1}$ used in the pulldown assay.

Figure 2. DDX5 depletion leads to a genome-wide accumulation of DNA-RNA hybrids particularly enriched at DSBs

(a) Left: Representative images of S9.6 immunofluorescence of U2OS cells depleted of BRCA2 (siBRCA2), DDX5 (siDDX5) or control cells (siC) expressing DDX5-GFP. The merged images show the signal of S9.6, nucleolin (nucleoli) antibodies and DAPI staining. Scale bar indicates 25 µm. Right: Quantification of S9.6 average nuclear intensity of U2OS cells depleted of BRCA2 (siBRCA2), DDX5 (siDDX5) or control cells (siC) expressing DDX5-GFP. The red line in the plot indicates the median, each symbol represents the value of a single cell. The statistical significance of the difference was calculated with Mann-Whitney U-test; the p-values show the significant difference. The data represent at least 235 cells per condition from three independent experiments. **(b)** Top: Representative images of *in situ* PLA performed with DDX5 and S9.6 antibodies (DNA-RNA hybrids) in EdU positive or negative U2OS cells. When indicated, cells were transfected with a plasmid expressing RNaseH1 (RH). Bottom: Quantification. At least 300 cells per condition were counted from three independent experiments. For statistical comparison of the differences between the samples we applied a Kruskal-Wallis test followed by Dunn's multiple comparison test, the p-values show significant differences. The red line in the plot indicates the median, each symbol represents a single PLA spot. See also Figure S3B. **(c)** Representative screenshot of a specific genomic region showing DRIPc-seq profiles at Watson (W) and Crick (C) strands in K562 cells depleted of DDX5 (siDDX5) or control cells (siC) from two independent experiments. The siC data were obtained from (GEO, GSE127979) [21]. **(d)** DNA-RNA hybrid distribution along protein-coding genes.

Gene metaplot representing the mean of antisense and sense DRIPc-seq signal from two independent experiments in K562 cells depleted of DDX5 (siDDX5) or control cells (siC). **(e)** DNA-RNA hybrid metaplot distribution over γH2AX ChIP-seq peaks, calculated from (GEO, GSE104800) [39]. Peak metaplot shows the mean of the DRIPc-seq signal from two independent experiments in K562 cells depleted of DDX5 (siDDX5) or control cells (siC). **(f)** Venn diagram representing the overlap between γH2AX-positive genes in K562 cells (γH2AX ChIP-seq) and genes that specifically accumulate hybrids in control cells (top) or in DDX5- depleted cells (bottom).

Figure 3. DDX5 and BRCA2 depleted cells accumulate DNA-RNA hybrids at DSBs sites. (a) Left: Representative images of *in situ* PLA between S9.6 and γH2AX antibodies in U2OS cells depleted of BRCA2 (siBRCA2), DDX5 (siDDX5) or control cells (siC). When indicated, cells were transfected with a plasmid expressing RNase H1 (RH) 24h before or treated with Cordycepin (Cordy) for 2h at 37°C before fixation. Single antibody controls from non-irradiated siC cells are shown. Scale bar indicates 10 μm. Right: Quantification of PLA spots per nucleus in each condition as indicated. For statistical comparison of the differences between the samples we applied a Kruskal-Wallis test followed by Dunn's multiple comparison test, the p-values show significant differences. The red line in the plot indicates the median, each symbol represents a single PLA spot. **(b)** DRIP-qPCR signal values at *RBMXL1*, *HIST1H2BG* and *SNRPN* loci in U2OS DIvA cells transfected with the indicated siRNAs and treated *in vitro* with RNase H1 (RH) pre-immunoprecipitation where indicated. The experiment was performed in both untreated cells (-OHT) and after tamoxifen addition (+OHT). The data represent the mean ± SEM from at least four independent experiments. The statistical

significance of the difference was calculated with unpaired t-test; the p-values show the significant difference.

Figure 4. BRCA2 enhances DDX5 retention at DNA damage sites. (a) Top: Scheme showing the experimental set up for laser irradiation in DDX5-GFP transfected U2OS cells depleted of BRCA2 (siBRCA2) or control cells (siC). Bottom left: Western blot showing the siRNA mediated knock-down of BRCA2 from U2OS cells transfected with DDX5-GFP. Bottom right: Live cell imaging of the recruitment of GFP-53BP1 or DDX5-GFP to DNA damage tracks at different time points as indicated. Exposure and processing were adjusted to best demonstrate stripes and anti-stripes. Scale bar indicates 10 μm. Right: Quantification of the percentage of transfected cells that exhibit DDX5-GFP “anti-stripe” pattern (reduced GFP signal at DNA damage tracks compared to the signal in the nucleus) at the times indicated in cells depleted of BRCA2 (siBRCA2) or treated with control siRNA (siC). The data represent the mean ± SEM from three independent experiments. **(b)** DDX5 ChIP-qPCR signal values at *RBMXL1* and *HIST1H2BG* loci in U2OS DIvA cells transfected with the indicated siRNAs and either untreated cells (-OHT) or after tamoxifen addition (+OHT). The data represent the mean ± SEM from two independent experiments. The statistical significance of the difference was calculated with unpaired t-Student test; the p-values show the significant difference. **(c)** Top: Representative images of immunofluorescence of U2OS DIvA cells depleted of BRCA2 (siBRCA2), DDX5 (siDDX5) or control cells (siC) and either untreated cells (-OHT) or after tamoxifen addition (+OHT), as indicated. Bottom: Quantification of the number of γH2AX foci per nucleus (left) and DDX5 nuclear intensity (right). The data represent at least 800 cells per condition from three independent experiments. The red line in the

plot indicates the median, each symbol represents the value of a single cell. The statistical significance of the difference was calculated with Mann-Whitney U-test; the p-values show the significant difference.

Figure 5. BRCA2 stimulates the R loop unwinding activity of DDX5. Left: PAGE gel showing a representative unwinding assays in which purified MBP-DDX5-GST (1-5 nM) was incubated with ^{32}P – labelled synthetic R loop substrate in presence or absence of 2 nM purified EGFP-MBP-BRCA2 (top gel) or 50 nM purified $BRCA2_{T1}$ (bottom gel). Right: Quantification of the unwinding experiments showing the percentage of free RNA relative to the R loop substrate (unwound product) as a function of DDX5 concentration alone (black) or in presence of BRCA2 (red) or $BRCA2_{T1}$ (pink). The data represent the mean ± SD of at least three independent experiments.

Figure 6. Cells bearing BRCA2 T207A show reduced BRCA2 interaction with DDX5 leading to increased DSB-associated DNA-RNA hybrids. (a) Left: GFP pull-down assay from whole cells extracts of BRCA2 deficient DLD1 expressing BRCA2 (WT) or the variant T207A (T207A). DLD1 $BRCA2^{+/+}$ (+/+) cell extracts are used as control for the GFP-trap. DDX5 and BRCA2 were detected with specific antibodies against DDX5 and BRCA2, respectively. StainFree images of the gels before transfer was used as loading control (cropped image is shown). Right: Quantification of the GFP-trap pull-down experiments calculated as the co-immunoprecipitated DDX5 with either BRCA2 WT or BRCA2-T207A relative to the input levels of DDX5 and the amount of immunoprecipitated EGFPMBP-BRCA2. Results are presented as the fold change compared to the BRCA2 WT clone. The data represents the mean ± SD of three independent experiments. Statistical

significance of the difference was calculated with unpaired t test; the p-values show the significant difference. **(b)** Top: Representative images of S9.6 immunofluorescence of DLD1 cells bearing BRCA2 (WT) or BRCA2-T207A (T207A). The merged images show the signal of S9.6, nucleolin (nucleoli) antibodies and DAPI staining. Scale bar indicates 25 µm. Bottom: Quantification of S9.6 average nuclear intensity of DLD1 cells bearing BRCA2 (WT) or BRCA2-T207A (T207A). The red line in the plot indicates the median, each symbol represents the value of a single cell. The data represent at least 1000 cells per condition from three independent experiments. The statistical significance of the difference was calculated with Mann-Whitney U-test; the p-values show the significant difference. **(c)** Relative DRIP-qPCR signal values at the *HIST1H2BG* locus in DLD1 cells bearing BRCA2 (WT) or BRCA2-T207A (T207A) and treated *in vitro* with RNase H1 (RH) pre-immunoprecipitation where indicated. The data represent the mean ± SEM from at seven independent experiments. The statistical significance of the difference was calculated with unpaired t-Student test; the p-values show the significant difference. **(d)** Left: Representative images of an *in situ* PLA between BRCA2 and DDX5 antibodies in DLD1 BRCA2 WT (WT) or BRCA2-T207A (T207A). Cells were fixed directly (-) or 4h post-irradiation (6Gy). Single antibody controls in untreated BRCA2 WT cells are shown. Scale bar indicates 10 µm. Right: Quantification of the number of PLA spots per nucleus. At least 500 cells were counted per condition from three independent experiments. For statistical comparison of the differences between the samples we applied a Kruskal-Wallis test followed by Dunn's multiple comparison test, the p-values show significant differences. The red line in the plot indicates the median, each symbol represents a single PLA spot. **(e)** Left: Representative images of *In situ* PLA performed between DDX5 and S9.6 (DNA-RNA hybrids) antibodies in BRCA2

deficient DLD1 cells (BRCA2$^{-/-}$) or cells bearing BRCA2 (WT) or BRCA2-T207A (T207A), as indicated. Cells were fixed directly or 4h post-irradiation (6Gy). Single antibody controls in non-irradiated BRCA2 WT cells are shown. Scale bar indicates 10 µm. Right**:** Quantification of the number of PLA spots per nucleus. At least 400 cells were counted per condition from three independent experiments. For statistical comparison of the differences between the samples we applied a Kruskal-Wallis test followed by Dunn's multiple comparison test, the p-values show significant differences. The red line in the plot indicates the median, each symbol represents a single PLA spot. **(f)** Left: Representative images of *In situ* PLA performed between γH2AX and S9.6 (DNA-RNA hybrids) antibodies in BRCA2 deficient DLD1 cells (BRCA2$^{-/-}$) bearing BRCA2 (WT) or BRCA2-T207A (T207A). When indicated, cells were transfected/treated with RNase H1 (RH) or Cordycepin (Cordy) prior to fixation. Single antibody controls in non-irradiated BRCA2 WT cells are shown. Scale bar indicates 10 µm. Right: Quantification of the number of PLA spots per nucleus. At least 400 cells were counted per condition from three independent experiments. For statistical comparison of the differences between the samples we applied a Kruskal-Wallis test followed by Dunn's multiple comparison test, the p-values show significant differences. The red line in the plot indicates the median, each symbol represents a single PLA spot. **(g)** Left: PAGE gel showing a representative unwinding assays in which purified MBP-DDX5-GST (1-5 nM) was incubated with ^{32}P – labelled synthetic R loop substrate in presence or absence of 50 nM purified BRCA2$_{T1}$-T207A. Middle: Quantification of the unwinding experiments showing the percentage of free RNA relative to the R loop substrate (unwound product) as a function of DDX5 concentration alone (black) or in presence of BRCA2$_{T1}$-T207A (green). The data represent the mean ± SD of at least three independent experiments. Right: SDS-PAGE showing 650 ng of

purified 2XMBP-BRCA2$_{T1}$-T207A used in the unwinding assay.

Figure 7. DDX5-BRCA2 interaction favors DSBs repair by homologous recombination. (a) Top: Representative immunofluorescence images of cells stained for RAD51 (green) in U2OS cells depleted of DDX5 (siDDX5) and in control cells (siC) in non-treated (NT) or different time points after exposure to IR (6Gy), as indicated. Scale bar indicates 10 μm. Bottom: Graph showing the average number of RAD51 repair foci in both cell lines. The data represent the mean ± SEM of three independent experiments. **(b)** Top**:** Representative immunofluorescence images of DLD1 BRCA2 deficient cells (BRCA2$^{-/-}$) or BRCA2$^{-/-}$ cells expressing BRCA2 WT or BRCA2-T207A in non-treated (NT) or at different time points post-IR (6 Gy), as indicated; stained for RAD51 (green). Bottom: Graph showing the average number of RAD51 repair foci in the three cell lines. The data represent the mean ± SEM of three independent experiments. **(c)** Left: Representative immunofluorescence images of DLD1 BRCA2 WT or BRCA2-T207A cells 4h post-irradiation (6Gy) stained for γH2AX foci and RPA. Right: Quantification of the number of γH2AX and RPA foci per nucleus, as indicated. The data represent at least 400 cells per condition from two independent experiments. For statistical comparison of the differences between the samples we applied a Kruskal-Wallis test followed by Dunn's multiple comparison test, the p-values show significant differences. The red line in the plot indicates the median, each symbol represents a single focus. **(d)** Left: Representative immunofluorescence images of DLD1 BRCA2-T207A cells 2h post-irradiation (6Gy), as indicated, stained for γH2AX and RAD51. Right: Quantification of the number of γH2AX foci (left) or RAD51 foci (right) per nucleus. When indicated, cells were transfected with a plasmid expressing RNase H1 (RH) 48h prior

fixation. The data shown is from at least 400 cells per condition from three independent experiments. For statistical comparison of the differences between the samples we applied a Kruskal-Wallis test followed by Dunn's multiple comparison test, the p-values show significant differences. The red line in the plot indicates the median; each symbol represents a single focus. See also Supplementary Figure 4c. **(e)** Model. DNA-RNA hybrid formation may be enhanced in the vicinity of DSBs due to the DNA rotation freedom provided by the break. Left: Through its interaction with DDX5, BRCA2 helps retain DDX5 at DSBs and stimulates its helicase activity to resolve the DNA-RNA hybrids. Removal of the RNA from the hybrid would trigger RPA binding to the exposed ssDNA followed by the subsequent loading of RAD51 by BRCA2 and the displacement of RPA to resume HR. Right: When the interaction of BRCA2 with DDX5 is impaired as in cells bearing the breast cancer variant BRCA2-T207A, DDX5 would not mediate hybrid removal, leading to hybrids that persist longer delaying the coating of the ssDNA by RPA. Eventually, the RNA from the hybrids would be cleared by other nucleases and helicases such as RNase H1 or Senataxin in a likely less efficient manner.

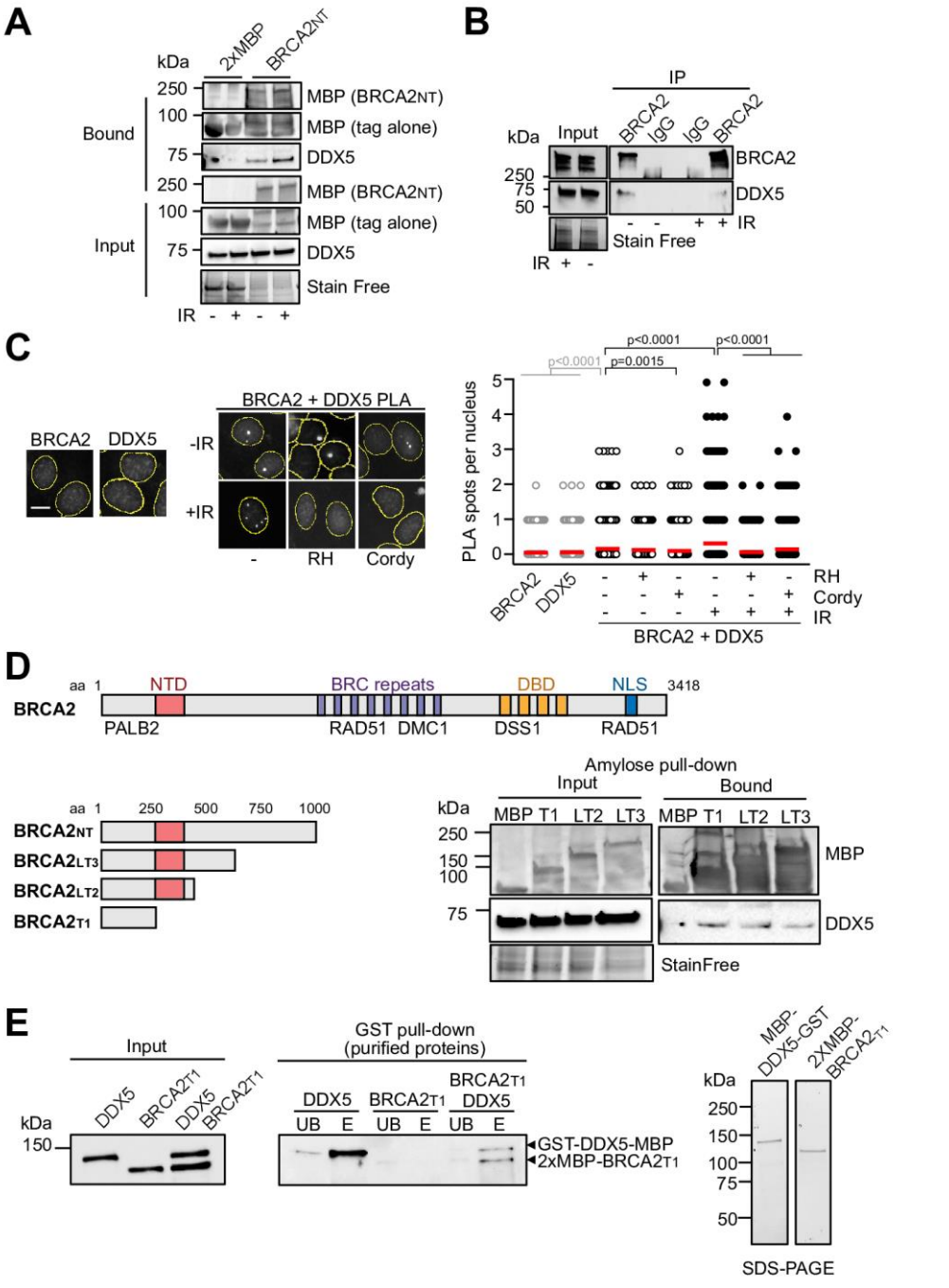
A
kDa
2xMBP
BRCA2NT
Bound
Input
250
100
75
MBP (BRCA2NT)
MBP (tag alone)
DDX5
Stain Free
IR - + - +
B
IP
Input
BRCA2
IgG
IgG
BRCA2
kDa
250
75
50
BRCA2
DDX5
Stain Free
IR - - + + IR
IR + -
C
BRCA2
DDX5
BRCA2 + DDX5 PLA
-IR
+IR
-
RH
Cordy
p<0.0001
p<0.0001
p<0.0001
p=0.0015
PLA spots per nucleus
RH
Cordy
IR
BRCA2 + DDX5
D
aa 1
NTD
BRC repeats
DBD
NLS
3418
BRCA2
PALB2
RAD51
DMC1
DSS1
RAD51
aa 1
250
500
750
1000
BRCA2NT
BRCA2LT3
BRCA2LT2
BRCA2T1
Amylose pull-down
Input
Bound
kDa
MBP T1
LT2
LT3
MBP T1
LT2
LT3
250
150
100
75
MBP
DDX5
StainFree
E
Input
GST pull-down
(purified proteins)
kDa
150
DDX5
BRCA2T1
DDX5
BRCA2T1
DDX5
BRCA2T1
DDX5
UB
E
UB
E
UB
E
GST-DDX5-MBP
2xMBP-BRCA2T1
MBP-DDX5-GST
2XMBP-BRCA2T1
kDa
250
150
100
75
50
SDS-PAGE

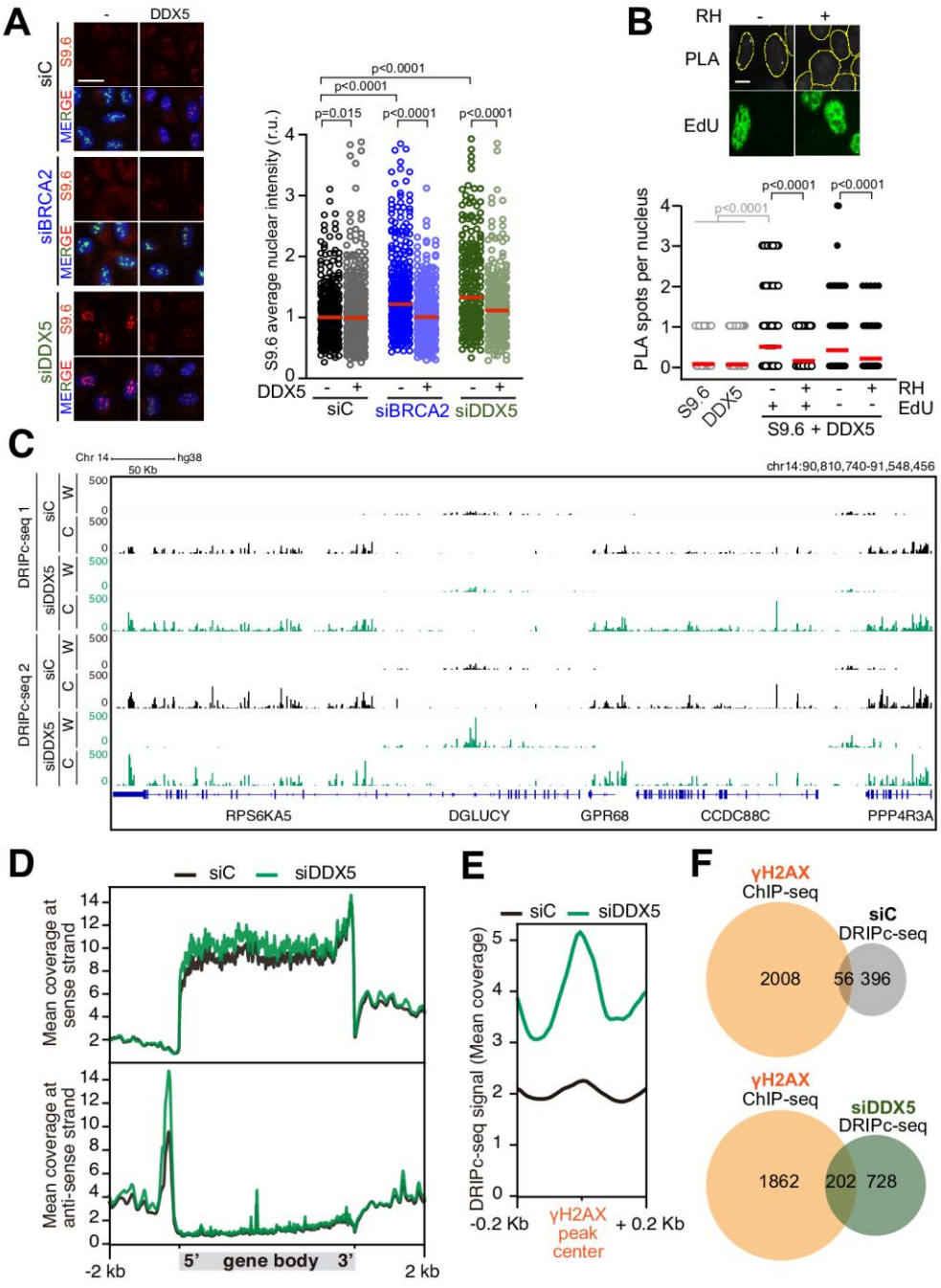
A
DDX5
siC
siBRCA2
siDDX5
S9.6
MERGE
S9.6 average nuclear intensity (r.u.)
p<0.0001
p<0.0001
p=0.015
p<0.0001
p<0.0001
DDX5
siC
siBRCA2
siDDX5
B
RH
PLA
EdU
PLA spots per nucleus
p<0.0001
p<0.0001
p<0.0001
S9.6
DDX5
RH
EdU
S9.6 + DDX5
C
Chr 14
hg38
50 Kb
chr14:90,810,740-91,548,456
DRIPc-seq 1
DRIPc-seq 2
siC
siDDX5
RPS6KA5
DGLUCY
GPR68
CCDC88C
PPP4R3A
D
siC
siDDX5
Mean coverage at sense strand
Mean coverage at anti-sense strand
-2 kb
5' gene body 3'
2 kb
E
siC
siDDX5
DRIPc-seq signal (Mean coverage)
-0.2 Kb
γH2AX peak center
+ 0.2 Kb
F
γH2AX ChIP-seq
siC DRIPc-seq
2008
56
396
γH2AX ChIP-seq
siDDX5 DRIPc-seq
1862
202
728

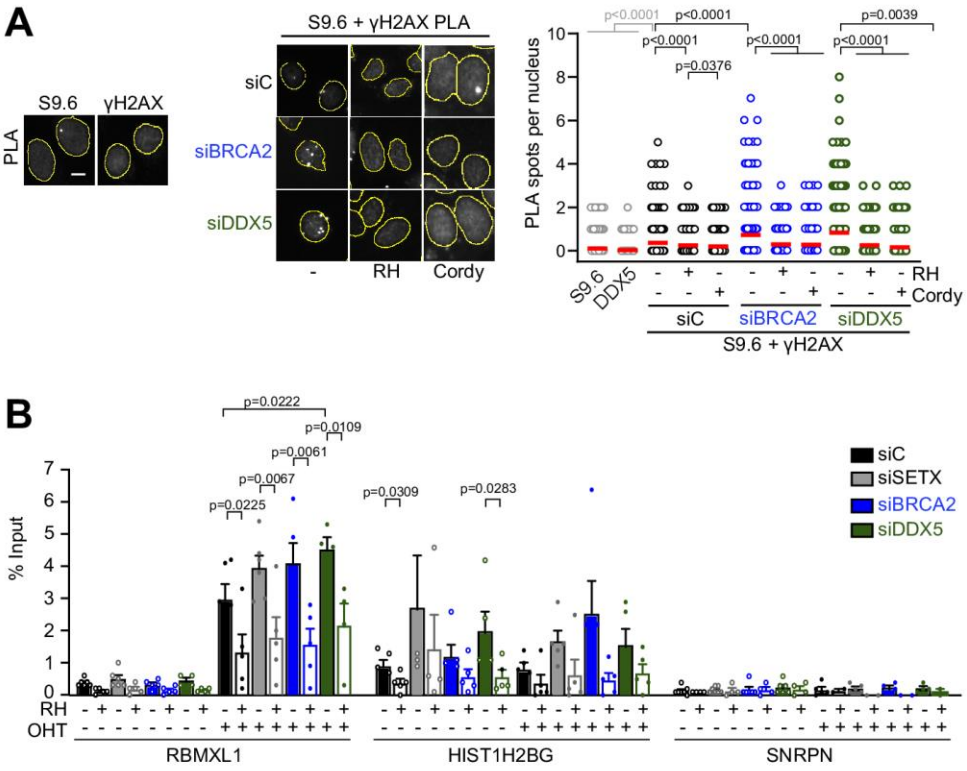
A
S9.6
γH2AX
PLA
S9.6 + γH2AX PLA
siC
siBRCA2
siDDX5
-
RH
Cordy
PLA spots per nucleus
p<0.0001
p<0.0001
p=0.0039
p<0.0001
p<0.0001
p<0.0001
p=0.0376
S9.6
DDX5
RH
Cordy
siC
siBRCA2
siDDX5
S9.6 + γH2AX
B
p=0.0222
p=0.0109
p=0.0061
p=0.0067
p=0.0225
p=0.0309
p=0.0283
% Input
siC
siSETX
siBRCA2
siDDX5
RH
OHT
RBMXL1
HIST1H2BG
SNRPN

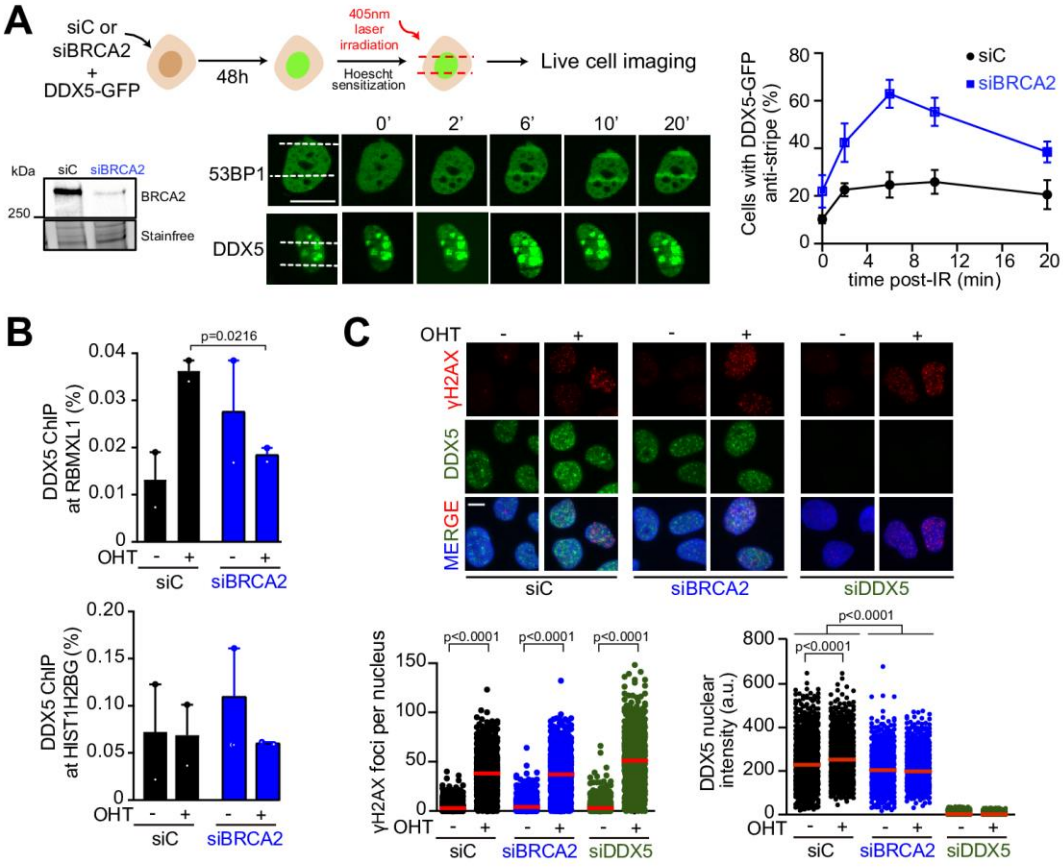
A
siC or siBRCA2 + DDX5-GFP
48h
405nm laser irradiation
Hoescht sensitization
Live cell imaging
kDa
siC
siBRCA2
250
BRCA2
Stainfree
0'
2'
6'
10'
20'
53BP1
DDX5
Cells with DDX5-GFP anti-stripe (%)
siC
siBRCA2
time post-IR (min)
B
p=0.0216
DDX5 ChIP at RBMXL1 (%)
OHT
siC
siBRCA2
DDX5 ChIP at HIST1H2BG (%)
C
OHT
γH2AX
DDX5
MERGE
siC
siBRCA2
siDDX5
γH2AX foci per nucleus
p<0.0001
DDX5 nuclear intensity (a.u.)

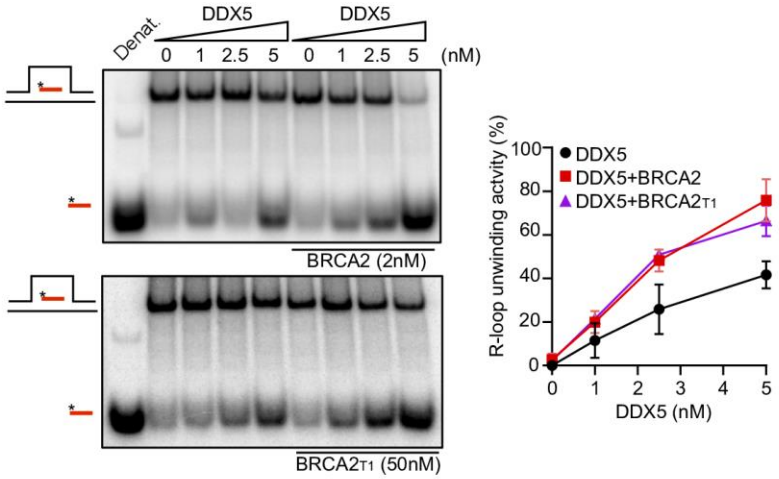
Denat.
DDX5
DDX5
0 1 2.5 5 0 1 2.5 5 (nM)
BRCA2 (2nM)
BRCA2T1 (50nM)
R-loop unwinding activity (%)
DDX5
DDX5+BRCA2
DDX5+BRCA2T1
DDX5 (nM)

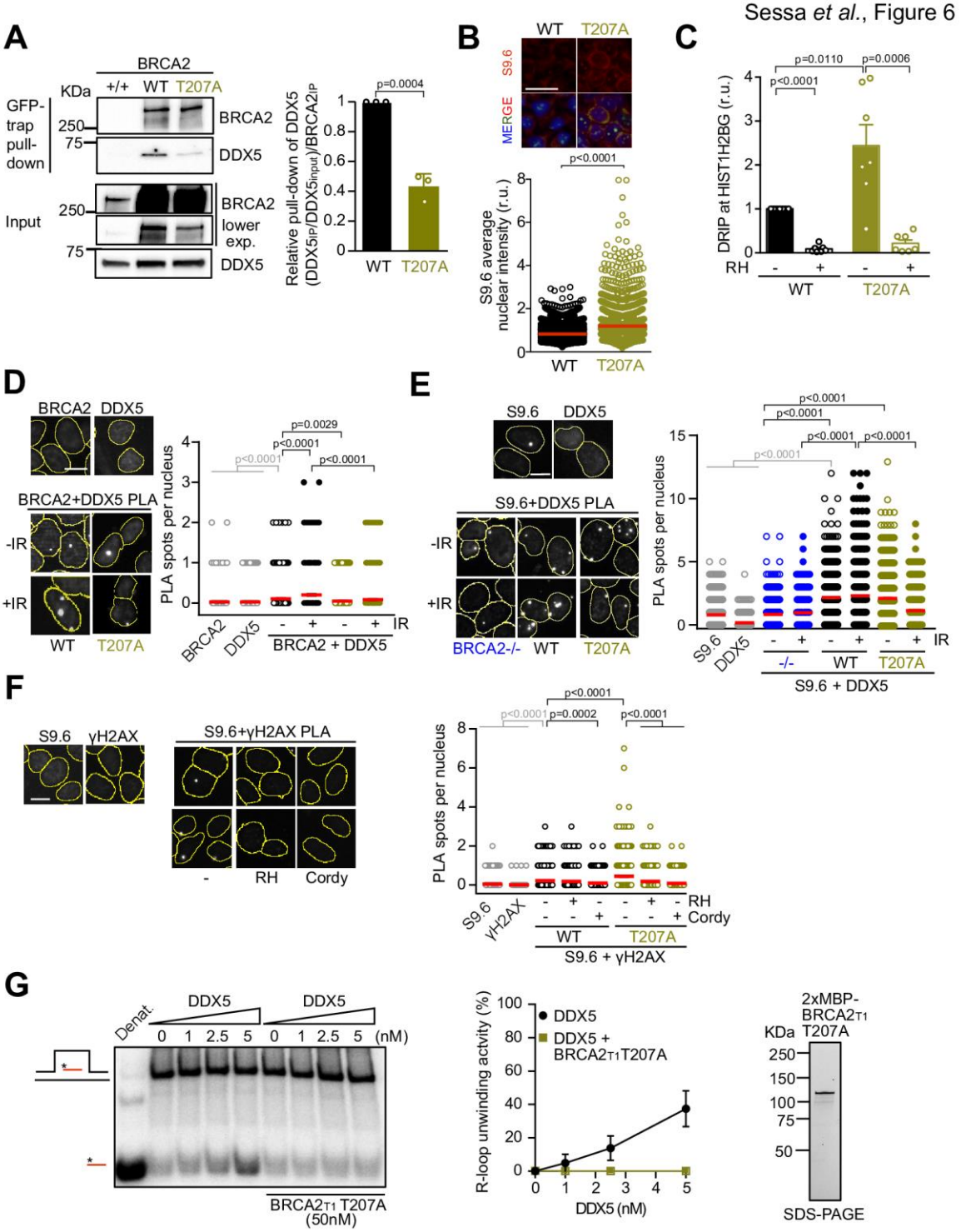
A
BRCA2
KDa
+/+
WT
T207A
GFP-trap pull-down
250
75
BRCA2
DDX5
Input
250
BRCA2
lower exp.
75
DDX5
Relative pull-down of DDX5 (DDX5IP/DDX5Input)/BRCA2IP
p=0.0004
WT
T207A
B
WT
T207A
S9.6
MERGE
p<0.0001
S9.6 average nuclear intensity (r.u.)
WT
T207A
C
p=0.0110
p=0.0006
p<0.0001
DRIP at HIST1H2BG (r.u.)
RH
WT
T207A
D
BRCA2
DDX5
BRCA2+DDX5 PLA
-IR
+IR
WT
T207A
p=0.0029
p<0.0001
p<0.0001
p<0.0001
PLA spots per nucleus
BRCA2
DDX5
IR
BRCA2 + DDX5
E
S9.6
DDX5
S9.6+DDX5 PLA
-IR
+IR
BRCA2-/-
WT
T207A
p<0.0001
p<0.0001
p<0.0001
p<0.0001
p<0.0001
PLA spots per nucleus
S9.6
DDX5
-/-
WT
T207A
IR
S9.6 + DDX5
F
S9.6
γH2AX
S9.6+γH2AX PLA
-
RH
Cordy
p<0.0001
p<0.0001
p=0.0002
p<0.0001
PLA spots per nucleus
S9.6
γH2AX
RH
Cordy
WT
T207A
S9.6 + γH2AX
G
Denat.
DDX5
DDX5
0 1 2.5 5 0 1 2.5 5 (nM)
BRCA2T1 T207A (50nM)
R-loop unwinding activity (%)
DDX5
DDX5 + BRCA2T1T207A
DDX5 (nM)
2xMBP-BRCA2T1 T207A
KDa
250
150
100
75
50
SDS-PAGE

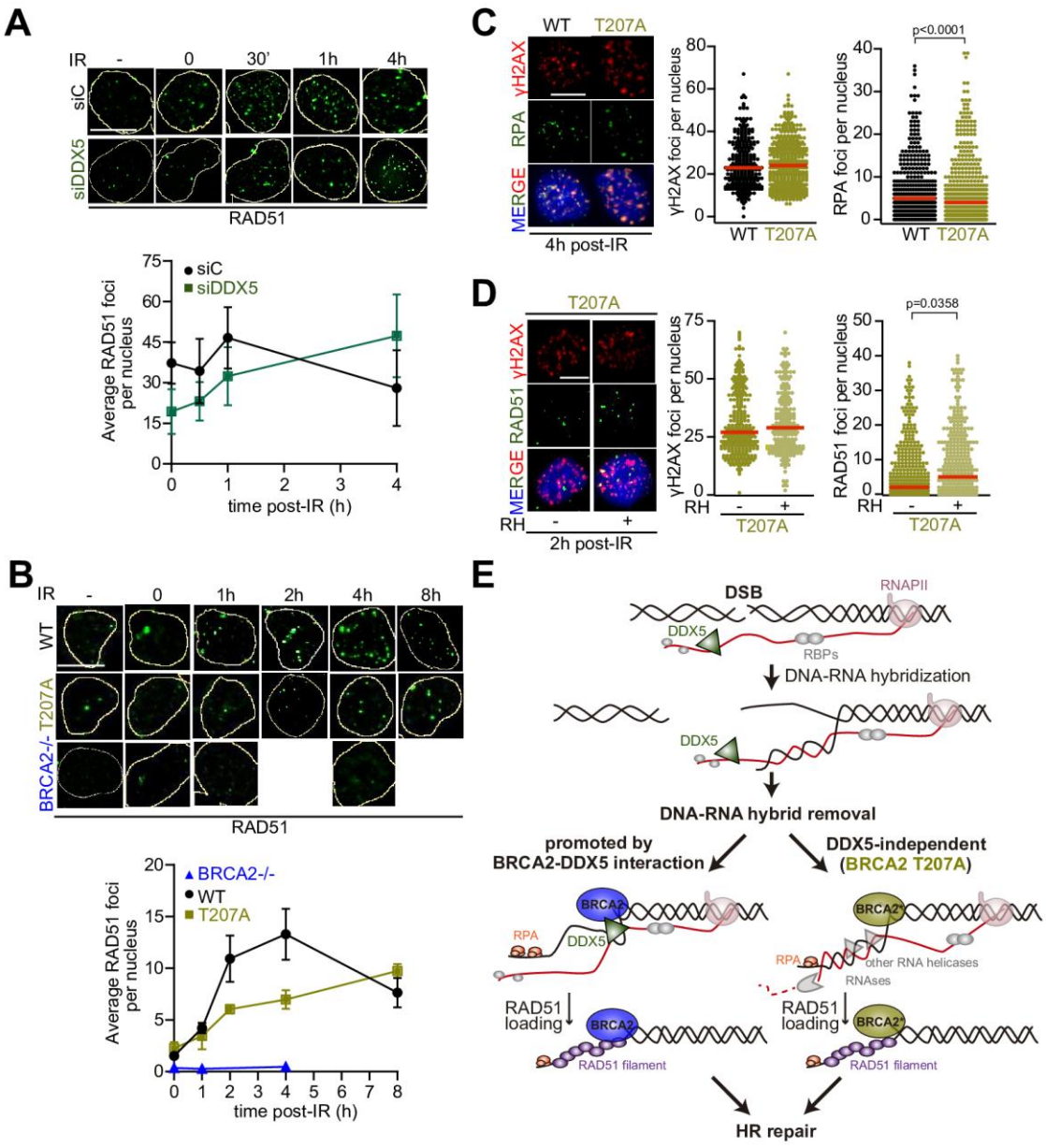
A
IR - 0 30' 1h 4h
siC
siDDX5
RAD51
Average RAD51 foci per nucleus
siC
siDDX5
time post-IR (h)
B
IR - 0 1h 2h 4h 8h
WT
BRCA2-/- T207A
RAD51
Average RAD51 foci per nucleus
BRCA2-/-
WT
T207A
time post-IR (h)
C
WT T207A
γH2AX
RPA
MERGE
4h post-IR
γH2AX foci per nucleus
RPA foci per nucleus
p<0.0001
WT T207A
D
T207A
γH2AX
RAD51
MERGE
RH - +
2h post-IR
γH2AX foci per nucleus
RAD51 foci per nucleus
p=0.0358
RH - +
T207A
E
DSB
RNAPII
DDX5
RBPs
DNA-RNA hybridization
DDX5
DNA-RNA hybrid removal
promoted by BRCA2-DDX5 interaction
DDX5-independent (BRCA2 T207A)
BRCA2
RPA
DDX5
RAD51 loading
RAD51 filament
other RNA helicases
RNAses
HR repair

Supplementary Figure 1. Related to Figure 1 and 2. DEAD-box proteins identified in the proteomics mass spectrometry screen and DNA-RNA hybrids levels in BRCA2- and DDX5-depleted cells. (a) DEAD-box helicases enriched in the $BRCA2_{NT}$ interactome. Label free protein quantification. (Left) BRCA2 (in italic) and DDX Protein ID present in the proteomics mass spectrometry screen. (Center) Heat-map showing fold enrichment of each protein in $BRCA2_{NT}$/ 2xMBP. Infinite-fold indicates proteins that are only present in $BRCA2_{NT}$ sample and not in pull-down performed with the 2xMBP. (Bottom) Heat-map log2 color scale. (Right) Bar graph showing protein abundance in molar fraction percentage (mol %) in each pull-down (yellow in 2xMBP, blue in $BRCA2_{NT}$) based on label free emPAI quantification (see Methods section). **(b)** Left: Representative immunofluorescence images of U2OS cells depleted of DDX5 (siDDX5), BRCA2 (siBRCA2) or control cells (siC) and stained with S9.6 antibody (DNA-RNA hybrids) and anti-nucleolin and counterstained with DAPI. Scale bar indicates 10 µm. Right: Quantification of the relative intensity of S9.6 staining. The data represent at least 500 cells per condition from three independent experiments. The red line in the scatter plot represents the median. For statistical comparison of the differences between the samples we applied a t test. The p-values show significant differences. **(c)** Representative images of *in situ* PLA experiment performed between DDX5 and S9.6 antibodies in U2OS cells. When indicated, cells were treated with Cordycepin (Cordy) for 2h at 37°C before fixation. Single antibody controls from untreated cells are shown. Scale bar indicates 10 µm. Right: Quantification of the number of PLA spots per nucleus in different conditions, as indicated. The data represent at least 200 cells per condition from three independent experiments. For statistical comparison of the differences between the samples we applied a Kruskal-Wallis test followed by

Dunn's multiple comparison test, the p-values show significant differences. The red line in the plot indicates the median, each symbol represents a single PLA spot.

Supplementary Figure 2. Related to Figure 3. DNA break detection by γH2AX ChIP in U2OS DIvA cells. γH2AX ChIP-qPCR signal values at *RBMXL1* and *HIST1H2BG* loci in U2OS DiVA cells transfected with the indicated siRNAs and either untreated cells (-OHT) or after tamoxifen addition (+OHT). The data represent the mean ± SEM from at least two independent experiments. The statistical significance of the difference was calculated with unpaired t-Student test; the p-values show the significant difference.

Supplementary Figure 3. Related to Figure 6. DNA-RNA hybrids associated with DNA breaks accumulate in BRCA2-T207A cells. (a) Quantification of the average nuclear intensity of S9.6 antibody in DLD1 BRCA2$^{+/+}$ and BRCA2$^{-/-}$ cells. The red line in the plot indicates the median, each symbol represents the value of a single cell. The data represent at least 2000 cells per condition from four independent experiments. The statistical significance of the difference was calculated with Mann-Whitney U-test; the p-values show the significant difference. **(b)** Relative DRIP-qPCR signal values at the *HIST1H2BG* locus in DLD1 BRCA2$^{+/+}$ and BRCA2$^{-/-}$ cells and treated *in vitro* with RNase H1 (RH) pre-immunoprecipitation where indicated. The data represent the mean ± SEM from at five independent experiments. The statistical significance of the difference was calculated with unpaired t-Student test; the p-values show the significant difference. **(c)** Quantification of the average nuclear intensity of S9.6 antibody in DLD1 BRCA2-WT (WT) or BRCA2-T207A (T207A) cells transfected with either a plasmid expressing GFP alone (-RH) or GFP-RNase H1 (+RH), as indicated. The red line in the plot indicates the median, each symbol represents the value of a

single cell. The data represent at least 170 cells per condition from two independent experiments. The statistical significance of the difference was calculated with Mann-Whitney U-test; the p-values show the significant difference.

Supplementary Figure 4. Related to Figure 7. γH2AX foci in DDX5-depleted U2OS cells and DLD1 cells bearing BRCA2-T207A variant exposed to IR. (a) Left: Representative immunofluorescence images of cells stained for γH2AX antibody in U2OS cells depleted of DDX5 (siDDX5) and in control cells (siC) in cells left untreated (-) or at different time points after exposure to IR (6Gy), as indicated. Scale bar indicates 10 μm. Right: graph showing the average number of γH2AX foci. The data represent the mean ± SEM of three independent experiments. **(b)** Left: Representative immunofluorescence images of three independent experiments of nuclear γH2AX foci in BRCA2 deficient DLD1 cells ($BRCA2^{-/-}$) or $BRCA2^{-/-}$ bearing BRCA2 WT or BRCA2-T207A variant in cells left untreated (-) or at different time points after exposure to IR (6Gy), as indicated. Scale bar indicates 10 μm. Right: Graph showing the average number of γH2AX foci. The data represent the mean ± SEM of three independent experiments. **(c)** Left: Representative immunofluorescence images of DLD1 BRCA2-T207A stained for γH2AX and RAD51. When indicated, cells were transfected with a plasmid expressing RNaseH1 (+RH) 48h prior fixation. Right: Quantification of the number of γH2AX foci (left) or RAD51 foci (right) per nucleus. The data shown is from at least 400 cells per condition from three independent experiments. For statistical comparison of the differences between the samples we applied a Kruskal-Wallis test followed by Dunn's multiple comparison test, the p-values show significant differences. The red line in the plot indicates the median; each symbol represents a single focus.

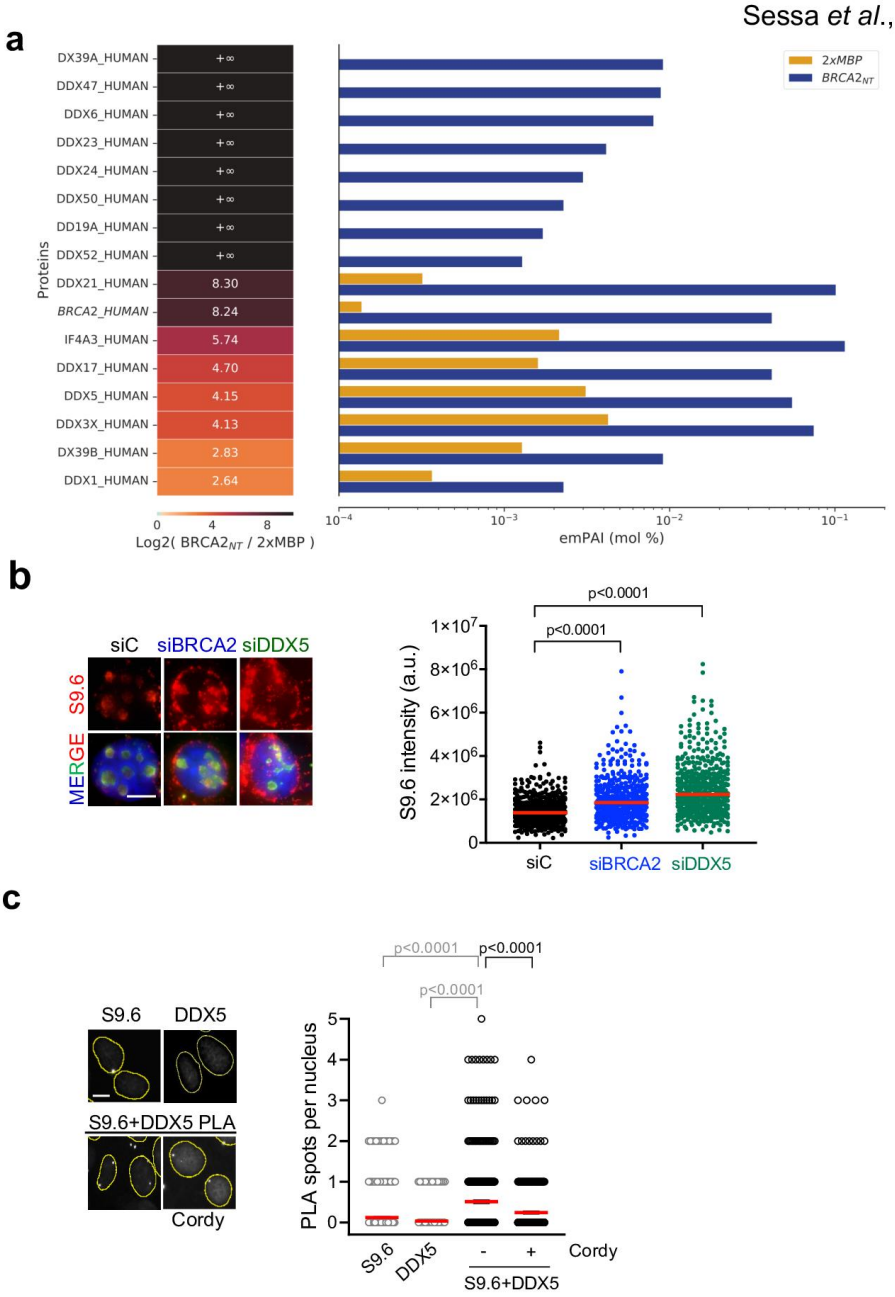
a
DX39A_HUMAN
DDX47_HUMAN
DDX6_HUMAN
DDX23_HUMAN
DDX24_HUMAN
DDX50_HUMAN
DD19A_HUMAN
DDX52_HUMAN
DDX21_HUMAN
BRCA2_HUMAN
IF4A3_HUMAN
DDX17_HUMAN
DDX5_HUMAN
DDX3X_HUMAN
DX39B_HUMAN
DDX1_HUMAN
+∞
8.30
8.24
5.74
4.70
4.15
4.13
2.83
2.64
Proteins
0 4 8
Log2(BRCA2NT / 2xMBP)
2xMBP
BRCA2NT
10−4 10−3 10−2 10−1
emPAI (mol %)
b
siC siBRCA2 siDDX5
S9.6
MERGE
p<0.0001
p<0.0001
1×10^7
8×10^6
6×10^6
4×10^6
2×10^6
0
S9.6 intensity (a.u.)
siC siBRCA2 siDDX5
c
S9.6 DDX5
S9.6+DDX5 PLA
Cordy
p<0.0001 p<0.0001
p<0.0001
PLA spots per nucleus
5 4 3 2 1 0
S9.6 DDX5 - + Cordy
S9.6+DDX5

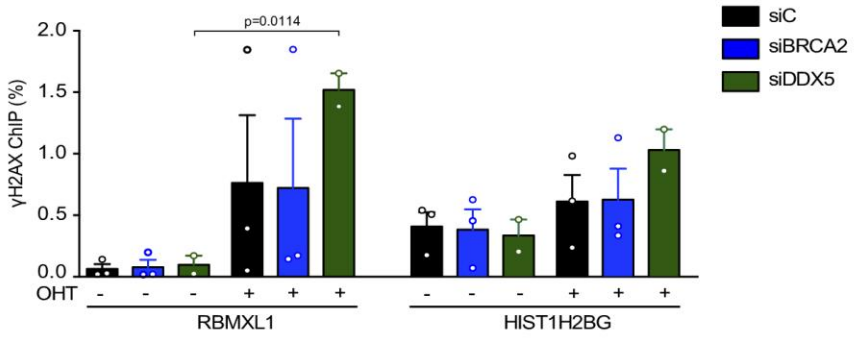
p=0.0114
siC
siBRCA2
siDDX5
γH2AX ChIP (%)
2.0
1.5
1.0
0.5
0.0
OHT
- - - + + +
- - - + + +
RBMXL1
HIST1H2BG

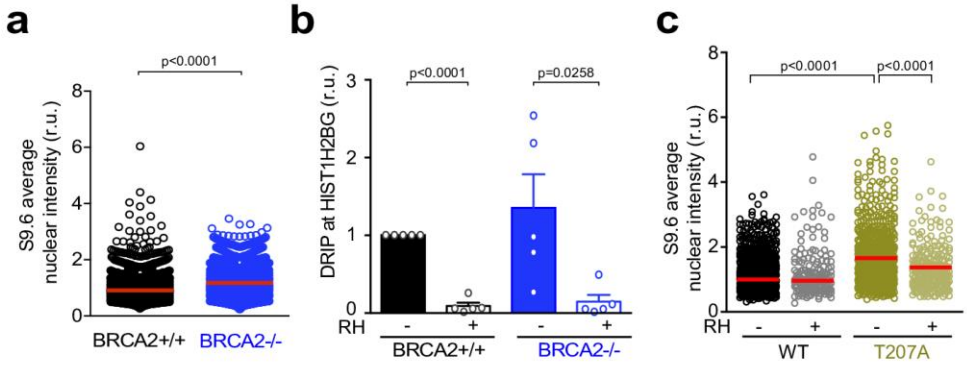
a
p<0.0001
S9.6 average nuclear intensity (r.u.)
0
2
4
6
8
BRCA2+/+
BRCA2-/-
b
p<0.0001
p=0.0258
DRIP at HIST1H2BG (r.u.)
0
1
2
3
RH
-
+
-
+
BRCA2+/+
BRCA2-/-
c
p<0.0001
p<0.0001
S9.6 average nuclear intensity (r.u.)
0
2
4
6
8
RH
-
+
-
+
WT
T207A

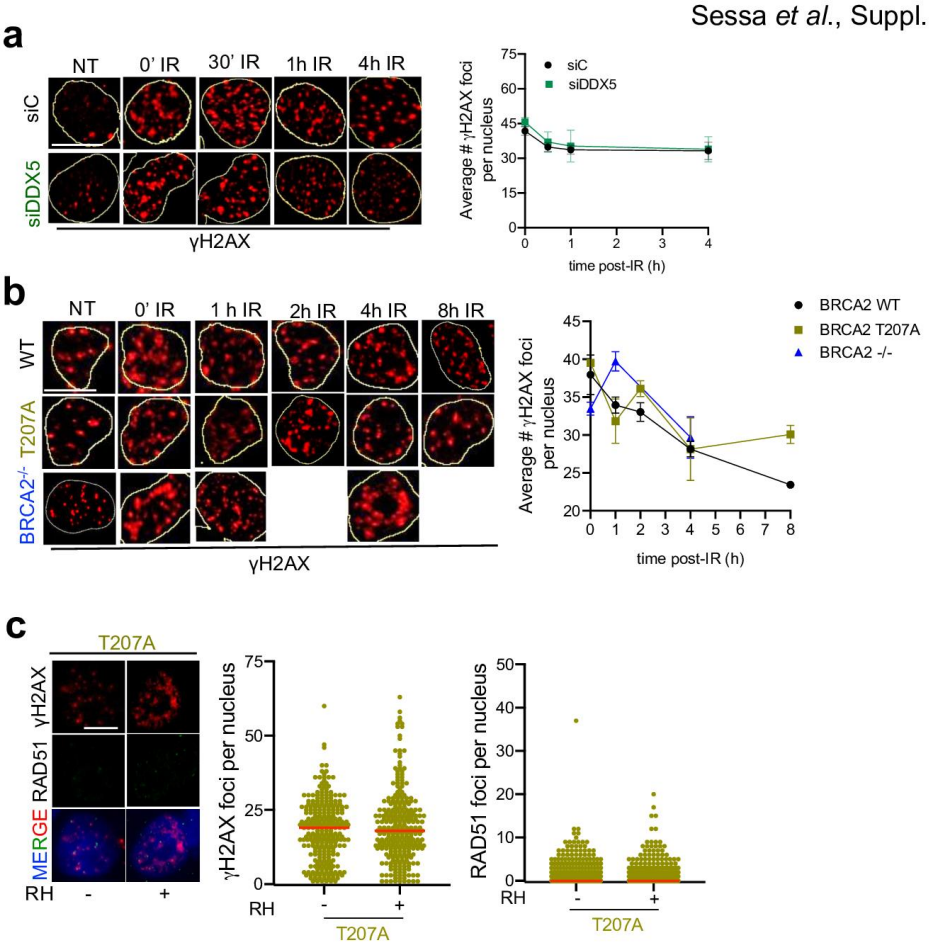
a
NT
0' IR
30' IR
1h IR
4h IR
siC
siDDX5
γH2AX
Average # γH2AX foci per nucleus
siC
siDDX5
time post-IR (h)
b
NT
0' IR
1 h IR
2h IR
4h IR
8h IR
WT
T207A
BRCA2-/-
γH2AX
Average # γH2AX foci per nucleus
BRCA2 WT
BRCA2 T207A
BRCA2 -/-
time post-IR (h)
c
T207A
γH2AX
RAD51
MERGE
RH
γH2AX foci per nucleus
RAD51 foci per nucleus
T207A

Sessa *et al*., Supplementary Tables 2-4 and legend supplementary Table 1

Supplementary Table 1. Protein partners identified in BRCA2$_{NT}$ interactome.

The list shows all the proteins identified in the proteomics mass spectrometry screen. Fold-enrichment for each protein (BRCA2$_{NT}$/2XMBP) is indicated, unique proteins in the BRCA2$_{NT}$ pull-down sample do not have a numerical value but only a emPAI (mol%). Only proteins for which the ratio BRCA2$_{NT}$/2xMBP >2 and those unique to BRCA2$_{NT}$ are shown. Protein abundance is expressed as emPAI (%) (exponentially modified protein abundance in molar fraction percentage) as previously described (Ishihama et al., 2005).

(Due to the size of the table, the content of this table is included as a separate Excel file: Supplementary Table 1)

Supplementary Table 2: Primers used to subclone DDX5 into the pEGFP-N3 vector

Construct	**Oligo name**	**Sequence (5'-3')**
DDX5-GFP	Fw: oAC953	CGTGTCGACATGTCGGGTTATTCGAGTG ACCGAGAC
	Rv: oAC967	CGTACCGGTCCTTGGGAATATCCTGTTG GCATTGGATAACC

Supplementary Table 3. siRNA used in this study

siRNA		
TARGET AND SEQUENCES (5'-3')	SOURCE	IDENTIFIER
BRCA2 CAGCGTTTGTGTATCGGGCAA	Qiagen	Cat# SI00000966
BRCA2 ON-TARGETplus SMARTpool	Dharmacon	Cat# L-021420-00
BRCA2 GAAGAAUGCAGGUUUAAUA	Dharmacon	Cat# D-003462-04
DDX5 GCUCUUUAUAUUGUGUGUUAU	Mazurek et al., 2012	N/A
SETX ON-TARGETplus SMARTpool	Dharmacon	Cat# L-003462-00
Non targeting oligonucleotide (siC)	Dharmacon	Cat# D-001810-01-20

Supplementary Table 4. DNA and RNA sequences used for R loop substrate preparation

Oligonucleotides		
NAME AND SEQUENCES (5'-3')	SOURCE	IDENTIFIER
oAC862 (PAGE purified) GTACCCGGGGATCCTCTAGAGTCGAGC GTCGATCCGAAACTTGGCACTGGCCGTC GTTTTACAAC	Song et al. 2017	N/A
oAC863 (PAGE purified) GTTGTAAAACGACGGCCAGTGCCTTTTC CCAGCCTCAATCTCATCACTCTAGAGGA TCCCCGGGTAC	Song et al. 2017	N/A
oAC864 (PAGE purified) GUUUCGGAUCGACGC	Song et al. 2017	N/A

nature COMMUNICATIONS

ARTICLE

https://doi.org/10.1038/s41467-020-15689-9 OPEN

Proper chromosome alignment depends on BRCA2 phosphorylation by PLK1

Åsa Ehlén[1,2], Charlotte Martin[1,2,8], Simona Miron[3,8], Manon Julien[3,4,8], François-Xavier Theillet[3], Virginie Ropars[3], Gaetana Sessa[1,2], Romane Beaurepere[1,2], Virginie Boucherit[1,2], Patricia Duchambon[5,6], Ahmed El Marjou[5,7], Sophie Zinn-Justin[3,9✉] & Aura Carreira[1,2,9✉]

The BRCA2 tumor suppressor protein is involved in the maintenance of genome integrity through its role in homologous recombination. In mitosis, BRCA2 is phosphorylated by Polo-like kinase 1 (PLK1). Here we describe how this phosphorylation contributes to the control of mitosis. We identify a conserved phosphorylation site at T207 of BRCA2 that constitutes a bona fide docking site for PLK1 and is phosphorylated in mitotic cells. We show that BRCA2 bound to PLK1 forms a complex with the phosphatase PP2A and phosphorylated-BUBR1. Reducing BRCA2 binding to PLK1, as observed in *BRCA2* breast cancer variants S206C and T207A, alters the tetrameric complex resulting in unstable kinetochore-microtubule interactions, misaligned chromosomes, faulty chromosome segregation and aneuploidy. We thus reveal a role of BRCA2 in the alignment of chromosomes, distinct from its DNA repair function, with important consequences on chromosome stability. These findings may explain in part the aneuploidy observed in *BRCA2*-mutated tumors.

[1] Institut Curie, PSL Research University, CNRS, UMR3348, F-91405 Orsay, France. [2] Paris Sud University, Paris-Saclay University CNRS, UMR3348, F-91405 Orsay, France. [3] Institute for Integrative Biology of the Cell (I2BC), CEA, CNRS, Univ Paris-Sud, Université Paris-Saclay, Gif-sur-Yvette, Cedex, France. [4] Department of Biology, École Normale Supérieure, 94230 Cachan, France. [5] Protein Expression and Purification Core Facility, Institut Curie, 26 rue d'Ulm, 75248 Paris, Cedex 05, France. [6] INSERM U1196, 91405 Orsay, Cedex, France. [7] CNRS UMR144, 12 rue Lhomond, 75005 Paris, France. [8] These authors contributed equally: Charlotte Martin, Simona Miron, Manon Julien. [9] These authors jointly supervised: Sophie Zinn-Justin, Aura Carreira. ✉email: sophie.zinn@cea.fr; aura.carreira@curie.fr

The BRCA2 tumor suppressor protein plays an important role in DNA repair by homologous recombination (HR)[1,2] that takes place preferentially during S/G2 phases of the cell cycle[3]. BRCA2 has also emerging functions in mitosis, for example, at the kinetochore, it forms a complex with BUBR1[4,5], a protein required for kinetochore–microtubule attachment and a component of the spindle assembly checkpoint (SAC)[6,7]. These two activities of BUBR1 involve different partners and are functionally distinct[8,9]. BRCA2 has been proposed to contribute to BUBR1 SAC activity[4,10], although due to confounding results in the BUBR1 interaction site in BRCA2, it is unclear if this interaction is direct[4,5]. At the end of mitosis, BRCA2 localizes to the midbody and assists cell division by serving as a scaffold protein for the central spindle components[11–13]. In mitosis, BRCA2 is a target of phosphorylation by PLK1 both in its N-terminal region[14,15] and in its central region[15], although the functional role of these phosphorylation events remains unclear.

PLK1 is a master regulator of the cell cycle that is upregulated in mitosis[16,17]. Among other functions, PLK1 directly binds and phosphorylates BUBR1 at several residues including the two tension-sensitive sites S676[18] and T680[19] in prometaphase allowing the formation of stable kinetochore–microtubule attachments. This activity needs to be tightly regulated to ensure proper alignment of the chromosomes at the metaphase plate[8,9,18]. The kinase activity of Aurora B is essential to destabilize erroneous kinetochore–microtubule interactions[20] whereas the phosphatase PP2A protects initial kinetochore–microtubule interactions from excessive destabilization by Aurora B[21]. This function is achieved through the interaction of PP2A-B56 subunit with BUBR1 phosphorylated at the Kinetochore Attachment and Regulatory Domain (KARD) motif (including residues S670, S676, and T680)[19]. Thus, the interplay between PLK1, BUBR1, Aurora B, and PP2A is necessary for the formation of stable kinetochore–microtubule attachments.

PLK1 is recruited to specific targets via its Polo-box domain (PBD)[22]. PBD interacts with phosphosites characterized by the consensus motif S-[pS/pT]-P/X[23]. These phosphosites are provided by a priming phosphorylation event, usually mediated by CDK1 or other proline-directed kinases[17]; however, there is also evidence that PLK1 itself might create docking sites ("self-priming") during cytokinesis[24,25].

Several BRCA2 sites have been suggested as phosphorylated by PLK1 in mitosis, some of which belong to a cluster of serines and threonines located in BRCA2 N-terminus around residue S193[14]. We set out to investigate which of these sites are phosphorylated by PLK1, and to reveal whether these phosphorylation events play a role in the regulation of mitotic progression. Here, we demonstrate that the two conserved residues S193 and T207 are phosphorylated by PLK1, and that phosphorylated BRCA2-T207 is a bona fide docking site for PLK1. By investigating the phenotype of BRCA2 missense variants that limit the phosphorylation of BRCA2-T207, we reveal an unexpected role for BRCA2 in the alignment of chromosomes at the metaphase plate. We demonstrate that phosphorylation of BRCA2-T207 by PLK1 facilitates the formation of a complex between BRCA2-PLK1-pBUBR1 and the phosphatase PP2A. A defect in this function of BRCA2 is manifested in chromosome misalignment, chromosome segregation errors, mitotic delay and aneuploidy, leading to chromosomal instability.

Results

Breast cancer variants alter PLK1 phosphorylation of BRCA2. Several missense variants of uncertain significance (VUS) identified in *BRCA2* in breast cancer patients are located in the N-terminal region predicted to be phosphorylated by PLK1 (around S193) (Breast information core (BIC)[26] and BRCA-Share[27]), summarized in Supplementary Table 1. To find out if any of these variants affected PLK1 phosphorylation in this region, we purified fragments comprising amino acids 1 to 250 of BRCA2 (hereafter $BRCA2_{1-250}$) from human embryonic kidney cells (HEK293T) and used an in vitro kinase assay to assess the phosphorylation by PLK1 of the fragments containing either the WT sequence, the different BRCA2 variants M192T, S196N, S206C, and T207A, or the mutant S193A, previously reported to reduce the phosphorylation of BRCA2 by PLK1[14]. As expected, S193A reduced the phosphorylation of $BRCA2_{1-250}$ by PLK1 (Fig. 1a, b). Interestingly, variants T207A and S206C also led to a 2-fold decrease in PLK1 phosphorylation of $BRCA2_{1-250}$ (Fig. 1a, b). In contrast, M192T and S196N did not significantly modify the phosphorylation of $BRCA2_{1-250}$ by PLK1 (Fig. 1a, b). The phosphorylation observed in the BRCA2 fragments is specific of the recombinant PLK1 kinase as it is PLK1 concentration dependent (Supplementary Fig. 1a, b) and when replacing the PLK1-WT by a kinase-dead (PLK1-KD) version of the protein (K82R)[28], purified using the same protocol, or adding a PLK1 inhibitor (BI2536) to the reaction, the phosphorylation of $BRCA2_{1-250}$ decreased significantly (Fig. 1c, lanes 4 and 5 compared to lane 3; Fig. 1d).

Together, these results show that VUS T207A and S206C identified in breast cancer patients impair phosphorylation of $BRCA2_{1-250}$ by PLK1 in vitro.

BRCA2-T207 is a target of phosphorylation by PLK1. The reduction of BRCA2 phosphorylation in $BRCA2_{1-250}$ containing T207A and S206C variants suggested that these residues could be targets for PLK1 phosphorylation. We investigated this possibility by following the PLK1 phosphorylation kinetics of two overlapping fragments of BRCA2 N-terminus comprising S206 and T207 (hereafter $BRCA2_{48-218}$ and $BRCA2_{190-284}$) using Nuclear Magnetic Resonance (NMR) spectroscopy (Fig. 2a). Together, these fragments cover a large N-terminal region of BRCA2 including the cluster of conserved residues around S193 (from amino acid 180 to amino acid 210; Supplementary Fig. 1c). NMR analysis allows residue-specific quantification of ^{15}N-labeled peptide phosphorylation. Figure 2b shows superimposed ^{1}H-^{15}N HSQC spectra of $BRCA2_{48-218}$ and $BRCA2_{190-284}$ before (black) and after (red) phosphorylation with recombinant PLK1. Analysis of these experiments revealed phosphorylation of S193 and of three other phosphosites, including T207, by PLK1 in the BRCA2 region from amino acid 48 to amino acid 284. Interestingly, while T219 and T226 conservation is poor, T207 and S193 are conserved from mammals to fishes (Supplementary Fig. 1c) suggesting that both residues are important for BRCA2 function.

BRCA2 variant T207A alters PLK1 phosphorylation kinetics. Having identified T207 as a target of phosphorylation of PLK1, we next compared the residue-specific phosphorylation kinetics in the polypeptide WT $BRCA2_{48-218}$ containing the variant T207A that displayed reduced overall phosphorylation (Fig. 1a, b). (The production of a ^{15}N-labeled recombinant fragment comprising S206C yielded an insoluble protein precluding NMR analysis). Time-resolved NMR experiments revealed that PLK1 phosphorylates significantly less $BRCA2_{48-218}$ containing the variant T207A than the WT peptide (Fig. 2c). The initial phosphorylation rate of S193 was decreased by a factor of 2 (Fig. 2d), and T207 was, as expected, not phosphorylated, being mutated into an alanine. Similar results were obtained using $BRCA2_{190-284}$ (Supplementary Fig. 2). This NMR analysis is consistent with the in vitro kinase assay performed using the $BRCA2_{1-250}$ fragment

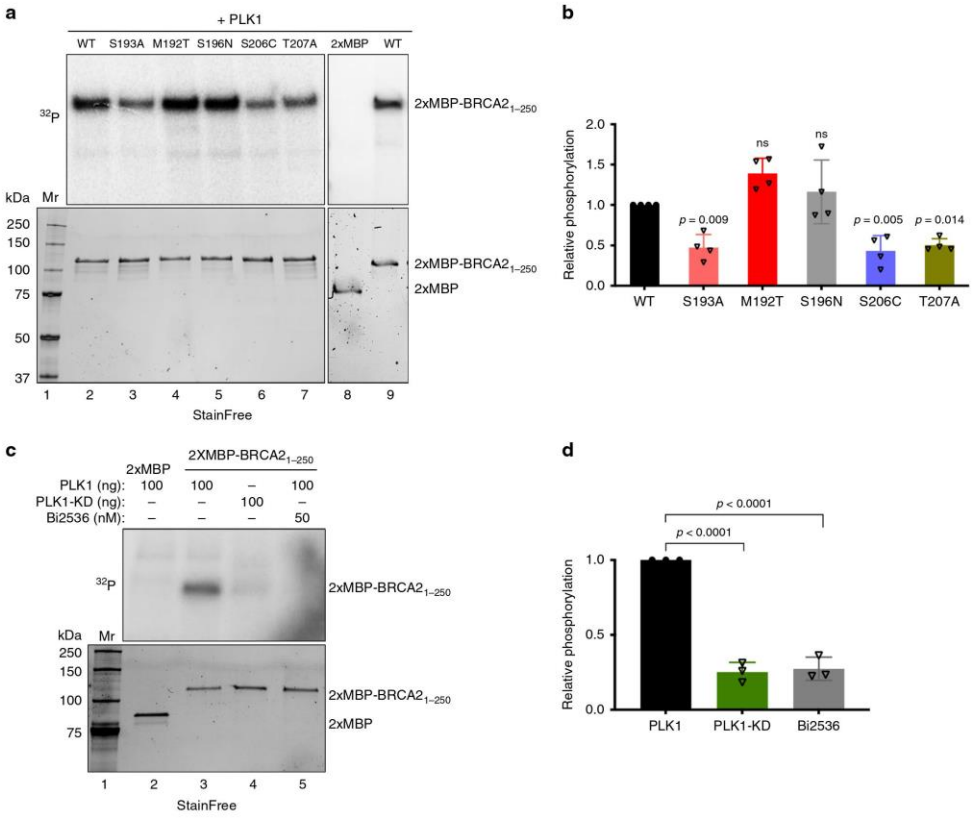

Fig. 1 BRCA2 VUS alter PLK1 phosphorylation of BRCA2$_{1-250}$. **a** PLK1 in vitro kinase assay with BRCA2$_{1-250}$. Top: The polypeptides encompassing 2×-MBP-BRCA2$_{1-250}$ WT or S193A, M192T, S196N, S206C, T207A mutations or the 2XMBP tag were incubated with recombinant PLK1 in the presence of γ^{32}P-ATP. The samples were resolved on 7.5% SDS-PAGE and the ^{32}P-labeled products were detected by autoradiography. Bottom: 7.5% SDS-PAGE showing the input of purified 2xMBP-BRCA2$_{1-250}$ WT and mutated proteins (0.5 µg) used in the reaction as indicated. Mr; molecular weight markers. **b** Quantification of the relative phosphorylation in (**a**). Data in (**b**) are represented as mean ± SD from four independent experiments. **c** PLK1 in vitro kinase assay performed as in (**a**) with recombinant PLK1 or the PLK1 kinase dead K82R mutant (PLK1-KD) together with BRCA2$_{1-250}$ WT as substrate, in the presence or absence of the PLK1 inhibitor BI2536 (50 nM) in the kinase reaction buffer. Mr; molecular weight markers. **d** Quantification of the relative phosphorylation in (**c**). Data in (**d**) are represented as mean ± SD from three independent experiments. **b**, **d** One-way ANOVA test with Dunnett's multiple comparisons test was used to calculate statistical significance of differences (the *p*-values show differences compared to WT (**b**) or PLK1 (**d**); ns (non-significant)). Source data are available as a Source Data file.

purified from human cells (Fig. 1), in which T207A reduces the phosphorylation of BRCA2$_{1-250}$ fragment by PLK1.

Variants T207A and S206C reduce the interaction of BRCA2 with PLK1. The finding that T207 is efficiently phosphorylated by PLK1 in BRCA2$_{48-218}$ and BRCA2$_{190-284}$ (Fig. 2b) together with the observation that T207A mutation causes a global decrease in the phosphorylation of these fragments (Fig. 2c; Supplementary Fig. 2) and the prediction that T207 is a docking site for PLK1$_{PBD}$ binding[23] made us hypothesize that T207 might be a "self-priming" phosphorylation event required for the interaction of PLK1 with BRCA2 at this site. If so, the variants that reduce phosphorylation of T207 by PLK1 would be predicted to alter PLK1$_{PBD}$ binding. To test this hypothesis, we examined the interaction of PLK1 with the VUS-containing polypeptides. We overexpressed 2xMBP-BRCA2$_{1-250}$ constructs carrying these variants in U2OS cells to detect the endogenous PLK1 that co-immunoprecipitates with 2xMBP-BRCA2$_{1-250}$ using amylose pull-down. As expected, overexpressed BRCA2$_{1-250}$ was able to interact with endogenous PLK1 from mitotic cells but not from asynchronous cells (predominantly in G1/S) where the levels of PLK1 are reduced (Fig. 3a, lane 2 compared to lane 1). Furthermore, the variants T207A and S206C showed a weaker interaction with PLK1 than the WT protein (Fig. 3a, pull-down lanes 4, 6 compared to lane 2, Fig. 3b) despite the protein levels of PLK1 remaining unchanged (Fig. 3a, compare PLK1 input lanes 4 and 6 to lane 2). In contrast, the effect of M192T and S196N on the

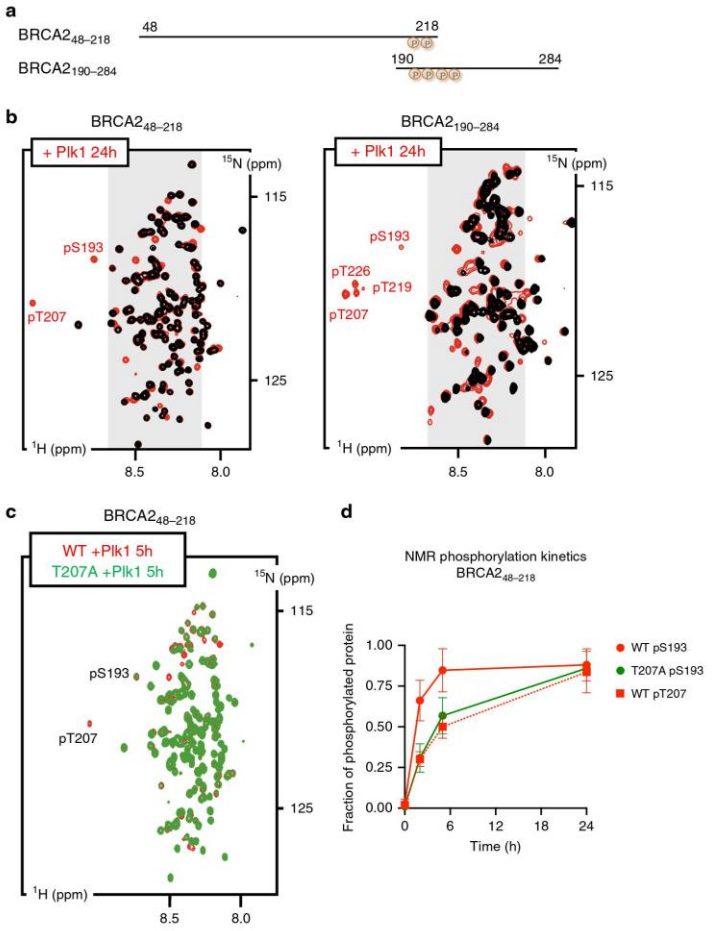

Fig. 2 PLK1 phosphorylates T207 in BRCA2$_{48–218}$ and BRCA2$_{190–284}$. Phosphorylation of BRCA2$_{48–218}$ and BRCA2$_{190–284}$ by PLK1 as observed by NMR. **a** Schematic view of the two overlapping BRCA2 fragments analyzed by NMR. Residues identified as phosphorylated in (**b**) are indicated. **b** Superposition of the ^{1}H-^{15}N HSQC spectra recorded before (black) and after (24 h; red) incubation with PLK1. Each spectrum contains one peak per backbone NH group. Most peaks are located in the gray region of the spectrum, indicating that they correspond to disordered residues. Assignment of each peak to a BRCA2 residue was performed using a classical heteronuclear NMR strategy. Peaks corresponding to phosphorylated residues are indicated. **c** Comparison of the phosphorylation kinetics recorded for BRCA2$_{48–218}$ WT and T207A. ^{1}H-^{15}N HSQC spectra of BRCA2$_{48–218}$WT (red) and T207A (green) recorded 5 h after addition of PLK1 are superimposed to highlight the overall decrease of phosphorylation observed for the mutant compared to the WT. **d** Fraction of phosphorylated protein deduced from the intensities of the peaks corresponding to the non-phosphorylated and phosphorylated residues plotted as a function of time. WT S193 and T207 timepoints are represented by red circles and squares, respectively, while T207A S193 timepoints are represented by green circles. The graph represents data as mean ± SD from three independent experiments. Source data are available as a Source Data file.

interaction was mild (Fig. 3a, compare pull-down lanes 10 and 12 to lane 8, Fig. 3b). These results suggest a self-priming phosphorylation by PLK1 on T207.

To provide further evidence that the PLK1-mediated phosphorylation of BRCA2 favors BRCA2 binding, we performed an in vitro kinase assay with recombinant proteins followed by an amylose pull-down and eluted the bound proteins with maltose. PLK1 was found in the maltose elution with BRCA2$_{1–250}$-WT demonstrating that PLK1-phosphorylated BRCA2$_{1–250}$ binds to PLK1 (Fig. 3c lane 4, Fig. 3d). In contrast, the fraction of PLK1 in the eluate of BRCA2$_{1–250}$-T207A was substantially reduced (Fig. 3c, lane 8 compared to lane 4, Fig. 3d) indicating that the phosphorylation of T207 is required for efficient binding to PLK1 and confirming our results with cell lysates (Fig. 3a, b). Strikingly, we observed no difference in PLK1 binding between BRCA2$_{1–250}$-WT phosphorylated by PLK1 or its kinase dead mutant (PLK1-

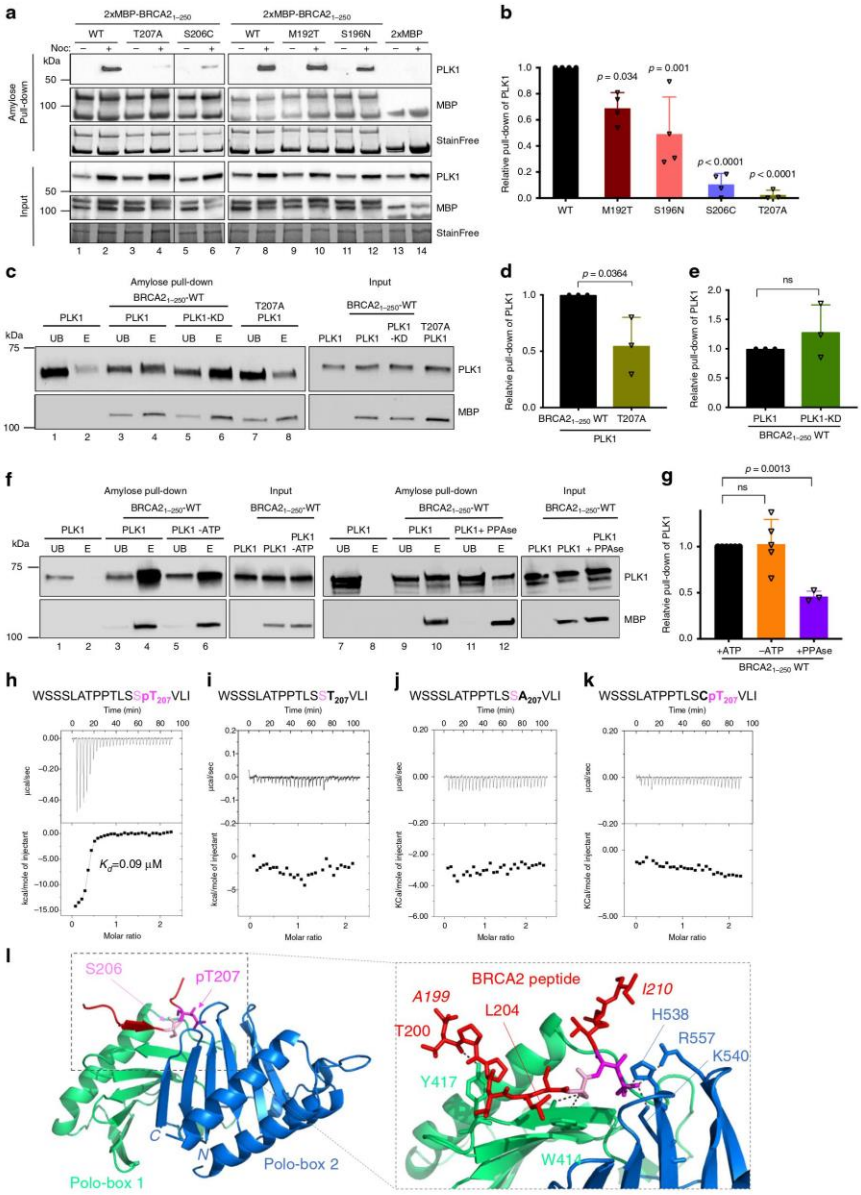

KD; Fig. 3c, lane 6 compared to lane 4, Fig. 3e) or in the absence of ATP (Fig. 3f, lane 6 compared to lane 4, Fig. 3g). However, pre-incubating $BRCA2_{1-250}$-WT with phosphatase before the addition of PLK1 resulted in a 2-fold decrease in the binding to PLK1 indicating that the phosphorylation of BRCA2 is required for the interaction with PLK1 (Fig. 3f lane 12 compared to 10, Fig. 3g).

T207 is a bona fide docking site for PLK1. To demonstrate the recognition of pT207 by PLK1, we measured the affinity of recombinant $PLK1_{PBD}$ (the target recognition domain of PLK1) for a synthetic 17 aa peptide comprising phosphorylated T207. Using isothermal titration calorimetry (ITC), we found that recombinant $PLK1_{PBD}$ bound to the pT207 peptide with an

Fig. 3 BRCA2 variants showing reduced phosphorylation by PLK1 impair PLK1 binding. a Amylose pull-down of U2OS transiently expressing 2xMBP-BRCA2$_{1-250}$ (WT), the variants (M192T, S196N, S206C, and T207A) or the 2XMBP-tag treated with nocodazole as indicated. 4–15% SDS-PAGE followed by WB using anti-PLK1 and anti-MBP antibodies. StainFree images are used as loading control (cropped image is shown). **b** Quantification of co-immunoprecipitated PLK1 with WT in (**a**), relative to the input levels of PLK1. Results are presented as the fold change compared to WT. The data represent the mean ± SD of three to four independent experiments (WT ($n = 4$), M192T ($n = 4$), S196N ($n = 4$), S206C ($n = 4$), T207A ($n = 3$)). One-way ANOVA test with Dunnett's multiple comparisons test was used to calculate statistical significance of differences (p-values compared to WT). **c** PLK1 (or PLK1-KD) as indicated in vitro kinase assay followed by amylose pull-down of BRCA2$_{1-250}$-WT or T207A. 10% SDS-PAGE followed by WB using anti-PLK1 and anti-MBP antibodies. **d, e** Quantification of the PLK1 pull-down in (**c**) relative to the PLK1 levels in the input. Results are presented as the fold change compared to BRCA2$_{1-250}$-WT in (**d**) and PLK1-WT in (**e**). The data represent the mean ± SD of three independent experiments, two-tailed unpaired t-test was used to calculate significance of differences (ns (non-significant)). **f** PLK1 in vitro kinase assay followed by amylose pull-down assay as in (**c**) Left panel: with or without ATP as indicated. Right panel: The 2×-MBP-BRCA2$_{1-250}$-WT polypeptide was pre-treated with phosphatase (FastAP) for 1 h before the amylose pull-down (**c**). In (c) and (**f**): UB: unbound, E: eluted. **g** Quantification of the PLK1 pull-down in (**f**) relative to the PLK1 levels in the input. Results are presented as the fold change compared to kinase assay performed with non-phosphatase treated BRCA2$_{1-250}$-WT in the presence of ATP. The data represent the mean ± SD of three to five independent experiments (+ATP ($n = 5$), −ATP ($n = 5$), +PPAse ($n = 3$)), one-way ANOVA test with Dunnett's multiple comparisons test was used to calculate statistical significance of differences (p-values compared to +ATP; ns (non-significant)). **h–k** Isothermal Titration Calorimetry (ITC) thermograms showing binding of PLK1$_{PBD}$ to a 17 aa BRCA2 peptide containing (**h**) pT207, (**i**) T207, (**j**) A207, (**k**) C206pT207. Residues S206 and pT207 are highlighted in pink (S206) and magenta (pT207) in the peptide sequences. **l** Left panel: 3D cartoon representation of the crystal structure of PLK1$_{PBD}$ (Polo-box 1 in green and Polo-box 2 in blue) bound to the BRCA2 peptide containing pT207 (in red except for S206 (pink, sticks) and pT207 (magenta, sticks)). Right panel: zoom in on the interface between PLK1$_{PBD}$ and the BRCA2 peptide (from A199 to I210). The amino acids of PLK1$_{PBD}$ and BRCA2 involved in the interaction are highlighted in sticks representation with hydrogen bonds depicted as dark gray dots. Source data are available as a Source Data file.

affinity of $K_d = 0.09 \pm 0.01$ μM (Fig. 3h), similar to the optimal affinity reported for an interaction between PLK1$_{PBD}$ and its phosphorylated target[23]. Consistently, PLK1$_{PBD}$ bound to the fragment BRCA2$_{190-284}$ with nanomolar affinity upon phosphorylation by PLK1 ($K_d = 0.14 \pm 0.02$ μM; Supplementary Fig. 3a), whereas it did not bind to the corresponding non-phosphorylated polypeptides (Fig. 3i, Supplementary Fig. 3b). Mutation T207A also abolished the interaction (Fig. 3j), in agreement with the pull-down experiments (Fig. 3a–d). More surprisingly, the phosphomimetic substitution T207D was not sufficient to create a binding site for PLK$_{PDB}$ (Supplementary Fig. 2c). A peptide comprising pT207 and the mutation S206C could not bind to PLK1$_{PBD}$ (Fig. 3k), as predicted from the consensus sequence requirement for PLK1$_{PBD}$ interaction[23]. Last, a peptide containing pS197, a predicted docking site for PLK1, bound with much less affinity to PLK1$_{PBD}$ than pT207 ($K_d = 17 \pm 2$ μM; Supplementary Fig. 2d).

Finally, we determined the crystal structure of PLK1$_{PBD}$ bound to the T207 phosphorylated peptide at 3.1 Å resolution (Supplementary Table 2). Analysis of this 3D structure showed that, as expected, the 17 aa BRCA2 phosphopeptide binds in the cleft formed between the two Polo boxes (Fig. 3l). Twelve residues of the peptide (from A199 to I210) are well structured upon binding, burying about 694 Å^2 in the interface with PLK1$_{PBD}$. The interface between BRCA2 and PLK1$_{PBD}$ is stabilized by 12 hydrogen bonds: the backbone of residues T200 to L209 as well as the side chain of S206 are bonded to residues from Polo Box 1, whereas the side chain of phosphorylated T207 is bonded to residues from Polo Box 2 (see the zoom view in Fig. 3l). The side chain of S206 participates in two hydrogen-bonding interactions with the backbone of W414, which explains the strict requirement for this amino acid at this position[23]. Moreover, the phosphate group of pT207 participates in three hydrogen-bonding interactions with the side chains of residues H538, K540, and R557 in Polo Box 2 (see the zoom view in Fig. 3l). This explains the critical dependence on phosphorylation for binding observed by ITC (Fig. 3h, i).

Thus, our biochemical and structural analyses demonstrate that the BRCA2-T207 phosphopeptide interacts with PLK1$_{PBD}$ as an optimal and specific PLK1$_{PBD}$ ligand. It supports a mechanism in which phosphorylation of T207 by PLK1 promotes the interaction of PLK1 with BRCA2 through a bona fide docking site for PLK1 and favors a cascade of phosphorylation events. In variant T207A, the absence of T207 phosphorylation impairs PLK1 docking explaining the reduction of binding to PLK1 and the global loss of phosphorylation by PLK1. S206C eliminates the serine residue at −1 position required for PLK1$_{PBD}$ interaction resulting as well in a strong reduction of BRCA2 binding.

Impairing T207 phosphorylation prolongs mitosis. PLK1 is a master regulator of mitosis[17]. To find out whether the interaction between BRCA2 and PLK1 was involved in the control of mitotic progression we examined the functional impact of the variants that reduce PLK1 phosphorylation at T207 (S206C and T207A) in the context of the full-length BRCA2 protein in cells. We generated stable cell lines expressing the BRCA2 cDNA coding for either the GFPMBP-BRCA2 WT or the variants to complement DLD1 BRCA2 deficient human cells (hereafter BRCA2$^{-/-}$) (Supplementary Fig. 4a). First, to confirm that the phosphorylation of T207 by PLK1 takes place in cells we raised a phospho-specific polyclonal antibody against a peptide encompassing pT207. Using an antibody against BRCA2 we detected a band that corresponds to the size of BRCA2 in cell extracts from BRCA2 WT cells, both in mitotic (nocodazole treated) and asynchronous cells, by Western blotting (Fig. 4a). When the same membrane was re-probed with the pT207-BRCA2 antibody a band corresponding to BRCA2 was detected only in the mitotic cells and not in the asynchronous cells (Fig. 4a, lane 1 and 2). In addition, mitotic cell extracts treated with phosphatase lost the signal indicating that the band corresponds to a phosphorylation event (Fig. 4a, lane 3). Finally, cells bearing BRCA2-T207A were detected with the BRCA2 antibody but showed reduced signal for the pT207 antibody (Fig. 4a, lane 4) providing evidence of the specificity of the antibody. We then tested the interaction of full-length BRCA2 with PLK1 in these stable clones by GFP pull-down assay. As expected, PLK1 readily co-purified with full-length BRCA2 WT from mitotic cells. Importantly, in cells expressing the variants S206C and T207A, the level of co-purified PLK1 was greatly reduced (Fig. 4ba, c), confirming the results obtained with the overexpressed BRCA2$_{1-250}$ fragments (Fig. 3a) now in the context of cells stably expressing the full-length BRCA2 protein. Thus, BRCA2 interaction with endogenous PLK1 is impaired in cells bearing variants S206C and T207A.

Also, the binding of BRCA2 to PLK1 in cells stably expressing full-length BRCA2 WT was not reduced by incubating the cells with a PLK inhibitor (BTO) (Supplementary Fig. 4b), consistently with results obtained in vitro (Fig. 3c). Altogether, these data

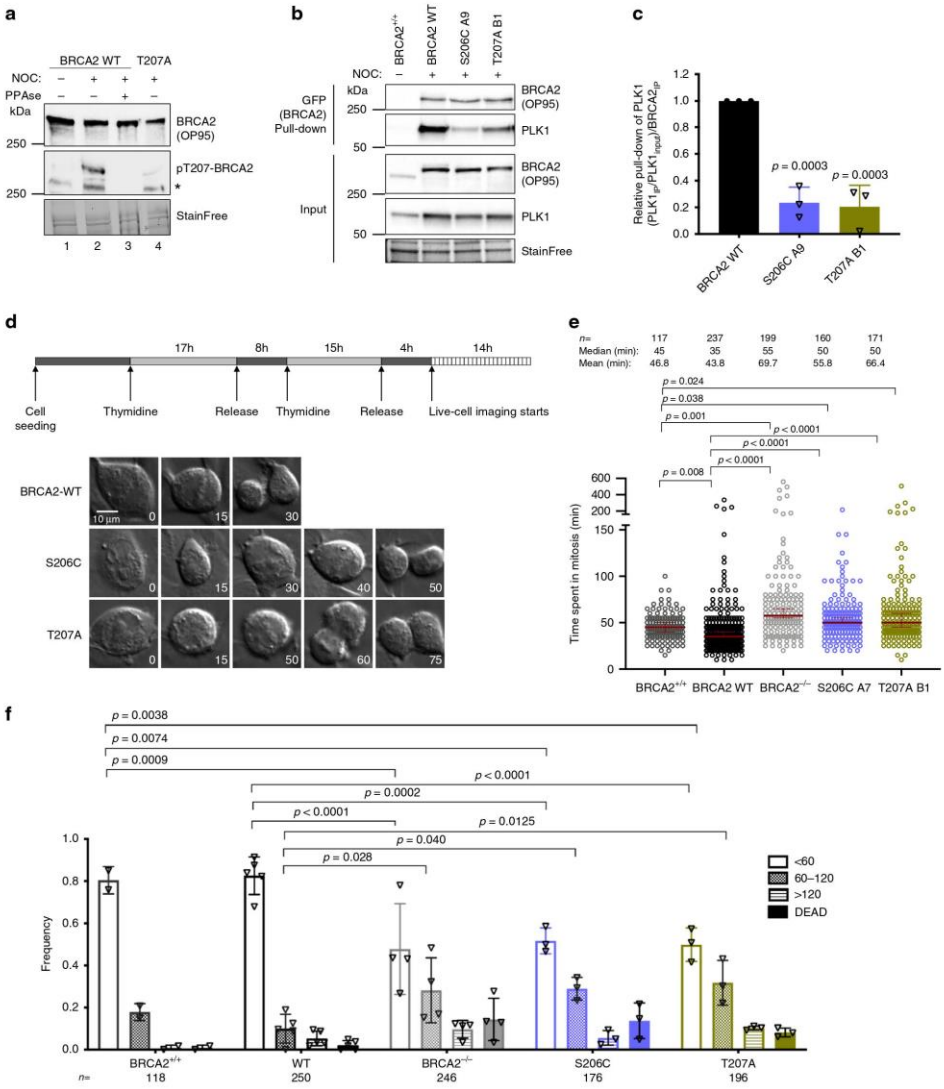

suggest that another binding site primed by a different kinase (presumably T77 phosphorylated by CDK1[29]) contributes to BRCA2 binding to PLK1. Consistent with this idea, the binding of overexpressed 2xMBP-BRCA2$_{1-250}$ to the endogenous PLK1 in U2OS cells was completely abolished in the presence of the CDK inhibitor (RO3306) (Supplementary Fig. 4c, lane 4 compared to lane 2).

Having confirmed that T207 was a docking site for PLK1 in cells, we next examined the impact of BRCA2 variants on mitosis. Therefore, we monitored the time taken for individual cells from mitotic entry (defined as nuclear envelope break down) to mitotic exit using live cell imaging. Cells expressing the endogenous BRCA2 (hereafter BRCA2$^{+/+}$) and the BRCA2 WT cells showed similar kinetics, they completed mitosis, on average, in 47 and 44 min, respectively (Fig. 4d, e) and the majority of the cells (80% for BRCA2$^{+/+}$ and 82% for BRCA2 WT) completed mitosis within 60 min (Fig. 4f). In contrast, cells expressing variants S206C and T207A augmented the time spent in mitosis (average time of 56 and 66 min, respectively, Fig. 4e). This trend was also observed in the frequency of cells dividing within 60 min (~49–51%),

Fig. 4 Cells bearing BRCA2 variants S206C and T207A prolong mitosis. a Protein levels of BRCA2 and pT207-BRCA2 in cells bearing BRCA2 WT or the T207A variant from whole cell lysates of nocodazole-arrested (100 ng/µl for 14 h) or asynchronous cells. 4–15% SDS-PAGE followed by WB using anti-BRCA2. The same blot was stripped and re-probed with anti-pT207-BRCA2 antibody. Lane 3 protein extracts were pre-treated with phosphatase (FastAP) for 1 h before loading onto the gel. Asterisk indicates a non-specific band. (**b**) GFP-trap pull-down of EGFPMBP-BRCA2 from cells bearing BRCA2 WT, S206C or T207A. 4–15% SDS-PAGE followed by WB using anti-BRCA2 and -PLK1 antibodies. Asynchronous DLD1 cells with endogenous BRCA2 ($BRCA2^{+/+}$) were used as control for the pull-down and StainFree images of the gels before transfer as loading control (cropped image is shown). **c** Quantification of co-immunoprecipitated PLK1 with EGFP-MBP-BRCA2 in (**b**) relative to the PLK1 protein levels in the input and the amount of pull-down EGFP-MBP-BRCA2 (($PLK1_{IP}$ /$PLK1_{input}$)/EGFP-MBP-$BRCA2_{IP}$) Results are presented as the fold change compared to the BRCA2 WT clone. The data represent the mean ± SD of three independent experiments. One-way ANOVA test with Dunnett's multiple comparisons test was used to calculate statistical significance of differences (*p*-values compared to WT). **d** Top: Synchronization scheme. Bottom: Representative still images of the time-lapse videos. Numbers represent time (min) after nuclear envelope break down (NEBD). Scale bar represents 10 µm. **e** Quantification of the time the cells spent in mitosis in (**d**). The red line indicates the median (95% CI). Each dot represents a single cell, *n* is the total number of cells from two to four independent experiments (45–60 cells per experiment) ($BRCA2^{+/+}$ ($n = 2$), WT C1 ($n = 5$), $BRCA2^{-/-}$ ($n = 4$), S206C A7 ($n = 3$), T207A B1 ($n = 3$)). Kruskal–Wallis one-way analysis followed by Dunn's multiple comparison test was used to calculate statistical significance of differences. **f** Frequency distribution of the time spent in mitosis in (**d**), including cells that fail to divide (DEAD). The error bars represent mean ± SD of two to four independent experiments ($BRCA2^{+/+}$ ($n = 2$), WT C1 ($n = 5$), $BRCA2^{-/-}$ ($n = 4$), S206C A7 ($n = 3$), T207A B1 ($n = 3$)). Two-way ANOVA test with Tukey's multiple comparisons test was used to calculate statistical significance of differences. Source data are available as a Source Data file.

compared to 82% in BRCA2 WT cells (Fig. 4f). Representative videos of the still images shown in Fig. 4d are included in Supplementary movies 1–3.

Taken together, the phosphorylation of T207 takes place in cells in mitosis. Cells altering this phosphorylation (bearing S206C and T207A variants) display a significant delay in mitotic progression compared to BRCA2 WT cells.

Docking of PLK1 at T207-BRCA2 favors a complex with PP2A and pBUBR1. BRCA2 forms a complex with BUBR1[4,5]. BUBR1 facilitates kinetochore–microtubule attachments via its interaction with the phosphatase PP2A. Phosphorylation of BUBR1 by PLK1 at the KARD motif comprising the tension-sensitive sites S676 and T680 promotes interaction with PP2A[19]. A defect in the phosphorylation of BUBR1 weakens its interaction with PP2A leading to mitotic delay[20,30]. The mitotic delay phenotype we observed in BRCA2 mutated cell lines led us to ask whether BRCA2 and PLK1 formed a tetrameric complex with pBUBR1 and PP2A. Using a GFP pull-down to capture GFP-MBP-BRCA2 from mitotic BRCA2 WT cells, we observed that PLK1, pT680-BUBR1 and PP2A were pull-down together with GFP-MBP-BRCA2, indicating the formation of a tetrameric complex (Fig. 5a). As described for pBUBR1[18,19], PLK1[31] and PP2A[21], we found BRCA2 at the kinetochore in mitotic cells (Supplementary Fig. 5a) as previously reported[4] supporting the idea that this complex takes place at the kinetochore.

Importantly, cells expressing the variants S206C or T207A showed a strong reduction in the interaction of BRCA2 with PLK1, PP2A, BUBR1 and pT680-BUBR1 in the context of the tetrameric complex (Fig. 5a, b). Moreover, the overall levels of BUBR1 and pBUBR1 were also reduced in cells bearing S206C and T207A variants compared to the WT cells, as detected by specific antibodies against BUBR1, pT680-BUBR1 (Fig. 5e–i) and pS676-BUBR1 (Supplementary Fig. 5d), and this was also the case in BRCA2 deficient cells (DLD1 $BRCA2^{-/-}$ cells) or U2OS cells depleted of BRCA2 by siRNA (Fig. 5f, g). Furthermore, we observed an overall reduction in the levels of pBUBR1 at the kinetochore (Fig. 5h, i) in cells expressing T207A compared to WT cells. Consistently, when we immunoprecipitated BUBR1 from mitotic cells and detected the levels of co-immunoprecipitated PP2A (PP2AC antibody), we observed that, although PP2A was readily copurified with BUBR1 in the BRCA2 WT cells, expressing BRCA2 variant T207A reduced the levels of PP2A by ~30% (Fig. 5c, d) suggesting that BRCA2 facilitates the formation of a complex between BUBR1-and PP2A.

Impaired phosphorylation of T207 leads to chromosome misalignment. The association of PLK1-phosphorylated BUBR1 with PP2A is required for the formation of stable kinetochore–microtubule attachments[18,19], a defect in this interaction resulting in chromosome misalignment. Therefore, we next examined whether cells expressing the BRCA2 variants S206C and T207A altered chromosome alignment. Following thymidine synchronization, the cells were treated with the Eg5 inhibitor Monastrol (100 µM) for 14 h followed by Monastrol washout and release for 1 h in normal media supplemented with the proteasome inhibitor MG132 to avoid exit from mitosis[18]. Chromosome alignment was then analyzed by immunofluorescence. Importantly, the analysis of cells expressing S206C and T207A variants showed high frequency of faulty chromosome congression compared to the BRCA2 WT clone (47% in S206C and 38% in T207 versus 24% in the BRCA2 WT clone), which was exacerbated in $BRCA2^{-/-}$ cells (63%) (Fig. 6a, b), as detected by signals of the centromere marker (CREST) outside the metaphase plate (Fig. 6b). Next, to find out if this defect in alignment was due to impaired stability of kinetochore–microtubule interactions as previously reported[6,18], we examined the presence of cold stable microtubules in cells bearing T207A mutation compared to BRCA2 WT cells. Following the same synchronization procedure as before (Fig. 6a), the cells were kept on ice for 15 min before fixation. Under these conditions, BRCA2 WT metaphase cells exhibited relatively intact bipolar spindles with most CREST-stained kinetochores attached to the microtubules (α-tubulin) (Fig. 6c). In stark contrast, almost all the kinetochore–microtubules attachments were lost in T207A mutated cells upon cold treatment (Fig. 6c) as measured by the relative intensity of α-tubulin in these cells with respect to BRCA2 WT cells (~6-fold reduction of the median) (Fig. 6d).

To better understand the mechanism behind the phenotype observed in our clones, we overexpressed a phosphomimic version of BUBR1 RFP-BUBR1-3D (S670D, S676D, T680D) in T207A mutated cells to test whether this form of BUBR1 could restore the misalignment phenotype as previously shown for BUBR1 depleted cells[19]. Surprisingly, T207A bearing cells overexpressing RFP-BUBR1-3D exhibited a similar misalignment phenotype (~38% of cells with misalignment) compared to the non-transfected cells (33%) (Fig. 7a, b). Moreover, BUBR1-3D, previously shown to be sufficient to restore PP2A binding in BUBR1 deficient cells[19], could not rescue the interaction of BUBR1 with PP2A in cells bearing BRCA2 S206C variant (Fig. 7c). This effect was not due to an increased localization of PLK1 at the kinetochore in the mutated cells, as the levels of PLK1 at the kinetochores remained unchanged (Supplementary

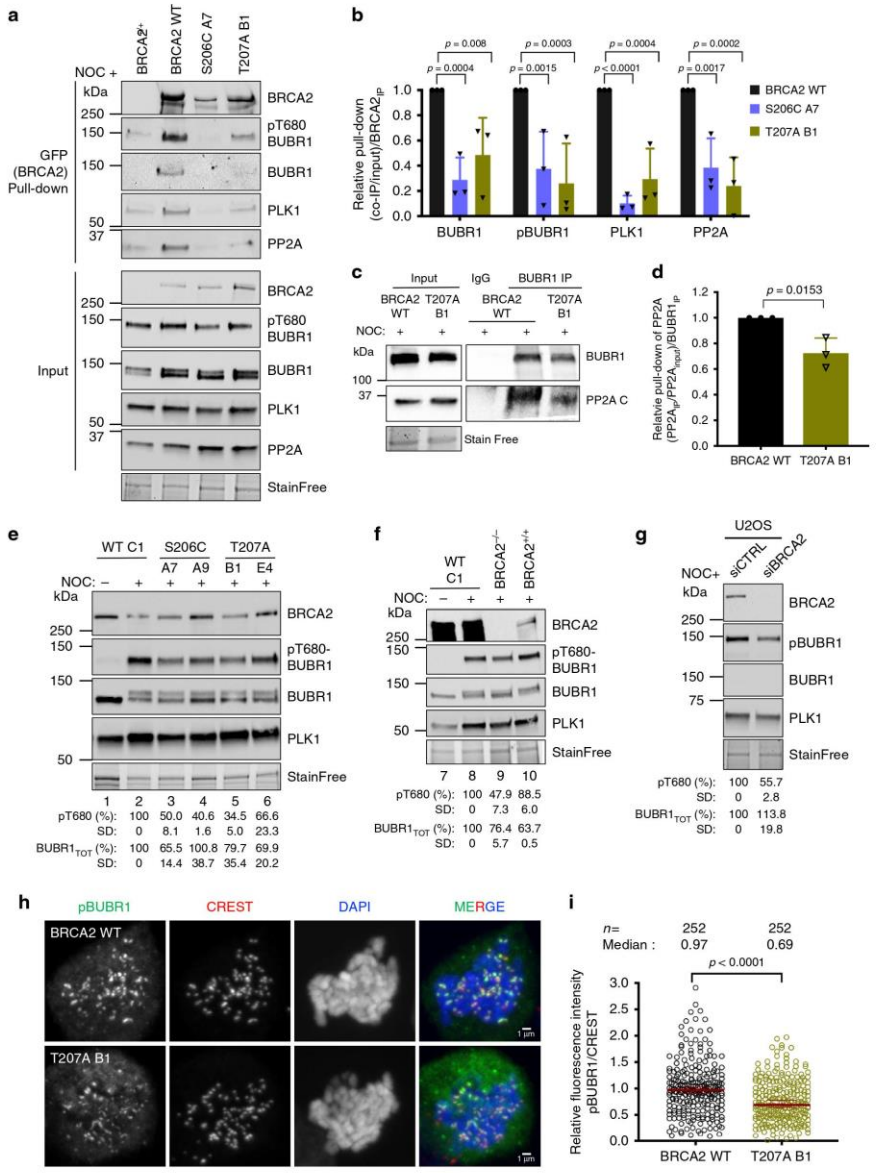

Fig. 6a, b), nor to an increased interaction of PLK1 with BUBR1 in the mutated cells (Supplementary Fig. 6c, d).

Together, these results strongly suggest that docking of PLK1 onto BRCA2 T207 facilitates the formation of a complex between phosphorylated BUBR1 and PP2A at the kinetochore that is essential for the stability of microtubule–kinetochore attachments with direct consequences in chromosome alignment. The fact that BUBR1-3D cannot rescue the phenotype favors the hypothesis that BRCA2 is required for PP2A-BUBR1 interaction.

Reduced T207 phosphorylation lead to defects in chromosome segregation. Unresolved chromosome misalignment as observed in cells altering BRCA2 phosphorylation by PLK1 is expected to drive chromosome missegregation. To find out if this was the case

Fig. 5 S206C and T207A impair the complex of BRCA2 with PLK1-BUBR1-PP2A and reduce the levels of pBUBR1 at the kinetochore. a Pull-down of BRCA2 using GFP-trap beads from mitotic cell extracts of cells bearing BRCA2 WT cells or the variant S206C and T207A. Complexes containing BRCA2-BUBR1/pBUBR1-PP2A-PLK1 were detected by 4–15% SDS-PAGE followed by WB using anti-BRCA2, -BUBR1, -pT680-BUBR1, -PLK1 and -PP2AC (PP2A catalytic subunit) antibodies. Mitotic BRCA2$^{+/+}$ cells were used as control pull-down. **b** Quantification of co-immunoprecipitated BUBR1, pBUBR1, PLK1 and PP2A with EGFPMBP-BRCA2 in (**a**), relative to the input levels of each protein and the amount of pull-down EGFP-MBP-BRCA2. Results are presented as the fold change compared to the BRCA2 WT clone. The data represent the mean ± SD of three independent experiments. Two-way ANOVA test with Dunnett's multiple comparisons test was used to calculate statistical significance of differences. **c** IP of endogenous BUBR1 from mitotic cell extracts of BRCA2 WT cells or BRCA2-T207A using mouse anti-BUBR1 antibody. Mouse IgG was used as control. 4–15% SDS-PAGE followed by WB using rabbit anti-BUBR1 and anti-mouse PP2AC antibodies. **d** Quantification of co-IPed PP2A in (**c**), relative to the input levels and the amount of IPed BUBR1. Results are presented as the fold change compared to the BRCA2 WT clone. The data represent the mean ± SD of three independent experiments. Unpaired two-tailed *t*-test was used to calculate statistical significance of differences. **e**–**g** WB showing the protein levels of endogenous BUBR1 and pT680-BUBR1 in nocodazole treated cells bearing BRCA2 WT or the variants, as indicated (**e**) BRCA2$^{-/-}$ or BRCA2$^{+/+}$ (**f**). **g** WB showing the protein levels of endogenous BUBR1 and pT680-BUBR1 in U2OS after depletion of endogenous BRCA2 by siRNA. **e**–**g** The mean $BUBR1_{TOT}$ and pBUBR1 signal relative to the stain free signal is shown for the nocadozole treated samples below the blots, results are presented as percentage compared to BRCA2 WT clone. The data represent the mean ± SD of three (**e**) and two (**f** and **g**) independent experiments. The protein levels of PLK1 in (**a**, **e**–**g**) are shown as a G2/M marker. **h** Representative images of the localization of pT680-BUBR1 in cells bearing BRCA2 WT or the variant T207A as indicated. CREST is used as centromere marker and DNA is counterstained with DAPI. Scale bar represents 1 µm. **i** Quantification of the co-localization of pT680-BUBR1 and CREST in (**h**). The data represent the intensity ratio (pT680-BUBR1:CREST) relative to the mean ratio of pT680-BUBR1:CREST for the GFP-MBP-BRCA2 WT calculated from two independent experiments (252 pairs of chromosomes analyzed). The red line in the plot indicates the median (95% CI) ratio, each dot represents a pair of chromosomes. Mann–Whitney two-tailed analysis was used to calculate statistical significance of differences. Source data are available as a Source Data file.

in cells expressing BRCA2 variants S206C and T207A, we examined chromosome segregation by immunofluorescence in cells synchronized by double-thymidine block and released for 15 h to enrich the cell population at anaphase/telophase stage (Fig. 7d). BRCA2$^{-/-}$ cells displayed, as expected, an increased proportion of chromosome bridges (39% vs 16% in cells expressing BRCA2 WT), whereas the fraction of lagging chromosomes was only mildly increased (7% vs 4% in BRCA2 WT). The percentage of chromosome bridges in cells expressing S206C and T207A was moderately increased (23% and 29%, respectively, compared to 16% in BRCA2 WT). However, the biggest difference was observed in the percentage of lagging chromosomes increasing between 3- and 5-fold in the cells bearing the variants compared to the BRCA2 WT cells (Fig. 7d, e).

Erroneous chromosome segregation generates aneuploid cells during cell division[30]. Given the strong chromosome segregation defects observed in cells expressing S206C and T207A we next analyzed the number of chromosomes in these cells. Total chromosome counts carried out on metaphase spreads revealed that 37.1% of BRCA2 WT cells exhibited aneuploidy with chromosome losses or gains. In the case of S206C and T207A, this number was elevated to 52.2% and 61.8% of the cells, respectively (Fig. 8a). An example of the images analyzed can be found in Fig. 8b. As the number of chromosomes was difficult to assess for cells with high content of chromosome gains we arbitrarily discarded cells that contained more than 65 chromosomes. Thus, tetraploid cells were not included in this measurement. Therefore, we determined the frequency of tetraploid cells by assessing the incorporation of BrdU and measuring the frequency of S-phase cells with >4 N DNA content (Fig. 8c). The frequency of tetraploidy in cells bearing the variants was <1% of the total population as in the BRCA2 WT cells (Fig. 8d), and the number of BrdU positive cells was also equivalent (Supplementary Fig. 7).

Together, these results indicate that, in addition to the severe chromosome misalignment phenotype, cells expressing S206C and T207A display high frequency of chromosome missegregation, including a strong induction of lagging chromosomes and a mild increase in chromosome bridges. As a consequence, the incidence of aneuploidy, but not tetraploidy, is greatly exacerbated in these cells.

The variants reducing PLK1 phosphorylation of BRCA2 do not alter HR. Since BRCA2 has a major role in DNA repair by HR, the prolonged mitosis observed in the VUS-expressing stable cell lines (Fig. 4) could result from checkpoint activation through unrepaired DNA. Thus, we performed a clonogenic survival assay in the stable clones after treatment with mitomycin C (MMC), an inter-strand crosslinking agent to which BRCA2 deficient cells are highly sensitive[32–35]. As expected, BRCA2 deficient cells (BRCA2$^{-/-}$) showed hypersensitivity to MMC treatment whereas BRCA2 WT cells complemented this phenotype almost to the same levels as the cells expressing the endogenous BRCA2 (BRCA2$^{+/+}$). Cells bearing variants S206C and T207A also complemented the hypersensitive phenotype of BRCA2$^{-/-}$ cells, although there was a mild effect compared to the BRCA2 WT cells (Fig. 9a). These results suggest that the delay in mitosis is not a consequence of checkpoint activation via unrepaired DNA.

Cells expressing VUS S206C and T207A showed a growth defect manifested in a reduced number of colonies (Supplementary Fig. 8a). To exclude a possible bias arising from the different ability to form colonies we used MTT assay. As shown in Fig. 9b, cells expressing S206C and T207A showed similar relative viability upon MMC treatment compared to BRCA2 WT cells or BRCA2$^{+/+}$, confirming our results. Similarly, the viability upon treatment with the poly (ADP-ribose) polymerase inhibitor (PARPi) Olaparib was not affected in cells bearing the variants (Fig. 9c).

To determine directly the levels of spontaneous DNA damage in these cells and their ability to form DNA repair foci, we measured the number of nuclear foci of the DSB marker γH2AX and RAD51 protein, in cells unchallenged (−IR) or 2 h after exposure to ionizing radiation (6 Gy, (+IR)). Our results show that in the absence of DNA damage, the number of γH2AX foci or RAD51 foci is comparable in all cell lines including in cells depleted of BRCA2 (Fig. 9d and Supplementary Fig. 8b); this is probably due to the high genome instability intrinsic to these cancer cells. In contrast, the number of RAD51 foci upon irradiation increased 5-fold in BRCA2$^{+/+}$ and BRCA2 WT cells and 3-fold in T207A bearing cells while it remained low in BRCA2 depleted cells, as expected (Fig. 9e). We conclude that the DNA repair foci are only mildly altered in cells expressing T207A. Representative images of these experiments are shown in Supplementary Fig. 8b.

A typical feature of replication stress is the appearance of micronuclei in daughter cells which generally contain DNA fragments. In contrast, micronuclei with centromeres suggest an event arising from lagging chromosomes involving whole chromosomes or chromatids. BRCA2 deficient cells displayed

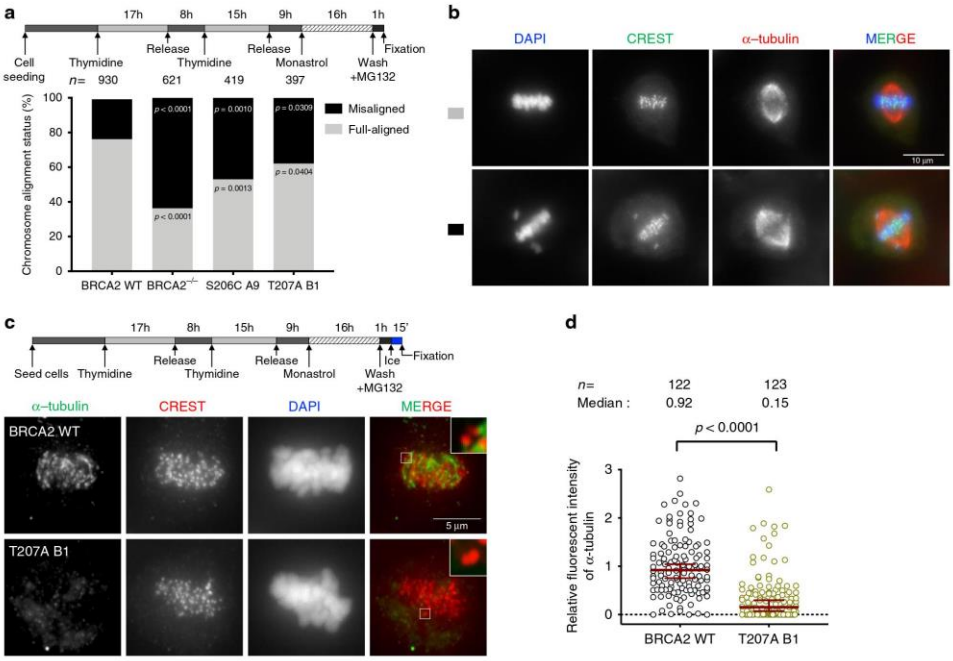

Fig. 6 Cells expressing BRCA2 variants S206C and T207A display reduced stability of kinetochore–microtubule attachments and misaligned chromosomes. **a** Top: Scheme of the double thymidine block procedure used to synchronize the DLD1 cells for the analysis of chromosome alignment. Bottom: Quantification of misaligned chromosomes outside the metaphase plate in DLD1 BRCA2 deficient cells (BRCA2$^{-/-}$) and BRCA2$^{-/-}$ cells stably expressing BRCA2 WT or the S206C and T207A variants. *n* indicates the total number of cells counted for each clone from two (BRCA2$^{-/-}$, S206C, and T207A) and four (BRCA2 WT) independent experiments. Statistical significance of the difference was calculated with unpaired two-way ANOVA test with Tukey's multiple comparisons test, the p-values show the significant differences. **b** Representative images of the type of chromosome alignment observed in cells quantified in (**a**), scale bar represents 10 µm. **c** Top: Scheme of the synchronization procedure for the analysis of cold stable microtubules in the BRCA2-WT and T207A stable clones. Bottom: Representative images of cold stable microtubules in cells expressing BRCA2 WT or the T207A variant. Cells treated according to the scheme were co-stained with α-tubulin and CREST, as centromere marker and DNA was counterstained with DAPI. Scale bar represents 5 µm. A zoom-in inset in the images show representative kinetochore–microtubule attachments in each cell line. **d** Quantification of the relative intensity of α-tubulin normalized to the one in BRCA2 WT cells in (**c**). The data represent the results from two independent experiments from a total of 122 (WT) and 123 (T207A) cells. The red line in the plot indicates the median intensity (95% CI), each dot representing the intensity for one cell. For statistical comparison of the differences between the samples we applied Mann–Whitney two-tailed analysis, the p-values show significant differences. Source data are available as a Source Data file.

an increased number of both types of micronuclei compared to BRCA2 WT cells. In contrast, cells bearing S206C or T207A variant did not change the number of micronuclei (Supplementary Fig. 8d, e) excluding strong replication stress-induced DNA damage in these cells.

Finally, to directly assess the HR proficiency, we performed a cell-based HR assay by DSB-mediated gene targeting using a site-specific transcription-activator like effector nuclease (TALEN) and a promoter-less mCherry donor flanked by homology sequence to the targeted locus[36]. DSB-meditated gene targeting results in mCherry expression from the endogenous promoter (Fig. 9f) which can be measured by flow cytometry (Supplementary Fig. 9). Using this system, BRCA2$^{+/+}$ and BRCA2 WT cells showed ~5% of mCherry positive TALEN-transfected cells (mean of 5.6% for BRCA2$^{+/+}$ and 4.9% for WT) whereas BRCA2$^{-/-}$ exhibited reduced mCherry expressing cells (1.8%), as expected. Importantly, TALEN-transfected cells expressing BRCA2 variants S206C and T207A showed no significant difference with the BRCA2 WT.

In summary, these results indicate that the role of BRCA2 in conjunction with PLK1 in mitosis is likely independent of the HR function of BRCA2 as the variants S206C and T207A affecting PLK1 phosphorylation of BRCA2 are only mildly sensitive to DNA damage, do not show an increased number of micronuclei, are able to recruit RAD51 to DNA damage sites (as shown for T207A) and are efficient at DSB-mediated gene targeting.

Discussion

Our results demonstrate that residues S193 and T207 of BRCA2 can be efficiently phosphorylated by PLK1 (Fig. 2), thus extending the consensus sequence for phosphorylation by this kinase: position 205 is a serine and not a negatively charged residue, as generally observed at PLK1 phosphorylation sites[23]. Moreover, pT207 constitutes a bona fide docking site for PLK1$_{PBD}$ (Fig. 3h–l) that is phosphorylated in mitotic cells (Fig. 4a). Accordingly, *BRCA2* missense VUS reducing the phosphorylation

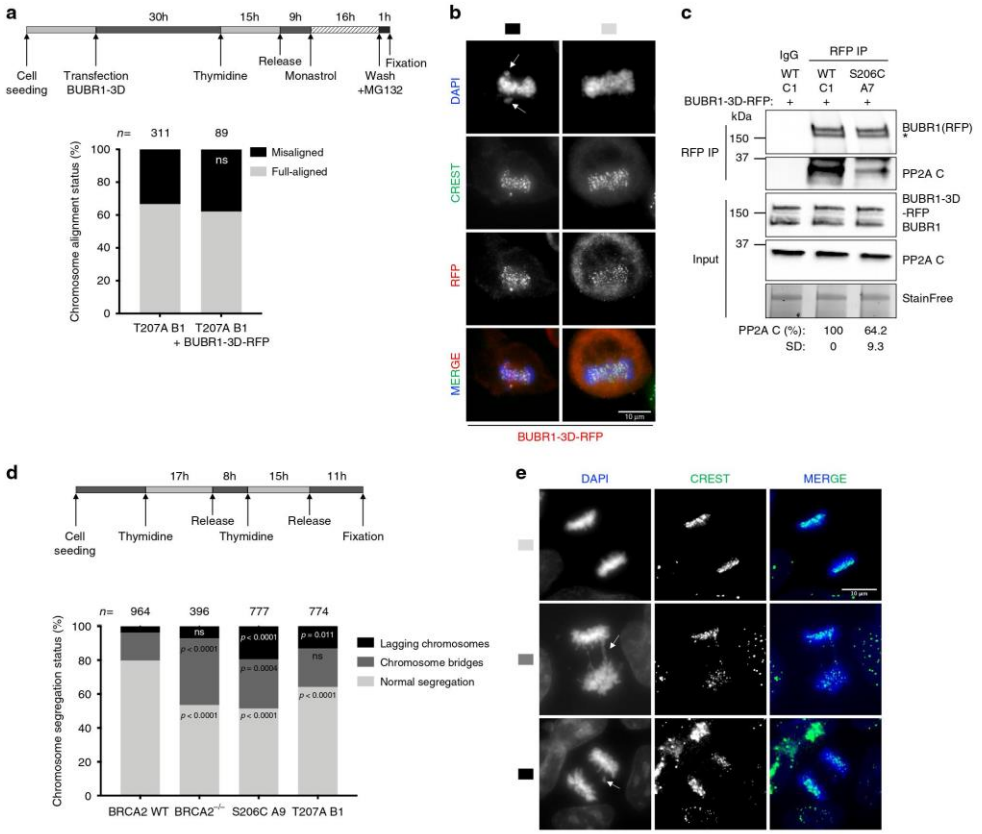

Fig. 7 Cells expressing BRCA2 variants S206C and T207A display aberrant chromosome segregation. a Top: Scheme of the synchronization procedure. Bottom: Quantification of misaligned chromosomes in BRCA2-T207A stable clones transiently overexpressing the 3xFLAG-BUBR1-3D-RFP mutant (S670D, S676D and T680D). *n* indicates the total number of cells counted from two independent experiments. Unpaired two-tailed *t*-test was used to calculate statistical significance of differences, ns (non-significant)). **b** Representative images of the type of chromosome alignment observed in cells overexpressing 3xFLAG-BUBR1-3D-RFP quantified in (**a**); scale bar represents 10 µm. **c** Co-immunoprecipitation of endogenous PP2A with transiently overexpressed 3xFLAG-BUBR1-3D-RFP mutant from mitotic cell extracts of BRCA2 WT cells or cells bearing the S206C variant using rabbit anti-RFP antibody. Rabbit IgG was used as control for the BUBR1 immunoprecipitation. The immunocomplexes were resolved on 4–15% SDS-PAGE followed by WB using mouse anti-BUBR1 and PP2AC antibodies. The amount of PP2A co-immunoprecipitated with BUBR1-3D-RFP relative to the input levels of PP2A and the amount of immunoprecipitated BUBR1-3D-RFP is presented below the blot as mean ± SD from two independent experiments. The data are presented relative to the non-treated BRCA2 WT. Asterisk denotes a non-specific band (**d**). Top: Scheme of the synchronization procedure. Bottom: Quantification of cells with aberrant chromosomes segregation in BRCA2$^{-/-}$ cells and in the clones stably expressing BRCA2 WT, S206C and T207A, as indicated. Two-way ANOVA test with Tukey's multiple comparisons test was used to calculate statistical significance of differences (the *p*-values show the significant differences compared to WT; ns (non-significant)). *n* in (**d**) indicates the total number of cells counted for each clone from two (BRCA2$^{-/-}$, S206C and T207A) and five (BRCA2 WT) independent experiments. **e** Representative images of the type of aberrant chromosome segregation observed in the cells quantified in (**d**), CREST antibody is used as marker of centromere; nuclei are revealed with DAPI counterstaining. Scale bar represents 10 µm. Source data are available as a Source Data file.

status of T207 (T207A, S206C) result in a decrease in BRCA2-PLK1 interaction (Fig. 3a–k, 4b). Cells expressing these two breast cancer variants in a BRCA2 deficient background display defective chromosome congression (Fig. 6a, b) to the metaphase plate due to a reduced microtubule–kinetochore stability (Fig. 6c, d), causing a substantial delay in mitosis progression (Fig. 4d–f).

Proper kinetochore–microtubule attachments require the interaction of BUBR1 with the phosphatase PP2A-B56 to balance Aurora B kinase activity[19,21]. This interaction is mediated through the phosphorylation of the KARD motif of BUBR1 by PLK1. BRCA2 does not alter PLK1 interaction with BUBR1 (Supplementary Fig. 6c, d). However, we found that BRCA2 forms a tetrameric complex with PLK1-pBUBR1-PP2A, and that this complex is strongly reduced in cells bearing BRCA2 variants S206C and T207A (Fig. 5a, b). Furthermore, cells bearing BRCA2 variants S206C and T207A show reduced overall levels of BUBR1

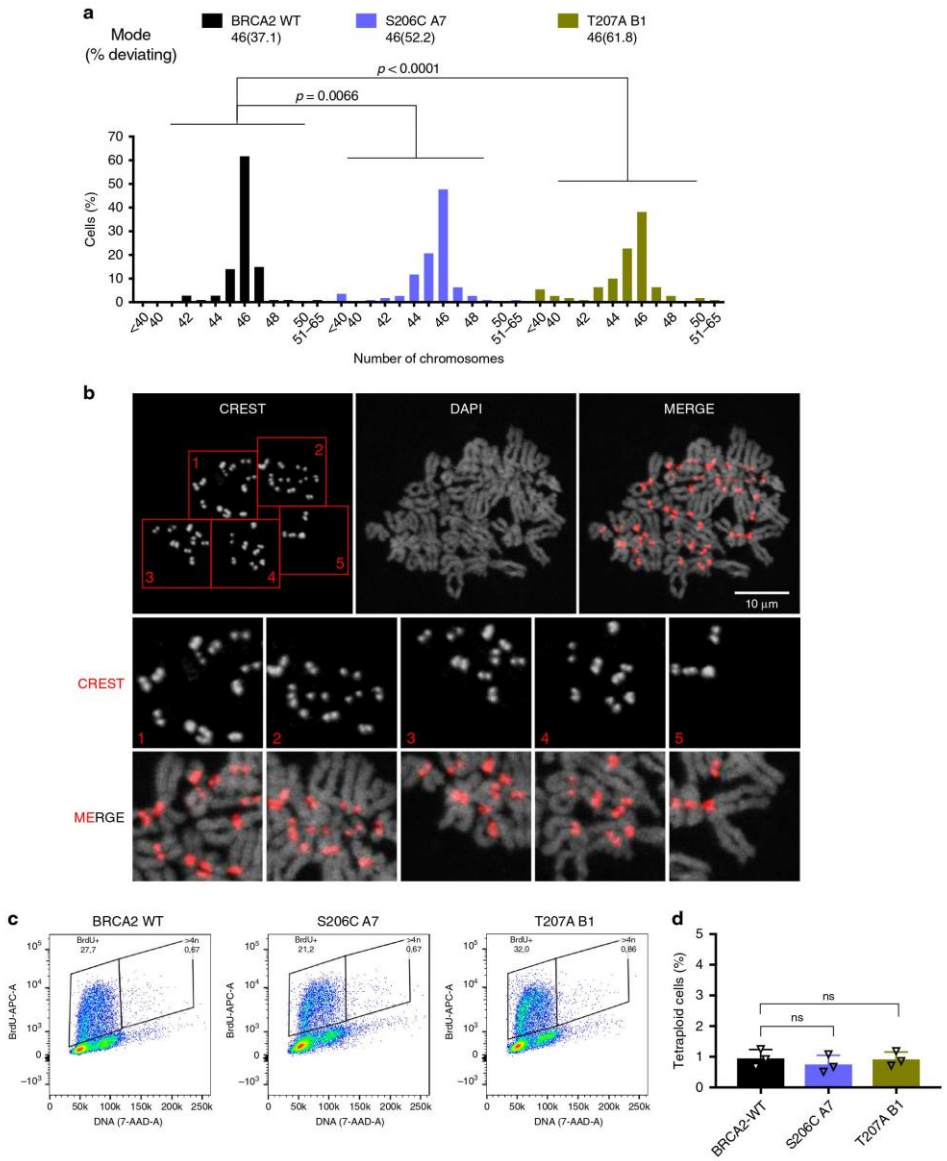

including pBUBR1(pT680) at the kinetochore (Fig. 5i). Importantly, the fact that in the BRCA2 mutated cells the interaction of PP2A with total BUBR1 is reduced (Fig. 5c, d) and that neither this interaction (Fig. 7c) nor the chromosome alignment defect can be rescued by BUBR1-3D overexpression (Fig. 7a, b) strongly suggests that PP2A needs to be in complex with PLK1-bound BRCA2 to bind BUBR1 and facilitate stable kinetochore–microtubules attachment for proper chromosome alignment.

Cells bearing T207A and S206C variants display chromosome segregation errors including lagging chromosomes and chromosome bridges (Fig. 7d, e). Importantly, these accumulated errors ultimately led to a broad spectrum of chromosome gains and losses (aneuploidy) compared to the wild type counterpart (Fig. 8a), but not to tetraploid cells (Fig. 8c, d), suggesting that cytokinesis per se, in which BRCA2 is also involved[11–13], is not affected.

Fig. 8 Cells expressing BRCA2 variants S206C and T207A exhibit aneuploidy. a Distribution of the number of chromosomes observed in metaphase spreads of stable clones expressing BRCA2 WT, S206C A7 or T207 B1, total number of cells counted; BRCA2 WT ($n = 105$), S206C A7 ($n = 111$) and T207A B1 ($n = 110$) from two independent experiments. Modal number of chromosomes and percentage deviating from the mode are shown at the top. Kruskal-Wallis one-way analysis followed by Dunn's multiple comparison test was used to calculate statistical significance of differences. The cell passage was between 5 and 9 (BRCA2 WT (p.6 and p.9), S206C A7 (p.5 and p.9) and T207A B1 (p.6 and p.9). **b** Representative image of two independent experiments of metaphase spreads of the DLD1 BRCA2 deficient stable cells bearing the S206C BRCA2 variant stained with CREST and counterstained with DAPI. In this example, the cell contains 45 chromosomes. **c**–**d** Analysis of S-phase tetraploid cells in cells bearing BRCA2 WT or the VUS S206C and T207A measured by flow cytometry after 20 min of BrdU incorporation. **c** Representative flow cytometry plots of cells stained with anti-BrdU-APC antibodies and 7-AAD (DNA). **d** Frequency of S-phase tetraploid cells in stable clones expressing BRCA2 WT or the VUS S206C and T207A. The data represents the mean ± SD of three independent experiments (cell passage: 6–10). One-way ANOVA test with Tukey's multiple comparisons test was used to calculate statistical significance of differences (the *p*-values show the difference compared to WT, ns: non-significant). Source data are available as a Source Data file.

Finally, the function of BRCA2-PLK1 interaction in mitosis seems to be independent of the HR function of BRCA2 as cells expressing these variants display mild sensitivity to DNA damage (MMC) and PARP inhibitors (Fig. 9a–c), normal recruitment of RAD51 to DNA damage sites (Fig. 9e, Supplementary Fig. 8b), absence of micronuclei (Supplementary Fig. 8d, e), rescue the chromosome bridges phenotype of BRCA2 deficient cells (Fig. 7d) and their HR activity, as measured by a DSB-mediated gene targeting assay (Fig. 9f, Supplementary Fig. 9). Nevertheless, we cannot rule out that the mild phenotype observed in cells bearing S206C and T207A may arise from a disrupted interaction with an unknown DNA repair factor that would bind to the region of BRCA2 where these variants localize.

Putting our results together we reveal an unexpected chromosome stability control mechanism that depends on the phosphorylation of BRCA2 by PLK1 at T207. We show that BRCA2 pT207 is a docking platform for PLK1 that ensures the efficient interaction of BUBR1 with PP2A phosphatase required for chromosome alignment. We propose the following working model (Fig. 9g): in cells expressing BRCA2 WT, PLK1 phosphorylates BRCA2 on T207 leading to the docking of PLK1 at this site. This step promotes the formation of a complex between BRCA2-PLK1-pBUBR1-PP2A in prometaphase at the kinetochore, leading to an enrichment of phosphorylated BUBR1 and the phosphatase PP2A to balance Aurora B activity (Fig. 9g, panel 1). Why is BRCA2 required for PP2A interaction with pBUBR1 and, is this regulated by PLK1? It has been reported that BRCA2 fragment from aa 1001 to aa 1255 ($BRCA2_{1001\text{-}1255}$) comprising a PP2A-B56 binding motif, binds to the B56 subunit of PP2A; in addition, the phosphorylation of positions 2 and 8 of this motif enhances the binding to B56[37]. In BRCA2, these positions are occupied by serines that are targets for PLK1. Therefore, it is likely that the recruitment of PLK1 by BRCA2 T207 would favor phosphorylation of $BRCA2_{1001\text{-}1255}$ and binding of the complex between BRCA2 and PLK1 to PP2A-B56. Non-exclusively, BUBR1 has been reported to bind directly BRCA2 although there are inconsistencies regarding the site of interaction[4,5]. Thus, either the direct interaction of BRCA2 with PP2A or with BUBR1 or both could be favoring the formation of a complex between PP2A and pBUBR1.

In cells expressing the variants that impair T207 phosphorylation (S206C, T207A), PLK1 cannot be recruited to pT207-BRCA2, impairing the formation of the complex with PLK1, PP2A and BUBR1 (Fig. 9g, panel 1′), which in turn reduces the amount of pBUBR1 and its binding to PP2A for stable kinetochore–microtubule interactions. This leads to chromosome misalignment defects that prolong mitosis (Fig. 9g, panel 2′); as a consequence, these cells exhibit increased chromosome segregation errors (Fig. 9g, panel 3′) and aneuploidy.

Although the individual BRCA2 variants analyzed here are rare (Supplementary table 1), the majority of pathogenic mutations recorded to date lead to a truncated protein either not expressed or mislocalized[38] which would be predicted to affect this function. Consistent with this idea, the BRCA2 deficient cells or cells transiently depleted of BRCA2 used in this study exhibit low levels of phosphorylated BUBR1 (Fig. 5f, g). Thus, the chromosome alignment function described here could be responsible, at least in part, for the numerical chromosomal aberrations observed in *BRCA2*-associated tumors[39].

Finally, the lack of sensitivity to the PARP inhibitor Olaparib observed in our cell lines (Fig. 9c) has important clinical implications as breast cancer patients carrying these variants are not predicted to respond to PARP inhibitor treatment (unlike *BRCA2*-mutated tumors that are HR-deficient).

Methods

Cell lines, cell culture, and synchronizations. The human cell lines HEK293T and U2OS cells (kind gift from Dr. Mounira Amor-Gueret) were cultured in DMEM (Eurobio Abcys, Courtaboeuf, France) media containing 25 mM sodium bicarbonate and 2 mM L-Glutamine supplemented with 10% heat inactive FCS (EuroBio Abcys). The BRCA2 deficient colorectal adenocarcinoma cell line DLD1 $BRCA2^{-/-}$ (Hucl, T. et al 2008) (HD 105-007) and the parental cell line DLD1 $BRCA2^{+/+}$ (HD-PAR-008) was purchased from Horizon Discovery (Cambridge, England). In DLD1 $BRCA2^{-/-}$ cell line, both alleles of BRCA2 contain a deletion in exon 11 causing a premature stop codon after BRC5 and cytoplasmic localization of a truncated form of the protein[40]. The cells were cultured in RPMI media containing 25 mM sodium bicarbonate and 2 mM L-Glutamine (EuroBio Abcys) supplemented with 10% heat inactive FCS (EuroBio Abcys). The DLD1 $BRCA2^{-/-}$ cells were maintained in growth media containing 0.1 mg/ml hygromycin B (Thermo Fisher Scientific). The stable cell lines of $DLD1^{-/-}$ BRCA2 deficient cells expressing BRCA2 WT or variants of interest generated in this study were cultured in growth media containing 0.1 mg/ml hygromycin B and 1 mg/ml G418 (Sigma-Aldrich). All cells were cultured at 37 °C with 5% CO_2 in a humidified incubator and all cell lines used in this study have been regularly tested negatively for mycoplasma contamination.

For synchronization of cells in mitosis, nocodazole (100–300 ng/ml, Sigma-Aldrich) was added to the growth media and the cells were cultured for 14 h before harvesting. For synchronization by double thymidine block, the cells were treated with thymidine (2.5 mM, Sigma-Aldrich) for 17 h, released for 8 h followed by a second thymidine (2.5 mM) treatment for 15 h.

Plasmids. 2XMBP-, human 2XMBP-$BRCA2_{1-250}$ and EGFP-MBP-BRCA2 subcloning in phCMV1 expression vector were generated as described[41–48]. In the case of 2XMBP and 2XMBP-$BRCA2_{1-250}$, a tandem of 2 nuclear localization signals from RAD51 sequence was added downstream the MBP-tag.

Point mutations (M192T, S193A, S196N, S206C, and T207A) were introduced in the 2xMBP-$BRCA2_{1-250}$, EGFP-MBP-BRCA2 vector using QuikChange II and QuikChange XL site-directed mutagenesis kit (Agilent Technologies), respectively (see Supplementary Tables 3, 4 for primer sequences).

For expression of $BRCA2_{48-218}$ in bacteria, an optimized gene coding for human His-tagged $BRCA2_{48-218}$ (WT and T207A) was synthetized by Genscript and cloned in a pETM13 vector (a TEV site being present between the tag and the BRCA2 fragment). For expression of $BRCA2_{190-284}$ in bacteria, the human $BRCA2_{190-284}$ was amplified by PCR using full-length BRCA2 as template (phCMV1-2xMBP-BRCA2, see Supplementary Table 5 for primer sequences). The PCR product was purified and digested with *BamH1* and *SalI* and cloned into in the pGEX-6P-1 vector (GE Healthcare) to generate GST-$BRCA2_{190-284}$. The point mutation T207A was introduced in the same way in $BRCA2_{190-284}$ as in 2xMBP-$BRCA2_{1-250}$ and the EGFP-MBP-BRCA2. The introduction of the point mutation was verified by sequencing (see Supplementary Tables 3, 4 for primer sequences).

The *PLK1* cDNA (Addgene pTK24) was cloned into the pFast-Bac HT vector using Gibson assembly (NEB) (see Supplementary Table 6 for primer sequences).

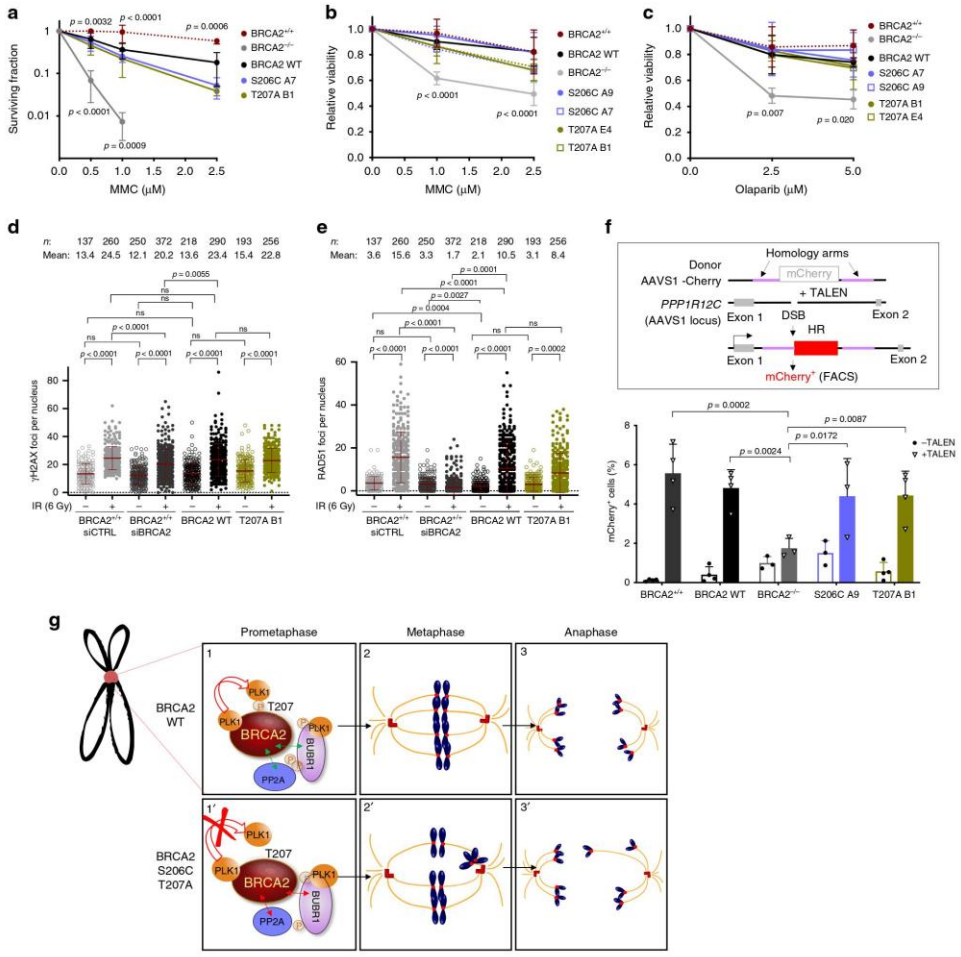

Fig. 9 The DNA repair proficiency is not affected in cells bearing BRCA2 variants S206C and T207A. a Quantification of the surviving fraction of BRCA2$^{+/+}$ or stable clones expressing BRCA2 WT or the variants S206C or T207A assessed by clonogenic survival upon exposure to MMC at concentrations: 0, 0.5, 1.0, and 2.5 μM. Data are represented as mean ± SD: BRCA2$^{+/+}$ (red) ($n = 3$), BRCA2$^{-/-}$ (gray) ($n = 6$), WT C1 (black) ($n = 6$), S206C A7 (blue) ($n = 3$), T207A B1 (green) ($n = 4$). **b**–**c** Quantification of the relative cell viability monitored by MTT assay upon treatment with increasing doses of MMC (**b**) or the PARP inhibitor Olaparib (**c**), as indicated. The data represent the mean ± SD of four (**b**) and three (**c**) independent experiments. **a**–**c** Two-way ANOVA test with Tukey's multiple comparisons test was used to calculate statistical significance of differences (the *p*-values show the significant differences compared to the BRCA2 WT clone). **d**–**e** Quantification of the number of γH2AX foci (**d**) or RAD51 foci per nucleus (**e**) 2 h after 6 Gy of γ-irradiation (+IR) versus non-irradiated conditions (−IR), in DLD1 BRCA2$^{+/+}$ cells depleted of BRCA2 (siBRCA2) or control cells (siCTRL) or cells bearing BRCA2 WT or the variant T207A. *n* indicates the total number of cells counted from two independent experiments. Kruskal-Wallis one-way analysis followed by Dunn's multiple comparison test was used to calculate statistical significance of differences. The red line in the plot indicates the mean ± SD, each dot represents a single focus. **f** Top: Scheme of the DSB-mediated gene targeting HR assay. Bottom: Frequency of mCherry positive cells in cells transfected with the promoter-less donor plasmid (AAVS1-2A-mCherry) without (−TALEN) or with (+TALEN) nucleases. The error bars represent mean ± SD of three to four independent experiments (BRCA2$^{+/+}$ ($n = 4$), WT ($n = 4$), BRCA2$^{-/-}$ ($n = 3$), S206C A9 ($n = 3$), T207A B1 ($n = 4$)). Two-way ANOVA test with Tukey's multiple comparisons test. **g** Model for the role of PLK1 phosphorylation of BRCA2 T207A by PLK1 in mitosis (see text for details). In panel 1 and 1′ the two-sided arrows represent a complex between the two proteins as indicated either favored by BRCA2 WT (green) or impaired in the BRCA2 mutated form (red); in panels 2, 2′, 3 and 3′ blue blobs represent chromosomes, red circles represent the kinetochores, red cylinders represent the centrioles and orange lanes represent the spindle microtubules. Source data are available as a Source Data file.

To produce PLK1-KD, the point mutation K82R was introduced in the pFast-Bac HT-PLK1 vector using QuikChange XL site-directed mutagenesis kit (see Supplementary Table 7 for primer sequences).

The Polo-like binding domain (PBD) of PLK1 (amino acid 326 to amino acid 603) was amplified from the pTK24 plasmid (Addgene) and cloned into a pT7-His6-SUMO expression vector using NEB Gibson assembly (Gibson Assembly Master Mix, New England BioLabs, Cat. #E2611S) (see Supplementary Table 7 for primer sequences). A plasmid containing a smaller PLK1 PBD fragment (amino acid 365 to amino acid 603) with a N-terminal GST tag was a kind gift from Dr. Anne Houdusse (Institute Curie, Paris).

To produce the phosphomimic BUBR1 mutant, we introduced the S670D, S676D and T680D point mutations in the pcDNA3-3xFLAG-BUBR1-RFP construct (kind gift from Dr. Geert JPL Kops) using QuikChange XL site-directed mutagenesis kit (see Supplementary Table 8 for primer sequences).

For the DSB-gene targeting assay, we replaced the GFP tag in the promoter-less AAVS1-2A-GFP-pA plasmid (kind gift from Dr. Carine Giovannangeli) with the mCherry tag from the pET28 mCherry plasmid using NEB Gibson Assembly (Gibson Assembly Master Mix, New England BioLabs, Cat. #E2611S). See Supplementary Table 11 for primer sequences.

Expression and purification of 2xMBP-BRCA2$_{1\text{-}250}$. The 2xMBP-BRCA2$_{1\text{-}250}$ was purified as previously described[49]. Briefly, ten 150 mm plates of HEK293T were transient transfected with the 2xMBP-BRCA2$_{1\text{-}250}$ using TurboFect (Thermo Fisher Scientific). The cells were harvested 30 h post-transfection, lysed in lysis buffer H (50 mM HEPES (pH 7.5), 250 mM NaCl, 1% NP-40, 5 mM EDTA, 1 mM DTT, 1 mM PMSF and EDTA-free Protease Inhibitor Cocktail (Roche)) and incubated with amylose resin (NEB) for 3 h at 4 °C. The 2xMBP-BRCA2$_{1\text{-}250}$ was eluted with 10 mM maltose. The eluate was further purified with Bio-Rex 70 cation-exchange resin (Bio-Rad) by NaCl step elution. The size and purity of the final fractions were analyzed by SDS-PAGE and western blotting using anti-MBP antibody. The 2xMBP-BRCA2$_{1\text{-}250}$ fragments containing the BRCA2 variants (M192T, S193A, S196N, S206C, and T207A) were purified following the same protocol as for WT 2xMBP-BRCA2$_{1\text{-}250}$.

Expression and purification of BRCA2$_{48\text{-}218}$ and BRCA2$_{190\text{-}284}$ for NMR. Recombinant ^{15}N-labeled (WT, T207A) and ^{15}N/^{13}C-labeled (WT) BRCA2$_{48\text{-}218}$were produced by transforming *Escherichia coli* BL21 (DE3) Star cells with the pETM13 vector containing human BRCA2$_{48\text{–}218}$ (WT and T207A). Recombinant ^{15}N-labeled (WT, T207A) and ^{15}N/^{13}C-labeled (WT, T207A) BRCA2$_{190\text{–}284}$ were produced by transforming *Escherichia coli* BL21 (DE3) Star cells with the pGEX-6P-1 vector containing human BRCA2$_{190\text{–}284}$ (WT and T207). Cells were grown in a M9 medium containing 0.5 g/l $^{15}NH_4Cl$ and 2 g/l ^{13}C-glucose when ^{13}C labeling was needed. The bacterial culture was induced with 1 mM IPTG at an OD_{600} of 0.8, and it was further incubated for 3 h at 37 °C. Harvested cells were resuspended in buffer A (50 mM Tris-HCl pH 8.0, 150 mM NaCl, 2 mM DTT, 1 mM EDTA) with 1 mM PMSF and 1X protease inhibitors cocktail (Roche) and disrupted by sonication. For BRCA2$_{48\text{-}218}$, clarified cell lysate was loaded onto Ni-NTA beads (Thermo Scientific) equilibrated with buffer A. After 1 h of incubation at 4 °C, beads were washed with buffer A containing 20 mM imidazole and eluted with buffer A containing 500 mM imidazole. The tag was cleaved by the TEV protease during a 2 hrs dialysis at 4 °C against 50 mM Tris-HCl pH 8.0, 150 mM NaCl, 1 mM EDTA 2 mM DTT. The sample was then boiled 10 min at 95 °C, spun down 5 min at 16,000 *xg* to remove thermosensitive contaminants and injected on Superdex 75 pg (GE Healthcare) equilibrated with 50 mM HEPES 1 mM EDTA pH 7.0. Sample concentration was calculated using its estimated molecular extinction coefficient of 9970 M^{-1} cm^{-1} at 280 nm. The protein sample was characterized for folding using NMR HSQC spectra, before and after the heating at 95 °C.

For BRCA2$_{190\text{–}284}$, clarified cell lysate was loaded onto Glutathione (GSH) Sepharose beads (GE Healthcare) equilibrated with buffer A. After 2 h of incubation at 4 °C, beads were washed with buffer A and eluted with buffer A containing 20 mM reduced glutathione. The tag was cleaved by the precision protease during an overnight dialysis at 4 °C against buffer B (50 mM HEPES pH 7.0, 1 mM EDTA) with 2 mM DTT and 150 mM NaCl. The cleaved GST-tag was removed by heating the sample for 15 min at 95 °C and spun it down for 10 min at 16,000*g*. Sample concentration was calculated using its estimated molecular extinction coefficient of 10,363 M^{-1} cm^{-1} at 280 nm. The protein sample was characterized for folding using NMR HSQC spectra, before and after the heating at 95 °C. BRCA2$_{190\text{–}284}$ was dialyzed overnight at 4 °C against buffer B with 2 mM DTT.

Expression and purification of PLK1 and PLK1-kinase dead (PLK1-KD). The recombinant 6xHis-PLK1 and 6xHis-PLK1-K82R mutant (PLK1-KD) were produced in sf9 insect cells by infection for 48 h (28 °C, 110 rpm shaking) with the recombinant baculovirus (PLK1-pFast-Bac HT vector). Infected cells were collected by centrifugation (1300 rpm, 10 min, 4 °C), washed with 1xPBS, resuspended in lysis buffer (1xPBS, 350 mM NaCl, 1% Triton X-100, 10% glycerol, EDTA-free Protease Inhibitor Cocktail (Roche), 30 mM imidazole). After 1 h rotation at 4 °C the lysate was centrifuged (25,000 rpm, 1 h, 4 °C) and the supernatant was collected, filtered (0.4 µm) and loaded immediately onto a Ni-NTA column (Macherey Nagel) equilibrated with Buffer A1 (1xPBS with 350 mM NaCl, 10% glycerol and 30 mM imidazole, the column was washed with buffer A2 (1xPBS with 10% glycerol) and the protein was eluted with Buffer B1 (1x PBS with 10% glycerol and 250 mM imidazole). The eluted protein was diluted to 50 mM NaCl with Buffer A before being loaded onto a cationic exchange Capto S column (GE Healthcare) equilibrated with Buffer A1cex (50 mM HEPES (pH 7.4), 50 mM NaCl and 10% glycerol), the column was washed with Buffer A1cex before elution with Buffer B1cex (50 mM HEPES (pH 7.4), 2 M NaCl and 10% glycerol). The quality of the purified protein was analyzed by SDS-PAGE and the proteins concentration was determined using Bradford protocol with BSA as standard. The purest fractions were pooled and dialyzed against storage buffer (50 mM Tris-HCl (pH7.5), 150 mM NaCl, 0.25 mM DTT, 0.1 mM EDTA, 0.1 mM EGTA, 0.1 mM PMSF and 25% Glycerol) and stored in -80 °C. The purified proteins can be seen in Supplementary Fig. 10.

Expression and purification of PLK1$_{PBD}$. The pT7-6His-Sumo-PLK1 PBD (326-603) plasmid was expressed in Tuner pLacI pRare cells (Protein Expression and Purification Core Facility, Institut Curie), 2 L of TB medium with Kanamycin and Chloramphenicol antibiotics were inoculated with cells from the pre-culture. The cells were grown at 37 °C until an OD_{600} of ~0.85. The temperature was decreased to 20 °C and the expression was induced by 1 mM IPTG overnight. The cells were harvested by 15 min of centrifugation at 4690*g*, at 4 °C. The cell pellets were suspended in 80 ml of 1 x PBS, pH 7.4, 150 mM NaCl, 10% glycerol, EDTA-free Protease Inhibitor Cocktail (Roche), 5 mM β-mercapto-ethanol (β-ME). The suspension was treated with benzonase nuclease and $MgCl_2$ at 1 mM final concentration for 20 min at 4 °C. The suspension was lysed by disintegration at 2 kbar (Cell disruptor T75, Cell D) followed by centrifugation at 43,000*g*, for 45 min, at 4 °C. The supernatant was loaded at 1 ml/min on a His-Trap FF-crude 5 mL column (GE Healthcare) equilibrated with PBS buffer, pH 7.4, 150 mM NaCl, 10% glycerol, 5 mM β-ME (A) and 20 mM imidazole. The proteins were eluted in a linear gradient from 0 to 100% with the same buffer (A) containing 200 mM imidazole, over 10 column volumes (CV). The purest fractions were pooled and dialyzed (8 kDa cut-off) against 20 mM Tris-HCl buffer, pH 8.0, 100 mM NaCl, 0.5 mM EDTA, 5 mM β-ME, 10% glycerol at 4 °C. 6xHis-SUMO Protease (Protein Expression and Purification Core Facility, Institut Curie) was added at 1/100 (w/w) and incubated overnight at 4 °C to cleave the 6His-SUMO tag. The cleaved PBD-PLK1 was purified using Ni-NTA agarose resin (Macherey Nagel), washed with the following buffer: 20 mM Tris-HCl pH 8.0, 100 mM NaCl, 0.5 mM EDTA, 5 mM β-ME and 10% glycerol. The sample was incubated with the resin for 1 h at 4 °C and the flow-through was collected. The sample was concentrated on an Amicon Ultra Centrifugal Filter Unit (10 kDa cut-off) and injected at 0.5 ml/min on a Hi-Load 16/60 Superdex column (GE healthcare), equilibrated with 20 mM Tris-HCl buffer, pH 8.0, 100 mM NaCl, 0.5 mM EDTA, 5 mM β-ME. The protein concentration was estimated by spectrophotometric measurement of absorbance at 280 nm. The purified protein is shown in Supplementary Fig. 10.

The GST-tagged PLK1$_{PBD}$ (365–603) was expressed in *E. coli* BL21 (DE3) STAR cells, induced with 0.5 mM IPTG at an OD_{600} of 0.6, and grown at 37 °C for 3 h. The PBD (365-603) was purified by glutathione affinity chromatography. After GST cleavage (using a 6His-TEV protease), the tag and the protease were retained using GST- and NiNTA-agarose affinity chromatography, and the PBD collected in the flow-through was further purified by gel filtration chromatography. The protein was dialyzed against a buffer containing 50 mM Tris-HCl pH 8, NaCl 150 mM, and 5 mM β-ME.

In vitro PLK1 kinase assay. 0.5 µg purified 2xMBP-BRCA2$_{1\text{-}250}$ or 25 ng RAD51 protein, was incubated with recombinant active PLK1 (0, 50 or 100 ng) or PLK1-kinase dead (100 ng) (purchased from Abcam or purified from sf9 insect cells as detailed above, see Figure EV11B for the comparison of the kinase activity of both PLK1 preparations) in kinase buffer (25 mM HEPES, pH 7.6, 25 mM ß-glycerophosphate, 10 mM $MgCl_2$, 2 mM EDTA, 2 mM EGTA, 1 mM DTT, 1 mM Na_3VO_4, 10 µM ATP and 1 µCi [γ^{32}P] ATP (Perkin Elmer)) in a 25 µl total reaction volume. After 30 min incubation at 30 °C the reaction was stopped by heating at 95 °C for 5 min in SDS-PAGE sample loading buffer. The samples were resolved by 7.5% SDS-PAGE and [γ^{32}P] ATP labeled bands were analyzed with PhosphorImager (Amersham Bioscience) using the ImageQuant™ TL software (GE Healthcare Life Science). To control for the amount of substrate in the kinase reaction, before adding [γ^{32}P] ATP, half of the reaction was loaded on a 7.5% stain free SDS-PAGE gel (BioRad), the protein bands were visualized with ChemiDoc XRS + System (BioRad) and quantified by the Image Lab™ 5.2.1 Software (BioRad). The relative phosphorylation of 2xMBP-BRCA2$_{1\text{-}250}$ was quantified as ^{32}P-labeled 2xMBP-BRCA2$_{1\text{-}250}$ (ImageQuant™ TL software) divided by the intensity of the 2xMBP-BRCA2$_{1\text{-}250}$ band in the SDS-PAGE gel (Image Lab™ 5.2.1 Software). In the control experiment where PLK1 inhibitor was used, 50 nM BI2536 (Selleck Chemicals) was added to the kinase buffer.

In vitro protein binding assay. To assess the interaction between recombinant PLK1 and BRCA2$_{1\text{-}250}$ after phosphorylation by PLK1, a kinase assay was performed with 0.2 µg recombinant PLK1 or PLK1-kinase dead (PLK1-KD) and 0.5 µg purified 2xMBP-BRCA2$_{1\text{-}250}$ (WT or the VUS T207) in kinase buffer supplemented

with 250 µM ATP (no [γ^{32}P] ATP) in a total reaction volume of 20 µl, one control reaction without ATP was performed with PLK1 and 2xMBP-BRCA2$_{1-250}$ WT. After 30 min incubation at 30 °C, 15 µl amylose beads was added to the reaction and incubated for 1 h at 4 °C. The beads were centrifuged at 2000*g* for 2 min at 4 °C and the unbound fraction was collected before the beads were washed three time in kinase buffer (no ATP) containing 0.5% NP-40 and 0.1% Triton X-100. Bound proteins were eluted from the beads with 10 mM maltose, protein complexes were separated by SDS-PAGE and analyzed by western blotting. To control for the amount of proteins in the reaction, 2 µl of the kinase reaction (before adding the amylose beads) was loaded as input. The protein bands were visualized with ChemiDoc XRS + System (BioRad) and quantified by the Image Lab™ 5.2.1 Software (BioRad). The relative pull-down of PLK1 was quantified as the intensity of the PLK1 band in the pull-down divided by the intensity of the PLK1 band in the input (ImageQuant™ TL software).

To discard possible remaining phosphorylation of the 2xMBP-BRCA2$_{1-250}$ fragment coming from the purification of the protein from HEK293T cells, the 2xMBP-BRCA2$_{1-250}$ fragment (WT or the variant T207) was incubated with kinase buffer (no added ATP) supplemented with FastAP Thermosensitive Alkaline Phosphatase (Thermo Fisher Scientific Cat. #EF0654) for 1 h at 37 °C before addition of recombinant PLK1 followed by 30 min incubation at 30 °C and 1 h incubation with amylose beads as described above.

NMR spectroscopy. NMR experiments were carried out at 283 K on 600 and 700 MHz Bruker spectrometers equipped with a triple resonance cryoprobe. For NMR signal assignments, standard 3D triple resonance NMR experiments were recorded on ^{15}N and ^{13}C labeled samples of BRCA2$_{48-218}$ WT and BRCA2$_{190-284}$ WT and T207A. Analyses of these experiments provided backbone resonance assignment for the non-phosphorylated and phosphorylated forms of these BRCA2 fragments. To follow the PLK1 phosphorylation kinetics, the ^{15}N labeled fragment BRCA2$_{48-218}$ (50 µM) was mixed to a first PLK1 sample at 0.1 µM and the ^{15}N labeled fragment BRCA2$_{190-284}$ (200 µM) was mixed to another PLK1 sample at 1.1 µM. The mixes were incubated at pH 7.8 and 298 K. For each time point, a 140 µl sample was heated during 10 min at 368 K to inactivate PLK1, D_2O was added, the pH was adjusted to 7.0 and a ^{1}H-^{15}N SOFAST-HSQC experiment [51] was recorded. The HSQC experiments were performed using 2048 ×256 time-points, 64 scans and an interscan delay of 80 ms. Data processing and analysis were carried out using the Topspin and CcpNmr Analysis 2.4.2 softwares.

Analysis of phosphorylation assays followed by NMR. In the HSQC spectra, the intensity of peaks of the phosphorylated residues pS193 and pT207, as well as the intensity of peaks corresponding to their non-phosphorylated form was retrieved at each time point of the kinetics. In order to estimate the fraction of phosphorylation for each residue at each point, the function $\text{Intensity}_{(\text{phospho})} = f[\text{Intensity}_{(\text{non-phospho})}]$ was drawn for each residue, the trendline was extrapolated to determine the intensity corresponding to the 100% phosphorylated residue and then the percentage of phosphorylation could be calculated at each time point by dividing peak intensities corresponding to the phosphorylated residue by the calculated intensity at 100% phosphorylation. Peaks corresponding to residues closed to a phosphorylated residue (L209 and V211 for pT207; D191, S197, and S195 for pS193) and thus affected by this phosphorylation were also treated using the same protocol and they were used to obtain a final averaged curve of the evolution of the percentage of phosphorylation at positions 193, 207 with time.

Isothermal titration calorimetry. ITC measurements were performed with the PLK1 PBD protein (amino acid 326 to amino acid 603) and BRCA2 peptides in 50 mM Tris-HCl buffer, pH 8.0 containing 150 mM NaCl and 5 mM β-ME, using a VP-ITC instrument (Malvern), at 293 K. We used automatic injections of 8 or 10 µl. The titration data were analyzed using the program Origin 7.0 (OriginLab) and fitted to a one-site binding model. To evaluate the heat of dilution, control experiments were done with peptide or protein solutions injected into the buffer. The peptides used for the ITC experiments were synthesized by GeneCust (Ellange, LU) or Genscript (Piscataway, NY). The peptides were acetylated and amidated at the N-terminal and C-terminal ends, respectively (see Supplementary Table 9 for peptide sequences). Only peptide BRCA2$_{190-284}$ was expressed in bacteria and purified as detailed above (see "Expression and purification of BRCA2$_{190-284}$ for NMR" section).

Crystallization and structure determination. The purified PBD protein (amino acid 365 to amino acid 603) was concentrated to 6 mg/ml, and mixed to the ^{194}WSSSLATPPTLSS{pT}VLI^{210} (pT207) BRCA2 peptide at a 3:1 molar ratio. The crystals were obtained by hanging drop vapor diffusion method at room temperature (293 K), by mixing 1 µl of complex with 1 µl of solution containing 10% PEG 3350, 100 mM BisTris pH 6.5, and 5 mM DTT. Diffraction data were collected at the Proxima 1 beamline (SOLEIL synchrotron, Gif-sur-Yvette, France). The dataset was indexed and integrated using XDS through the autoPROC package[52]. The software performs an anisotropic cut-off (Tickle et al., STARANISO (2018) Global Phasing Ltd.) of merged intensity data, a Bayesian estimation of the structure amplitudes, and applies an anisotropic correction to the data. The structure was solved by molecular replacement using PHENIX (Phaser) software[53]. Two molecules of PBD were consecutively positioned. Electron density for the peptide was clearly visible in the position previously reported in other PBD structures in complex with phosphorylated peptides (PDB 4O56 or 3P35). Refinement was performed using BUSTER[54] and PHENIX[55]. The model was built with Coot[56]. A summary of crystallographic statistics is shown in Supplementary Table 2. The figures were prepared using Pymol v.1.7.4.0 (Schrödinger, LLC).

Generation of stable DLD1 clones. For generation of DLD1 BRCA2$^{-/-}$ cell lines stably expressing human BRCA2 variants of interest, we transfected one 100 mm plate of DLD1 BRCA2$^{-/-}$ cells at 70% of confluence with 10 µg of a plasmid containing human EGFP-MBP-tagged BRCA2 cDNA (corresponding to accession number NM_000059) using TurboFect (Thermo Fisher Scientific), 48 h post-transfection the cells were serial diluted and cultured in media containing 1 mg/ml G418 (Sigma-Aldrich) for selection. Single cells were isolated and expanded. To verify and select the clones, cells were resuspended in cold lysis buffer H (50 mM HEPES (pH 7.5), 250 mM NaCl, 1% NP-40, 5 mM EDTA, 1 mM DTT, 1 mM PMSF and EDTA-free Protease Inhibitor Cocktail (Roche)), incubated on ice for 30 min, sonicated and centrifuged at 10,000*g* for 15 min, 100 µg total protein lysate was run on a 4–15% SDS-PAGE followed by immunoblotting using BRCA2 and GFP antibodies to detect EGFP-MBP-BRCA2. Clones with similar expression levels were selected for functional studies.

The presence of the point mutations in the genome of the clones was confirmed by extraction of genomic DNA using Quick-DNA™ Universal Kit (ZYMO Research) followed by amplification of the N-terminal of BRCA2 (aa 1-267) by PCR using a forward primers that binds to the end of MBP and a reverse primer that binds to amino acid 267 in BRCA2, the presence of the point mutations was confirmed by sequencing of the PCR product (see Supplementary Table 4 and 10 for primer sequences).

Cell extracts, immunoprecipitation and western blotting. For the interaction between BRCA2$_{1-250}$ and endogenous PLK1, U2OS cells were transfected with 2xMBP-BRCA2$_{1-250}$ construct (WT, M192T, S193A, S196N, T200K, S206C, and T207A) using TurboFect (Thermo Fisher Scientific), 30 h post-transfection cells were synchronized by nocodazole (300 ng/ml), harvested and lysed in extraction buffer A (20 mM HEPES (pH 7.5), 150 mM NaCl, 0.1% NP40, 2 mM EGTA, 1.5 mM $MgCl_2$, 50 mM NaF, 10% glycerol, 1 mM Na_3VO_4, 20 mM ß-glycerophosphate, 1 mM DTT and EDTA-free Protease Inhibitor Cocktail (Roche)). After centrifugation at 18,000*g* for 15 min, the supernatant was incubated with amylose resin (NEB) for 1.5 h at 4 °C. The beads were washed five times in extraction buffer before elution with 10 mM maltose. Bound proteins were separated by SDS-PAGE and analyzed by western blotting. Where PLK1 and CDK1 inhibitor was used, the cells were synchronized in mitosis by nocodazole (14 h) followed by 2 h treatment with PLK1 inhibitor (50–100 nM BI2536 (Selleck Chemicals) or 50 µM BTO-1 (Sigma-Aldrich)) or the CDK1 inhibitor (10 µM, Ro-3306, (Selleck Chemicals)) before being harvested. The cells were lysed in extraction buffer A, pre-cleared by centrifugation and total protein lysate was separated by SDS-PAGE and analyzed by western blotting. Where proteasome inhibitor was used during the mitotic block, the cells were synchronized by nocodazole for 14 h before the MG-132 (50 µM, Sigma-Aldrich) was added to the media and the cells were cultured for additional 2 h before harvesting.

For analysis of pBUBR1, BUBR1, pT207-BRCA2 and BRCA2 levels in mitosis, nocodazole (100 ng/ml) treated DLD1 BRCA2$^{-/-}$ clones were lysed in extraction buffer A, pre-cleared by centrifugation and total protein lysate was separated by SDS-PAGE and analyzed by western blotting.

For analysis of the interaction between BRCA2-PLK1, BRCA2-BUBR1 and for the protein complex BRCA2-pBUBR1/BUBR1-PP2A(C)-PLK1 in mitosis, DLD1 BRCA2$^{-/-}$ stable clones expressing EGFP-MBP-BRCA2 (WT or the VUS S206C or T207A) were synchronized with nocodazole, harvested and lysed in extraction buffer A. The lysate were pre-cleared by centrifugation before incubation with GFP-TRAP beads (Chromotek) for 2 h at 4 °C to pull-down EGFP-MBP-BRCA2. Around 3 mg total protein lysate was used per pull-down. The beads were washed 5 times in extraction buffer A and 2 times in extraction buffer A with 500 mM NaCl. Bound proteins were eluted by boiling the samples for 4 min in 3x SDS-PAGE sample loading buffer (SB), eluted proteins were separated by SDS-PAGE and analyzed by western blotting using anti-mouse PLK1, anti-mouse BUBR1, anti-rabbit pT680-BUBR1, anti-mouse PP2A-C and anti-mouse BRCA2 (OP95) antibodies.

For immunoprecipitation of endogenous BUBR1, nocodazole treated DLD1 BRCA2$^{-/-}$ stable clones expressing BRCA2 WT or the variants (S206C or T207A) were lysed in extraction buffer A. After centrifugation, 2000–3000 µg total protein lysate was pre-cleared by incubation with 20 µl Protein G PLUS-Agarose (Santa Cruz, sc-2002) for 30 min at 4 °C. The pre-cleared lysate was incubated with 1.25 µg BUBR1 mouse antibody or control mouse IgG overnight at 4 °C before addition of 40 µl Protein G PLUS-Agarose, the lysate was incubated for additional 30 min before immunoprecipitates were collected by centrifugation. After four washes in extraction buffer A and two washes in extraction buffer A with 500 mM NaCl, the beads were re-suspended in SB, boiled and the immunocomplexes were analyzed by western blotting using anti-rabbit BUBR1, anti-mouse PLK1 and anti-mouse PP2A-C antibodies.

For the interaction between the phosphomimic BUBR1-3D mutant (S670D, S676D and T680D) and endogenous PP2A, the DLD1 BRCA2$^{-/-}$ stable clones expressing BRCA2 WT or the S206C variant was transient transfected with the pcDNA3-3xFLAG-BUBR1-3D-RFP construct. The transfection media was replaced 30 h post-transfection with fresh growth media containing 0.1 µg/ml nocadozole and the cells were incubated additional 14 h before harvesting. The cells were lysed and an immunoprecipitation was performed as described above for the BUBR1 immunoprecipitation using rabbit anti-tRFP antibody (Cat.#AB233, Evrogen) to pull-down the 3xFLAG-BUBR1-3D-RFP protein. Immunocomplexes were analyzed by western blotting using anti-mouse BUBR1 and anti-mouse PP2A-C antibodies.

For all Western blots, the protein bands were visualized with ChemiDoc XRS + System (BioRad) and quantified by the Image Lab^{TM} 5.2.1 Software (BioRad). For the relative expression levels (Fig. 5g-i, Supplementary Fig. 5d), the intensity of the band of interest was divided by the intensity of the signal from the stain free gel. The results are presented as percentage compared to BRCA2 WT clone. To calculate the relative co-immunoprecipitation (co-IP)/co-pull-down of a protein of interest, the intensity of the band in the co-IP was divided by the intensity of the band in the input (ImageQuant^{TM} TL software), the ratio co-IP:input of the protein of interest was then divided by the intensity of the band of the immunoprecipitated protein. StainFree images of the gels before transfer were used as loading control for the input and cropped image is shown in the figures.

Antibodies used for western blotting. mouse anti-MBP (1:5000, R29, Cat. #MA5-14122, Thermo Fisher Scientific), mouse anti-BRCA2 (1:1000, OP95, EMD Millipore), rabbit anti-pT207-BRCA2 (raised for this study using the peptide ^{203}TLSS-pT-VLIVRNEEAC as antigen, Genscript) (1:1000), anti-GFP (1:5000, Protein Expression and Purification Core Facility, Institut Curie), mouse anti-PLK1 (1:5000, clone 35-206, Cat. #05-844, EMD Millipore), mouse anti-BUBR1 (1:1000, Cat. #612502, BD Transduction Laboratories), rabbit anti-BUBR1 (1:2000, Cat. #A300-386A, Bethyl Laboratories), mouse anti-PP2A C subunit (1:1000, clone 1D6, Cat. #05-421, EMD Millipore), rabbit anti-pT680-BUBR1 (1:1000, EPR 19958, Cat. #ab200061, Abcam), and rabbit anti-pS676-BUBR1 (1:1000, R193, kind gift from Dr. Erich A. Nigg). Horseradish peroxidase (HRP) conjugated 2nd antibodies used: mouse-IgGκ BP-HRP (IB: 1:10 000, Cat. #sc-516102, Santa Cruz), goat anti-rabbit IgG-HRP (IB: 1:5000, Cat. #sc-2054, Santa Cruz), goat anti-mouse IgG-HRP (1:10 000, Cat.#115-035-003, Interchim), goat anti-rabbit IgG-HRP (1:10 000, Interchim, Cat.#111-035-003).

siRNA transfection. For analysis of the pT680-BUBR1 levels in U2OS cells after transient depletion of endogenous BRCA2 with RNAi, U2OS cells were transfected with 200 nM siRNA targeting the 3′UTR of BRCA2 (siBRCA2 #1: SI00000966, Qiagen) using jetPRIME (Polyplus Transfection, Cat.#114-07). As control, the cells were transfected with the 200 nM of the si-control RNA (siRNA control ON-TARGETplus Non-targeting Pool. D-001810-10-05, Thermo Scientific) The transfection media was replaced 30 h post-transfection with fresh growth media containing 0.1 µg/ml nocadozole and the cells were incubated additional 14 h before harvesting. Total protein lysate was extracted as described above and 30–50 µg total protein lysate was resolved on a 4–15% SDS-PAGE and analyzed by western blotting using anti-mouse BRCA2 (OP95), anti-mouse BUBR1, anti-rabbit pT680-BUBR1 and anti-mouse PLK1 antibodies (see above for reference number).

For depletion of endogenous BRCA2 in DLD1 BRCA2$^{+/+}$ cells for analysis of γH2AX and RAD51 foci, the cells were transfected with a combination of the BRCA2 5′UTR siRNA (SI00000966, Qiagen) and IAC204 (Dharmacon D-003462-04) (100 nM each) or the ON-TARGET plus Non-targeting oligonucleotide D-001810-04-20, Thermo Scientific 100 nM) and fixed and expose to IR 30 h post-transfection (see Supplementary Fig. 8c for the Western blot showing BRCA2 depletion) for analysis of DNA repair foci (see Supplementary Fig. 8c for the Western blot showing BRCA2 depletion).

Phosphatase treatment. DLD1 BRCA2$^{-/-}$ cells stably expressing EGFP-MBP-BRCA2 WT were synchronized in mitosis by nocodazole (14 h), harvested, lysed in extraction buffer A without phosphatase inhibitors (NaF, Na_3VO_4 and ß-glycerophosphate), and pre-cleared by centrifugation. For detection of pT207-BRCA2 and BRCA2, 20 U FastAP Thermosensitive Alkaline Phosphatase (Thermo Fisher Scientific Cat. #EF0654) was added to 200 µg of total protein lysate in FastAP Buffer in a total reaction volume of 60 µl. After 1 h incubation at 37 °C the reaction was stopped by heating at 95 °C for 5 min in SDS-PAGE sample loading buffer, 30 µl of the reaction was loaded on a 4–15% SDS-PAGE gel, the gel was transferred onto nitrocellulose membrane and the levels of pT207-BRCA2 were analyzed by western blotting using anti-pT207-BRCA2 antibody. For detection of pBUBR1 and BUBR1, increased amount (0-20U) of FastAP Thermosensitive Alkaline Phosphatase was added to 15 µg of total protein lysate in FastAP Buffer in a total reaction volume of 60 µl followed by same protocol as described for pT207-BRCA2, the levels of pS676/pT680-BUBR1 were analyzed by western blotting using anti-pS676/pT680-BUBR1 antibodies.

Cell survival and viability assays. For clonogenic survival assay, DLD1 BRCA2$^{-/-}$ cells stably expressing full-length EGFP-MBP-BRCA2 and the variants (S206C and T207A) were treated at 70% of confluence with Mitomycin C (Sigma-Aldrich) at concentrations: 0, 0.5, 1.0, and 2.5 µM. After 1 h drug treatment the cells were serial diluted in normal growth media containing penicillin/streptomycin (Eurobio) and seeded in triplicates into 6-well plates. The media was changed every third day, after 10–12 days in culture the plates were stained with crystal violet, colonies were counted and the surviving fraction was determined for each drug concentration.

Cell viability was assessed with 3-[4,5-Dimethylthiazol-2-yl]-2,5-diphenyltetrazolium bromide (MTT, #M5655, Sigma Aldrich) after treatment with MMC and the PARP inhibitor Olaparib (AZD2281, Ku-0059436, #S1060, Selleck Chemicals). For MMC, the cells were plated in triplicates in 96-well microplates (3000–5000 cells/well) the day before treatment. The cells were washed once in PBS before addition of serum-free media containing MMC at the concentrations: 0, 1.0 and 2.5 µM. After 1 h treatment the cells were washed once in PBS and incubated for 72 h in normal growth media before the viability was measured by MTT assay. For PARP inhibition, the cells were seeded 4 h before 4 days treatment in normal growth media with Olaparib at concentrations: 0, 2.5 and 5.0 µM.

HR assays. We applied a DSB-mediated gene targeting strategy using site-specific TALEN nucleases to quantify HR in cells. DLD1 BRCA2$^{-/-}$ cells stably expressing full-length GFPMBP-BRCA2 and the variants (S206C and T207A) were transfected using AMAXA technology (Lonza) nucleofector kit V (Cat. #VCA-1003) with 3 µg of the promoter-less donor plasmid (AAVS1-2A-mCherry) with or without 1 µg of each AAVS1-TALEN encoding plasmids (TALEN-AAVS1-5′ and TALEN-AAVS1-3′, see Supplementary Table 12 for sequences, kind gift from Dr. Carine Giovannangeli). For each transfection, 1 ×10^6 cells were transfected using program L-024, the cells were seeded in 6-well plate in culture media without selection antibiotics. The day after transfection the media was changed to media with selection and 48 h post-transfection the cells were trypsinized and reseeded on a 10-cm culture dish and cultured for additional 5 days. The percentage of mCherry positive cells was analyzed on a BD FACSAria III (BD Bioscience) using the FACSDiva software and data were analyzed with the FlowJo 10.4.2 software (Tree Star Inc.).

Analysis of tetraploid cells. For the analysis of S-phase tetraploid cells in the DLD1 BRCA2$^{-/-}$ stable clones, the cells were incubated with 10 µM BrdU for 20 min before they were harvest, fixed and stained for cell cycle analysis using a APC-BrdU flow kit (BD Bioscience, Cat. #552598) following the manufacturer's instructions.

Labeled cells were analyzed on a BD FACSCanto II (BD Bioscience) using the FACSDiva software and data were analyzed with the FlowJo 10.4.2 software (Tree Star Inc.).

Immunofluorescence. Kinetochore localization: For staining of pT680-BUBR1 and PLK1 at the kinetochore, DLD1 BRCA2$^{-/-}$ stable clones expressing EGFP-MBP-BRCA2-WT or the variant T207A were seeded on coverslips and treated with nocodazole (0.25 µg/ml) for 4 h, fixed with 4% PFA in PBS containing 0.5% Triton X-100 for 20 min at room temperature. The coverslips were rinsed three times in PBS-T and blocked for 30 min with 4% BSA in PBS before incubation with primary antibodies (human anti-CREST (1:100, Cat. #15-234-0001, Antibodies Online) together with either rabbit anti-pT680-BUBR1 (1:500, clone EPR 19958, Abcam, Cat. #ab200061) or mouse anti-PLK1 (1:500, clone F-8, Santa Cruz Biotechnology, Cat. #sc-17783), diluted in PBS-T with 5% BSA overnight at 4 °C. After three washes of 5 min in PBS-T the coverslips were incubated for 2 h incubation at room temperature with respective Alexa Fluor conjugated secondary antibody (for pBUBR1; goat anti-human Alexa-488 (1:1000, Cat. #A11013, Life Technologies) and donkey anti-rabbit Alexa-488 (1:1000, Cat. #A-21206, Thermo Fisher Scientific), for PLK1; goat anti-human Alexa-633 (1:500, Cat. #A21091, Life Technologies) together with either donkey anti-rabbit Alexa-488 (1:1000, Cat. #A-21206, Thermo Fisher Scientific) or donkey anti-mouse Alexa-488 (1:1000, Cat. #A-21202, Thermo Fisher Scientific) diluted in PBS-T with 5% BSA. After two washes of 5 min in PBS-T and one rinse in PBS the coverslips were mounted on microscope slides.

For staining of BRCA2 at the kinetochore, U2OS was transient transfected with GFPMBP-BRCA2 construct using TurboFect (Thermo Fisher Scientific). The cells were seeded on coverslips 24 h post-transfection and incubated for another 24 h before nocadozole (0.25 µg/ml) was added. The cells were treated for 4 h followed by fixation as described above for kinetochore localization of pBUBR1, pAuroraB and PLK1. BRCA2 was detected by rabbit anti-BRCA2 (1:500, CA1033, EMD Millipore) and Alexa-488 secondary antibody (donkey anti-rabbit Alexa-488 (1:1000, Cat. #A-21206, Thermo Fisher Scientific), CREST was detected by human anti-CREST (1:100, Cat. #15-234-0001, Antibodies Online) and Alexa-633 secondary antibody (1:500, Cat. #A21091, Life Technologies)), diluted in PBS-T with 5% BSA.

Phosphatase inhibitors (50 mM NaF, 1 mM Na_3VO_4, and 20 mM ß-glycerophosphate) were added to all buffers.

Cold stable kinetochore–microtubules, chromosome alignment and segregation: DLD1 BRCA2$^{-/-}$ cells and the stable clones expressing EGFP-MBP-BRCA2 WT or the variants (S206C and T207A) were seeded on coverslips in 6-well tissue

culture plates and synchronized in mitosis. For analysis of chromosome alignment, the cells were synchronized by double thymidine (2.5 mM, Sigma-Aldrich) block, released for 9 h followed by treatment with Monastrol (100 µM, Sigma-Aldrich) for 16 h. After incubation with Monastrol the cells were washed twice in PBS before 1 h incubation in media containing the proteasome inhibitor MG-132 (10 µM, Sigma-Aldrich). To detect cold-stable microtubules cells were synchronized using the same protocol as for the chromosome alignment followed by 15 min of cold treatment on ice before fixation. For chromosome segregation analysis, the cells were synchronized by double thymidine block and released in normal growth media for 11 h.

After synchronization, the cells were fixed with 100% methanol for 15 min at -20 °C, rinsed once in PBS before permeabilization with PBS containing 0.1% Triton-X for 15 min at room temperature. Nonspecific epitope binding was blocked with 4% BSA (Sigma-Aldrich) in PBS. The coverslips were rinsed in PBS, incubated with primary antibody (mouse anti-α-tubulin (1:5000, GT114, Cat. #GTX628802, Euromedex) and human anti-CREST (1:100, Cat. #15-234-0001, Antibodies Online)) diluted in PBS containing 0.1% Tween-20 (PBS-T) and 5% BSA for 1 h at room temperature. After incubation, the coverslips were washed three times of 5 min in PBS-T before being incubated for 1 h at room temperature with Alexa Fluor conjugated secondary antibody (donkey anti-mouse Alexa-594 (1:1000, Cat. #A-21203, Thermo Fisher Scientific) and goat anti-human Alexa-488 (1:1000, Cat. #A11013, Life Technologies)) diluted in PBS-T with 5% BSA. The coverslips were washed two times of 5 min each in PBS-T followed by one rinse in PBS before being mounted on microscope slides.

For the analysis of chromosome alignment in cells expressing the phosphomimic BUBR1-3D mutant (S670D, S676D and T680D), the DLD1 BRCA2$^{-/-}$ stable clones expressing the T207A variant was transient transfected with the pcDNA3-3xFLAG-BUBR1-3D-RFP construct using TurboFect. The day after transfection the cells were seeded on coverslips in 6-well tissue culture plates, synchronized in mitosis and prepared for immunofluorescence.

Aneuploidy: For aneuploidy analysis the cells were treated with nocodazole for 14 h (0.1 µg/ml) to enable chromosome spread; the cells were rinsed in PBS, incubated for 10 min with KCl (50 mM) at room temperature before they were spread on coverslips at 900 rpm for 5 min in a Cytospin 4 (Thermo Scientific). The cells were fixed with 3% paraformaldehyde (PFA) in PBS for 20 min followed by 15 min permeabilization in PBS containing 0.1% Triton X-100. The coverslips were rinsed three times in PBS, blocked with 5% BSA in PBS before incubation with human anti-CREST primary antibody (1:100, Cat. #15-234-0001, Antibodies Online) diluted in PBS overnight at 4 °C. After incubation the coverslips were washed three times of 5 min in PBS before 1 h incubation at room temperature with Alexa Fluor conjugated secondary antibody (goat anti-human Alexa-555 (1:1000, Cat. #A-21433, Thermo Fisher Scientific)) diluted in PBS. After three washes of 5 min in PBS the coverslips were mounted on microscope slides.

γH2AX and RAD51 foci: For the detection of γH2AX and RAD51 foci, the cells were seeded on coverslips the day before 6 Gy γ-irradiation (GSR D1, Cs-137 irradiator). Two hours after irradiation, the coverslips were washed twice in PBS followed by one wash in CSK Buffer (10 mM PIPES, pH 6.8, 0.1 M NaCl, 0.3 M sucrose, 3 mM $MgCl_2$, EDTA-free Protease Inhibitor Cocktail (Roche)). The cells were permeabilized for 5 min at room temperature in CSK buffer containing 0.5% Triton X-100 (CSK-T) followed by one rinse in CSK buffer and one rinse in PBS before fixation for 20 min at room temperature with 2% PFA in PBS. After one rinse in PBS and one in PBS-T, the cells were blocked for 5 min at room temperature with 5% BSA in PBS-T before incubation for 2 h at room temperature with primary antibodies diluted in PBS-T with 5% BSA. After primary antibody incubation, the coverslips were rinsed in PBS-T followed by two washes of 10 min in PBS-T and blocked for 5 min at room temperature with 5% BSA in PBS-T before incubation for 1 h at room temperature with respective Alexa Fluor conjugated secondary antibody diluted in PBS-T with 5% BSA. After one rinse in PBS-T and two washes of 10 min in PBS-T the coverslips were rinsed in PBS before being mounted on microscope slides. γH2AX foci were detected by mouse anti-pSer139-γH2AX (1:1000, clone JBW301, EMD-Millipore, Cat. #05-636) and secondary antibody donkey anti-mouse Alexa-594 (1:1000, Cat. #A-21203, Thermo Fisher Scientific). RAD51 foci were detected by rabbit anti-RAD51 (1:100, clone H-92, Santa Cruz Biotechnology, Cat. #sc-8349), followed by secondary antibody donkey anti-rabbit Alexa-488 (1:1000, Cat. #A-21206, Thermo Fisher Scientific).

For the analysis of γH2AX and RAD51 foci in DLD1 BRCA2$^{+/+}$ cells depleted of BRCA2 by siRNA, the DLD1 BRCA2$^{+/+}$ cells were transient transfected with siRNA targeting BRCA2 (see section siRNA transfection above). The day after transfection the cells were seeded on coverslips in 6-well tissue culture plates and radiated as described above.

Micronuclei: For analysis of micronuclei, DLD1 BRCA2$^{-/-}$ cells and the stable clones expressing EGFP-MBP-BRCA2 WT or the variants (S206C and T207A) were seeded on coverslips in 6-well tissue culture plates the day before fixation. Centromeres were detected by human anti-CREST primary antibody (1:100, Cat. #15-234-0001, Antibodies Online) and Alexa Fluor conjugated secondary antibody (goat anti-human Alexa-555 (1:1000, Cat. #A-21433, Thermo Fisher Scientific)).

All coverslips were mounted on microscope slides with ProLong Diamond Antifade Mountant with DAPI (Cat. #P36966, Thermo Fisher Scientific).

Image acquisition and analysis: For analysis of DNA repair foci, chromosome alignment and segregation, images were acquired in an upright Leica DM6000B wide-field microscope equipped with a Leica Plan Apo 63x NA 1.4 oil immersion objective. The camera used is a Hamamatsu Flash 4.0 sCMOS controlled with the MetaMorph2.1 software (Molecular Devices). For Fig. 6a and 7a, 7 to 20 Z-stacks were taken at 0.2 µm intervals to generate a maximal intensity projection image using ImageJ. For the analysis of γH2AX and RAD51 foci, 26 Z-stacks were taken at 0.2 µm intervals to generate a maximal intensity projection using the Image J software (1.51 s, NIH). For the BUBR1-3D-RFP chromosome alignment experiment, RFP negative cells on the same coverslips were used as control.

The number of γH2AX foci per nucleus were counted by a customized macro using a semi-automated procedure; the nucleus was defined by an auto-threshold (Otsu, Image J) on DAPI, a mask was generated and applied onto the Z-projection to count foci within the nucleus. For the definition of foci we applied the threshold plugin IsoData (ImageJ software (1.51 s, NIH)) and for the quantification of foci we used the tool Analyze Particles (ImageJ software (1.51 s, NIH)) setting a range of 5-100 pixels^2 to select only particles that correspond to the size of a focus. RAD51 foci were quantified using the plugin Find Maxima onto the Z-projection with a prominence of 1000.

For analysis of cold stable microtubules images were acquired in an upright Leica DM6000B wide-field microscope equipped with a Leica Plan Apo 100x NA 1.4 oil immersion objective. The camera used is a Hamamatsu Flash 4.0 sCMOS controlled with the MetaMorph2.1 software (Molecular Devices), 20 Z-stacks were taken on metaphase cells at 0.5 µm intervals to generate a maximal intensity projection image using the ImageJ software (1.51 s, NIH). The quantification of the intensity of α-tubulin in metaphase cells was performed in the area of the spindle subtracting the background of α-tubulin signal from a different area in the same cell. The data were then normalized to the mean intensity of the BRCA2 WT cells.

For analysis of aneuploidy, kinetochore localization and micronuclei images were acquired in an inverted confocal Leica SP5 microscope with a plan Apo 63x NA 1.4 oil immersion objective with the lasers 405, 488, 561 and 633 nm. For Fig. 8b (aneuploidy), Z-stacks were taken at 0.13 µm intervals to generate a maximal intensity projection image using the ImageJ software (1.51 s, NIH). For the counting of chromosomes in the aneuploidy experiment, the quantification was performed in zoomed areas counting the CREST signal in separated stacks to ensure the counting of all chromosomes. We were able to count up to 65 chromosomes with certainty, thus >65 CREST signals were discarded and not included in the analysis.

For the analysis of kinetochore localization, Z-stacks were taken at 0.21 µm intervals to generate a sum slice projection image using ImageJ, six pairs of chromosomes per cell were analyzed in 15-21 cells per experiment from two individual experiment. The results from the quantifications (Fig. 5i, Supplementary Fig. 6b) is represented as the ratio between the intensities for pBUBR1/PLK1 and the CREST signal relative to the mean ratio observed for the BRCA2 WT complemented cells. For the images in Fig. 5h (pBUBR1:CREST), Supplementary Fig. 6a (PLK1:CREST) and Supplementary Fig. 8e (micronuclei), Z-stacks were taken to generate a maximal intensity projection image using the ImageJ software (1.51 s, NIH), except for DAPI where the image is from one Z-stack.

Time-lapse video microscopy of mitotic cells. For phase-contrast video-microscopy DLD1 BRCA2$^{-/-}$ cells stably expressing full-length EGFP-MBP-BRCA2 and the variants (S206C and T207A) were seeded in 35 mm Ibidi µ-Dishes (Ibidi, Cat. #81156), synchronized by double thymidine block, released and cultured for 4 h in normal growth media before the filming was started. The cells were imaged for 16 h every 5 min, at oil-40X using an inverted video-microscope (Leica DMI6000) equipped with electron multiplying charge coupled device (EMCCD) camera controlled by the MetaMorph2.1 software (Molecular Devices). Images were mounted using the Image J software (1.51 s, NIH).

Statistical analysis. In all graphs error bars represent the standard deviation (SD) from at least three independent experiments unless otherwise stated, scatter dot plots show median with 95% CI. Statistical significance of differences was calculated with unpaired two-tailed *t*-test, one/two-way ANOVA with Dunnett's or Tukey's multiple comparisons test, Mann–Whitney two-tailed or Kruskal–Wallis one-way analysis followed by Dunn's multiple comparisons test as indicated in the figure legends. All analyses were conducted using GraphPad Prism version Mac OS X 8.3.0 (328).

Reporting summary. Further information on research design is available in the Nature Research Reporting Summary linked to this article.

Data availability

The data that support the findings of this study are available from the corresponding authors upon reasonable request. The source data for Fig. 1a–d; Fig. 2; Fig. 3a–k; Fig. 4a–f; Fig. 5a–i; Figs. 6a, 6d; Fig. 7a, c, d; Fig. 8a, d; Fig. 9a–f; Supplementary Fig. 1a, b; Supplementary Figu. 2b, c; Supplementary Fig. 3a–d; Supplementary Fig. 4a, c; Supplementary Fig. 5b–d; Supplementary Fig. 6b–d; Supplementary Fig. 7d; Supplementary Fig. 8c–d; Supplementary Fig. 10a, b; are available as a Source Data file.

The PDB files used during structure analysis can be retrieved using the PDB codes 4O56 and 3P35 on the PDB website: https://www.rcsb.org. The final X-ray structure of the PLK1 PBD bound to the phosphorylated BRCA2 peptide is also available on this website, under the code 6GY2.

Received: 8 October 2019; Accepted: 20 March 2020;
Published online: 14 April 2020

References

1. Moynahan, M. E., Pierce, A. J. & Jasin, M. BRCA2 is required for homology-directed repair of chromosomal breaks. *Mol. Cell* **7**, 263–272 (2001).
2. Jensen, R. B., Carreira, A. & Kowalczykowski, S. C. Purified human BRCA2 stimulates RAD51-mediated recombination. *Nature* **467**, 678–683 (2010).
3. Saleh-Gohari, N. & Helleday, T. Conservative homologous recombination preferentially repairs DNA double-strand breaks in the S phase of the cell cycle in human cells. *Nucleic Acids Res.* **32**, 3683–3688 (2004).
4. Choi, E. et al. BRCA2 fine-tunes the spindle assembly checkpoint through reinforcement of BubR1 acetylation. *Dev. Cell* **22**, 295–308 (2012).
5. Futamura, M. et al. Potential role of BRCA2 in a mitotic checkpoint after phosphorylation by hBUBR1. *Cancer Res.* **60**, 1531–1535 (2000).
6. Lampson, M. A. & Kapoor, T. M. The human mitotic checkpoint protein BubR1 regulates chromosome-spindle attachments. *Nat. Cell Biol.* **7**, 93–98 (2005).
7. Lara-Gonzalez, P., Westhorpe, F. G. & Taylor, S. S. The spindle assembly checkpoint. *Curr. Biol.* **22**, R966–R980 (2012).
8. Elowe, S. et al. Uncoupling of the spindle-checkpoint and chromosome-congression functions of BubR1. *J. Cell Sci.* **123**, 84–94 (2010).
9. Zhang, G., Mendez, B. L., Sedgwick, G. G. & Nilsson, J. Two functionally distinct kinetochore pools of BubR1 ensure accurate chromosome segregation. *Nat. Commun.* **7**, 12256 (2016).
10. Park, I. et al. HDAC2/3 binding and deacetylation of BubR1 initiates spindle assembly checkpoint silencing. *FEBS J.* **284**, 4035–4050 (2017).
11. Mondal, G. et al. BRCA2 localization to the midbody by filamin A regulates cep55 signaling and completion of cytokinesis. *Dev. Cell* **23**, 137–152 (2012).
12. Daniels, M. J., Wang, Y., Lee, M. & Venkitaraman, A. R. Abnormal cytokinesis in cells deficient in the breast cancer susceptibility protein BRCA2. *Science* **306**, 876–879 (2004).
13. Takaoka, M., Saito, H., Takenaka, K., Miki, Y. & Nakanishi, A. BRCA2 phosphorylated by PLK1 moves to the midbody to regulate cytokinesis mediated by nonmuscle myosin IIC. *Cancer Res.* **74**, 1518–1528 (2014).
14. Lin, H.-R., Ting, N. S. Y., Qin, J. & Lee, W.-H. M phase-specific phosphorylation of BRCA2 by Polo-like kinase 1 correlates with the dissociation of the BRCA2-P/CAF complex. *J. Biol. Chem.* **278**, 35979–35987 (2003).
15. Lee, M., Daniels, M. J. & Venkitaraman, A. R. Phosphorylation of BRCA2 by the Polo-like kinase Plk1 is regulated by DNA damage and mitotic progression. *Oncogene* **23**, 865–872 (2004).
16. Zitouni, S., Nabais, C., Jana, S. C., Guerrero, A. & Bettencourt-Dias, M. Polo-like kinases: structural variations lead to multiple functions. *Nat. Rev. Mol. Cell Biol.* **15**, 433–452 (2014).
17. Barr, F. A., Silljé, H. H. W. & Nigg, E. A. Polo-like kinases and the orchestration of cell division. *Nat. Rev. Mol. Cell Biol.* **5**, 429–440 (2004).
18. Elowe, S., Hümmer, S., Uldschmid, A., Li, X. & Nigg, E. A. Tension-sensitive Plk1 phosphorylation on BubR1 regulates the stability of kinetochore microtubule interactions. *Genes Dev.* **21**, 2205–2219 (2007).
19. Suijkerbuijk, S. J. E., Vleugel, M., Teixeira, A. & Kops, G. J. P. L. Integration of kinase and phosphatase activities by BUBR1 ensures formation of stable kinetochore-microtubule attachments. *Dev. Cell* **23**, 745–755 (2012).
20. Hauf, S. et al. The small molecule Hesperadin reveals a role for Aurora B in correcting kinetochore-microtubule attachment and in maintaining the spindle assembly checkpoint. *J. Cell Biol.* **161**, 281–294 (2003).
21. Foley, E. A., Maldonado, M. & Kapoor, T. M. Formation of stable attachments between kinetochores and microtubules depends on the B56-PP2A phosphatase. *Nat. Cell Biol.* **13**, 1265–1271 (2011).
22. Elia, A. E. H., Cantley, L. C. & Yaffe, M. B. Proteomic screen finds pSer/pThr-binding domain localizing Plk1 to mitotic substrates. *Science* **299**, 1228–1231 (2003).
23. Elia, A. E. H. et al. The molecular basis for phosphodependent substrate targeting and regulation of Plks by the Polo-box domain. *Cell* **115**, 83–95 (2003).
24. Neef, R. et al. Phosphorylation of mitotic kinesin-like protein 2 by polo-like kinase 1 is required for cytokinesis. *J. Cell Biol.* **162**, 863–875 (2003).
25. Kang, Y. H. et al. Self-regulated Plk1 recruitment to kinetochores by the Plk1-PBIP1 interaction is critical for proper chromosome segregation. *Mol. Cell* **24**, 409–422 (2006).
26. Szabo, C., Masiello, A., Ryan, J. F. & Brody, L. C. The breast cancer information core: database design, structure, and scope. *Hum. Mutat.* **16**, 123–131 (2000).
27. Béroud, C. et al. BRCA share: a collection of clinical BRCA gene variants. *Hum. Mutat.* **37**, 1318–1328 (2016).
28. Golsteyn, R. M., Mundt, K. E., Fry, A. M. & Nigg, E. A. Cell cycle regulation of the activity and subcellular localization of Plk1, a human protein kinase implicated in mitotic spindle function. *J. Cell Biol.* **129**, 1617–1628 (1995).
29. Yata, K. et al. BRCA2 coordinates the activities of cell-cycle kinases to promote genome stability. *Cell Rep.* **7**, 1547–1559 (2014).
30. Santaguida, S. & Amon, A. Short- and long-term effects of chromosome mis-segregation and aneuploidy. *Nat. Rev. Mol. Cell Biol.* **16**, 473–485 (2015).
31. Lera, R. F. et al. Decoding Polo-like kinase 1 signaling along the kinetochore-centromere axis. *Nat. Chem. Biol.* **12**, 411–418 (2016).
32. Kraakman-van der Zwet, M. et al. Brca2 (XRCC11) deficiency results in radioresistant DNA synthesis and a higher frequency of spontaneous deletions. *Mol. Cell. Biol.* **22**, 669–679 (2002).
33. Bryant, H. E. et al. Specific killing of BRCA2-deficient tumours with inhibitors of poly(ADP-ribose) polymerase. *Nature* **434**, 913–917 (2005).
34. Brunet, E. et al. Chromosomal translocations induced at specified loci in human stem cells. *Proc. Natl Acad. Sci. USA* **106**, 10620–10625 (2009).
35. Hockemeyer, D. et al. Efficient targeting of expressed and silent genes in human ESCs and iPSCs using zinc-finger nucleases. *Nat. Biotechnol.* **27**, 851–857 (2009).
36. Hertz, E. P. T. et al. A Conserved Motif Provides Binding Specificity to the PP2A-B56 Phosphatase. *Mol. Cell* **63**, 686–695 (2016).
37. Wu, C.-G. et al. PP2A-B' holoenzyme substrate recognition, regulation and role in cytokinesis. *Cell Discov.* **3**, 17027–19 (2017).
38. Spain, B. H., Larson, C. J., Shihabuddin, L. S., Gage, F. H. & Verma, I. M. Truncated BRCA2 is cytoplasmic: implications for cancer-linked mutations. *Proc. Natl Acad. Sci. USA* **96**, 13920–13925 (1999).
39. Gretarsdottir, S. et al. BRCA2 and p53 mutations in primary breast cancer in relation to genetic instability. *Cancer Res.* **58**, 859–862 (1998).
40. Hucl, T. et al. A syngeneic variance library for functional annotation of human variation: application to BRCA2. *Cancer Res.* **68**, 5023–5030 (2008).
41. Nicolai, von, C., Ehlen, A., Martin, C., Zhang, X. & Carreira, A. A second DNA binding site in human BRCA2 promotes homologous recombination. *Nature Communications* **7**, 12813 (2016).
42. Martinez, J. S. et al. BRCA2 regulates DMC1-mediated recombination through the BRC repeats. *Proc Natl Acad Sci USA* **113**, 3515–3520 (2016).
43. Schanda, P., Kupče, Ê. & Brutscher, B. SOFAST-HMQC experiments for recording two-dimensional heteronuclear correlation spectra of proteins within a few seconds. *J. Biomol. NMR* **33**, 199–211 (2005).
44. Vonrhein, C. et al. Data processing and analysis with the autoPROC toolbox. *Acta Crystallogr D Biol Crystallogr* **67**, 293–302 (2011).
45. Adams, P. D. et al. PHENIX: a comprehensive Python-based system for macromolecular structure solution. *Acta Crystallogr D Biol Crystallogr* **66**, 213–221 (2010).
46. Smart, O. S. et al. Exploiting structure similarity in refinement: automated NCS and target-structure restraints in BUSTER. *Acta Crystallogr D Biol Crystallogr* **68**, 368–380 (2012).
47. Afonine, P. V. et al. Towards automated crystallographic structure refinement with phenix.refine. *Acta Crystallogr D Biol Crystallogr* **68**, 352–367 (2012).
48. Emsley, P., Lohkamp, B., Scott, W. G. & Cowtan, K. Features and development of Coot. *Acta Crystallogr D Biol Crystallogr* **66**, 486–501 (2010).

Acknowledgements

The authors thank members of the AC lab for fruitful comments on the manuscript and Davide Panigada and Jose M. Jimenez-Gomez for the illustration of chromosomes in Fig. 9. We thank Rene H. Medema for useful discussions on this work including the cell synchronization protocol used in Fig. 7. We also thank Juan S. Martinez for construct $BRCA2_{1-250}$, Anne Houdusse for construct PLK1365-603, Carine Giovannangeli for TALEN plasmids, Eric Nigg for pS676-BUBR1 antibody and Geert JPL Kops for BUBR1-RFP construct. We acknowledge the Cell and Tissue Imaging Facility of the Institut Curie (PICT), a member of the France BioImaging National Infrastructure (ANR-10-INBS-04), and the French Infrastructure for Integrated Structural Biology (https://www.structuralbiology.eu/networks/frisbi, ANR-10-INSB-05-01). We thank Charlene Lasgi from the Flow Cytometry platform of Institut Curie, Orsay. We thank Guillaume Hoffmann and Jose A. Marquez from the HTXLab (Grenoble, France), funded by the European Community's Seventh Framework Programme H2020 under iNEXT (grant agreement No. 653706). This work was supported by the ATIP-AVENIR CNRS/INSERM Young Investigator grant 201201, FRM "Amorcage Jeunes Equipes" Young Investigator grant AJE20110 and Institut National du Cancer INCa-DGOS_8706 to A.C. and S.Z.J.; A. E. was supported by the Swedish Society for Medical Research.

Author contributions

A.E. purified WT and mutated $BRCA2_{1-250}$, established the stable $DLD1^{-/-}$ cell lines, performed kinase assays, pull-down assays, Western blots, time-lapse microscopy experiments, mitotic index measurements by FACS, clonogenic survival and MTT assays as well as the statistical analysis for all the experiments. C.M. performed Western blot of pT207, IF and image acquisition of cold-stable microtubules, metaphase plate alignment, chromosome segregation and karyotype analysis. M.J. performed the NMR experiments

assisted by S. M., F.T., and S.Z.J. M.J. and S.M. purified $PLK1_{PBD}$ and performed the ITC experiments. S.M. solved the X-ray structure assisted by V.R. R.B. and G.S. performed IF, image acquisition and quantification of DNA repair foci. V.B. assisted establishing stable clones and performing clonogenic survival assays. P.D. purified $PLK1_{PBD}$. A.M. cloned and produced PLK1 and PLK1-KD from insect cells. A.C., A.E., and S.Z.J. designed the experiments. A.C. and S.Z.J. supervised the work. A.C. wrote the paper with important contributions from all authors.

Competing interests
The authors declare no competing interests.

Additional information
Supplementary information is available for this paper at https://doi.org/10.1038/s41467-020-15689-9.

Correspondence and requests for materials should be addressed to S.Z.-J. or A.C.

Peer review information *Nature Communications* thanks Georges Mer, Elmar Schiebel and the other, anonymous, reviewer(s) for their contribution to the peer review of this work. Peer reviewer reports are available.

Reprints and permission information is available at http://www.nature.com/reprints

Publisher's note Springer Nature remains neutral with regard to jurisdictional claims in published maps and institutional affiliations.

Open Access This article is licensed under a Creative Commons Attribution 4.0 International License, which permits use, sharing, adaptation, distribution and reproduction in any medium or format, as long as you give appropriate credit to the original author(s) and the source, provide a link to the Creative Commons license, and indicate if changes were made. The images or other third party material in this article are included in the article's Creative Commons license, unless indicated otherwise in a credit line to the material. If material is not included in the article's Creative Commons license and your intended use is not permitted by statutory regulation or exceeds the permitted use, you will need to obtain permission directly from the copyright holder. To view a copy of this license, visit http://creativecommons.org/licenses/by/4.0/.

© The Author(s) 2020

Supplementary information

Ehlen *et al*.,

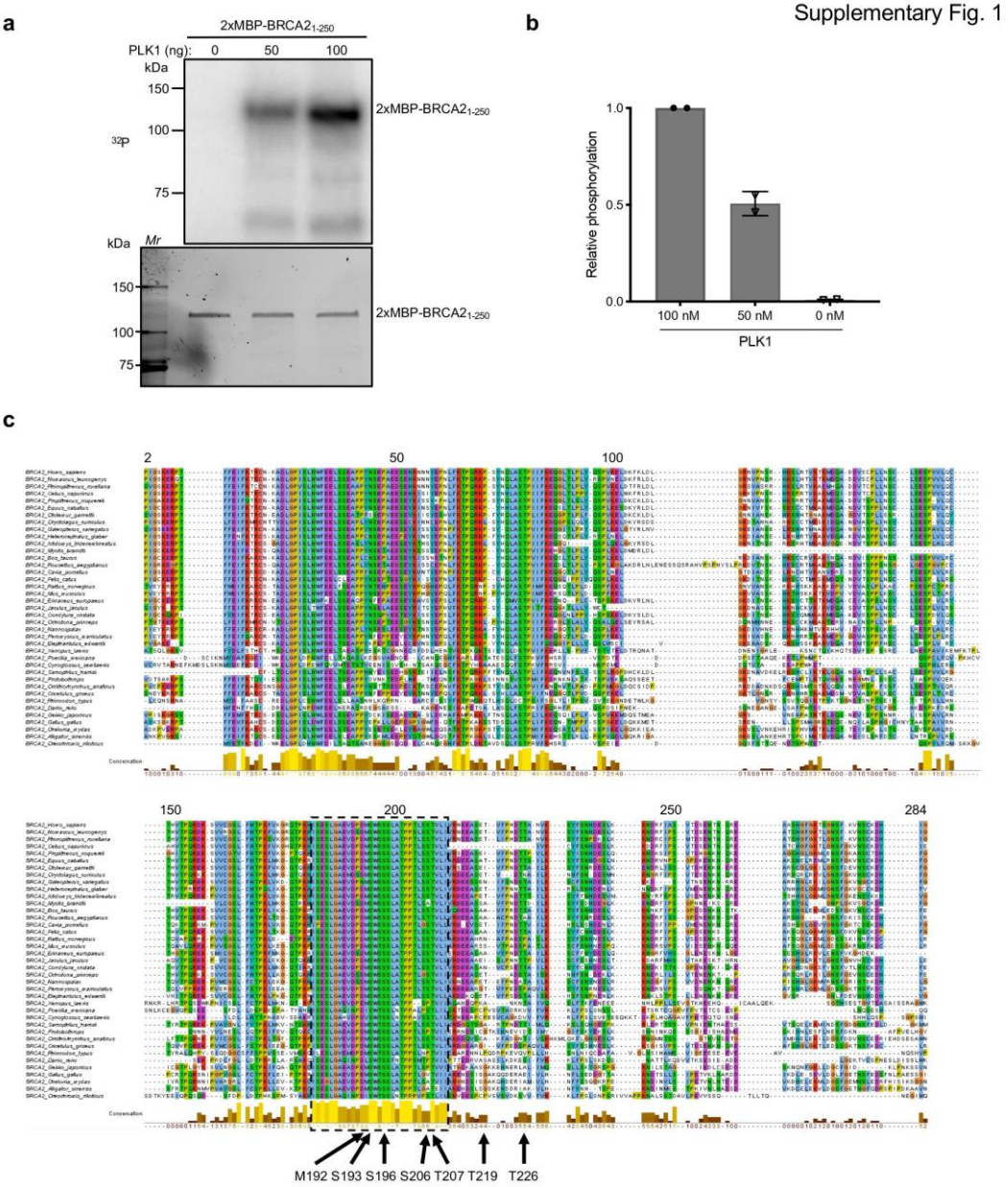
a
2xMBP-BRCA2$_{1-250}$
PLK1 (ng): 0 50 100
kDa
150
100
75
^{32}P
2xMBP-BRCA2$_{1-250}$
kDa
Mr
150
100
75
2xMBP-BRCA2$_{1-250}$
b
Relative phosphorylation
1.0
0.5
0.0
100 nM
50 nM
0 nM
PLK1
c
2
50
100
150
200
250
284
M192 S193 S196 S206 T207 T219 T226

Supplementary Figure 1. Related to Figure 1. **PLK1 phosphorylation of the N-terminal region of BRCA2 and conservation of PLK1 phosphosites**

(a) PLK1 *in vitro* kinase assay with $BRCA2_{1-250}$. Top: The polypeptide 2x-MBP-$BRCA2_{1-250}$ WT was incubated with increased concentrations (0, 50 and 100 ng) of recombinant PLK1 in the presence of γ^{32}P-ATP. The samples were resolved on 4-15% SDS-PAGE and the ^{32}P-labeled products were detected by autoradiography. Bottom: 4-15% SDS-PAGE showing the input of 2xMBP-$BRCA2_{1-250}$ WT (0.5 μg) used in the reaction. **(b)** Quantification of the relative phosphorylation in (a). Data are represented as mean ± SD from two independent experiments. **(c)** Alignment of the region 2-284 of human BRCA2 with the N-terminal regions of BRCA2 from 40 different species. Amino acids conserved in more than 30 % of the species are highlighted with coloured background. A dashed line box identifies the highly conserved cluster around S193 (amino acid 180 to amino acid 210). Arrows show the amino acids cited in this manuscript (including the PLK1 phosphosites). Source data is available as a Source Data file.

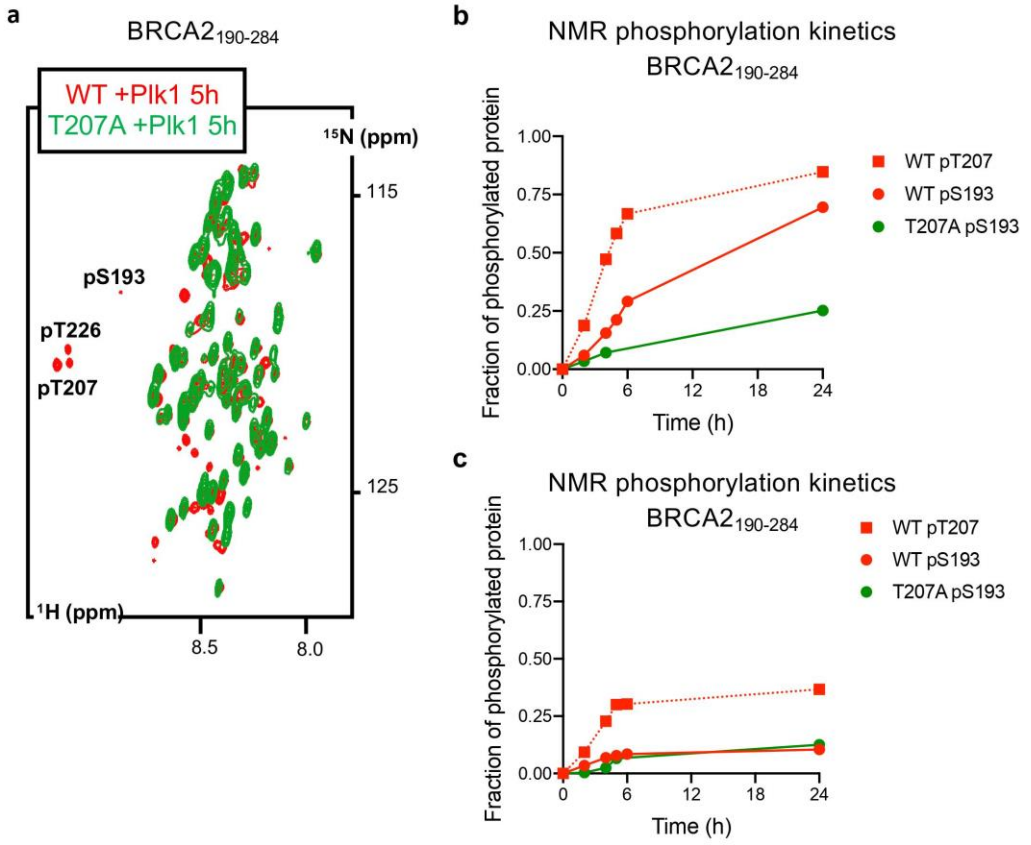
a
BRCA2190-284
WT +Plk1 5h
T207A +Plk1 5h
15N (ppm)
115
125
pS193
pT226
pT207
1H (ppm)
8.5
8.0
b
NMR phosphorylation kinetics
BRCA2190-284
Fraction of phosphorylated protein
1.00
0.75
0.50
0.25
0.00
0
6
12
18
24
Time (h)
WT pT207
WT pS193
T207A pS193
c
NMR phosphorylation kinetics
BRCA2190-284
Fraction of phosphorylated protein
1.00
0.75
0.50
0.25
0.00
0
6
12
18
24
Time (h)
WT pT207
WT pS193
T207A pS193

Supplementary Figure 2. Related to Figure 2. **PLK1 phosphorylation kinetics of $BRCA2_{190-284}$ WT vs T207A**

(a) Superimposition of the ^{1}H-^{15}N HSQC spectra recorded on the ^{15}N labelled fragments $BRCA2_{190-284}$ WT (red) and T207A (green) after 5h of incubation with PLK1. The conditions are the same as in Figure 1. **(b,c)** Comparison of the phosphorylation kinetics of $BRCA2_{190-284}$ WT and T207A performed with two different PLK1 samples. The percentage of phosphorylation deduced from the intensities of the peaks corresponding to the non-phosphorylated and phosphorylated residues is plotted as a function of time. WT S193 and T207 time points are represented by red circles and squares, respectively, while T207A S193 timepoints are represented by green circles. Source data is available as a Source Data file.

Supplementary Fig. 3

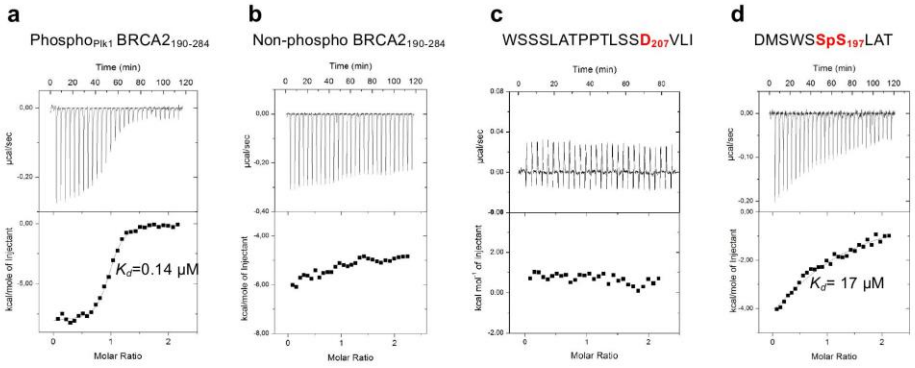

Supplementary Figure 3. Related to Figure 3. **Isothermal Titration Calorimetry (ITC) thermogram showing binding of PLK1$_{PBD}$ to the fragment BRCA2$_{190-284}$ or a 10 aa BRCA2 peptide containing pS197**

Thermogram showing the binding affinity of PLK1$_{PBD}$ to the **(a)** phosphorylated or **(b)** non-phosphorylated BRCA2$_{190-284}$ fragment, purified from bacteria as explained in the Methods section and also used in the NMR experiments. **(c)** Thermogram showing the binding affinity of PLK1$_{PBD}$ to a 17 aa BRCA2 synthetic peptide comprising T207D (WSSSLATPPTLSSD$_{207}$VLI). **(d)** Thermogram showing the binding affinity of PLK1$_{PBD}$ to a 10 aa BRCA2 synthetic peptide comprising pS197. Source data is available as a Source Data file.

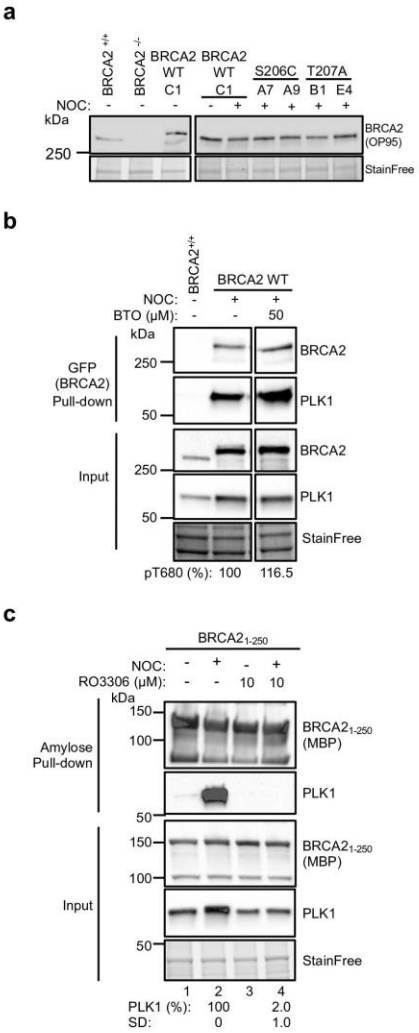
a
BRCA2 +/+
BRCA2 -/-
BRCA2 WT C1
BRCA2 WT C1
S206C A7 A9
T207A B1 E4
NOC: - - - - + + + + + +
kDa
250
BRCA2 (OP95)
StainFree
b
BRCA2+/+
BRCA2 WT
NOC: - + +
BTO (μM): - - 50
kDa
GFP (BRCA2) Pull-down
250
50
BRCA2
PLK1
Input
250
50
BRCA2
PLK1
StainFree
pT680 (%): 100 116.5
c
BRCA2 1-250
NOC: - + - +
RO3306 (μM): - - 10 10
kDa
Amylose Pull-down
150
100
50
BRCA2 1-250 (MBP)
PLK1
Input
150
100
50
BRCA2 1-250 (MBP)
PLK1
StainFree
1 2 3 4
PLK1 (%): 100 2.0
SD: 0 1.0

Supplementary Figure 4. Related to Figures 3-8**. BRCA2 protein levels in DLD1 BRCA2$^{-/-}$ stable clones bearing BRCA2 WT and variants utilized in this study and effect of PLK1 and CDK1 inhibitors on the interaction between BRCA2 and PLK1**

(a) BRCA2 protein levels in total cell extracts from DLD1 cells stably expressing EGFP-MBP-BRCA2 WT (BRCA2 WT C1) or the variants S206C (clones A7 and A9) and T207A (clones B1 and E4) as detected by western blot using anti-BRCA2 (OP95) antibody. **(b)** The effect of PLK1 inhibitors on the interaction between BRCA2 WT and PLK1. BRCA2 WT cells were treated with nocodazole (100 ng/ml, 14h), then treated with the PLK1 inhibitor BTO (50 μM, 2h) before harvesting. BRCA2 was pull-down with GFP-trap beads, immunocomplexes were resolved on 4-15% SDS-PAGE followed by WB using anti-PLK1 and -MBP antibodies. Unsynchronized BRCA2$^{+/+}$ were used as control of pull-down and StainFree images of the gels before transfer were used as loading control (cropped image is shown). The amount of PLK1 co-IPed with BRCA2 relative to the input levels of PLK1 and the amount of pull-down BRCA2 is presented below the blot, relative to non-treated BRCA2 WT. **(c)** The effect of CDK1 inhibitors on the interaction between 2xMBP-BRCA2$_{1-250}$ and PLK1. U2OS cells transiently transfected with the 2xMBP-BRCA2$_{1-250}$ WT, were arrested in mitosis with nocodazole (300 ng/ml, 14h) and then treated with CDK1 inhibitor (Ro-3306 50nM, 2h) before amylse pull-down. Complexes were resolved on 4-15% SDS-PAGE followed by WB using anti-PLK1 and anti-MBP antibodies. The amount of PLK1 co-immunoprecipitated with 2xMBP-BRCA2$_{1-250}$ relative to the input levels of PLK1 and the amount of pull-down 2xMBP-BRCA2$_{1-250}$ is presented below the blot as mean ± SD from three independent experiments. The data is presented relative to the non-treated BRCA2 WT. Imunoblots in (a) and (c) are representative of three independent experiments. Source data is available as a Source Data file.

Supplementary Fig 5

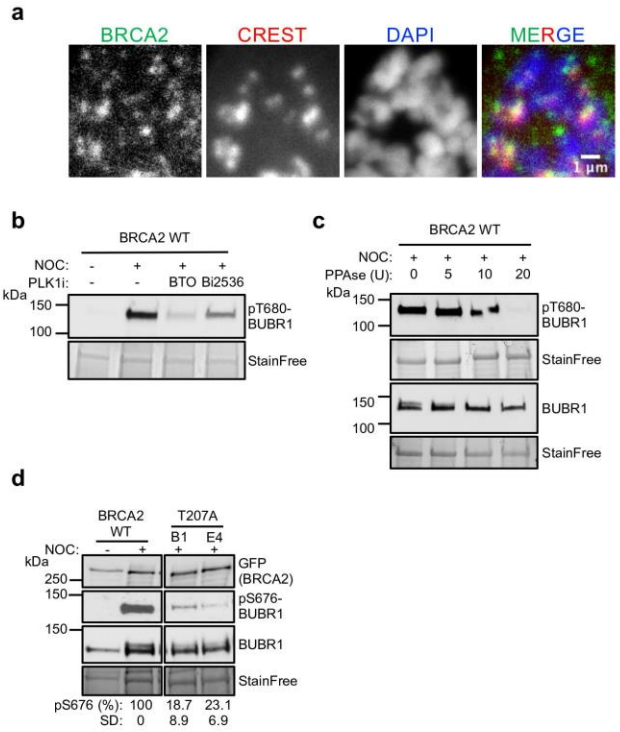

Supplementary Figure 5. Related to Figure 5**. BRCA2 at the kinetochores and effect of PLK1 inhibitors and phosphatase treatment on pT680-BUBR1.**

(a) Representative images of the localization of BRCA2 in nocodazole-arrested U2OS transient expressing GFP-MBP-BRCA2 WT. BRCA2 is detected by anti-BRCA2 rabbit antibody (CA1033), CREST is used as centromere marker and DNA is counterstained with DAPI. Scale bar represents 1 μm. The figures are representative of three independent experiments**. (b)** Protein levels of pT680-BUBR1 in BRCA2 WT stable clone after treatment with PLK1 inhibitors. After 14h culture with media containing nocodazole (100 ng/μl), PLK1 inhibitors (Bi2536 (50 nM) or BTO (50 μM)) were added to the media and the cells were cultured for additional 2h before harvesting. The level of pT680-BUBR1 was analyzed in the total protein extract by western blot. **(c)** Phosphatase (Fast AP) treatment of total protein lysate extracted from DLD1 BRCA2 WT cells treated with nocodazole (100 ng/μl) for 14h. **(d)** Western blot showing the expression levels of endogenous BUBR1 and pS676-BUBR1 in nocodazole treated stable clones of DLD1 BRCA2 deficient cells ($BRCA2^{-/-}$) expressing GFPMBP-BRCA2 WT (BRCA2 WT) or T207A variant. The levels of pS676-BUBR1 was analyzed in the total protein extract by western blot. The mean pBUBR1 signal relative to the stain free signal is shown for the nocadozole treated samples below the blots. Results are presented normalized to the protein levels for BRCA2 WT. The data represents the mean ± SD of two independent experiments. Imunoblots in (b-d) are representative of two (b, d) and three (c) independent experiments. Source data is available as a Source Data file.

Supplementary Fig. 6

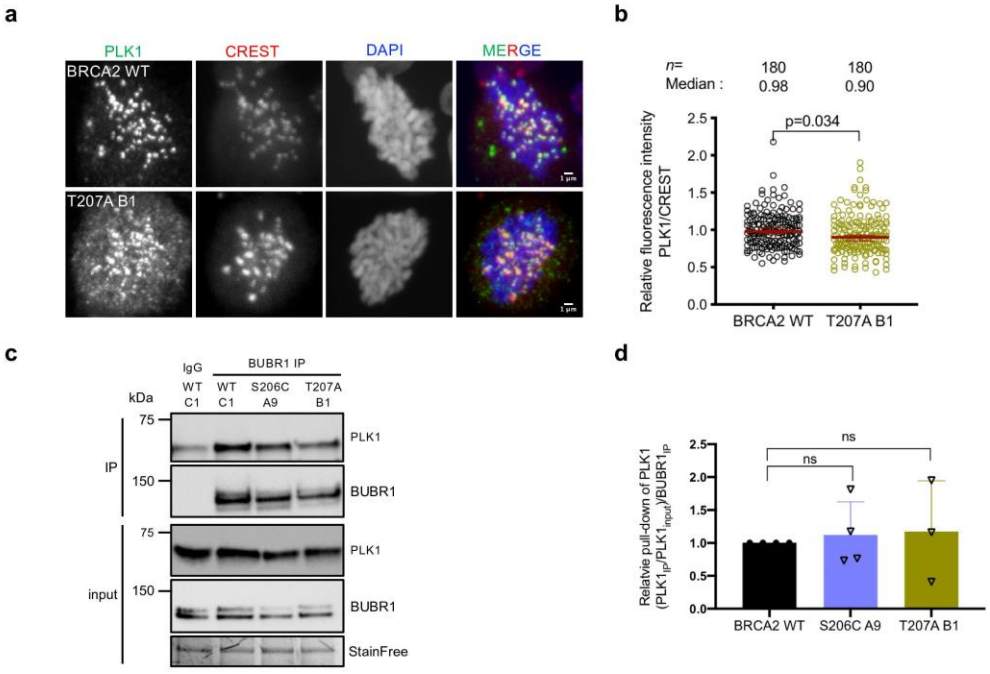

Supplementary Figure 6. Related to Figure 5. **Localization of BRCA2 and PLK1 at the kinetochores and PLK1-BUBR1 complex in cells bearing variant T207A compared to WT**

(a) Representative images of the localization of PLK1 in nocodazole-arrested DLD1 BRCA2$^{-/-}$ cells stably expressing GFP-MBP-BRCA2 WT or the variant T207A as indicated. CREST is used as centromere marker and DNA is counterstained with DAPI. Scale bar represents 1 μm. **(b)** Quantification of the co-localization of PLK1 and CREST in (a). The data represents the intensity ratio (PLK1:CREST) relative to the mean ratio of PLK1:CREST for the GFP-MBP-BRCA2 WT calculated from a total of 180 pairs of chromosomes analysed from two independent experiments (6 pairs of chromosomes/cell from 15 cells). The red line in the plot indicates the median (95% CI) ratio, each dot represents a pair of chromosomes. For statistical comparison of the differences between the samples we applied a Mann-Whitney two-tailed analysis, the p-values show significant difference. **(c)** Co-immunoprecipitation of endogenous PLK1 with endogenous BUBR1 from mitotic cell extracts of BRCA2 WT cells or cells expressing the variants S206C or T207A using mouse anti-BUBR1 antibody. Mouse IgG was used as control for the BUBR1 immunoprecipitation. The immuno-complexes were resolved on 4-15% SDS-PAGE followed by western blotting, the interactions were revealed by rabbit anti-BUBR1 and mouse anti-PLK1 antibodies. **(d)** Quantification of co-immunoprecipitated PLK1 in (c), relative to the input levels and the amount of immunoprecipitated BUBR1. Results are presented as the fold change compared to the BRCA2 WT clone. The data represents the mean ± SD of three to four independent experiments (WT (n=4), S206C A9 (n=4) and T207A B1 (n=3)). Statistical significance of the difference was calculated with one-way ANOVA test with Dunnett's multiple comparisons test, the p-values show the significant difference, ns: non-significant. Source data is available as a Source Data file.

Supplementary Fig. 7

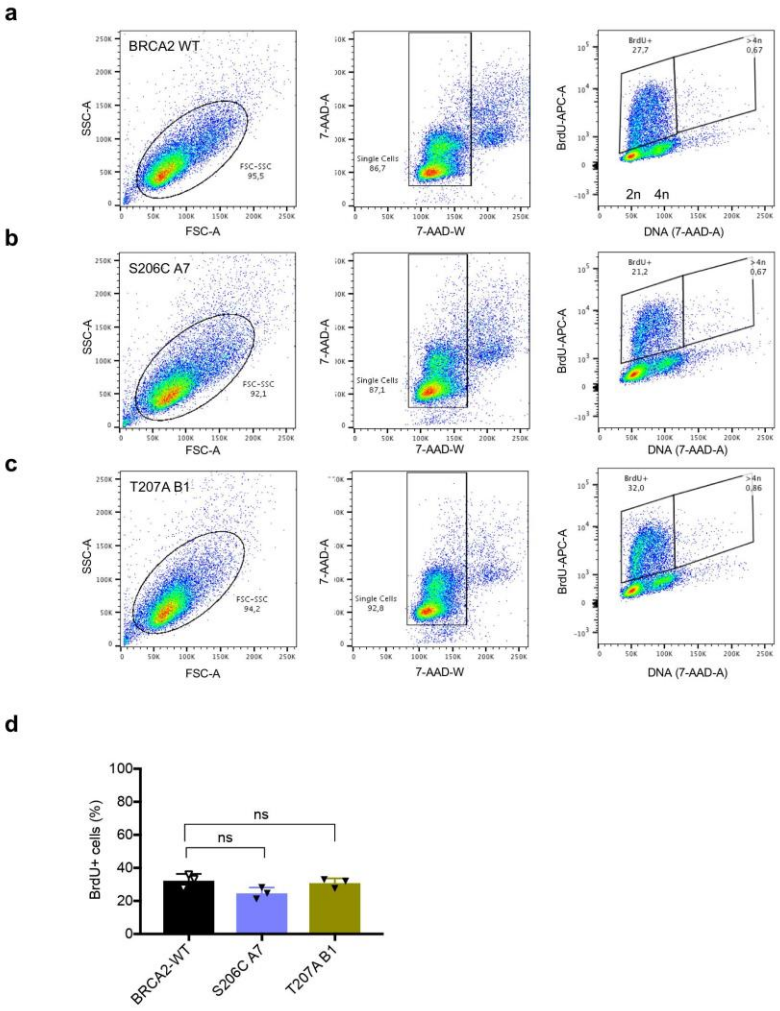

Supplementary Figure 7. Related to Figure 7**. BrdU incorporation measured by flow cytometry of DLD1 BRCA2$^{-/-}$ stable cell lines expressing BRCA2 WT or BRCA2 variants S206C and T207A.**

(a-c) Representative flow cytometry plots for the analysis of S-phase tetraploid cells (quantified in Figure 7c, d) in the stable DLD1 BRCA2 deficient cells expressing BRCA2 WT (a) or the VUS S206C (b) and T207A (c). Viable cells were gated from the Forward Scatter (FSC-A) versus Side Scatter (SSC-A) plots and displayed in a 7-AAD-W versus 7-AAD-A plot to exclude doublets. The gated singlet population was displayed in a APC-A (BrdU) versus 7-AAD-A (DNA) plot. The S-phase tetraploid population was gated as BrdU^{+} cells with DNA content >4N. 20,000 singlet events were collected for each experiment. **(d)** Frequency of BrdU^{+} cells in the stable clones expressing BRCA2 WT or the VUS as indicated. The data represents the mean ± SD of three independent experiments. Statistical significance of the difference was calculated with one-way ANOVA test with Tukey's multiple comparisons test (the p value show the difference compared to WT, ns: non-significant). Source data is available as a Source Data file.

Supplementary Fig. 8

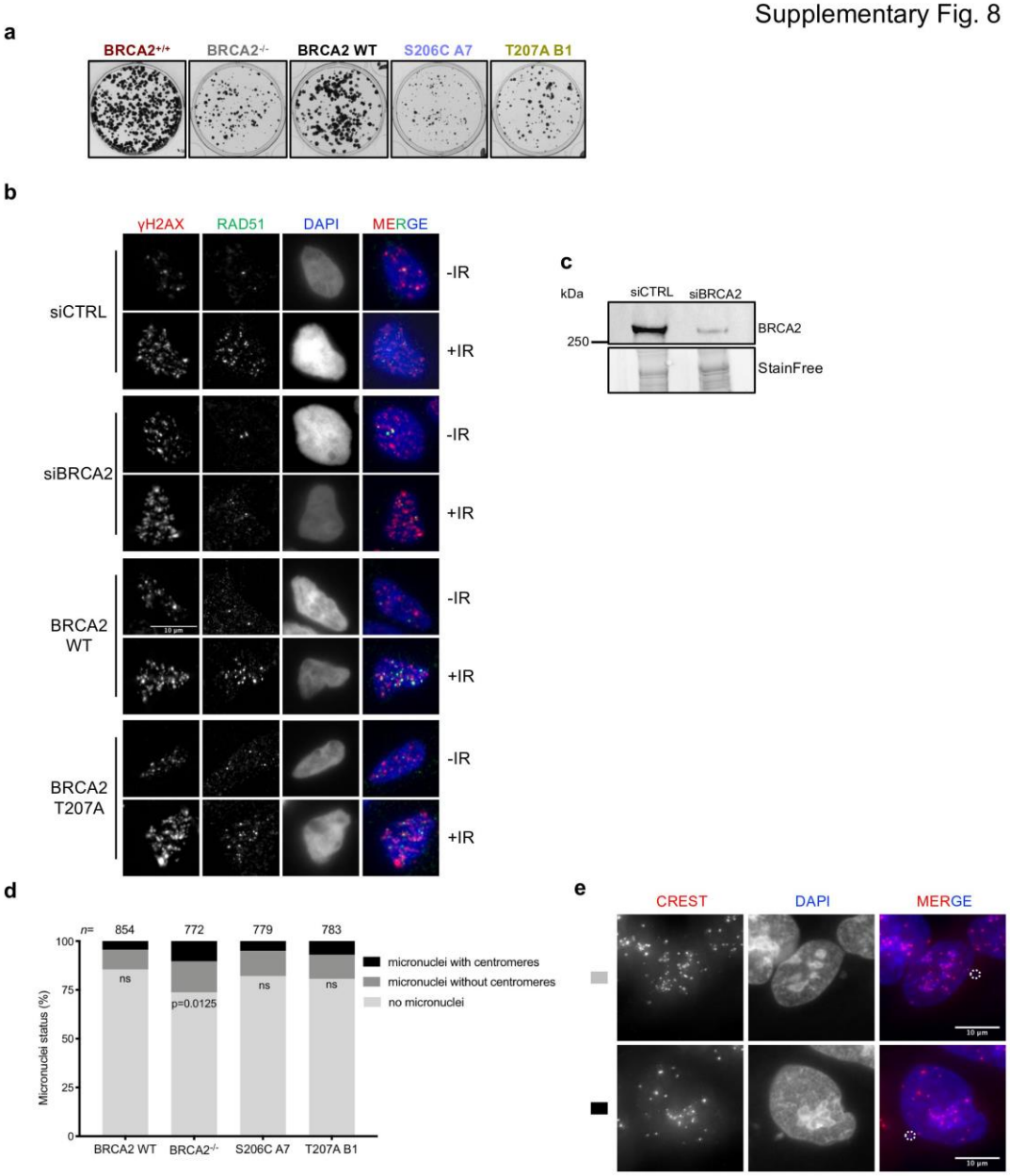

Supplementary Figure 8. Related to Figure 8**. Plating efficiency of unchallenged DLD1 BRCA2$^{-/-}$ stable clones expressing EGFP-MBP-BRCA2 WT or the variants. and representative images of DNA damage foci in these cells. Micronuclei in BRCA2$^{-/-}$ stable cell lines and BRCA2$^{-/-}$ expressing BRCA2 WT or BRCA2 variants S206C and T207A.** **(a)** Representative plates showing the number of colonies in unchallenged conditions of the cells assessed for MMC-clonogenic survival assay quantified in Fig. 9a (500 cells seeded per 6-well plate). **(b)** Representative immunofluorescence images of two independent experiments of nuclear γH2AX and RAD51 foci in DLD1 BRCA2$^{+/+}$ cells depleted of BRCA2 (siBRCA2), BRCA2$^{+/+}$control cells (siCTRL), DLD1 BRCA2 deficient cells (BRCA2$^{-/-}$) stably expressing BRCA2 WT or the variant T207A, in non-treated (-IR) or two hours after exposure to 6 Gy of γ-irradiation (+IR), as indicated in the images and as quantified in Fig. 9d, 9e. Scale bar represents 10 μm. **(c)** Representative Western blot of two independent experiments showing the levels of endogenous BRCA2 in the siRNA transfected cells imaged in (b) and analysed in Fig. 9d, 9e, at the time for radiation. **(d)** Frequency of micronuclei with and without centromeres in DLD1 BRCA2 deficient cells (BRCA2$^{-/-}$) and BRCA2$^{-/-}$ clones stably expressing BRCA2 WT or the variants S206C and T207A. *n* indicates the total number of cells counted for each clone from two independent experiments. Statistical significance of the difference was calculated with two-way ANOVA test with Tukey's multiple comparisons test, the p-values show the significant difference, ns: non-significant. **(e)** Representative images of micronuclei with and without centromeres observed in cells quantified in (d), scale bar represents 10 μm. Source data is available as a Source Data file.

Supplementary Fig. 9

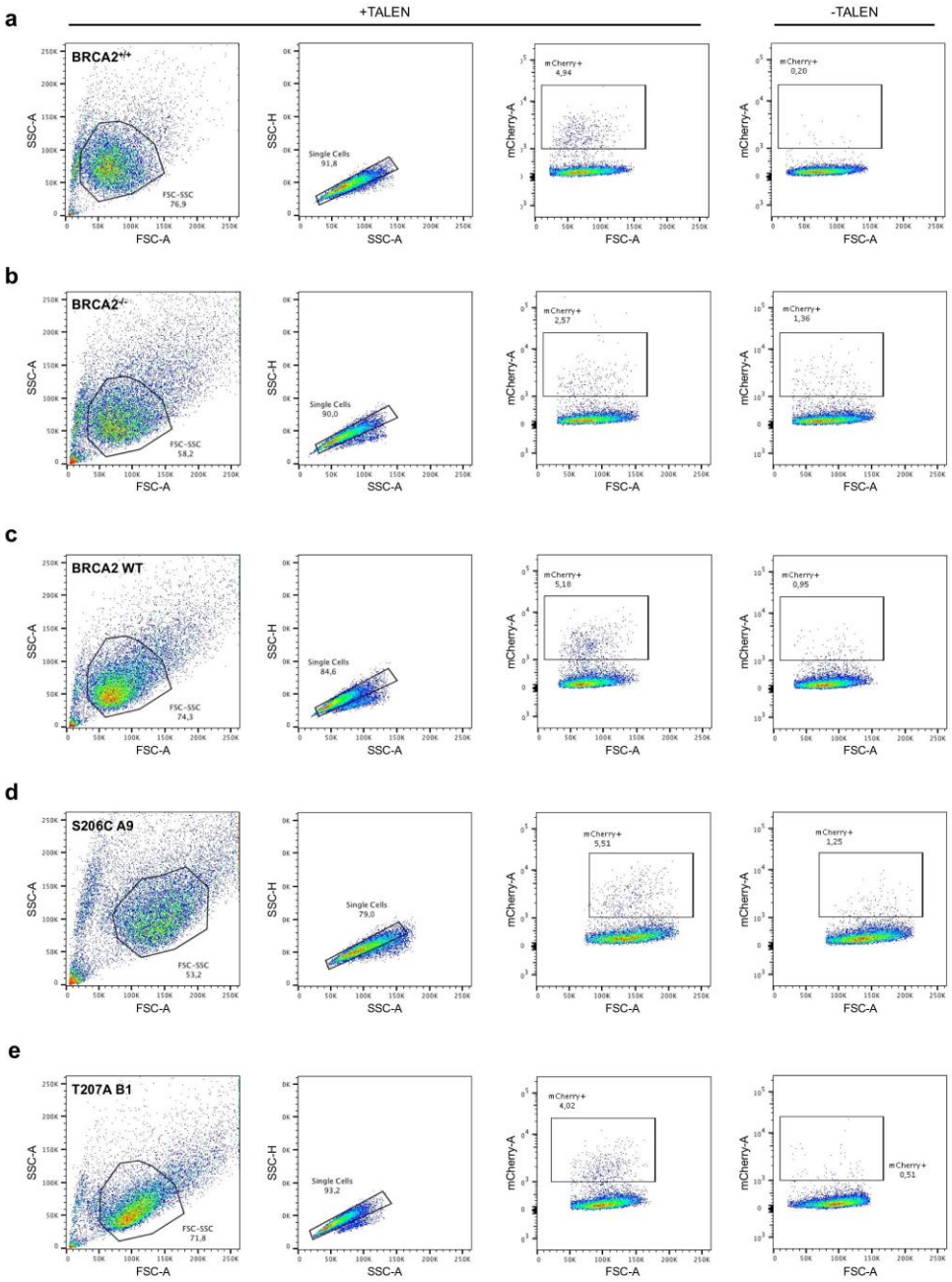

Supplementary Figure 9. Related to Figure 8f**. Frequency of mCherry positive cells measured by flow cytometry of DLD1 BRCA2$^{-/-}$ stable cell lines expressing BRCA2 WT or BRCA2 variants S206C and T207A.**

(a-e) Representative flow cytometry plots for the analysis of mCherry positive cells in the HR assay (quantified in Fig. 9f) in DLD1 cells with endogenous BRCA2 (BRCA2$^{+/+}$) (a), DLD1 BRCA2 deficient cells (BRCA2$^{-/-}$) (b), BRCA2 deficient cells expressing BRCA2 WT (c) or the VUS S206C (d) and T207A (e). Viable cells were gated from the Forward Scatter (FSC-A) versus Side Scatter (SSC-A) plots and displayed in a SSC-H versus SSC-A plot to exclude doublets. The gated singlet population was displayed in a mCherry-A versus FSC-A plot. The mCherry positive population was gated from non-transfected cells. 10 000 singlet events were collected for each experiment. Source data is available as a Source Data file.

Supplementary Figure 10

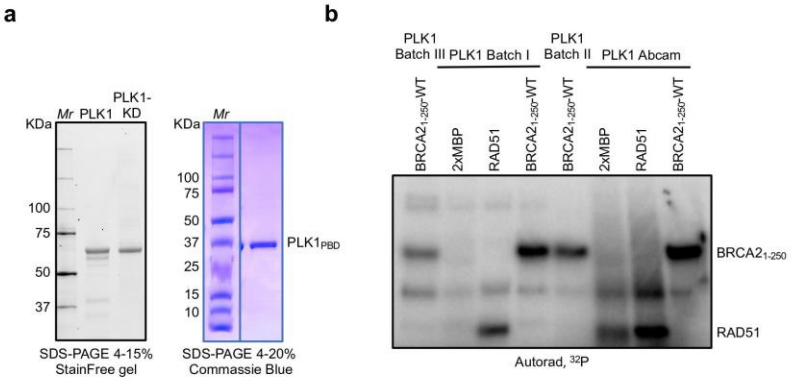

Supplementary Figure 10. SDS-PAGE of the PLK1, PLK1-KD and PLK1-PBD recombinant proteins utilized in this study and comparison of the kinase activity of each batch of PLK1

(a) SDS-PAGE showing purified PLK1, PLK1-K82R mutant (PLK1-KD) and $PLK1_{PBD}$. Human PLK1 was expressed and purified from sf9 insect cells using Ni-NTA column followed by a second purification step with a cationic exchange Capto S column. Purified PLK1 and PLK1-K82R protein (3 µg) were loaded on a 4-15% SDS-PAGE Stain-Free gel. For purification of $PLK1_{PBD}$, 6His-Sumo-$PLK1_{PBD}$ was expressed and purified from bacteria using a His-TRAP column, the His-tag was cleaved with 6xHis-SUMO Protease and the cleaved $PLK1_{PBD}$ was further purified using Ni-NTA agarose resin. The purified protein was loaded on a 4-20% SDS-PAGE (1.4 µg) and detected by Coomassie staining. *Mr;* molecular weight markers. **(b)** *In vitro* kinase assay with the purified PLK1 (0.1 µg) from (a) or PLK1 purchased from Abcam, 0.1 µg PLK1 was used in the kinase reaction with either RAD51 (25 ng) or purified 2xMBP-$BRCA2_{1-250}$ WT (0.5 µg) as substrate in the presence of [γ^{32}P]-ATP. The samples were resolved by 7.5 % SDS-PAGE and ^{32}P-labeled products were detected by autoradiography. Source data is available as a Source Data file.

Supplementary Table 1: Number of records in ClinVar and BRCAShare data bases of the variants identified in breast cancer patients altering the amino acids investigated in this work. The specific VUS utilized in this study are highlighted in bold.

VUS	ClinVar	BRCAShare
M192T	2	0
S196I	4	0
S196N	4	3
S196T	1	0
S206C	1	1
S206Y	1	0
T207A	3	0
T207I	4	0

Supplementary Table 2: Statistics table for the crystal structure of PBD_pT207, a complex between the Polo-Box Domain of human PLK1 (aa 365 to aa 603) and the 17aa peptide pT207 of BRCA2 (aa 194 to aa 210, threonine 207 being phosphorylated).

	PBD_T207 phosphorylated (PDB 6GY2)
Data collection	
Space group	P_1
Cell dimensions :	
a, *b*, *c* (Å)	50.000 56.040 61.030
α, β, γ (°)	80.79 79.23 65.05
Molecules per a.u	2
Resolution (Å)	59.70 – 3.106 (3.106 – 3.16)
R_{merge}	0.056 (0.346)
R_{meas}	0.076 (0.466)
R_{pim}	0.051 (0.31)
I/σ (I)	10.1 (2.3)
$CC_{1/2}$	0.997 (0.821)
Completeness (spherical, %)	93.7 (96.9)
Redundancy	1.94 (1.977)
B Wilson (Å²)	76.9 (78.86)
Multiplicity	1.9 (2.0)

Refinement	
Resolution (Å)	22.57 - 3.11 (3.11 – 3.15)
No. reflections	9911
R_{work} / R_{free}	0.189/0.215
No. Atoms	
Protein	3788
Heterogen atoms	28
Water	22
R.m.s. deviations	
Bond lengths (Å)	0.007
Bond angles (°)	0.97

*Values in parentheses are for highest-resolution shell.

Supplementary Table 3: Primers used to introduce point mutations in EGFPMBP-BRCA2, 2xMBP-BRCA2$_{1-250}$, GST-BRCA2$_{190-284}$ constructs

Mutation	Oligo name	Sequence (5'-3')
S193A	Fw : oAC543	CCC ACC CTT AGT TCT GCT GTG CTC ATA GTC
	Rv : oAC544	GAC TAT GAG CAC AGC AGA ACT AAG GGT GGG
M192T	Fw : oAC283	GTGGATCCTGATACGTCTTGGTCAAGTTC
	Rv : oAC284	GA ACT TGA CCA AGA CGT ATC AGG ATC CAC
S196N	Fw : oAC026	CCTGATATGTCTTGGTCAAATTCTTTAGCTACA CCACC
	Rv : oAC027	GGTGGTGTAGCTAAAGAATTTGACCAAGACAT ATCAGG
S206C	Fw : oAC028	CCACCCACCCTTAGTTGTACTGTGCTCATAGTC AG
	Rv : oAC029	CTGACTATGAGCACAGTACAACTAAGGGTGGG TGG
T207A	Fw : oAC545	GGA TCC TGA TAT GGC TTG GTC AAG TTC TTT AGC

	Rv : oAC546	GCT AAA GAA CTT GAC CAA GCC ATA TCA GGA TCC

Supplementary Table 4: Sequencing primers

Construct	Oligo name	Binding site	Sequence (5'-3')
GFPMBP-BRCA2, GST-BRCA2$_{190-284}$	Rv : oAC131	aa 273 BRCA2	TTAGTTCGACTTATCCAATGTGGTCTTT
2xMBP-BRCA2$_{1-250}$	Fw : oAC149	aa 1-6 BRCA2	TTATTTGCTAGCCCTATTGGATCCAAAGAG
PLK1	Fw : oAC907	aa 38 PLK1	AAAGAGATCCCGGAGGTCCTAGTG

Supplementary Table 5: Primers used to subclone BRCA2$_{190-284}$ into the pGEX-6P-1 vector

Construct	Oligo name	Sequence (5'-3')
BRCA2$_{190-284}$	Fw: oAC130	TTAGGATCCATGTCTTGGTCAAGTTCT
	Rv: oAC131	TTAGTTCGACTTATCCAATGTGGTCTTT

Supplementary Table 6: Primers used to subclone *PLK1* cDNA into pFastBac HT

Primer name	Sequence (5'-3')
GA_pFBtev_R	GCCCTGAAAATACAGGTTTTCGGTCGTTGGGAT

GA_pFB_UTR_F	TTGTCGAGAAGTACTAGAGGATCATAATCA
GA_hPLK_F	ATCCCAACGACCGAAAACCTGTATTTTCAGGGCATGAGTGCTGCAGTGACTGCA
GA_hPLK_R	TGATTATGATCCTCTAGTACTTCTCGACAATTAGGAGGCCTTGAGACGGTT

Supplementary Table 7: Primers used to introduce K82R point mutation in pFastBAC-PLK1 vector to produce PLK1-KD and to subclone $PLK1_{PBD}$ (aa 326-603) into pT7-His6-SUMO

Product	Oligo name	Sequence (5'-3')
K82R-PLK1	Fw : oAC905	GCG GGCAGGATTGTGCCTAAG
	Rv : oAC906	CTTAGGCACAATCCTGCCCGC
$PLK1_{PBD}$	GA_PLKPDBwt_F	ATTGAGGCTCACCGCGAACAGATTGGTGGCTCGATTGCTCCCAGCAGCCT
	GA_PLKPDBwt_R	TTCCTTTCGGGCTTTGTTAGCAGCCGGTCATTAGGAGGCCTTGAGACGGT

Supplementary Table 8: Primers used to introduce S670D, S676D and T680D point mutations in pcDNA3-3xFlagBUBR1-RFP construct

Name	Sequence (5'-3')
oAC884	CAA GAA GCT GGA CCC AAT TAT TGA AGA CGA TCG TGA AGC CGA CCA CTC CTC
oAC885	GAG GAG TGG TCG GCT TCA CGA TCG TCT TCA ATA ATT GGG TCC AGC TTC TTG

Supplementary Table 9: Synthetic peptide sequences for Isothermal Titration Calorimetry (ITC) and X-ray crystallography

Peptide	Sequence
pS197	DMSWSS{pS}LAT
T207	WSSSLATPPTLSSTVLI
pT207	WSSSLATPPTLSS{pT}VLI
T207A	WSSSLATPPTLSSAVLI
T207D	WSSSLATPPTLSSDVLI
CpT207	WSSSLATPPTLSC{pT}VLI

Supplementary Table 10: Primers for amplifying BRCA2 (aa 1-267) from genomic DNA

Primer name	Sequence (5'-3')
Fw : oAC035	GGTCGTCAGACTGTCGATGAAGCC
Rv : oAC056	CAAAGAGAAGCTGCAAGTCATGGATTTGAAAAAACATC AGGG

Supplementary Table 11: Oligos used for replacing GFP in AAVS1-2A-GFP to mCherry using Gibson Assembly strategy

Construct	Oligo name	Sequence (5'-3')
AAVS1-2A	Fw: oAC537	TAAAGCGGCCGCGTCGAGTCTAGAGGG
	Rv: oAC538	CATCTCGAGCCTAGGGCCGGG
AAVS1-2A-mCherry	Fw: oAC539	cccggccctaggctcgagatgGTGAGCAAGGGCGA GGAGGATAAC

	Rv: oAC540	ctctagactcgacgcggccgctttaCTTGTACAGCTCGTCCATGCCGC

Supplementary Table 12: TALEN sequences used in DSB-mediated gene targeting assay

Name	Sequence (5'-3')
TALEN AAVS 5'	TCCCCTCCACCCCACAGT
TALEN AAVS 3'	AGGATTGGTGACAGAAAA

université PARIS-SACLAY

ECOLE DOCTORALE N°582 : CANCEROLOGIE : BIOLOGIE - MEDECINE - SANTE (CBMS)

Titre : Rôle de l'association entre BRCA2 et DDX5 lors de la réponse aux dommages de l'ADN

Mots clés : BRCA2, recombinason homologue, cancer du sein, intéraction proteine-proteine, DDX5, DNA-RNA hybrids

Résumé :

Un nombre croissant d'études soutiennent le fait que les protéines majeures du métabolisme des ARN, telles que les hélicases ARN, sont impliquées dans la réponse aux dommages à l'ADN. Cette activité est généralement accomplie par leur interaction avec des facteurs de réparation de l'ADN. BRCA2, une protéine suppressive de tumeurs, joue un rôle crucial dans la réparation des cassures double-brin (CDB) de l'ADN par recombinaison homologue (RH) et donc, est un facteur essentiel pour l'intégrité du génome. Les cellules déficientes pour BRCA2 accumulent des hybrides ADN-ARN ou R-loops, une source de dommage à l'ADN, suggérant ainsi l'importance de cette protéine dans la prévention ou la suppression de ces structures. Toutefois, le rôle spécifique de BRCA2 dans la résolution des hybrides ADN-ARN reste inconnu.

Afin de connaître des potentiels partenaires de BRCA2, une analyse par spectrométrie de masse réalisée dans notre laboratoire a révélé un enrichissement en protéines impliquées dans le métabolisme de l'ARN, comme les hélicases ARN. Ces résultats nous ont menés à examiner la coopération entre BRCA2 et les hélicases ARN dans la séparation des structures ADN-ARN. Nous avons d'abord confirmé l'interaction entre l'hélicase ARN DDX5 et BRCA2, qui est améliorée dans les cellules exposées à γ-irradiation. Ensuite, nous avons réduit l'interaction aux premiers 250 aa de BRCA2 (BRCA2T1) et avons constaté que celle-ci est directe en utilisant des protéines purifiées. En collaboration avec le laboratoire du docteur A. Aguilera (Cabimer, SP), nous avons montré que la déplétion de DDX5 conduit à une accumulation des hybrides ADN-ARN dans l'entièreté du génome, particulièrement aux sites de dommages à l'ADN. De plus, nos résultats indiquent que DDX5 localise aussi aux hybrides ARN-ADN qui se forment à proximité de CDB.

De manière intéressante, nous avons constaté que BRCA2 est important pour la rétention de DDX5 aux sites de dommage à l'ADN induit par l'irradiation laser. Notamment, des tests de déroulement de brins in vitro en utilisant les protéines purifiées DDX5 et BRCA2 ont révélé que BRCA2 stimule l'activité de déroulement des R-loops de DDX5. Un variant de signification inconnue (VSI) trouvé dans de patients atteints de cancer du sein situé dans la région BRCA2T1 (T207A) réduit l'interaction de BRCA2 avec DDX5 et conduit à l'accumulation des hybrides ADN-ARN. Les cellules exprimant stablement BRCA2-T207A montrent également une diminution de l'association de DDX5 avec les hybrides ARN-ADN, en particulier lors d'une exposition de cellules à a l'irradiation. L'analyse de l'efficacité de la réparation des CDB par RH dans les cellules déficientes en DDX5 ou exprimant BRCA2-T207A, montre une cinétique retardée de l'apparition des foyers de réparation RAD51 lors de l'irradiation, ce qui suggère un rôle actif de l'interaction BRCA2-DDX5 pour assurer la réparation par RH efficacement. En accord avec cette hypothèse, la ribonucléase RNAseH1, qui dégrade spécifiquement la fraction d'ARN dans les structures d'ADN-ARN, restaure partiellement le phénotype de cinétique des foyers RAD51 dans les cellules BRCA2 T207A. De plus, les cellules portant le variant BRCA2-T207A ont également montré un nombre réduit de foyers RPA par rapport aux cellules qui expriment BRCA2 sauvage, témoins d'un défaut dans l'étape qui précède le chargement de RAD51 aux CDB.

Ensemble, nos résultats suggèrent que les hybrides ADN-ARN représentent un obstacle à la réparation des CDB par RH et révèlent BRCA2 et DDX5 en tant que facteurs actifs dans leur suppression.

Title : Role of the interaction of BRCA2 and DDX5 in DNA damage response

Keywords : BRCA2, homologous recombination, breast cancer, protein-protein interaction, DDX5, DNA-RNA hybrids

Abstract : Increasing evidence support the idea that proteins involved in RNA metabolism such as RNA binding proteins (RBPs) and RNA helicases are directly implicated in the DNA damage response (DDR). This activity is generally achieved through their interaction with DNA repair factors.

BRCA2 is a tumor suppressor protein that plays an important role in the repair of DNA double-strand breaks (DSBs) by homologous recombination (HR) as well as protecting stalled replication forks from unscheduled degradation; therefore, it is essential to maintain genome integrity. Interestingly, BRCA2 deficient cells accumulate DNA-RNA hybrids or R-loops, a known source of DNA damage and genome instability, providing evidence for its role in either R-loop prevention or processing. However, the specific role of BRCA2 on these structures remains poorly understood.

A mass spectrometry screen to identify partners of BRCA2 performed in our laboratory revealed an enrichment of proteins involved in RNA metabolism such as RNA helicases. These findings led us to investigate whether BRCA2 could cooperate with these candidate interacting RNA helicases in processing DNA-RNA structures. First, we confirmed the interaction of BRCA2 and the DEAD-box RNA helicase DDX5, which we found is enhanced in cells exposed to ·-irradiation. Then, we narrowed down the interaction to the first 250 aa of BRCA2 (BRCA2T1) and found that it is direct using purified proteins. In collaboration with A. Aguilera lab (Cabimer, SP), we could show that depletion of DDX5 leads to a genome-wide accumulation of DNA-RNA hybrids that is particularly enriched at DNA damage sites. DDX5 associates with DNA-RNA hybrids that form in the vicinity of DSBs. Interestingly, we found that BRCA2 is important for the retention of DDX5 at laser irradiation-induced DNA damage. Notably, in vitro R-loop unwinding assays using purified DDX5 and BRCA2 proteins revealed that BRCA2 stimulates the R-loop helicase activity of DDX5.

A breast cancer variant of unknown clinical significance (VUS) located in BRCA2T1 (T207A) reduced the interaction between BRCA2 and DDX5 and led to the accumulation of DNA-RNA hybrids. Cells stably expressing BRCA2-T207A also showed a decreased association of DDX5 with DNA-RNA hybrids, especially upon irradiation. Notably, monitoring RAD51 foci to evaluate HR-mediated DSBs repair efficiency in either DDX5-depleted cells or in BRCA2-T207A cells resulted in a delayed kinetics of appearance of RAD51 foci upon irradiation suggesting an active role of BRCA2-DDX5 interaction in ensuring timely HR repair. In agreement with this, overexpression of the RNAseH1 ribonuclease, that specifically degrades the RNA moiety in DNA-RNA structures, partially restored RAD51 kinetics phenotype of BRCA2-T207A cells. Moreover, cells bearing BRCA2-T207A variant also showed a reduced number of RPA foci compared to BRCA2 WT expressing cells, a step that precedes RAD51 loading at DSBs.

Taken together, our results are consistent with DNA-RNA hybrids being an impediment for the repair of DSBs by HR and reveal BRCA2 and DDX5 as active players in their removal.